



THESE INSA Rennes
sous le sceau de l'Université européenne de Bretagne
pour obtenir le titre de
DOCTEUR DE L'INSA DE RENNES
Spécialité : Génie Civil

présentée par
Jiong ZHANG
ECOLE DOCTORALE : SDLM
LABORATOIRE : LGCGM

Experimental and Numerical Investigations of Flow and Solid Transport in Urban Area

Thèse soutenue le 13.03.2012
devant le jury composé de :

Abdelhak AMBARI
Professeur à l'E.N.S.A.M. d'Angers / *président*
Didier MAROT
Maître de Conférences HDR à l'I.U.T. de Saint-Nazaire / *rapporteur*
Nicolas LECOQ
Maître de Conférences HDR à l'Université de Rouen / *rapporteur*
Keld Rømer RASMUSSEN
Professeur à l'Université d'Aarhus, Danemark / *examineur*
Alexandre VALANCE
Directeur de Recherche à l'Université de Rennes 1 / *examineur*
Pascal DUPONT
Maître de Conférences à l'I.N.S.A. de Rennes / *Co-encadrant*
Mustapha HELLOU
Professeur à l'I.N.S.A. de Rennes / *Directeur de thèse*

Experimental and Numerical Investigations of Flow and Solid Transport in Urban Area

Jiong ZHANG



En partenariat avec



To my parents

Acknowledgments

This work has been done in the Laboratoire de Génie Civil et Génie Mécanique (LGCGM) of the Institut National des Sciences Appliquées de Rennes (INSA de Rennes). I would like to express my gratitude to my directeurs de la recherche, Prof. Mustapha HELLOU and MCF Pascal DUPONT for their inspiration, guidance, encouragement and friendship during the course of this work. Working with them has been a rewarding and enjoyable experience.

As a recipient of China Scholarship Council (CSC) scholarship I want to thank CSC for the financial support, and the Education Section of the Chinese Embassy in France for their help and kind attention.

I also wish to express my appreciation to the rapporteurs, MCF-HDR Didier MAROT and MCF-HDR Nicloas LECOQ, and all the members of the committee, Prof. Abdelhak AMBARI, Prof. Keld Rømer RASMUSSEN, and Prof. Alexandre VALANCE, for their valuable comments and review of this dissertation.

Special appreciation is extended to M. Jean-Jacques KERMAREC, the technical personal in laboratory of Géosciences Rennes, Mme. Nathalie CHOLLET the secretary of our laboratory, Dr. Guoqing JING and Dr. Boumedienne BENMEZROUA, who used to work in laboratory of LGCGM for their help and encouragement.

I would also like to thank the secretariat de l'Ecole doctorale for their help, encouragement and kind attention.

I would also like to thank all Ph.D. students from the laboratory: Amphone VONGVIXAY, Thai-Hoa NGUYEN, Soksan CHHUN, Baghdad KROUR, Sovanvichet LIM, Nhan-Hoa NGUYEN, Son-Tung PHAM, Ty SOY, Khac Chien THAI ...

Also, I would like to thank all my friends from INSA de Rennes: Dr. Cunsheng ZHANG, Dr. Pengcheng MU, Dr. Fan SUN, Dr. Hui BIAN, Dr. Ming LIU, Dr. Xiao BAI, Dr. Fen ZHOU, Yanyan CAO, Yun LUO, Cong BAI, Xing-Rong CHU, Shunying ZHANG, Linning PENG, Jinglin ZHANG ... for their encouragement and friendship.

Finally, my deepest gratitude goes to my parents, for their forever support and love. You are always who I can count on, and you will always be.

Acknowledgments

Contents

Chapter 1 Introduction	7
1.1 General background.....	7
1.2 Objectives of this research.....	8
1.3 Structure of thesis	8
Chapter 2 Literature Review of Particle Transport.....	11
2.1 Introduction	11
2.2 A brief review of pipe flow and open channel flow	11
2.2.1 Pipe flow.....	12
2.2.2 Open channel flow.....	15
2.3 Flow over and within the saturated porous medium.....	18
2.4 Critical velocity for particle erosion.....	21
2.5 The transport of sediment particles	24
2.6 Sediments clogging in the porous medium.....	29
Chapter 3 Numerical Method.....	31
3.1 Introduction	31
3.2 Computational Fluid Dynamics (CFD)	32
3.2.1 Governing equations.....	32
3.2.1.1 Law of mass conservation	33
3.2.1.2 Law of conservation of momentum.....	33
3.2.1.3 Energy equations	33
3.2.2 Standard $k-\varepsilon$ model	33
3.2.3 Numerical analysis method	34
3.2.3.1 Discretization method.....	34
3.2.3.2 Derivation of algebraic equations.....	36
3.2.3.3 Under-relaxation.....	38
3.2.4 Volume of Fluid (VOF) method.....	38
3.3 Discrete Element Method (DEM)	39

3.3.1 Particles movement	39
3.3.2 Time-step.....	41
3.3.3 Damping	41
3.3.4 Contact Model	42
3.4 CFD and DEM two-way coupling.....	43
3.5 Validation test of the method	45
3.6 Conclusions	50
Chapter 4 Experimental Method	51
4.1 Description of the experimental settings	51
4.1.1 Design of hydraulic parameters in the study	51
4.1.2 Flow channel	52
4.1.3 Water supply.....	54
4.1.4 The measure of flow rate.....	54
4.1.5 Particle adding device.....	55
4.1.6 Porous bed	55
4.2 Measure of the particle velocity	58
4.3 Measure of the flow velocity field by a PIV system	58
4.4 Conclusions	62
Chapter 5 Free Surface Flow over a Porous Bed in an Open Channel	63
5.1 Introduction	63
5.1.1 Experimental setup.....	63
5.1.2 Process of the experiment.....	64
5.1.3 Numerical setup.....	65
5.2 Parameters of the study	65
5.3 Results and analysis.....	66
5.3.1 Raw results	66
5.3.2 Reference case	68
5.3.3 Flow regimes	69
5.3.4 Flow depth.....	70

5.3.4.1 Influence of channel slope.....	70
5.3.4.2 Influence of flow rate	71
5.3.5 Velocity distributions above and within the porous region.....	72
5.3.5.1 Influence of channel slope.....	72
5.3.5.2 Influence of flow rate	74
5.3.6 Shear velocity	76
5.3.7 Turbulent kinetic energy above and within the porous region	81
5.3.7.1 Influence of channel slope.....	81
5.3.7.2 Influence of flow rate	83
5.4 Conclusions	86
Chapter 6 Particle Incipient Motion over a Porous Bed.....	89
6.1 Introduction	89
6.1.1 Experimental setup.....	89
6.1.2 Process of the experiment.....	90
6.1.3 Numerical setup.....	91
6.2 Parameters of the study	91
6.3 Results and analysis.....	92
6.3.1 Influence of channel slope.....	92
6.3.2 Influence of particle diameter.....	95
6.4 Conclusions	99
Chapter 7 Particle Transport over a Porous Bed.....	101
7.1 Introduction	101
7.1.1 Experimental setup.....	101
7.1.2 Process of the experiment.....	102
7.1.3 Numerical setup.....	103
7.2 Parameters of the study	103
7.3 Results and analysis.....	105
7.3.1 Raw results	105
7.3.2 Particle transport velocity.....	105

7.3.2.1 Influence of channel slope.....	106
7.3.2.2 Influence of flow rate	107
7.3.2.3 Influence of particle diameter.....	108
7.3.3 Analysis of particle velocity distribution along the vertical direction.....	109
7.3.3.1 Influence of channel slope.....	110
7.3.3.2 Influence of inflow rate	113
7.3.3.3 Influence of particle diameter.....	115
7.3.4 Analysis of particle motion in flow	118
7.3.5 Analysis of horizontal component of particle velocity distribution in ascent and descent motion.....	121
7.3.6 The mean vertical component of particle velocity distribution in ascent and descent motion.....	123
7.3.7 Formula for determining the velocity of particle.....	126
7.4 Conclusions	128
Chapter 8 Sediment Clogging Phenomenon in an Open Channel with a Porous Bed ..	131
8.1 Introduction	131
8.1.1 Experimental setup.....	131
8.1.2 Process of the experiment.....	132
8.2 Parameters of the study	133
8.3 Results and analysis.....	134
8.3.1 Sediment clogging.....	134
8.3.2 Sediment transport rate over porous bed	135
8.3.2.1 Influence of inflow rate	136
8.3.2.2 Influence of channel slope.....	139
8.3.2.3 Influence of particle diameter.....	142
8.3.2.4 Influence of seepage outflow rate.....	144
8.3.2.5 Empirical bed-load transport relation	145
8.4 Conclusions	146
Chapter 9 General Conclusions	149
9.1 Free surface flow over a porous bed in an open channel.....	149

9.2 Particle incipient motion over a porous bed	150
9.3 Particle transport over a porous bed	151
9.4 Sediment clogging phenomenon in an open channel with a porous bed	152
9.5 Suggestions for further research.....	152
9.5.1 From experimental point of view	152
9.5.2 From numerical point of view	153
References	155
Appendix	161
List of Symbols	175

Chapter 1

Introduction

1.1 General background

In modern society, land development can increase the amount of stormwater runoff and its associated pollutant loads to receiving waters (Barrett et al., 1998). Several authors have studied stormwater runoff carries off dissolved, colloidal and solids components from the urban surfaces (e.g. Chang and Crowley, 1993 and Ball et al., 2000).

A porous medium is a material containing large number of randomly located voids (pores) of sizes greater than the microscopic interatomic scale such as soil, rocks, sponge, etc. Transport phenomena at the interface between a fluid and porous medium has remained an important topic of research because of their fundamental interest in understanding the phenomena of infiltration into the porous medium and its wide field of applications in industry and environmental analyses, for example, urban hydrology, river hydraulics, pollution and remediation of soils, water treatment, etc.

As in urban hydrology field, the erosion and clogging phenomena of road cause a lot of economic losses and even threaten the people's lives, because these are the results of an effect of sediment transport caused by flow after rains, a better understanding of details of flow structures near the surface of road (a kind of porous medium) will help to improve the design of road and provide optimized solutions.

Chapter 1: Introduction

Flows over a porous medium are the flows combined both over and through the porous medium. Because of the interaction between surface flow and seepage flow inside porous region, this interaction affects both the flow discharge and the sediment discharge.

In recent years, due to the development of the computational capacity, a complex computational fluid dynamics (CFD) could be performed. Meanwhile the discrete element method (DEM), developed by Cundall and Strack (1979), has been used extensively to investigate the behavior of granular solids subjected to a variety of loading conditions with the goal of understanding and predicting quantitative results.

1.2 Objectives of this research

The aim of this research was to study the characteristics of a free surface flow over a porous bed in an open channel and the sediment transport by this kind of flow numerically and experimentally.

A 3D CFD-DEM method was used for simulation of complicated behavior including interaction between particle and fluid in the combined domain, involving both a porous region and a clear fluid region. This methodology will have a wider application to granular solids transport in flows in general.

A series of laboratory experiments were carried out using a channel consists of a platform with supports that allow adjustment of the slope, and a layer of porous media was placed at the bottom of the channel. A Particle Image Velocimetry (PIV) system was used to obtain the flow velocity field and a high speed camera was used to capture the velocity of particles.

1.3 Structure of thesis

The thesis is divided into eight chapters. A brief outline of each chapter is described below.

Chapter 1 presents the background and objectives of this research.

Chapter 2 reviews the literature relevant to this thesis. It focuses on flows over and within a porous medium and particle transport.

Chapter 3 describes numerical method used in this research. That includes the Equations of fluid dynamics, Equations of particles and CFD-DEM two-way coupling method.

Chapter 4 describes the experimental method to validate simulation results. That includes the experimental design and measuring methods.

Chapter 1: Introduction

Chapter 5 studies the characteristics of a free surface flow over a porous bed in an inclined open channel numerically and experimentally. Effects of the dynamic characteristics of open channel and porous bed, such as channel slope, inflow rate, and seepage outflow rate, on the free surface flow are investigated.

Chapter 6 focuses on the problem in studying critical velocity of grain over porous medium in open channel.

Chapter 7 presents the research on single particle transport in open channel over a porous bed. Effects of the dynamic characteristics of porous medium, including channel slope, inflow rate, seepage outflow rate, and particle size on the particle movement are further investigated.

Chapter 8 aims at solving the problem in studying sediment clogging in open channel over a porous bed.

Chapter 9 summarizes the general conclusions of the whole thesis and makes recommendations for further work.

Chapter 2

Literature Review of Particle Transport

2.1 Introduction

Sediment dynamics in geophysical flows has been the centre of a great deal of research over the last century. In recent years, because of the development of the computational capacity, complex CFD and DEM calculation could be performed to understand the phenomenon at the grain scale.

This review consists of three main parts:

- A brief review of pipe flow and open channel flow;
- A review of flows over and within a porous medium;
- A review of the critical velocity for particles;
- A review of the sediment transport in open channel flow;
- A brief review of the particle clogging in the porous medium.

2.2 A brief review of pipe flow and open channel flow

The flow of water in a conduit may be either an open channel flow or a pipe flow. Compared with pipe flow the open channel flow differ in one important aspect that it must have a moving free surface, whereas pipe flow has none.

Chapter 2: Literature Review of Particle Transport

It is much more difficult to solve problems of flow in open channels than in pipes. Flow conditions in open channels are complicated by the position of the free surface which could change with time and space, and also by the fact that the depth of the flow, the discharge rate, and the slopes of the channel bottom and of the free surface are all inter dependent.

Treatment of roughness also poses a greater problem in open channels than in pipes. Although there may be a wide range of roughness in a pipe from polished metal to highly corroded iron, open channels may be of polished metal up to natural channels with long grass and roughness interacting with the flow depth.

2.2.1 Pipe flow

One of the most particular cases of flow may be laminar flow. This flow is characterized by fluid particles moving along smooth paths in laminas or layers, with one layer gliding smoothly over an adjacent layer.

In the case of laminar flow, the Hagen–Poiseuille law gives the pressure drop in a fluid flowing through a long pipe of uniform cross-section, which can be derived directly from the Navier–Stokes equation (White, 2003). The assumptions of the equation are that the flow is laminar, viscous and incompressible and that the flow passes through a constant circular cross-section that is substantially longer than its diameter. The Hagen–Poiseuille equation is:

$$U_w = \frac{\Delta H}{\Delta L} \frac{\rho g D_H^2}{32\mu} \quad (2-1)$$

where U_w is the mean velocity; ΔH is the head loss due to friction; D_H is the pipe diameter; μ is the viscosity of the flow; g is the gravity.

Taking the Darcy-Weisbach formula for head loss due to friction:

$$\Delta H = f \frac{\Delta L}{D_H} \frac{U_w^2}{2g} \quad (2-2)$$

Take (2-2) into the equation Hagen-Poiseuille (2-1), then the friction coefficient f is:

$$f = \frac{64}{Re} \quad (2-3)$$

with the Reynolds number Re is defined as:

$$Re = \frac{U_w D_H}{\nu} \quad (2-4)$$

The Reynolds number Re is the criterion for determining the type of flow. The limits for laminar and turbulent are:

Laminar: $Re < 2000$

Chapter 2: Literature Review of Particle Transport

Turbulent: $Re > 4000$

Ludwig Prandtl (1875-1953), the German genius engineer, introduced the boundary layer theory in 1904. One of his earliest students, Paul R. H. Blasius, provided a mathematical basis for boundary-layer drag and showed as early as 1911 that the resistance to flow through smooth pipes could be expressed in terms of the Reynolds number for both laminar and turbulent flows. His phenomenological formula is the first correlation ever made for the turbulent pipe flow, between the friction factor and the Reynolds number:

$$f = \frac{0.3164}{Re^{1/4}} \quad (2-5)$$

The range of application is $4000 < Re < 10^5$ (Streeter and Wylie, 1981).

From 1931 to 1933, Johann Nikuradse performed his classical measurements in rough pipes. Nikuradse (1933) took a number of smooth pipes of diameter 2.5, 5 and 10 cm, and tightly coated the inside walls with uniform grains of graded sand. The relative roughness of each tube was then defined as k_s/D_H , where k_s was the diameter of the sand grains and D_H the diameter of the tube. The advantages of dimensionless numbers had been well learned from Reynolds. Nikuradse took pressure drop and velocity profile measurements in the pipes and obtained the corresponding $f-Re$ graphs which are illustrated on Figure 2-1.

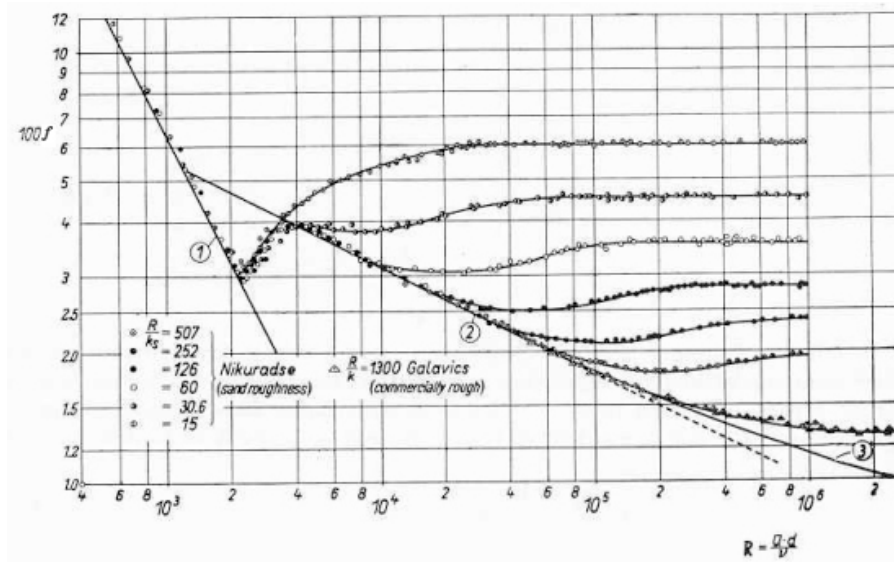


Figure 2-1. The friction factor vs. Reynolds number diagram resulted from the experiments with sand-grain roughness by Nikuradse (1933). The figure is taken from Schlichting (1968)

Nikuradse observed that at low Reynolds numbers the laminar friction factor correlation is valid irrespective of the grain size. However, turbulent friction correlation, after an onset point, increases monotonically with k_s/D_H . For any given relative roughness, the friction

Chapter 2: Literature Review of Particle Transport

factor eventually becomes constant at higher Reynolds numbers. Based on these observations, Nikuradse introduced the roughness Reynolds number $Re_* = k_s U_* / \nu$ in order to characterize the observed behavior of turbulent flow in rough pipes.

The hypothesis of the existence of a boundary layer assisted Nikuradse to explain the behavior of the curves in Figure 2-1. At the walls, there can be no cross velocities except on a molecular scale. Hence, there must be a thin layer called sub-layer close to each wall through which the velocity increases from zero (actually at the wall) to some finite velocity sufficiently far away from the wall for an eddy to exist. Although this viscous layer is very thin, it has a marked effect on the behavior of the total flow in the pipe. All real surfaces (even polished ones) have some degree of roughness. If the peaks of the roughness do not protrude through the viscous sub-layer ($Re_* < 7$) then the surface may be described as hydraulically smooth and the wall resistance is limited to that caused by viscous shear within the fluid. Within the second range ($7 < Re_* < 70$), there will be a transition zone, where an increase in the resistance factor was observed for an increasing Reynolds number. The resistance factor depends upon both the Reynolds number and relative roughness. Within the third range ($Re_* > 70$), the resistance factor is independent of the Reynolds number:

$$\frac{1}{\sqrt{f}} = -2.0 \log_{10} \frac{k_s}{3.7 D_H} \quad (2-6)$$

Further experiments and analytical investigations to derive a resistance formula for rough pipes were carried out in England by Colebrook (1939) in the late 1930's and followed by an engineer from Princeton, Lewis F. Moody (1944). Moody's landmark paper appeared after those of Nikuradse and Schlichting and represented the first easily applied and universally accepted method of comparing flow resistance for fully developed flow in commercially-rough pipes.

Chapter 2: Literature Review of Particle Transport

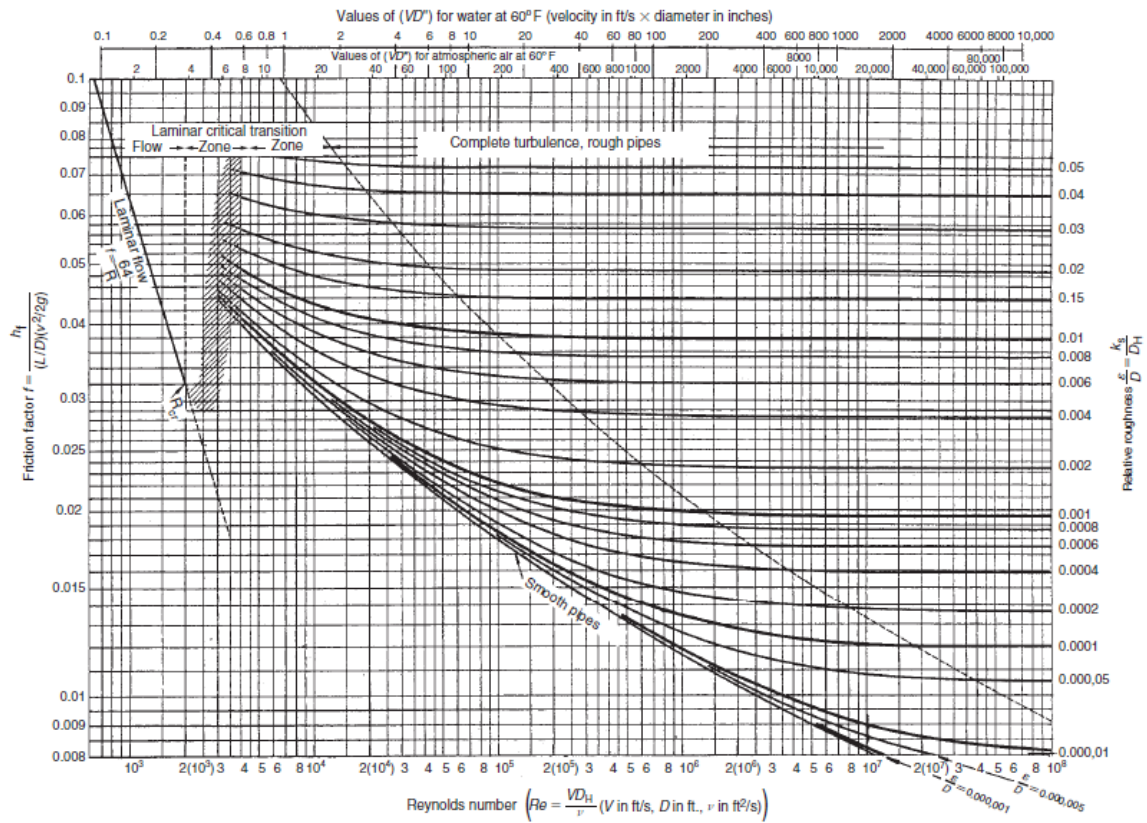


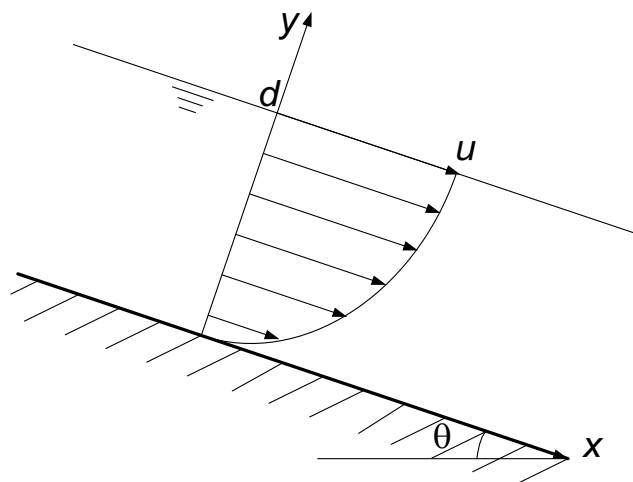
Figure 2-2. Moody diagram. The figure is taken from Chanson (2004)

2.2.2 Open channel flow

As in pipes, the flow in an open channel may be either laminar or turbulent. In practice, hydraulic radius $R_H = D_H/4$ is often used for an open channel as a mean flow depth, and the thresholds become:

Laminar: $Re < 500$

Turbulent: $Re > 1000$



Chapter 2: Literature Review of Particle Transport

Figure 2-3. Sketch of the flow over an inclined plane

Considering a viscous incompressible fluid flow over a wide inclined plane with a uniform velocity distribution, under gravity force, using the Navier–Stokes equation, we can deduce the velocity distribution along y direction as follows:

$$u = \frac{\rho g \sin \theta}{2\mu} y(2d - y) \quad (2-7)$$

and the relation between flow rate per unit width and flow depth is:

$$q = \frac{\rho g \sin \theta}{3\mu} d^3 \quad (2-8)$$

where u is the velocity distribution along y direction, θ is the inclination angle of the plane, d is the flow depth, q is the flow rate per unit width.

The first empirical equation to calculate the energy losses in turbulent flow was given by Antoine Chézy in 1775, called Chézy equation:

$$U_w = C_{Chézy} \sqrt{\frac{D_H}{4} \sin \theta} \quad (2-9)$$

where $C_{Chézy}$ is the Chézy coefficient (units $\text{m}^{1/2}/\text{s}$), which is not constant and expresses the importance of roughness. D_H is the hydraulic diameter and θ is the channel slope (e.g. Henderson, 1966).

Many studies have been performed for evaluating $C_{Chézy}$ for different natural and manmade channels. Some forms of the relationships are used by today's engineers, one of them is known as Manning formula:

$$C_{Chézy} = \frac{1}{n_{Manning}} \left(\frac{D_H}{4} \right)^{1/6} \quad (2-10)$$

and Equation (2-9) becomes:

$$U_w = \frac{1}{n_{Manning}} \left(\frac{D_H}{4} \right)^{2/3} \sqrt{\sin \theta} \quad (2-11)$$

where $n_{Manning}$ is the Manning coefficient (units $\text{s}/\text{m}^{1/3}$).

There have been several other names of this formula or ones similar and consequently in some countries the same equation is named after one of these people, some of these names are Strickler, Gauckler, Gauguillet and Hagen.

Chapter 2: Literature Review of Particle Transport

The Manning equation has the great benefits that it is simple, accurate and use extensively since a long time. There are different values of $n_{Manning}$ for a wide range of open channels. Table 2-1 gives a list of a few typical values of Manning coefficient.

Table 2-1. Typical values of Manning coefficient

Channel type	Surface material and form	$n_{Manning}$ range
River	earth, straight	0.02-0.025
	earth, meandering	0.03-0.05
	gravel (75-150mm), straight	0.03-0.04
	gravel (75-150mm), winding	0.04-0.08
Unlined canal	earth, straight	0.018-0.025
	rock, straight	0.025-0.045
Lined canal	concrete	0.012-0.017
Lab. models	mortar	0.011-0.013
	Perspex	0.009

The shear velocity is a measure of shear stress and velocity gradient near the boundary, a large shear velocity U_* implies large shear stress and large velocity gradient. Generally, there are four methods to estimate the shear velocity: Reynolds stress, logarithmic law, parabolic law and a global approach.

The logarithmic law method is based on the velocity distribution in the region $y/d < 0.6$, can be described by the logarithmic law: $\frac{u}{U_*} = \frac{1}{\kappa} \ln\left(\frac{y}{k_s}\right) + C$, where κ is the von Karman constant (equal to 0.41), and C is a constant.

Einstein and El-Samni (1949) proposed a modified logarithmic law for the flow over a surface with large roughness: $\frac{u}{U_*} = \frac{1}{\kappa} \ln\left(\frac{y+y_0}{k_s}\right) + C$, where y_0 is the distance of the theoretical wall below the top of the spheres whose diameter is k_s , they chose a value of $y_0 = 0.2k_s$.

Cheng and Chiew (1998) suggested a modified logarithmic law for the influence of vertical seepage flow: $\frac{u}{U_*} = \frac{1}{\kappa} \ln\left(\frac{y}{y_0}\right) + \frac{V_s}{4U_*} \left(\frac{1}{\kappa} \ln\left(\frac{y}{y_0}\right)\right)^2$, where V_s is the vertical mean seepage flow rate due to the injection or suction.

2.3 Flow over and within the saturated porous medium

The first characteristic of a porous medium is the porosity measured by the porosity factor which is the ratio of volume of voids (or pores) to the total volume including both solids and voids. The porosity factor Φ for sediment bed of rivers ranges usually from 0.26 to 0.48.

Another characteristic of a porous medium is the permeability. For a one-dimensional flow through the pores of the sediment bed, the velocity of seepage is given by the Darcy law:

$$U_s = K \frac{\Delta H}{\Delta L} \quad (2-12)$$

where U_s is the mean flow velocity in porous medium, which is also called Darcy velocity, K is the coefficient of permeability, and ΔH is the head loss over a distance ΔL . The coefficient of permeability K not only depends on the permeability of the soil but also on the properties of the fluid and dimensional analysis yields (Raudkivi and Callander, 1976):

$$K = k_p \frac{\rho g}{\mu} \quad (2-13)$$

where k_p is the intrinsic permeability (in m^2), ρ is the fluid density, g is the gravity constant and μ is the fluid dynamic viscosity. The intrinsic permeability depends only on the structure of the porous medium. Typical values of the coefficient of permeability are given in Table 2-2 (Raudkivi and Callander, 1976):

Table 2-2. Typical values of the coefficient of permeability

Soil type	Fine sand	Silty sand	Silt
$K \text{ (m/s)}$	5×10^{-4} to 1×10^{-5}	2×10^{-5} to 1×10^{-6}	5×10^{-6} to 1×10^{-7}

Darcy law is no longer validated when the permeability is large or velocity is large. Moreover the Darcy law could just get the mean flow velocity across the section of porous media, but could not describe the details of the flow structure in the pores.

Li and Garga (1998) presented analytical results for the turbulent seepage flow occurring at the transition zone (between the fluid zone and the pressure seepage zone) of gravel river reaches or nonconventional rockfill spillways. They proposed an approach based on analyses between porous media and pores network. The flow velocity in the pores U_v may be defined as:

$$U_v = \frac{U_s}{\Phi} \quad (2-14)$$

where Φ is the porosity.

Chapter 2: Literature Review of Particle Transport

The Darcy-Weisbach formula expressed the friction coefficient:

$$f = \frac{\Delta H}{\Delta L} \frac{2gD_H\Phi^2}{U_s^2} \quad (2-15)$$

Based on experiments, Hansen (1992) concluded that the friction coefficient is linked with Reynolds number like:

$$f = \frac{a}{Re} + b \quad (2-16)$$

where a, b are coefficients. Hence, the Reynolds number Re may be written as:

$$Re = \frac{U_v D_H}{\nu} = \frac{U_s D_H}{\nu \Phi} \quad (2-17)$$

The Equation (2-16) could be used in both laminar and turbulent flows. The constant coefficient b is negligible for small Reynolds number and Equation (2-16) is changed into Poisseuille's law. When Reynolds number increases f tends to be a constant value of b , and the stability of f is a characteristic of the turbulent flow in porous media.

The combination of Equations (2-15), (2-16) and (2-17) lead to a general equation of flows over and in porous medium:

$$\frac{\Delta H}{\Delta L} = \frac{av}{2gD_H^2\Phi} U_s + \frac{b}{2gD_H\Phi^2} U_s^2 \quad (2-18)$$

The flow phenomena and momentum transfer at the porous/fluid interface have also been studied by several investigators. Beavers and Joseph (1967) used a porous block with high permeability in a closed channel in their experimental study, and found an empirical relationship for the interfacial slip velocity. The empirical relationship used is

$$\frac{dU_w}{dy} = \frac{\alpha}{\sqrt{k_p}} (U_{int} - U_s) \quad (2-19)$$

where k_p is porous medium permeability; α is slip parameter; U_w is flow velocity over the porous surface; U_{int} is interfacial velocity; and U_s is Darcy velocity within the porous bed. They used the momentum equation for fully developed laminar flow and the above mentioned relationship as an interfacial condition for calculating: (i) the velocity distribution over the porous media; (ii) the interfacial velocity U_{int} ; and (iii) the increase in mass flow over the permeable bed with regard to that with an impermeable bed.

Poulikakos and Kazmierczak (1987), Rudraiah (1985), and Vafai and Thiyagaraja (1987) used the Navier-Stokes equations for the flow above the porous medium and the Darcy equations for the flow in the porous medium. They used continuity conditions at the interface for both velocity and shear stresses, calculated the interfacial velocity and the velocity distribution above and inside the porous region.

Chapter 2: Literature Review of Particle Transport

Sahraoui and Kaviany (1992) showed that a variable viscosity should be used in the Darcy-Brinkman equations for an accurate calculation of the velocity near the interface and inside the porous layer. Ochoa-Tapia and Whitaker (1995a, b) have developed a stress jump condition based on the nonlocal form of the volume averaged Stokes equations and explored the use of a variable porosity model as a substitute for the jump condition. This approach did not successfully represent of all experimental data, but provided an insight into the complexities of the interfacial region between a porous medium and a free flow.

Choi and Waller (1997) applied a macroscopic single domain approach to treat complex interaction of the flow near the interfacial region. The flow was laminar and the results showed the importance of viscous shear in the channel flow. They concluded that the Darcy law is inappropriate to be used in the interfacial region.

James and Davis (2001) used microscopic models for Stokes flow in a channel partially filled with an array of circular cylinders. The porosity was 0.9 or greater, simulating fibrous porous media. They concluded that the external flow penetrates the porous layer very little even for sparse arrays and that the apparent slip velocity at the interface is about one quarter of the velocity predicted by the Brinkman model.

Zippe and Graf (1983), based on experimental findings, found that the boundary resistance of the tested permeable surface is higher than that of the non-permeable boundary with same roughness.

Shimizu et al. (1990) based on experimental findings, concluded a mathematical model of the velocities within the porous medium under turbulent flow, However, the model was based on a function of the slip interfacial velocity, which is not known a priori. Thus, applying such a model is rather difficult. Mendoza and Zhou (1992) and Zhou and Mendoza (1993) presented the turbulent flow characteristics over a porous bed and the velocity distribution in surface flow, however, the details of transport phenomena near the boundary of the permeable interface was not investigated.

Hahn et al. (2002) applied direct numerical simulation (DNS) to the fluid region only for turbulent flow conditions. They found a significant skin-friction reduction at the permeable wall, a decrease of the viscous sub-layer thickness, and a weakening of the near-wall vortices.

Either microscopic or macroscopic model can be used in the numerical investigation of the turbulent flow over the porous region. Most of the studies on porous medium flow apply macroscopic models within a two-dimensional (2D) porous bed. Pedras and de Lemos (2000) presented a macroscopic turbulent model which was a $k-\varepsilon$ model based on the formulations

developed from the numerical results. Chan et al. (2007) presented the numerical solutions for turbulent 2D flow in a channel with a porous medium, they applied a single-domain approach and concluded that the level of turbulent penetration depends strongly on the damping effect of the porous medium itself. However using the macroscopic models could not have detailed insight into the flow structure. Hence, due to the development of the computational capacity, a complex computational fluid dynamics (CFD) could be performed. Prinos et al. (2003) presented microscopic computation of flow over and within a porous bed. They also provided very valuable measured data.

2.4 Critical velocity for particle erosion

It is important to understand the mechanism of sediment incipience for investigating sediment transport.

For an open channel flow with a porous bed, the forces acting on each sediment particle are shown in Figure 2-4.

- The gravity force $\rho_s g \Omega_s$;
- The buoyancy force $F_b = \rho g \Omega_s$;
- The drag force $C_d \rho A_s U_w^2 / 2$;
- The lift force $C_L \rho A_s U_w^2 / 2$;
- The inter-granular forces (contact forces).

where Ω_s is the volume of the particle, A_s is a characteristic particle cross-sectional area, C_d and C_L are the drag and lift coefficients, respectively, U_w is a characteristic flow velocity next to the porous bed.

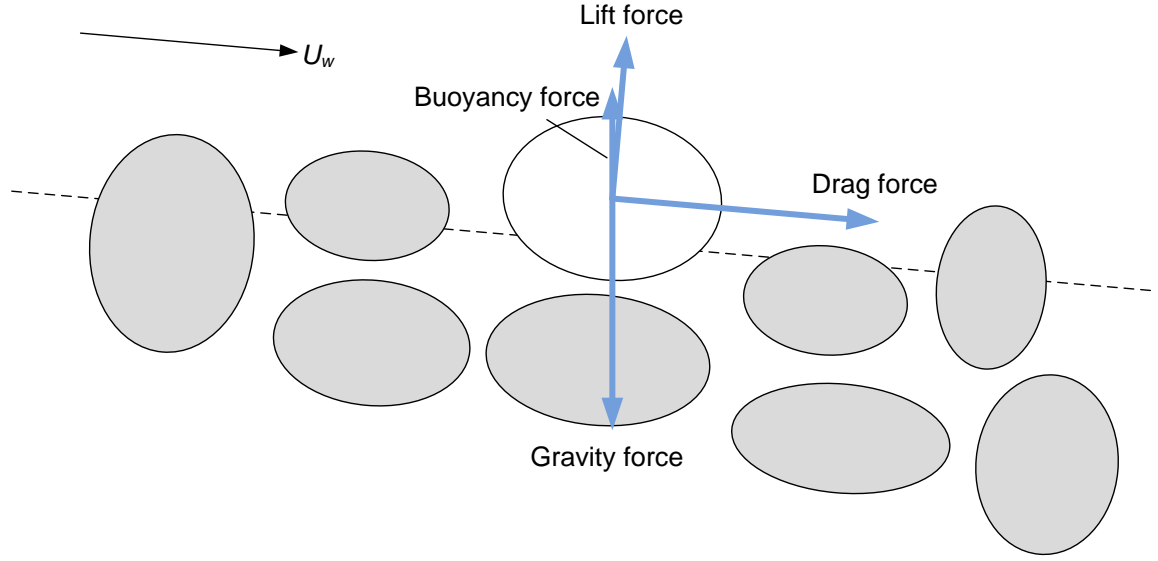


Figure 2-4. Forces acting on a sediment particle (inter-granular forces not shown for the purpose of clearness)

The gravity force and the buoyancy force act both in the vertical direction while the drag force acts in the flow direction and the lift force in the direction perpendicular to the flow direction (Figure 2-4). The inter-granular forces are related to the grain disposition and packing.

There is a sediment transport when the force acting on particles is big enough for moving them, so the sediment transport is a phenomenon with a threshold. The threshold of sediment motion cannot be defined with an exact precision but most experimental observations have provided reasonably accurate and consistent results.

The relevant parameters for the analysis of sediment transport threshold are: the bed shear stress τ_0 , the sediment density ρ_s , the fluid density ρ , the grain diameter d_s , the gravity acceleration g and the fluid viscosity μ :

$$f_1(\tau_0; \rho; \rho_s; \mu; g; d_s) = 0 \quad (2-20a)$$

In dimensionless terms, it yields:

$$f_2\left(\frac{\tau_0}{\rho g d_s}; \frac{\rho_s}{\rho}; \frac{d_s \sqrt{\rho \tau_0}}{\mu}\right) = 0 \quad (2-20b)$$

Introducing the shear velocity U_* defined as:

$$U_* = \sqrt{\frac{\tau_0}{\rho}} \quad (2-21)$$

In uniform equilibrium flow down an open channel, the shear velocity equals:

$$U_* = \sqrt{g \frac{D_H}{4} \sin \theta} \quad (2-22)$$

Equation (2-20) can be changed into:

$$f_3 \left(\frac{U_*}{\sqrt{g d_s}}; \frac{\rho_s}{\rho}; \rho \frac{d_s U_*}{\mu} \right) = 0 \quad (2-20c)$$

The first term is in a form of the Froude number. The second is the relative density. The last term is a shear Reynolds number or particle Reynolds number.

In 1936, Shields introduced a dimensionless parameter τ_* called the Shields parameter, defined as:

$$\tau_* = \frac{\tau_0}{(\rho_s - \rho) g d_s} \quad (2-23)$$

A critical value of this parameter $(\tau_*)_c$ may be defined at the inception of bed motion. Shields (1936) showed that $(\tau_*)_c$ is primarily a function of the shear Reynolds number $Re_* = U_* d_s / \nu$ (Figure 2-5).

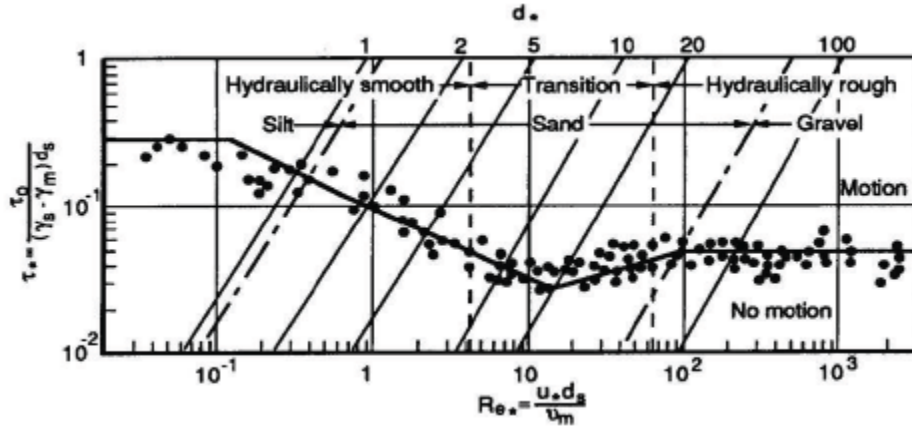


Figure 2-5. Shields diagram: Shields parameter as a function of the particle Reynolds number for sediment in water

For sediment particles in water, the Shields diagram exhibits different trends corresponding to different turbulent flow regimes:

- The smooth turbulent flow ($Re_* < 5$) $0.035 < (\tau_*)_c$;
- The transition regime ($5 < Re_* < 70$) $0.03 < (\tau_*)_c < 0.04$;
- The fully rough turbulent flow ($70 < Re_*$) $0.03 < (\tau_*)_c < 0.06$.

For fully rough turbulent flows, the critical Shields parameter $(\tau_*)_c$ is nearly constant, and the critical bed shear stress for bed load motion becomes linearly proportional to the sediment size:

$$(\tau_o)_c \propto d_s \quad \text{Fully rough turbulent flow} \quad (2-24)$$

The inception of bed load motion may be affected by several parameters: particle size distribution, bed slope, bed forms and material cohesion (van Rijn, 1993).

2.5 The transport of sediment particles

When the bed shear stress exceeds a critical value, sediments are transported. For bed-load transport, the basic modes of particle motion include rolling motion, sliding motion and saltation motion. Saltation refers to the transport of sediment particles in a series of irregular jumps and bounces along the bed (Figure 2-6). The sediment transport can damage the environment and destroy human infrastructure. Figure 2-7 shows the landslide in Zhouqu County in China that occurred at midnight on August 8, 2010, which has killed More than 1471 people, was caused by heavy rainfall and flooding.

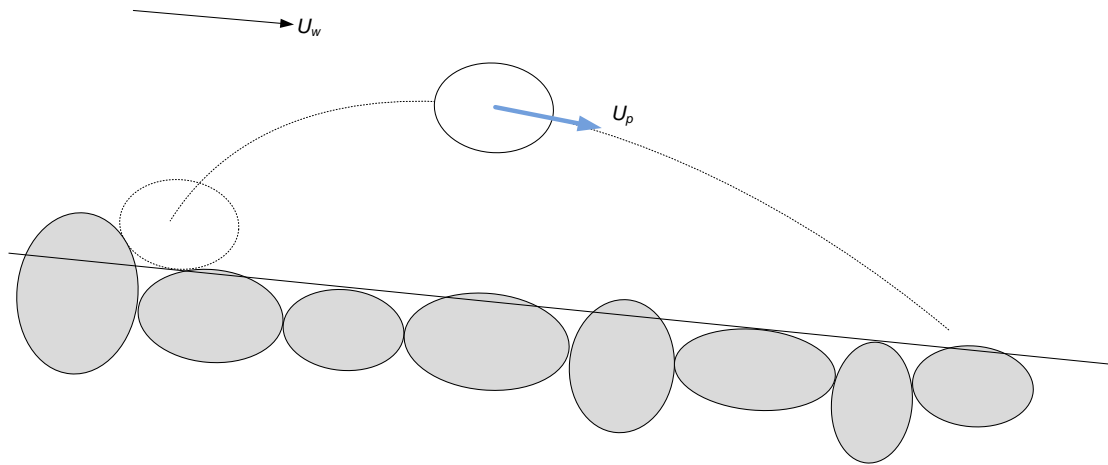
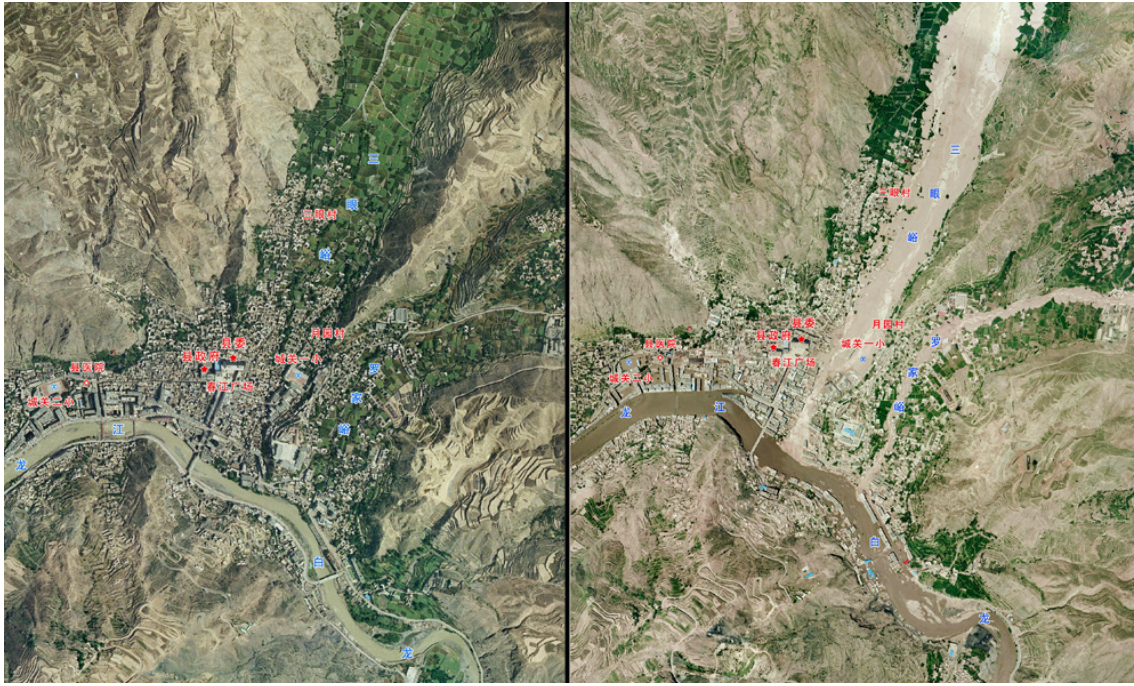


Figure 2-6. Sketch of saltation motion

Chapter 2: Literature Review of Particle Transport



(a)



(b)



(c)

Figure 2-7. Landslides strike Zhouqu County, China, August 8, 2010. (a) A handout photo from the State Bureau of Surveying and Mapping shows a combo of satellite images showing Zhouqu before (left) in July, 2008 and after the recent landslide (right), taken on August 8, 2010. (b) An aerial view of the town of Zhouqu shortly after a deadly flood-triggered landslide, seen on August 8, 2010. (c) Chinese rescuers search for survivors in the aftermath of a landslide. (Xinhua Images)

Krumbein (1942) studied the effect of particle shape on sediment transportation based on experiments. He related the observed behavior to the settling velocities of particles. The experiments were confined to the bed movement of single particles of different shapes, over a hydraulically smooth bed, for turbulent flow. He found a relationship between sphericity and the ratio of particle velocity to mean flow velocity, U_p/U_w , as a function of the Froude number.

$$\frac{U_p}{U_w} = \left(\frac{U_p}{U_w} \right)_0 (1 - \exp(-bFr)) \quad (2-25)$$

where U_p is the particle velocity; U_w is the mean flow velocity; b is a constant parameter; Fr is Froude number.

Chapter 2: Literature Review of Particle Transport

Kalinske (1942) reported that the Froude number Fr has no physical significance in regard to the movement of particles on the bed. Kalinske proposed that the particle velocity should be related to critical velocity of the particle. Kalinske concluded the following expression:

$$U_p = c_a(U_w - U_c) \quad (2-26)$$

where c_a : constant parameter; U_c : critical velocity for a particle. Kalinske used his model and Krumbein's data found the best agreement for $0.9 < c_a < 1.0$.

Einstein (1950) suggested that the particle velocity in the bed-load motion is equal to 11.6 times of shear velocity ($U_p = 11.6U_*$).

Ippen and Verma (1955) analyzed the motion of particles in turbulent flow over fixed beds of different roughness in flume experiments. They found that after a transition of variable length, U_w/U_p reached a constant value over a wide range of Re and that the particle velocity increased directly with size, and related this to the fact that larger particles are exposed to higher flow velocity. They obtained the following equation:

$$\frac{U_w}{U_p} = 1 + \frac{1}{12} \left(\frac{\rho_s}{\rho} - 1 \right) \left(\frac{k_s}{d_s} \right) \left(\frac{1}{\sqrt{S_o}} \right) \quad (2-27)$$

where ρ_s/ρ : the relative density of grains; d_s : particle diameter; k_s : roughness size; S_o : slope of energy gradient.

Meland and Norrman (1966) studied the interactive effects of water velocity, bed roughness, and particle size on the transport rate of single particles over rough beds by turbulent flows, keeping particle shape, density and bed packing constant. They explained the phenomena of larger particles move faster than smaller ones for a given bed roughness and shear velocity, First, larger particles ride higher off the bed, being thus exposed to greater velocities, and second, the rolling resistance decreases when the ratio of particle size to roughness size is increased. They also concluded that at high shear velocities and small bed roughness, the particle velocity tends to be constant with size. They also found that transport velocities were higher on beds of tightly packed solid beds than in corresponding loosely packed glass beads. But this effect was most noticeable at high transport stages, and decreased, or even reversed for low shear velocities.

Ikeda (1971) studied theoretically the mechanics of the motion of a single spherical grain rolling on the bed, by considering the four main forces acting on the particle: drag, lift, gravity and friction with the bed. The resulting particle velocity is as follows:

$$\frac{U_p}{U_*} = \frac{U_w}{U_*} - \left[\frac{4}{3} c_\mu \frac{\left(\frac{\rho_s}{\rho} - 1 \right) g d_s}{(c_\mu C_L + C_d) U_*^2} \right]^{1/2} \quad (2-28)$$

where U_* : shear velocity; c_μ : sliding friction coefficient; C_d and C_L : the drag and lift coefficients respectively.

Bagnold (1973) assumed the particle velocity equals to the difference between flow velocity at corresponding water depth and settling velocity of particle: $U_p = U - w_0$.

Francis (1973) studied the motion of a single grain rolling on the bed. The experiments were conducted in which heavy solid grains are observed as they are propelled one at a time by a water stream over a fixed, plane, bed of grains of the same sort.. Francis found a satisfactory correlation between the particle velocity, U_p and the particle settling velocity, w_0 . He also concluded that rounded particles always roll faster than angular ones.

Jan (1992) studied the relative contribution of the stresses developed in granular fluid flows. Jan determined how much each of the examined stresses contributed to the total stress acting on a rolling sphere. Experiments were conducted for the steady movement of a sphere rolling down smooth and rough inclined surface in air, water and salad oil. An equation was derived expressing the velocity of a sphere rolling down a rough incline without acceleration or deceleration based on the principle of conservation of momentum. The average terminal velocity U_p was derived as follows:

$$U_p = \sqrt{\frac{(\rho_s - \rho) g d_s (\sin \theta - n_\mu \cos \theta)}{f_c \rho_s + \frac{3}{4} C_d \rho}} \quad (2-29)$$

where ρ_s , ρ : particle and fluid densities; C_d : drag coefficient; θ bed slope angle; f_c : coefficient of restitution (0.667); and n_μ : bulk friction coefficient (0.13). Both f_c and n_μ were determined from experimental data. The tested particle was identical to those comprising the roughness over which it rolled in Jan's experiments. Roughness particles were tightly spaced in a single layer on a smooth wooden bed of a tilting flume. Jan found that velocity is independent of rolling particle density; collision stresses increase with increased bed inclination.

Bigillon (2001) conducted an experiment in an inclined, narrow, glass-sided channel, 2m in length and 20 cm in height. The channel inclination angle ranged from 0° to 12°. Two types of spherical particles (glass beads and steel beads, with the density of 2500 and 7750 kg/m³ respectively) were used in the experiments. The water supply at the channel entrance was controlled by an electromagnetic flow meter. The flow depth was a few particle

diameters. The channel bed was made up of regularly disposed half-cylinders of equal size. Bigillon used three sizes of cylinder with a radius of 1.5 mm, 3 mm, and 4 mm. A single particle was dropped from above into the water stream 1 m upstream from the measuring window. The motion of mobile beads was recorded using a high speed camera. For each flow condition (U_w, θ), the variability of the results was evaluated by repeating the run between three and five times, and only the average value was reported. The standard deviation was low relative to the mean (less than 5%) when the particle rolled. Fifty experimental data points were collected and the variability for hydraulic and particle parameters include: the range of shear velocity $U_* = 0.018\text{-}0.038$ m/s, particle diameter $d_s = 1.5$ mm and 3 mm, $\rho_s/\rho = 2.5$ (glass bead) and 7.75 (steel bead), $k_s = 1.5$ mm and 3 mm, bed slope $S_o = 0.02$ and 0.05, mean flow velocity $U_w = 0.223\text{-}0.492$ m/s, flow depth $d = 2.13\text{-}28.65$ mm, and observed bed-load particle velocity $U_p = 0.076\text{-}0.496$ m/s.

2.6 Sediments clogging in the porous medium

When the sediment transport capacity is smaller in the channel, the sediments transported by fluid will deposit and small particles attempt to percolate through the porous medium. When the size or concentration of small percolating particles is too large, clogging of pores can occur which can modify the permeability of the crossed medium. The literature on the sediments clogging phenomena in channel flows is hard to find, but the transport of small spherical particles through packings of larger spheres in vertical system has already been studied both experimentally and numerically.

Nguyen (2007) studied experimentally the sediment transport into porous medium. Based on the structure of road, Nguyen developed a model of porous media using two layers of glass particles placed in a transparent tank with a regulation value at the bottom. The upper layer is 5 cm thick, made up by 4 mm glass particles, and the porosity is 0.3; the lower layer is 10 cm thick, made up by a mixture of 12 mm and 15 mm glass particles, and the porosity is 0.31. First, the porous media is saturated by water. Second, use the regulation value to keep the initial water depth drop at 1 mm/s, lay the sand with diameters from 0.1 to 0.5 mm evenly on the surface of the porous medium. Then, the saturate with water till the initial level, and start a series of 10 cycles of drainage and refill. For studying the influence of surface status, silicone oil was also used to soak the porous media before the saturation of water. According to the observations, Nguyen concluded that the increase of mass of sand laid on the surface of porous media could decreases of infiltration rate, and the decrease could be enhanced because of oil soak; the oil soaked sand penetrate less deeply into the porous media than the clean sand because of the adhesion force.

Chapter 2: Literature Review of Particle Transport

Remond (2010) studied numerically the percolation of small particles (with a diameter of 1 cm) through a periodic random loose packing of large beads (with a diameter of 10 cm) with Distinct Element Method (DEM). Results show that a steady state is rapidly reached where the mean velocity and mean vertical velocity of small particles are both constant. These mean velocities decrease with an increase in friction coefficient and in small particle concentration. This influence is much less evident for the friction coefficient values larger than or equal to 0.5. The distribution of small particles throughout the crossed packing becomes rapidly heterogeneous. Small particles concentrate in some pores where the density can reach values larger than the density of the random loose packing. The proportion of particles blocked in these pores varies linearly with concentration. The narrow throats of the porous medium responsible for blocking are identified. And increasing the friction coefficient leads to an increase in the number of clogged pores.

Haselbach (2006) studied both theoretically and experimentally runoff on a permeable concrete block. A relation between the permeability of the sand-clogged pervious concrete block system, the porosity of the block near the surface and the permeability of the sand was established as follows:

$$K_{eff} = \Phi_{top}K \quad (2-30)$$

where K_{eff} : the permeability of the sand-clogged pervious concrete block; Φ_{top} : the porosity of the block near the surface; K : the permeability of the sand. Permeability was then measured for pervious concrete systems fully covered with extra fine sand in a flume using simulated rainfalls. Two different slopes (2% and 10%) were used. Rainfall rates were simulated for the combination of direct rainfall and for additional stormwater runoff from adjacent areas. A computer-monitored scale was used to record the change in weight of the runoff water collected over time. The concrete block was approximately 31 cm in length, 31 cm in width and 16 cm in depth with a surface area of 948 cm². The block was placed on self compacted 15 cm thick sand which in turn was placed on a perforated wooden board wrapped with a layer of geo-synthetic filter able to contain the sand. This entire set-up was inside a plastic container with a drainage hole at the bottom. To simulate a varying range of sand clogging, wet sand was placed over the block at three different depths (1.3, 2.5 and 5 cm). The sand was also distributed over the flume surface for an additional 30 cm upslope of the block to minimize channeling effects at the flume/pervious interface. The experimental results correlated well with the calculated permeability of the pervious concrete system fully covered on the surface with sand.

Chapter 3

Numerical Method

3.1 Introduction

The characteristics of a free surface flow over a porous bed in a three-dimensional (3D) inclined open channel are investigated using a microscopic approach. Figure 3-1 shows the flow investigated here. The rectangular channel is partially filled with a layer of porous material. A free surface flow passes longitudinally from left to right. At the bottom, the seepage outflow rate can be controlled.

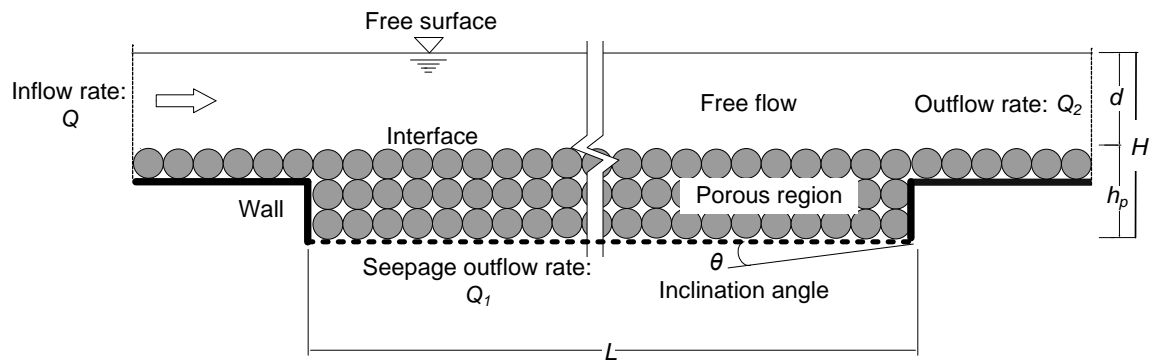


Figure 3-1. Sketch of computational domain with boundary conditions in a 2D view

In this chapter the numerical methods applied in the study are introduced. For this objective, a combination of Computational Fluid Dynamics (CFD) and Discrete Element Method (DEM) is used to simulate the behavior including interaction between particles and fluid. The governing equations are solved using the commercial software PFC3D 4.0 (2008) and CCFD

(2007). In order to validate the results obtained by the CFD-DEM coupling, we compare them to the results of two test cases from literatures:

- The flow in a porous medium studied experimentally by Shimizu et al. (1990).
- The turbulent flow in the fluid over the porous medium studied both experimentally and numerically by Prinos et al. (2003).

3.2 Computational Fluid Dynamics (CFD)

The history of CFD started in the early 1960's. Around that time, it became an acronym for a combination of physics, numerical mathematics, and to some extent, computer sciences employed to simulate fluid flows. Since the early 1970s, commercial computer codes became available, making CFD an important component of engineering practice. With the beginning of the 1980's, the solution of first two-dimensional and later also three-dimensional Euler equations became feasible. With the mid 1980's, the focus started to shift to the significantly more demanding simulation of viscous flows governed by the Navier-Stokes equations. Together with this, a variety of turbulence models evolved with different degree of numerical complexity and accuracy. Nowadays, CFD methodologies are routinely employed in the fields of aircraft, turbo-machinery, car and ship design. Furthermore, CFD is also applied in environment, meteorology, oceanography, geotechnics, and in oil recovery, etc...

3.2.1 Governing equations

The three laws governing the fluid motion are the following:

1. The law of conservation of mass (transport of mass);
2. Newton's second law of motion (transport of momentum);
3. The first law of thermodynamics (transport of energy).

Governing equations are described by integral expressions using control volume Ω surrounded by surface area S , a surface element as dS and its associated, outward pointing unit normal vector \vec{n} as shown in Figure 3-2. In addition, \vec{V}_s here is the transfer velocity of the boundary. When \vec{V}_s is the same as velocity \vec{V} of the continuum, the equations of motion are described by a Lagrangian form and when $\vec{V}_s = 0$, they are described by an Eulerian form.

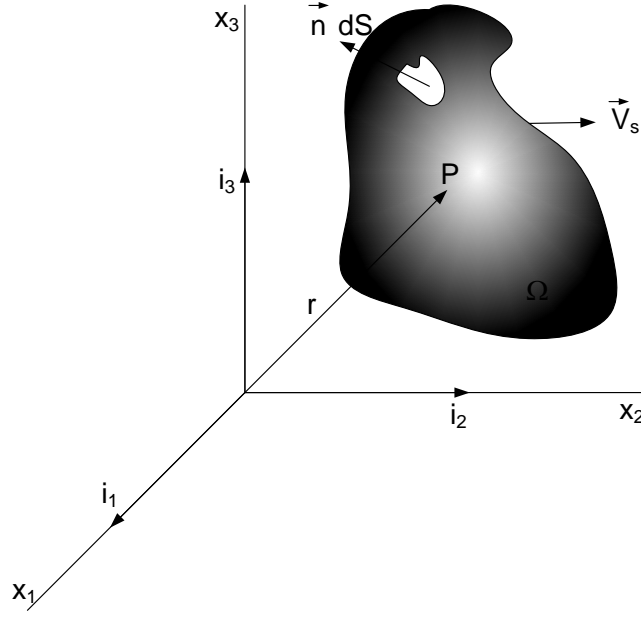


Figure 3-2. Control volume

3.2.1.1 Law of mass conservation

The mass conservation law is known as the equation of continuity and is represented by the following equation.

$$\frac{d}{dt} \int_{\Omega} \rho d\Omega + \int_S \rho (\vec{V} - \vec{V}_s) \cdot \vec{n} dS = 0 \quad (3-1)$$

where dS is the surface element.

3.2.1.2 Law of conservation of momentum

By means of applying Newton's second law to the control volume of Figure 3-2, the following equation known as Cauchy's first law of motion is derived.

$$\frac{d}{dt} \int_{\Omega} \rho \vec{V} d\Omega + \int_S \rho \vec{V} (\vec{V} - \vec{V}_s) \cdot \vec{n} dS = \int_S \vec{\tau} \cdot \vec{n} dS + \int_{\Omega} \vec{f}_b d\Omega \quad (3-2)$$

where $\vec{\tau}$ is a Cauchy stress tensor and \vec{f}_b is the volume force per unit volume.

3.2.1.3 Energy equations

$$\frac{d}{dt} \int_{\Omega} \rho E d\Omega + \int_S \rho E (\vec{V} - \vec{V}_s) \cdot \vec{n} dS = \int_S \vec{q}_h \cdot \vec{n} dS + \int_{\Omega} s_h d\Omega \quad (3-3)$$

Where E is the total energy per unit mass, \vec{q}_h is a heat flux vector and s_h is a heat source.

3.2.2 Standard k - ε model

The standard k - ε model is often used to model turbulent flow. Turbulent kinetic energy k and eddy dispersion rate ε are modeled by the following transport equations.

$$\begin{aligned} \frac{d}{dt} \int_{\Omega} \rho k d\Omega + \int_S \rho k (\vec{V} - \vec{V}_S) \cdot \vec{n} dS \\ = \int_S \left(\mu + \frac{\mu_t}{\sigma_k} \right) \text{grad} k \cdot \vec{n} dS + \int_{\Omega} (P + P_B - \rho \varepsilon) d\Omega \end{aligned} \quad (3-4)$$

$$\begin{aligned} \frac{d}{dt} \int_{\Omega} \rho \varepsilon d\Omega + \int_S \rho \varepsilon (\vec{V} - \vec{V}_S) \cdot \vec{n} dS \\ = \int_S \left(\mu + \frac{\mu_t}{\sigma_{\varepsilon}} \right) \text{grad} \varepsilon \cdot \vec{n} dS \\ + \int_{\Omega} (C_1 P_s \frac{\varepsilon}{k} + C_2 \rho \frac{\varepsilon^2}{k} + C_3 \max(P_B, 0) \frac{\varepsilon}{k} - C_4 \rho \varepsilon \text{div} \vec{V}) d\Omega \end{aligned} \quad (3-5)$$

where μ is the viscosity coefficient of the fluid, and the eddy viscosity coefficients μ_t is represented as:

$$\mu_t = C_{\mu} \rho \frac{k^2}{\varepsilon} \quad (3-6)$$

Turbulent kinetic energy generated by shear P_s and the effect due to buoyancy P_B are modeled as:

$$P_s = \frac{2}{3} (\mu_t \text{div} \vec{V} + \rho k) \text{div} \vec{V} \quad (3-7)$$

$$P_B = -\frac{\mu_t}{\rho \sigma_T} g \cdot \text{grad} \rho \quad (3-8)$$

where C_{μ} , C_1 , C_2 , C_3 , C_4 , σ_k , σ_{ε} , σ_T are experimental constants and Table 3-1 shows their values.

Table 3-1. Experimental constants in standard k - ε model

C_{μ}	C_1	C_2	C_3	C_4	σ_k	σ_{ε}	σ_T	σ_{ci}
0.09	1.44	1.92	1.44	-0.33	1.0	1.3	0.9	0.9

3.2.3 Numerical analysis method

The governing equation and the standard turbulent model can be uniformly described as follows:

$$\begin{aligned} \frac{d}{dt} \int_{\Omega} \rho \varphi d\Omega + \int_S \rho \varphi (\vec{V} - \vec{V}_S) \cdot \vec{n} dS \\ = \int_S \Gamma_{\varphi} \text{grad} \varphi \cdot \vec{n} dS + \int_S q_{\varphi S} \cdot \vec{n} dS + \int_{\Omega} q_{\varphi \Omega} d\Omega \end{aligned} \quad (3-9)$$

where φ is called conservative variables. Γ_{φ} is a diffusion coefficient of φ .

3.2.3.1 Discretization method

Chapter 3: Numerical Method

In order to handle values such as velocity, temperature, turbulent energy k , and eddy dispersion rate ε , discretization is performed using the format of Equation (3-9).

Generally, there are four discretization methods, finite difference method, finite element method, finite analytic method and finite volume method. In this research a finite volume method is used to perform discretization based on non-structural lattices. The advantages of using a finite volume method are shown below.

First, finite volume methods ensure that the discretization is conservative, i.e., mass, momentum, and energy are conserved in a discrete sense. While this property can usually be obtained using a finite difference formulation, it is obtained naturally from a finite volume formulation. Second, finite volume methods do not require a coordinate transformation in order to be applied on irregular meshes. As a result, they can be applied on unstructured meshes consisting of arbitrary polyhedra in three dimensions or arbitrary polygons in two dimensions. This increased flexibility can be used to great advantage in generating grids about arbitrary geometries.

The CCFD uses a collocated grid to arranged variables in center of a cell. If the symbols of Figure 3-3 are used, Equation (3-9) will be written as follows.

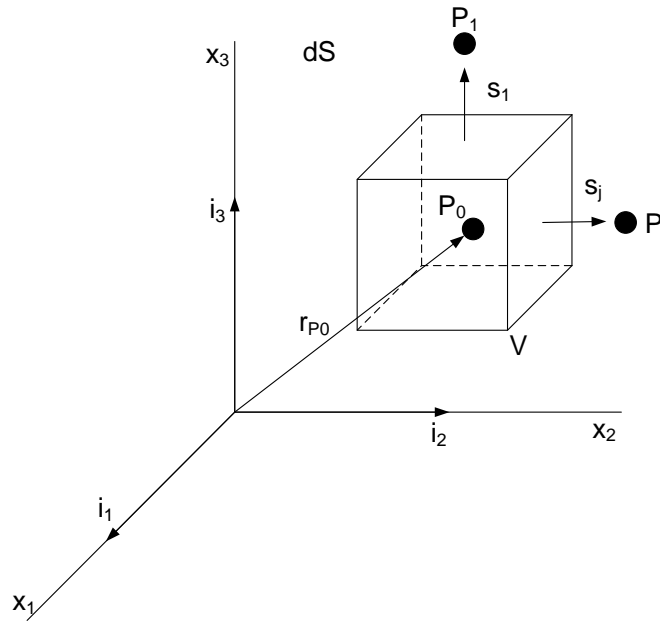


Figure 3-3. Variable arrangement

$$\begin{aligned} \frac{d}{dt} \int_{\Omega} \rho \varphi d\Omega + \sum_{j=1}^{n_f} \int_S \rho \varphi (\vec{V} - \vec{V}_S) \cdot \vec{n} dS \\ = \sum_{j=1}^{n_f} \int_{S_j} \Gamma_{\varphi} \text{grad} \varphi \cdot \vec{n} dS + \sum_{j=1}^{n_f} \int_{S_j} q_{\varphi S} \cdot \vec{n} dS + \int_{\Omega} q_{\varphi \Omega} d\Omega \end{aligned} \quad (3-10)$$

where n_f is the number of surfaces comprising a cell. The first term on the left side of Equation (3-10) is an unsteady term and the second term is an advective term. The first term on the right side is a diffusion term and the second and third terms are both source terms.

The following procedure is completed in order to evaluate the integral terms appearing in Equation (3-10).

1. Shape data processing to calculate the surface integral and cubic volume integral
2. Select approximation method of cubic volume integral
3. Select interpolation method of variables
4. Select discretization method for advective terms
5. Select integral scheme
6. Calculate velocity of cell interface

3.2.3.2 Derivation of algebraic equations

A SIMPLE method has been used as a solution method of equation (3-10). The linear simultaneous equation derived when applying a SIMPLE method is as follows (Patanker, 1980).

The unsteady terms of equation (3-10) use an implicit method of first order precision to perform discretization as follows.

$$\frac{d}{dt} \int_{\Omega} \rho \varphi d\Omega \approx \frac{(\rho \varphi \Omega)_{P_0} - (\rho \varphi \Omega)_{P_0}^{m-1}}{\delta t_m} \quad (3-11)$$

where ρ is density, φ is a conservative variable, δt_m is a time unit.

The flux of variable φ that passes through the cell surface is as follows.

$$C_j = \int_{S_j} \rho \varphi (\vec{V} - \vec{V}_S) \cdot \vec{n} dS \approx \dot{m}_j \varphi_j^* \quad (3-12)$$

where φ_j^* represents the value at the center of the surface comprising the cell and \dot{m}_j is the mass flux on the surface of the cell derived by the following equation.

$$\dot{m}_j = \int_{S_j} \rho(\vec{V} - \vec{V}_S) \cdot \vec{n} dS \approx \rho_j^* (V_j^* \cdot S_j - \dot{V}_j) \quad (3-13)$$

ρ_j^* and v_j^* are the density and velocity at the cell surface.

Flux on the cell surface due to diffusion of variable φ is approximated by the following equation.

$$D_j = \int_{S_j} \Gamma_\varphi \text{grad} \varphi \cdot \vec{n} dS \approx \Gamma_{\varphi,j} (\text{grad} \varphi)_j^* \cdot S_j \quad (3-14)$$

where, Γ_φ is a diffusion coefficient on the cell surface.

The source acting on surfaces such as heat flux acting on the surface of a physical object and the source acting on cubic volume such as acceleration of gravity during heat generation or at the location of flow while performing heat transfer analysis is approximated as follows:

Surface source:

$$\begin{aligned} Q_{\varphi S} &= \int_S q_{\varphi S} \cdot \vec{n} dS \\ &\approx \begin{cases} \sum_{j=1}^{n_f} \left(\left[\mu_{eff} (\text{grad} V)^T - \left(\frac{2}{3} \mu_{eff} \text{div} V + p \right) \mathbf{I} \right]_j \cdot i_i \right) \cdot S_j, & \text{for } \varphi = V_i \\ 0, & \text{for } \varphi = c_i, E, k, \varepsilon \end{cases} \end{aligned} \quad (3-15)$$

Cubic volume source:

$$Q_{\varphi \Omega} = \int_{\Omega} q_{\varphi \Omega} d\Omega \approx (q_{\varphi \Omega})_{P_0} \Omega_{P_0} \quad (3-16)$$

From Equations (3-10) to (3-16), Equation (3-9) becomes a linear equation using the value of φ at the center of the cell and the value φ at the adjacent cell. It can be written as follows:

$$a_{\varphi_0} \varphi_{P_0} - \sum_{j=1}^{n_f} a_{\varphi_j} \varphi_{P_j} = b_\varphi \quad (3-17)$$

where each term is calculated as:

$$a_{\varphi_j} = \Gamma_{\varphi_j} \frac{S_j \cdot S_j}{d_j \cdot S_j} - \min(\dot{m}_j, 0) \quad (3-18)$$

$$a_{\varphi_0} = \sum_{j=1}^{n_f} a_{\varphi_j} + \frac{(\rho \Omega)_{P_0}^{m-1}}{\delta t_m} \quad (3-19)$$

$$\begin{aligned}
 b_\varphi = & \sum_{j=1}^{n_f} \Gamma_{\varphi_j} \left((\text{grad}\varphi)_j \cdot S_j - \overline{\text{grad}\varphi} \cdot d_j \frac{S_j \cdot S_j}{d_j \cdot S_j} \right) \\
 & - \sum_{j=1}^{n_f} \frac{\gamma_\varphi}{2} \dot{m}_j \left((r_j - r_{P_0}) \cdot (\text{grad}\varphi)_{P_0} + (r_j - r_{P_j}) \cdot (\text{grad}\varphi)_{P_j} \right. \\
 & \left. + (r_j - r_{P_j}) \cdot (\text{grad}\varphi)_{P_j} \right) + Q_{\varphi_S} + Q_{\varphi_\Omega} \\
 & + \sum_{B=1}^{n_B} a_{\varphi_B} + \frac{(\rho\Omega\varphi)_{P_0}^{m-1}}{\delta t_m}
 \end{aligned} \tag{3-20}$$

where $n_b = n_f - n_i$ is the number of boundaries.

A SIMPLE algorithm uses the following procedure:

1. Uses an already known value to form and linearize coefficient matrix a_{φ_j} and source term b_φ for Equation (3-17). The linear simultaneous equation of this result is derived:

$$A_\varphi \varphi = b_\varphi \tag{3-21}$$

where A_φ is a matrix of $N \times N$. Vector φ is a dependent variable vector in the center of N number of cells and b_φ is a source vector.

2. Equation (3-21) is solved for each dependent variable. Because each coefficient matrix and the right side are approximated using the previous step value at this time, solving this equation is not strictly required.

3. Repeats until steps 1 and 2 are a predetermined convergence error.

3.2.3.3 Under-relaxation

When Equation (3-21) is calculated, variations in the values will increase rapidly often making it impossible to perform stable calculations. Because of this, the CCFD transforms the coefficient matrix and right side vector of Equation (3-21) as shown below:

$$A_\varphi \rightarrow A_\varphi + \frac{1 - \beta_\varphi}{\beta_\varphi} D_\varphi, \quad b_\varphi \rightarrow b_\varphi + \frac{1 - \beta_\varphi}{\beta_\varphi} D_\varphi \varphi^{k-1} \tag{3-22}$$

where β_φ is a relaxation coefficient and is a value between 0 and 1, D_φ is a diagonal term of matrix A_φ and φ^{k-1} is a value before one step of the reiteration process.

3.2.4 Volume of Fluid (VOF) method

A method used for advecting an interface is the volume of fluid method originally developed by Hirt and Nichols (1981). This method uses a fluid fraction variable F , which varies between 0 and 1, indicating the fraction of each computational cell that is filled with a fluid

phase. This VOF function F is then advected according to the local flow velocity. More accurate schemes for advecting the volume fractions have been developed after that. A comprehensive review is given by Rider and Kothe (1998). Generally, there are two classes of methods, namely piecewise constant and piecewise linear reconstructions of the interface, dependent on the required accuracy of the interface and the reconstruction.

3.3 Discrete Element Method (DEM)

DEM is a popular numerical technique for computing the behavior of discrete particles. This method was originally applied by Cundall (1971) to problems in rock mechanics. The method is based on the use of an explicit numerical scheme in which the interactions between a finite number of particles are monitored contact by contact and the motion of the particles is modeled particle by particle. Each contact follows a soft contact approach where an overlap of particles is accepted. This overlap is not a real phenomenon but instead intends to model the deformation of the interacting bodies at a contact point in an indirect way. The particles are treated as rigid bodies and the overlap during a contact is assumed to be relatively small compared to the particle size.

The DEM scheme relies upon the assumption that a small enough time step should be chosen to ensure that, during a single time step, others disturbances do not propagate from any particle further than its immediate neighbors. DEM has the capacity of modeling materials at microscopic levels and analyzing multiple interacting bodies undergoing large displacements and rotations, thus capturing all the phenomena that relates to the particulate nature of granular media. Following the pioneering work of Cundall and Strack (1979), research into DEM has increased dramatically in light of its potential.

3.3.1 Particles movement

The force-displacement law is used to find contact forces from known (and fixed) displacements, the Newton's second law gives the motion of the particles resulting from the known (and fixed) forces acting on them. The Figure 3-4 presents the calculation cycle scheme.

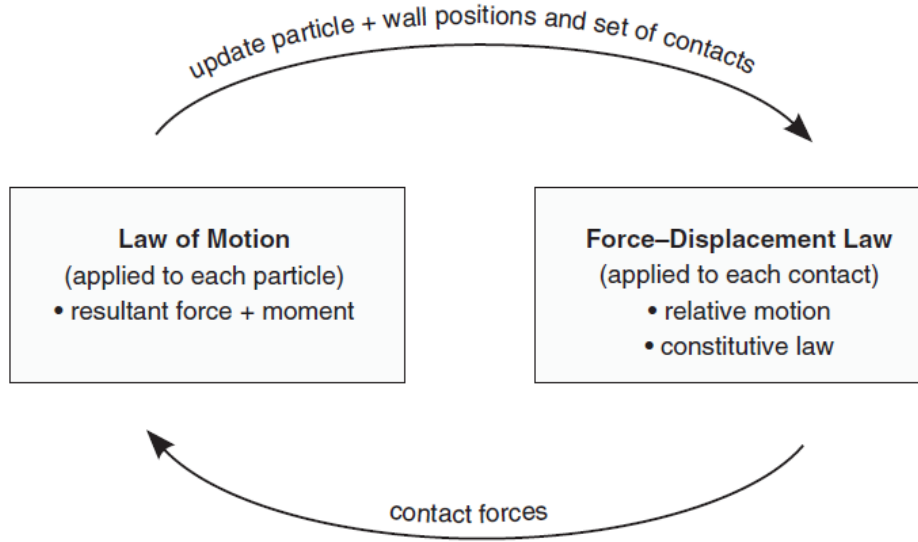


Figure3-4. DEM calculation cycle scheme

The solid movements are determined by writing Newton's dynamic relations. The motion of a single rigid particle is determined by the resultant force and moment vectors acting upon it, and can be described in terms of the translational motion of a point in the particle and the rotational motion of the particle. The translational motion of the center of mass is described in terms of its position, x_i , velocity, \dot{x}_i , and acceleration, \ddot{x}_i ; the rotational motion of the particle is described in terms of its angular velocity, ω_i , and angular acceleration, $\dot{\omega}_i$. The corresponding equations that describe translation and rotation of the particle about its center of mass are developed as:

$$m\ddot{x}_i = \left(\sum_{c=1}^{N_c} F_i^c \right) + mg_i \quad (3-23)$$

$$I\dot{\omega} = \sum_{c=1}^{N_c} M_i^c \quad (3-24)$$

where m is the mass of the particle, N_c is the number of contacts, \ddot{x}_i is acceleration of the solid centroid, F_i^c and g_i are the i th components of the contact force F and the gravity g , I is the inertia of the block, $\dot{\omega}$ is the angular acceleration of the solid centroid, M_i^c is moment of i th particle.

In order to solve the Newton's equations in a discrete way, the DEM describe the translational and rotational accelerations at time t in terms of the velocity values at mid-intervals. The accelerations are calculated as:

$$\ddot{x}_i^{(t)} = \frac{1}{\Delta t} \left(\dot{x}_i^{(t+\Delta t/2)} - \dot{x}_i^{(t-\Delta t/2)} \right) \quad (3-25)$$

$$\dot{\omega}_i^{(t)} = \frac{1}{\Delta t} \left(\omega_i^{(t+\Delta t/2)} - \omega_i^{(t-\Delta t/2)} \right) \quad (3-26)$$

where $\ddot{x}_i^{(t)}$ and $\dot{\omega}_i^{(t)}$ are the linear and angular accelerations of the particle centroid respectively.

Using Equations (3-23) to (3-26), the velocities at mid-intervals become:

$$\dot{x}_i^{(t+\Delta t/2)} = \dot{x}_i^{(t-\Delta t/2)} + \left(\frac{F_i^{(t)}}{m} + g_i \right) \Delta t, \text{ where } F_i^{(t)} = \sum_{c=1}^{N_c} F_i^c \quad (3-27)$$

$$\dot{\omega}_i^{(t+\Delta t/2)} = \dot{\omega}_i^{(t-\Delta t/2)} + \left(\frac{M_i^{(t)}}{I} \right) \Delta t, \text{ where } M_i^{(t)} = \sum_{c=1}^{N_c} M_i^c \quad (3-28)$$

So the velocities are used to update the position of the particle center as:

$$x_i^{(t+\Delta t)} = x_i^{(t)} + \dot{x}_i^{(t+\Delta t/2)} \Delta t \quad (3-29)$$

3.3.2 Time-step

The time step referred to in DEM simulations is the duration between two consecutive iterations. DEM usually uses an explicit and central time-finite-difference scheme. Although this explicit numerical scheme is more computationally efficient than the implicit numerical scheme, there is a limitation that it is only conditionally stable; so small time steps must be used. If the used time step is greater than a critical time step, the scheme is unstable and the simulation outcomes are unreliable. For a three-dimensional collection of particles, a critical time-step is found for each body by applying Equation (3-29) separately to each degree of six degrees of freedom.

$$t_{crit} = \begin{cases} \sqrt{m/k^{tran}}, & \text{(translational motion)} \\ \sqrt{I/k^{rot}}, & \text{(rotational motion)} \end{cases} \quad (3-30)$$

where k^{tran} and k^{rot} are the translational and rotational stiffnesses, respectively, and I is the moment of inertia of the particle. The final critical time-step is taken to be the minimum of all critical time-steps computed for all degrees of freedom of all bodies.

3.3.3 Damping

Kinetic energy may be dissipated in two ways in DEM: frictional sliding and damping. Frictional sliding is a real phenomenon, whereas damping is artificially introduced to dissipate energy to achieve a steady state packing within a reasonable time frame. DEM software, such as PFC3D supports two forms of damping: viscous damping and local damping. Viscous damping acts at each contact while local damping acts on each particle in the whole system.

Local damping applies a damping force, with magnitude proportional to unbalanced force, to each ball. The damping force is controlled by the damping constant α , whose default value is 0.7. Local damping is inappropriate for particles in free flight under gravity. In order to obtain realistic energy dissipation, it may be necessary to set all local damping coefficients to zero, and implement a viscous damping.

Viscous damping adds normal and shear dashpots at each contact. These dashpots act in parallel with the existing contact model, and provide forces that are proportional to the relative velocity difference between the two contacting entities (ball-ball or ball-wall). When viscous damping is used in a PFC3D model in a dynamic situation, such as a free-flight simulation, appropriate viscous damping constants should be specified for the simulation to reproduce a realistic response.

Kawaguchi et al. (1992) derived the relation by solving the equations of motion for free vibration with viscous damping. In our simulations we set the value of viscous damping as 0.04.

3.3.4 Contact Model

The constitutive behavior of a material is simulated in PFC3D by associating a contact model with each contact. PFC3D provides two standard contact models include the linear and Hertz models. Component behaviors that are provided by these models include stiffness, slip and bonding. The contact stiffnesses relate the contact forces and relative displacements in the normal and shear directions. The normal stiffness is a secant stiffness,

$$F_i^n = k^n U_i^n n_i \quad (3-31)$$

where F_i^n is the normal contact force vector, k^n is the normal stiffness, U^n is the relative contact displacement in the normal direction. The shear stiffness is a tangent stiffness,

$$\Delta F_i^n = -k^s \Delta U_i^s \quad (3-32)$$

where ΔF_i^n is the shear elastic force-increment vector, k^s is the shear stiffness at the contact, ΔU_i^s is the shear component of the contact displacement-increment vector, occurring over a time-step of Δt .

Slip behavior is provided by enforcing a relation between shear and normal force, such that the two contacting entities may slip relative to one another. The slip behavior is defined by the friction coefficient μ_c at the contact. The maximum allowable shear contact force:

$$F_{\max}^s = \mu_c |F_i^n| \quad (3-33)$$

where μ_c is taken to be the minimum friction coefficient of the two contacting entities. If $|F_i^s| > F_{\max}^s$, then slip is allowed to occur.

The value of friction coefficient μ_c of particle - particle and particle - wall used in our simulations is 0.4 (Grigoriev et al., 1997).

PFC3D allows particles to be bonded together at contacts. The two standard bonding behaviors are embodied in contact bonds and parallel bonds. Both bonds can be envisioned as a kind of glue joining the two particles.

3.4 CFD and DEM two-way coupling

The flow in the whole flow region is calculated from the continuity and the Navier-Stokes equations with a porosity term and an additional body force term to account for the presence of particles in the fluid, which are given by

$$\frac{\partial \Phi}{\partial t} + \vec{V} \cdot (\Phi \vec{V}) = 0 \quad (3-34)$$

$$\rho \frac{\partial \Phi \vec{V}}{\partial t} + \rho \vec{V} \cdot \vec{\nabla} (\Phi \vec{V}) = \Phi \vec{\nabla} p + \mu \vec{\nabla}^2 (\Phi \vec{V}) + \vec{f}_b + \rho \Phi \vec{g} \quad (3-35)$$

where ρ is the density of the fluid, Φ is porosity, \vec{V} is the fluid velocity, p is the fluid pressure, μ is the dynamic viscosity of the fluid, \vec{f}_b is a body force per unit volume, and \vec{g} is the gravitational acceleration. The porosity and body force in these fluid elements are determined by the DEM.

The equations of motion for particles with an additional force term to account for interaction with the fluid are expressed as:

$$m \frac{\partial \vec{V}_p}{\partial t} = \vec{f}_{mech} + \vec{f}_{fluid} + m \vec{g} \quad (3-36)$$

$$\frac{\partial \vec{\omega}}{\partial t} = \frac{\vec{M}}{I} \quad (3-37)$$

where \vec{V}_p is the particle velocity, m is the particle mass, \vec{f}_{fluid} is the total force applied by the fluid on the particle, \vec{f}_{mech} is the sum of additional forces acting on the particle, \vec{g} is the gravitational acceleration, $\vec{\omega}$ is the particle angular velocity, I is the moment of inertia and \vec{M} is the moment acting on the particle.

\vec{f}_{fluid} is made up of two parts: the drag force and a force due to the fluid pressure gradient:

$$\vec{f}_{fluid} = \vec{f}_{drag} + \frac{4}{3}\pi r^3(\vec{\nabla}p + \rho\vec{g}) \quad (3-38)$$

$$\vec{f}_{drag} = \vec{f}_0\Phi^{-\chi} \quad (3-39)$$

where \vec{f}_0 is the force on a single particle. The $\Phi^{-\chi}$ term is an empirical factor to account for the local porosity. This correction term makes the force applicable to both fixed and fluidized porosity systems and for a large range of Reynolds numbers (Di Felice, 1994 and Xu, 1997).

The single particle force in an infinite medium is defined as:

$$\vec{f}_0 = \left(\frac{1}{2}C_d\rho\pi r^2|\vec{V}_p - \vec{V}|(\vec{V}_p - \vec{V}) \right) \quad (3-40)$$

where r is the particle radius, C_d is a drag coefficient, has been given by Dallavalle (1948):

$$C_d = \left(0.63 + \frac{4.8}{\sqrt{Re_p}} \right)^2 \quad (3-41)$$

The particle Reynolds number, Re_p is:

$$Re_p = \frac{d_s\rho|\vec{V}_p - \vec{V}|}{\mu} \quad (3-42)$$

The empirical coefficient χ is defined as:

$$\chi = 3.7 - 0.65\exp\left[-\frac{(1.5 - \log_{10} Re_p)^2}{2}\right] \quad (3-43)$$

The body force per unit volume, \vec{f}_b , in each fluid element is determined as:

$$\vec{f}_b = \frac{\sum_j \vec{f}_{drag}^j}{\Omega} \quad (3-44)$$

where Ω is the volume of the fluid element.

DEM and CFD two-way coupling is numerically achieved as follows (Figure 3-5). Equations (3-34) and (3-35) are solved with the CFD code CCFD, and Equations (3-36)-(3-44) are solved with the DEM code PFC3D. The porosity and the body force are determined in PFC3D and divided by volume in CCFD. The fluid velocity and fluid pressure in every element are determined by CCFD and send to PFC3D in each coupling data exchange.

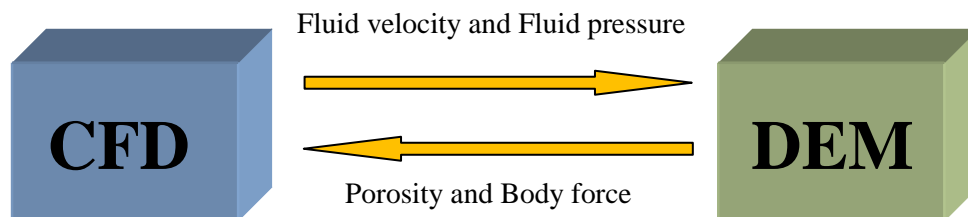


Figure 3-5. DEM and CFD two-way coupling

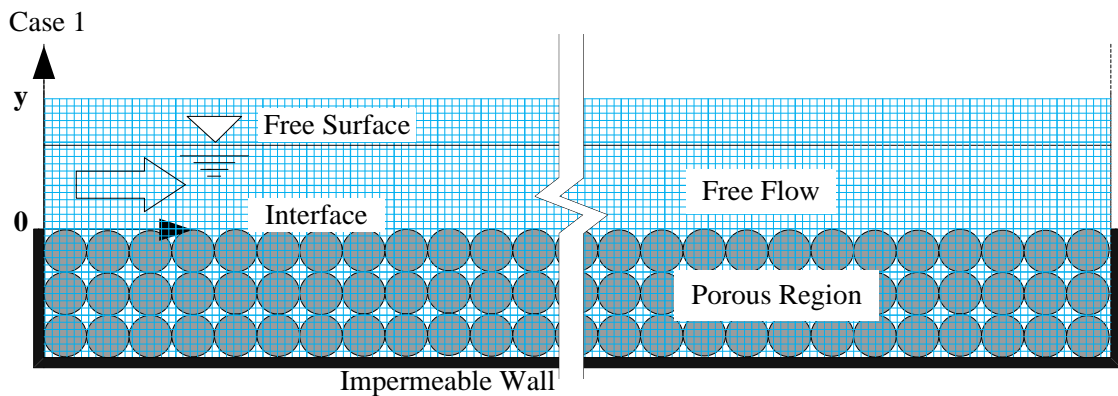
3.5 Validation test of the method

The best way to examine and increase the understanding of the numerical simulation is to compare it with the existing experimental and the simulation data. Accordingly, the computational conditions, including inlet flow velocity, the depth of free surface flow, thickness and porosity of porous regions, position of interface and channel slope were set to match the conditions of the available reference data.

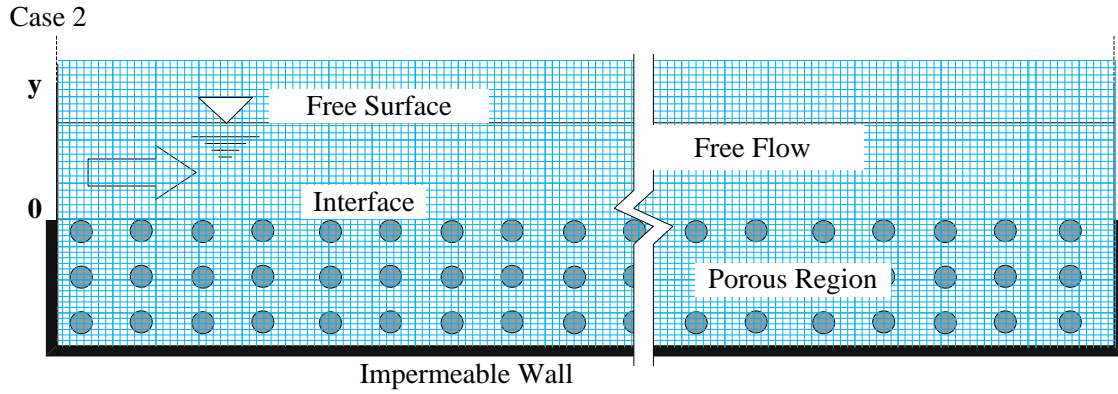
Table 3-2. Measured experimental parameters from Shimizu et al. (1990) (cases 1a, 1b, 1c) and Prinos et al. (2003) (cases 2a, 2b)

Case	Φ	H (m)	d (m)	d/H	S_o	U_w (m/s)	Re
1a	0.3800	0.1458	0.0567	0.3889	2×10^{-3}	0.435	2.351×10^4
1b	0.3800	0.1752	0.0861	0.4914	2×10^{-3}	0.487	3.869×10^4
1c	0.3800	0.1781	0.0591	0.3318	2×10^{-3}	0.417	2.339×10^4
2a	0.8286	0.0850	0.0300	0.3529	2×10^{-3}	0.253	7.581×10^3
2b	0.8286	0.1050	0.0500	0.4762	2×10^{-3}	0.287	1.437×10^4

where Φ is the porosity of the porous media, H is the whole channel depth, d is the clear fluid depth, S_o is the channel slope, U_w is the mean velocity of the free flow. The Reynolds number is defined as $Re = \frac{U_w d_H}{\nu}$.



Side view of Shimizu et al. (1990)'s experiments

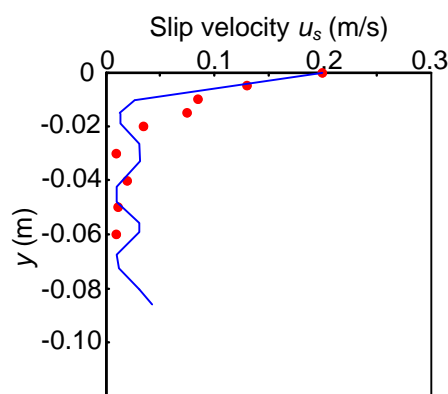


Side view of Prinos et al. (2003)'s experiments

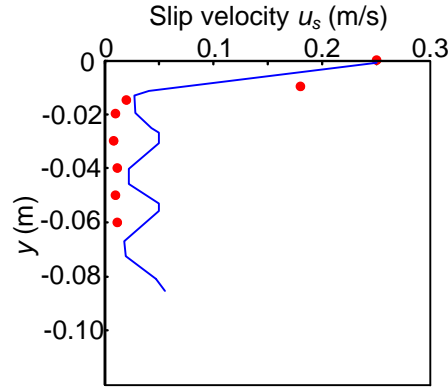
Figure 3-6. Schematic diagram of the model tests

Case 1: Shimizu et al. (1990) performed experiments modelling of flow in a laboratory flume (8 m long, 0.21 m wide) partially filled with glass beads (with diameter, $D = 2.97$ cm). The glass beads were arrayed as the porous medium. The geometric and hydrodynamic characteristics are shown in Figure 3-6 case 1 and Table 3-2 (1a, 1b and 1c), respectively.

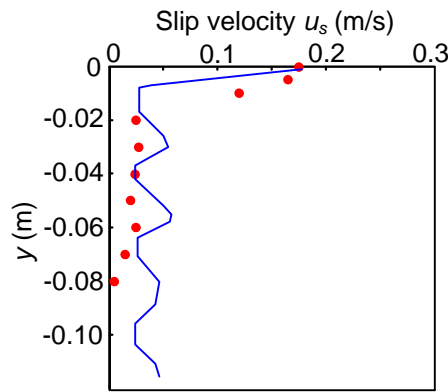
Figure 3-7 compares the computed longitudinal velocity distributions u_s below the fluid/porous interface with the experimental data obtained by Shimizu et al. (1990). Notably, the present numerical model accurately represents the general trend of the velocity distributions. The interface velocity values are quite high, with values varying from 0.17 to 0.26, which are much higher than the respective laminar flow values over a porous medium, as predicted by Choi and Waller.



(1a)



(1b)



(1c)

Figure 3-7. Comparison of velocity distribution within porous medium. Lines, computations; symbols, measurements (Shimizu et al. 1990)

Case 2: Prinos et al. (2003) investigated fully developed and uniform flow in a flume with a porous bed. The flume was 12 m long, 0.25 m wide and 0.5 m high. The porous bed was simulated using spatially periodic rods ($D = 10$ mm) in a non-staggered arrangement. The geometric and hydrodynamic characteristics are shown in Figure 3-6 (case 2) and Table 3-2 (2a and 2b), respectively.

Figure 3-8 plots the turbulent velocities above the fluid/porous interface in both the cases, as obtained by using the present model. The velocities are presented in dimensionless coordinates $y^+ (= yU_*/\nu)$ and $u^+ (= u/U_*)$ to enable them to be directly compared with both the measured and computed data by Prinos et al. (2003). The logarithmic law in the fully turbulent region, $u^+ = (1/\kappa) \ln(y^+) + C$ ($\kappa = 0.41$, $C = 5.29$), for flow over a smooth impermeable bed are also plotted. The presence of the porous medium causes a significant reduction of the velocities in the clear fluid region, compared to the flow over the smooth impermeable bed. This is due to the action of turbulent shear stress and the penetration of

turbulence inside the porous region, which reduces the mean velocities above the porous region. Similar trends are observed in the measured velocity distribution. The present model indicates superior agreement with the measured data over the computed data given by Prinos et al. 2003, which may be due to the periodicity boundary conditions were applied in the direction of the mean flow by Prinos et al. 2003, but the present model simulates the channel used in laboratory experiments in the same dimension.

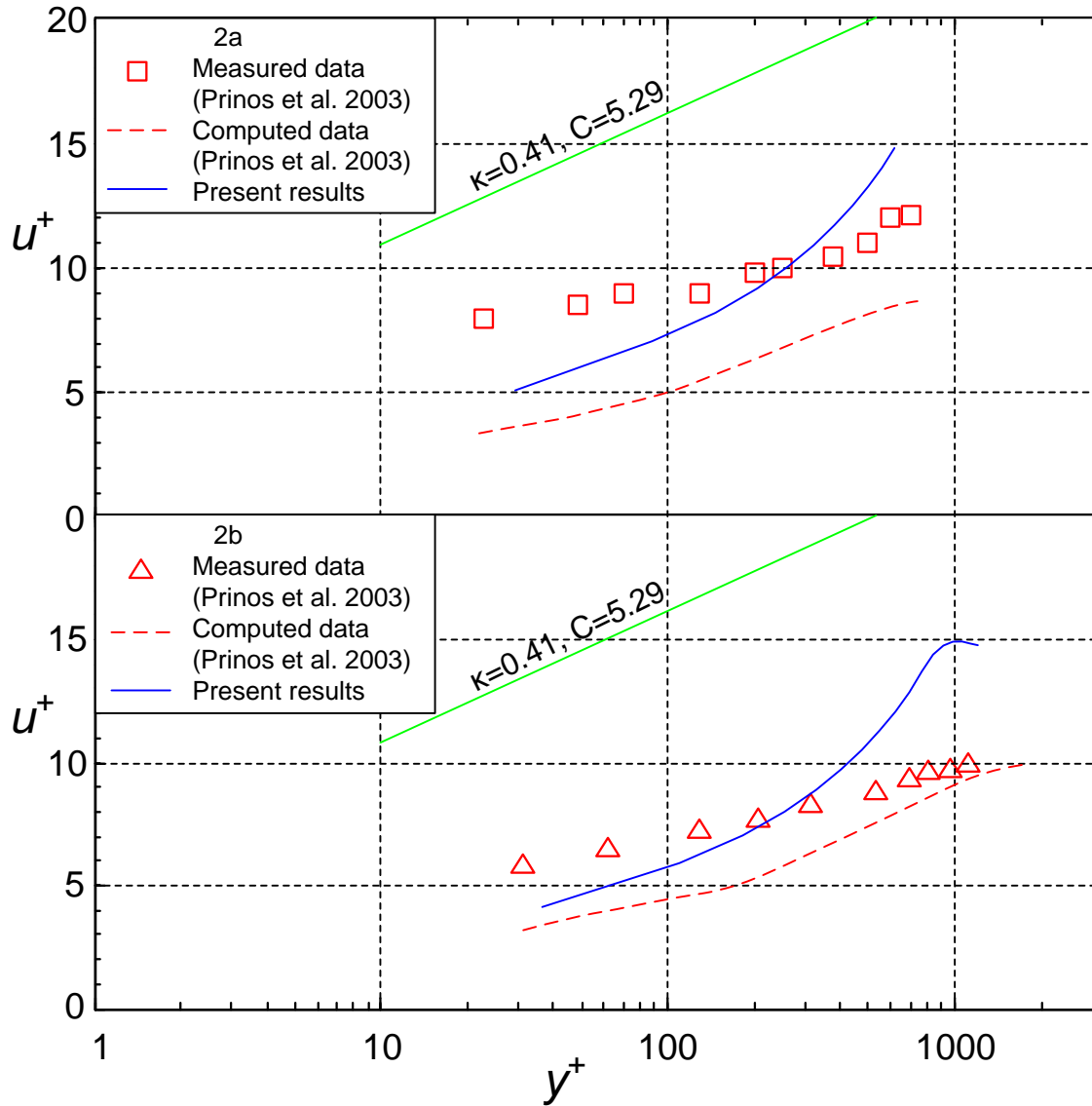


Figure 3-8. Turbulent velocity distribution in the free flow above porous region in dimensionless coordinates. Lines, computations; symbols, measurements (Prinos et al. 2003)

Figure 3-9 shows the normalized turbulent kinetic energy $k^+ (= k/U_*^2)$ for these two cases (2a and 2b) using the present model, the corresponding measured and simulated data by Prinos et al. (2003) are also plotted on this figure. The penetration of turbulence kinetic

energy into the porous region appears significant, and the maximum values of k^+ occur extremely close to the interface. Within the porous region, the present model approximates the data simulated by Prinos et al. (2003) in an average sense. On the other hand, in the clear fluid region our model and measured data are higher than the data simulated by Prinos et al. (2003), this is because Prinos et al. (2003) used a 2D model, but the measured data and present model is 3D.

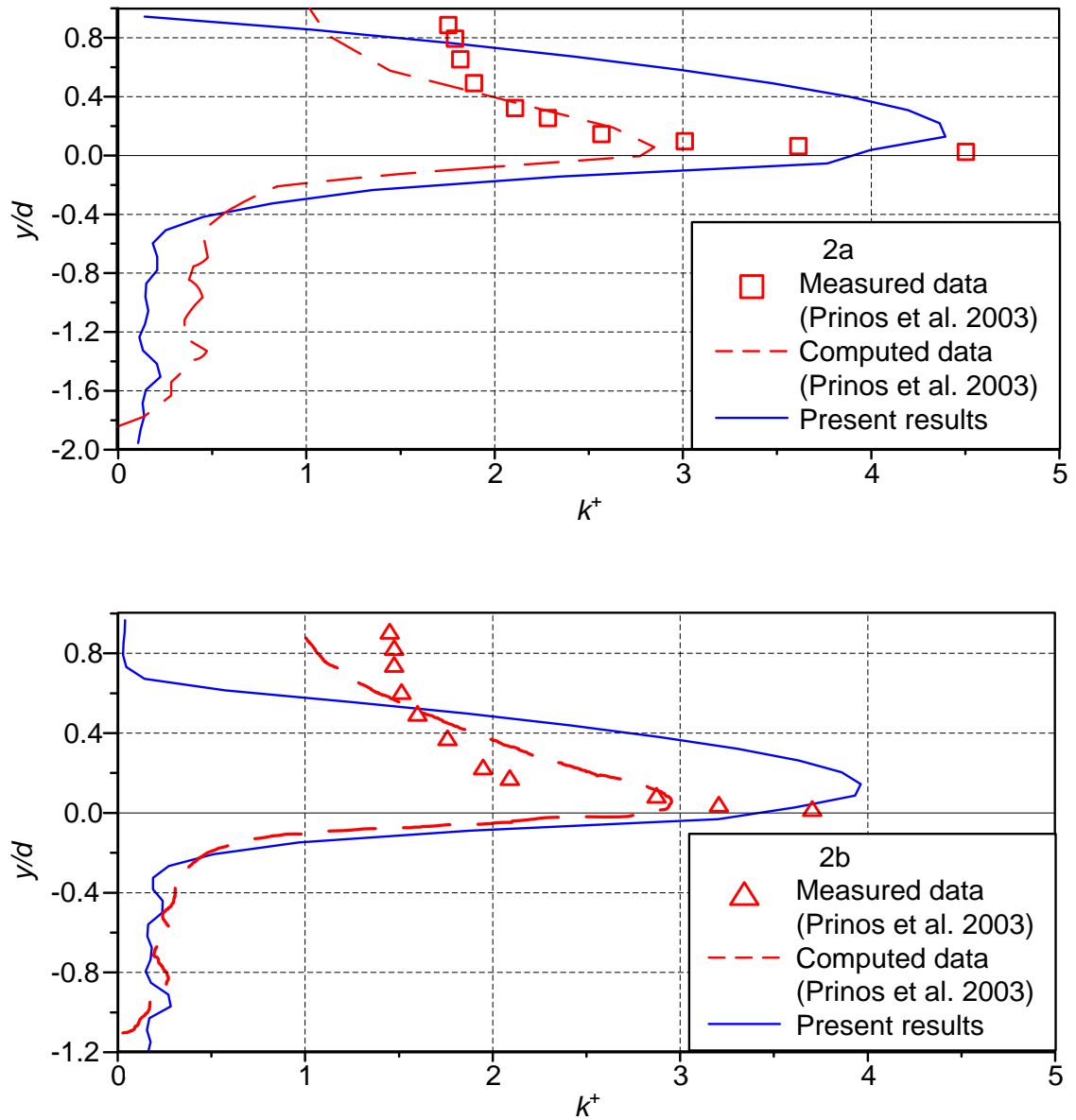


Figure 3-9. Turbulent kinetic energy over the whole depth. Lines, computations; symbols, measurements (Prinos et al. 2003)

3.6 Conclusions

This chapter presents the numerical solutions for turbulent 3D flow in an open channel with a porous medium. A numerical method was conducted with the CFD-DEM two-way coupling method. The fluid flow in the open channel is simulated using CFD; and the porous bed placed at the bottom of the channel and the particles transported by fluid are simulated by DEM. The porosity of particles, body force, fluid velocity and fluid pressure are terms accounting for the connection of the CFD and DEM. A comparison with the experimental data available in the literature validates this numerical tool. Velocity distributions in the free fluid flow region and in the porous flow region both agree well with the experiment data given by previous literatures.

Chapter 4

Experimental Method

In this chapter the experimental settings used in our particle transport experiment in open channel are presented and the measuring methods to capture the velocity of particles and the velocity field are introduced.

4.1 Description of the experimental settings

4.1.1 Design of hydraulic parameters in the study

Nezu and Rodi (1986) show that if the channel width is 5 times bigger than the flow depth, then the influence of side wall can be ignored, because our flume is 3 cm wide so a flow depth under 6 mm is suggested. Because we intend to study the particle transport around the critical velocity, so the Shields diagram (shown in Figure 2-5) is used to determine the critical flow condition. When flow depth $d=0.006$, slope $S_o=0.0175$ and particle diameter $d_s=0.002$, the Shields parameter and particle Reynolds number are got $\tau^*=0.032$ and $Re_p=64.2$, by checking the Shield diagram we can find it is just round the critical flow condition. Using Manning equation we can get the mean flow velocity $U_w=0.44$ m/s, and the critical flow rate could be determined by equation:

$$Q = U_w dB$$

So the flow rate $Q=4.7$ l/min.

As we want to study the interaction between the particle and porous bed, so the length of the porous bed can be determined by L_s is larger than 10 times the saltation distance of a

Chapter 4: Experimental Method

particle transported by flow. By observation, the length of the porous bed $L_s=0.1$ m is sufficient for more than 10 contacts between particle and porous bed.

For uniform equilibrium we suggest seepage outflow rate $Q_I < Q/10$, so the maximum flow slope change S_f over a 0.1 m porous bed is:

$$S_f = \frac{\Delta d}{L_s} = \frac{0.1d}{L_s} = \frac{0.1 \times 0.006}{0.1} = 0.006$$

The maximum flow slope change is small compared to bed slope. The maximum seepage downward velocity V_s is as:

$$V_s L_s B = \frac{U_w dB}{10}$$

$$V_s = \frac{d}{10L_s} U_w = 0.006 U_w = 0.0026 \text{ m/s}$$

For a porous medium has a porosity $\Phi=0.476$, the maximum flow velocity in the pores V_v is:

$$V_v = \frac{U_s}{\Phi} = \frac{0.006 U_w}{0.476} = 0.013 U_w = 0.0055 \text{ m/s}$$

The maximum flow velocity in the pores is about 100 times smaller than the mean flow velocity, so the influence of seepage outflow rate is very limited to the main flow in the open channel.

The parameters in our study then can be determined as follows:

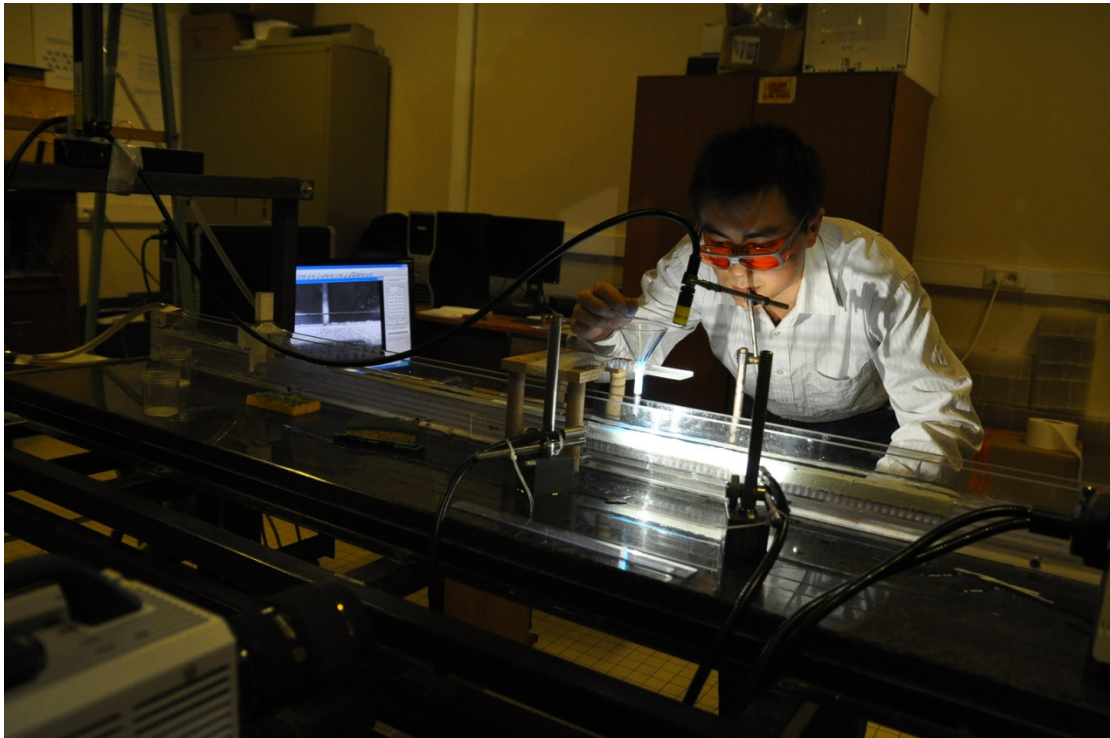
1. Channel slope S_o varied from 0.0035 to 0.0244 (Angle of channel θ varied from 0.2° to 1.4°).
2. Inflow rate Q varied from 3.2 l/min to 6.8 l/min.
3. Seepage outflow rate Q_I varied from 0 to 10% of the inflow rate Q .
4. Particle diameter d_s varied from 1 mm to 4 mm.

4.1.2 Flow channel

The equipment used in experiment is a rectilinear open channel with total length of 2 m, width of 30 mm and depth of 8.5 mm (Figure 4-1). This equipment has been borrowed from Geosciences Laboratory of University of Rennes 1. This channel permits to create a free surface flow. This characteristic is very important to study those behaviors happened in real nature, like situations in channels or rivers and run off on road after storm. The channel is

Chapter 4: Experimental Method

made up by Plexiglas entirely, which can provide a good view from both sides. It is based on a smooth marble surface and supported by an adjustable steel structure which gives the ability to change the inclination with an electric motor. At the end of the channel flow drops into a tank contains a filter which collects grains, and clear water will be pumped into a constant level tank, and then goes to the entrance of the channel. There is a device sites at the entrance portion of the channel intend to reduce turbulences, bubbles, etc. because of the sudden change of section. This device is made up by a porous media and following by an array of straws with a diameter of 5 mm and a length of 10 cm.



(a)

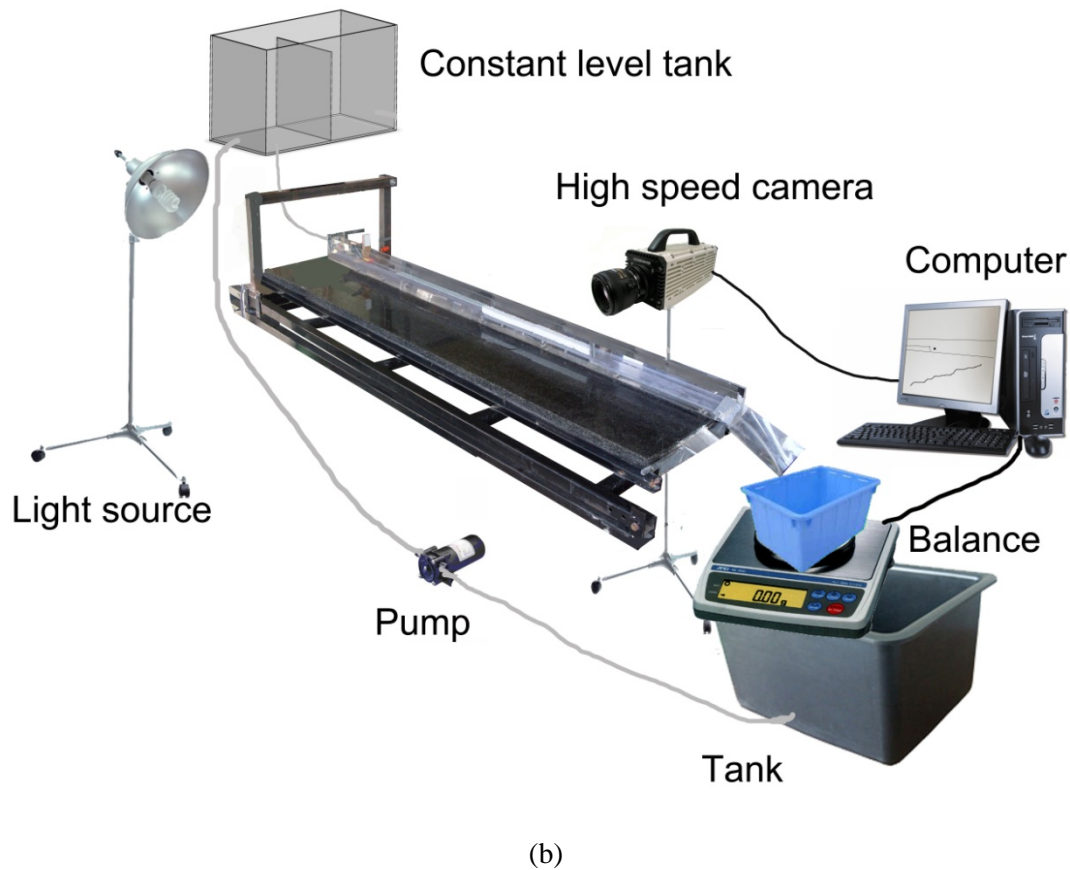


Figure 4-1. Experiment system scheme; (a), photo of the experiment system; (b), scheme

4.1.3 Water supply

The flow in the channel is supplied by a gravity flow from a tank placed at about 1 m high over the channel. To maintain a constant level in the tank, a vertical board separates the tank into two parts, there will be an overflow when the height of incoming water reaches the top of vertical board. This apparatus ensures the constant inflow pressure and flow rate to the channel. A regulation valve is installed in front the entrance of the channel to adjust flow rate to the value we want. Finally, a pump sits next to the recycling tank at the end of channel lift the water to the constant level tank, close the circuit. This water supply system by gravity can provide a flow rate up to 7 L/min, which correspond to a maximum depth-averaged velocity of 0.38 m/s (with an inclination angle of 0.6°).

When the flow condition (e.g. inflow rate, seepage outflow rate, channel slope, etc.) changes, the depth of free surface flow in the channel is then depended by flow resistance.

4.1.4 The measure of flow rate

We use an A&D GX-4000 electronic balance and a tank placed at the end of the channel to measure the flow rate. The water will be received entirely by this tank during the measurement and the electronic balance placed under this tank connected with computer can

Chapter 4: Experimental Method

gives a mass of the tank every second, so the volume flow rate Q in unit of L/min is calculated as follows:

$$Q = (m_{\Delta t+1} - m_{\Delta t}) \times 60/1000$$

where $(m_{\Delta t+1} - m_{\Delta t})$ is the change of mass of tank every second. The repeatability of the electronic balance is 0.01 g, therefore the standard deviation the measurements of the flow rate is 0.0009 L/min. The principle advantages of this measure method are its high precision and without pressure loss.

4.1.5 Particle adding device

The device for adding particles (Figure 4-2) allows the particles to be added into the flow easily. In order to reduce the energy of the particles, sponge is pasted over the inner surface of funnel, and the pipe of the funnel is thin enough to allow just only one particle passes, and it is changeable when the diameter of particle is changed. The distance between the end of the pipe and the bottom of the channel is about 5 mm. The advantages of this device are as follows: the particles can be easily added into the flow at the same position one by one, the initial energy of each particle can be equal and minimized.

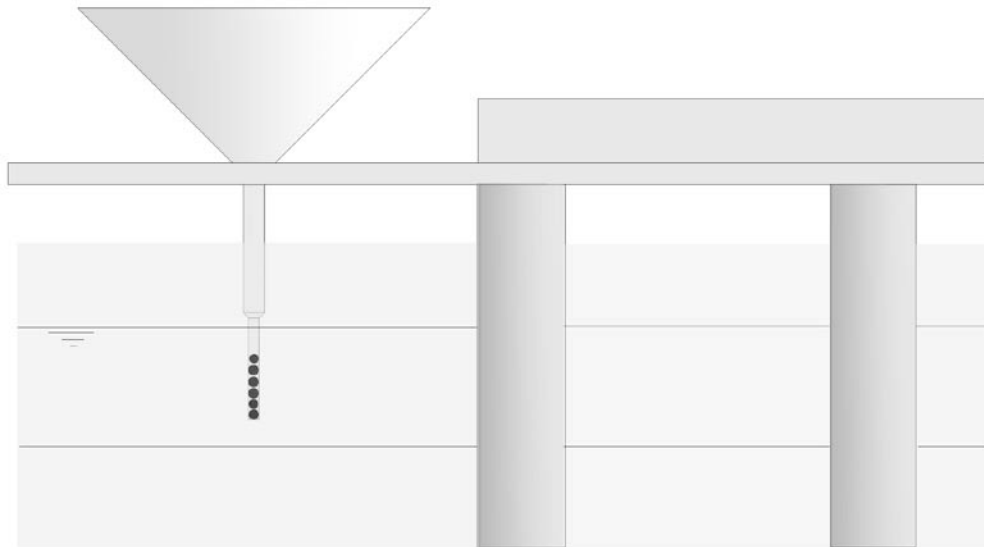


Figure 4-2. Particle adding device scheme and side view of the flow channel

4.1.6 Porous bed

The main objective of this research is to study the interaction between free surface flow and porous bed. Thus an artificial porous medium has been performed. During the first

Chapter 4: Experimental Method

experiments, the size of porous bed is 500 mm×30 mm×20 mm, and it is made up 2 mm glass round particles, in order to fix the particles forming the porous bed, paint has been used as a glue (Figure 4-3).

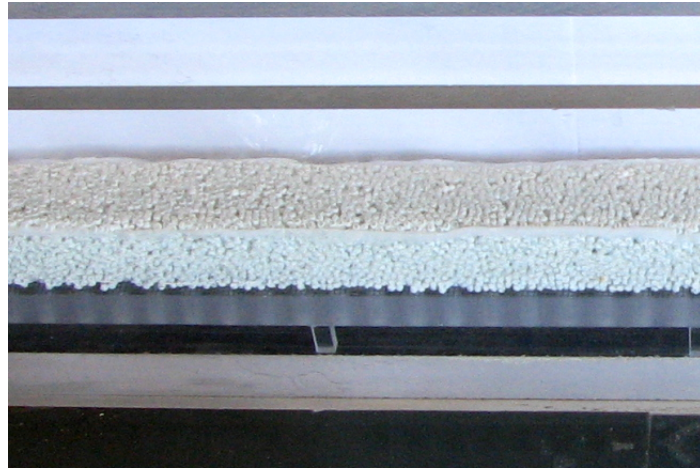


Figure 4-3. Porous bed used during the first experiments

After several experiments some problems have been detected. Firstly, with paint in the hole between particles, the porosity of the porous media cannot easily be calculated; secondly, during the experiments, the surface of porous bed would be eroded by the flow, ruts forms, when some particles leave their positions, which could increase the average surface roughness and influence the motion of transported particles; thirdly, this kind of porous bed would be very easily destroyed when it is taken out of the channel for cleaning, because its structure is not strong. These technical limitations made us to conceive a new method to construct porous bed.

The new method is to use the magnetic stainless steel balls (Figure 4-4). There are several advantages of this kind of balls, such as, they could be used to compose the porous media with different porosity without any glue, so they could be disassembled and reused, the precision of diameter is very good, and the magnetic force between the balls is big enough to protect the structure of porous media counter the flow.



Figure 4-4. Magnetic stainless steel balls

Spherical particles of equal size theoretically may be packed in five different ways (White and Walton, 1937) as shown in Figure 4-5, e.g. (1) cubical with a porosity of 47.64%, (2) single-staggered or cubical-tetrahedral with a porosity of 39.55%, (3) double-staggered with a porosity of 30.20%, (4) pyramidal, and (5) tetrahedral; the porosities in the latter two are identical, 25.95%.

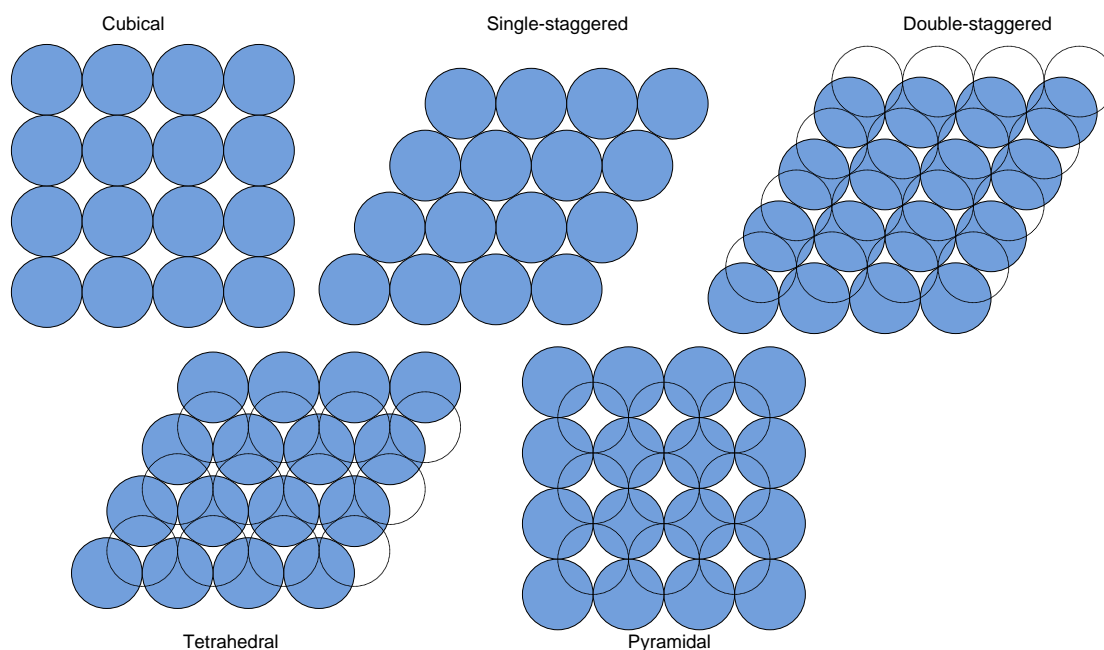


Figure 4-5. Illustration of the various packing models presented by White and Walton (1937)

In our study, a cubic pack (Figure 4-4) with 2010 pieces 3 mm magnetic stainless steel balls are employed, the size of porous bed is 201 mm×30 mm×9 mm. Under the porous bed is a permeable layer in chemical fiber. The third layer is a plastic board with holes. There are pillars to support all these layers and at the end of the void layer a pipe is used to drain the

filtered water outside of the channel. Outside of the study zone plastic boards with a single layer of magnetic balls spread on it are used to level up the bottom of the channel to the same level of the porous bed.

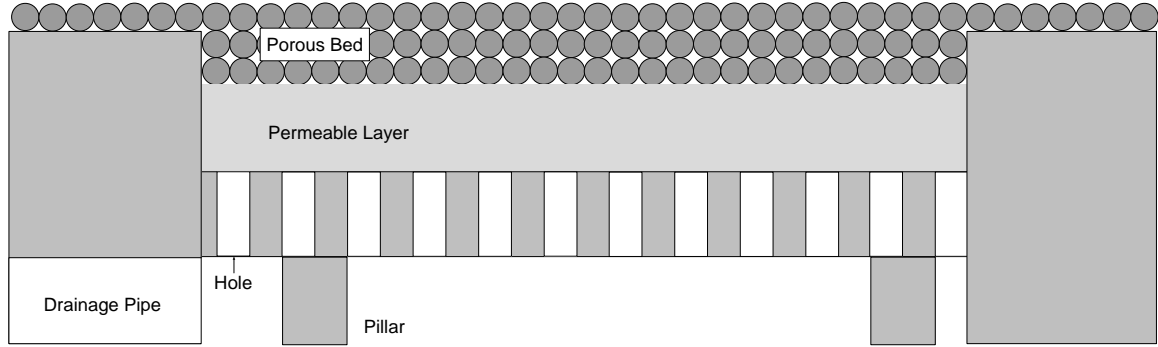


Figure 4-5. Structure of the porous bed

4.2 Measure of the particle velocity

In our experiment, movement of particles was captured by a PHOTRON Fastcam APX-RS high speed camera, which could provide 1024×1024 pixel resolution up to 3,000 frames per second (fps). We are interested mainly to visualize the flow in the longitudinal direction, hence a high resolution in this direction is requested. However, in view to reduce the size of images, we have reduced the resolution in the transverse direction. A resolution of 1024×128 pixels and a frame rate of 250 images per second have been chosen. In this study, the spatial resolution of the images taken by high speed camera is 1 pixel standing for 0.1 mm. This frame rate allows displaying the movement of particles properly. The software ImageJ has been used to treat the images. With the method of subtractions between two successive images, a series of particles' positions could be obtained. The change of the particle's position $(\Delta x_i, \Delta y_i)$ corresponding to a timestep of Δt_i between two successive images, permits to calculate the velocity components in flat (x, y) as follows:

$$u_{pi} = \frac{\Delta x_i}{\Delta t_i} \quad (4-1)$$

$$v_{pi} = \frac{\Delta y_i}{\Delta t_i} \quad (4-2)$$

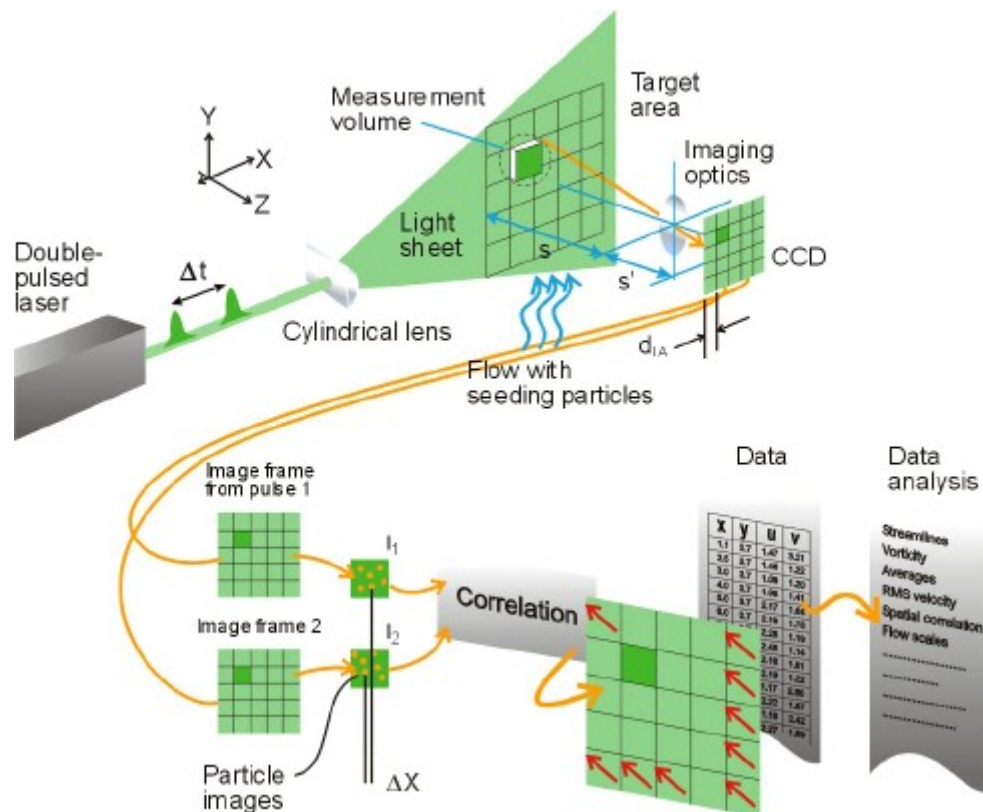
4.3 Measure of the flow velocity field by a PIV system

The flow velocity field is obtained by a Particle Image Velocimetry (PIV) system. A PIV is an optical technique to measure instantaneous 2D velocity fields. A PIV system typically consists of a laser with sheet optics, one digital camera, and a computer with a timer unit to

Chapter 4: Experimental Method

control the system and store the data. Velocity fields are measured in a planar 2D domain. The measurement plane is cut in the flow by a laser sheet and the measurement area in this plane is cropped by the field of view of the camera. A schematic view of the apparatus and its typical layout is shown in figure 4-6. The measurement frequency depends on the hardware. Typically the measurement frequency is in the order of 10 Hz.

PIV is based on determining the movement of a group of particles seeded into the flow. The area of interest is illuminated by two consecutive short-duration light pulses produced by a laser. The duration of the light pulses and the time interval between the pulses is typically 10 ns and 10 to 100 microseconds, respectively. The light scattered from the seeding particles is acquired during both laser pulsed by a digital camera (a double-frame image) and stored for subsequent analysis. The velocity of the particles can be estimated by finding the displacement of the particles between the laser pulses. Since the time separation between the laser pulses is known and the camera is calibrated to yield the displacement in the object plane, the flow velocity can be resolved. The image is divided into small sub-regions called interrogation areas, the size of sub-regions may be adjusted from 16×16 pixels to 64×64 pixels, the local displacement of the particles is determined within each interrogation area. In this way, from one double-frame image, several thousand velocity vectors are computed, which are arranged to a rectangular grid.



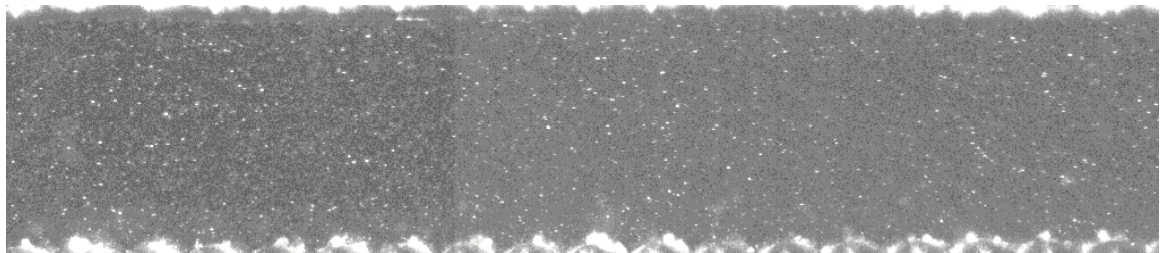
Chapter 4: Experimental Method

Figure 4-6. Schematic diagram of PIV velocity field measurement system (The figure is taken from www.dantecdynamics.com)

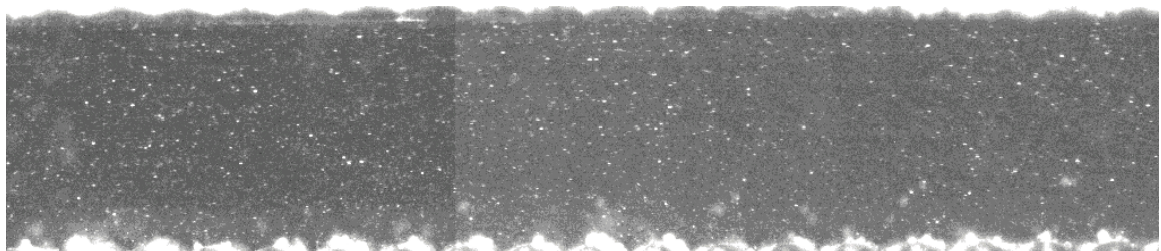
We don't have a double-pulsed laser in our laboratory; instead there is a continuous laser. By adjusting the time between two frames of the double-frame image, the measurements of flow velocity field are performed well with the PIV system.

In our experiment, a 500 nm continuous laser with a power of 5W provided by Stabilite® 2017 ion laser systems is used. A DANTEC FLOWSENSE camera (resolution of 2048×2048 pixels) is used to detect the position of the particles. An acquisition corresponding to 100 double-frame images is employed, the interval time between every capture is $1000 \mu\text{s}$, and the time between the two frames of a double-frame is $500 \mu\text{s}$. The software used for the PIV measurement and images treatment is the DynamicStudio V3.14 developed by Dantec Dynamics. The size of the particles is about $50 \mu\text{m}$.

An example of a double-frame image for PIV computation (flow condition: inflow rate $Q = 6 \text{ l/min}$ and channel slope $S_o = 0.0105$) is given in Figure 4-7. An instantaneous velocity field could be gotten from a double-frame image, and a set of instantaneous velocity fields can be used for ensemble averaging. Conventional statistics such as mean velocities for each cartesian component can be computed. In Figures 4-8 we present a mean velocity field measured from the 100 double-frame images for the example case. Figure 4-9 presents a time-averaged velocity field for the example case. Figures 4-10 shows a streamwise mean velocity profile above the porous medium computed from Figure 4-9. In our experiments, the resolution of the PIV system is 0.03 mm , the precision for the velocity measuring is hard to evaluate, we estimate that it is in the class of mm/s .



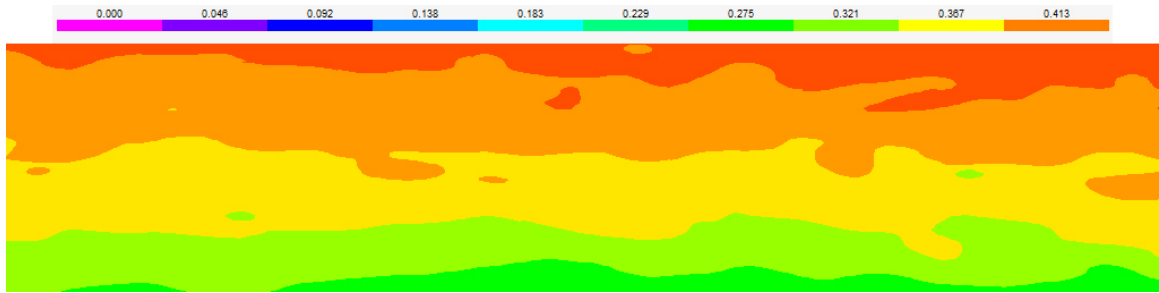
(a) First frame



Chapter 4: Experimental Method

(b) Second frame

Figure 4-7. A double-frame image for PIV computation



Figures 4-8. Mean velocity field scalar map computed for a set of instantaneous velocity fields

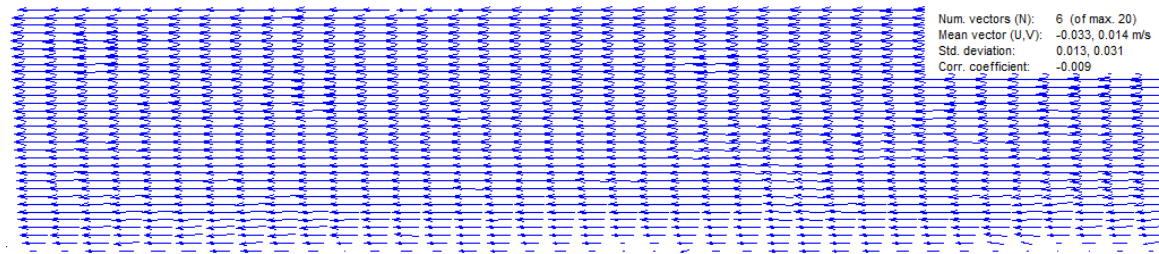
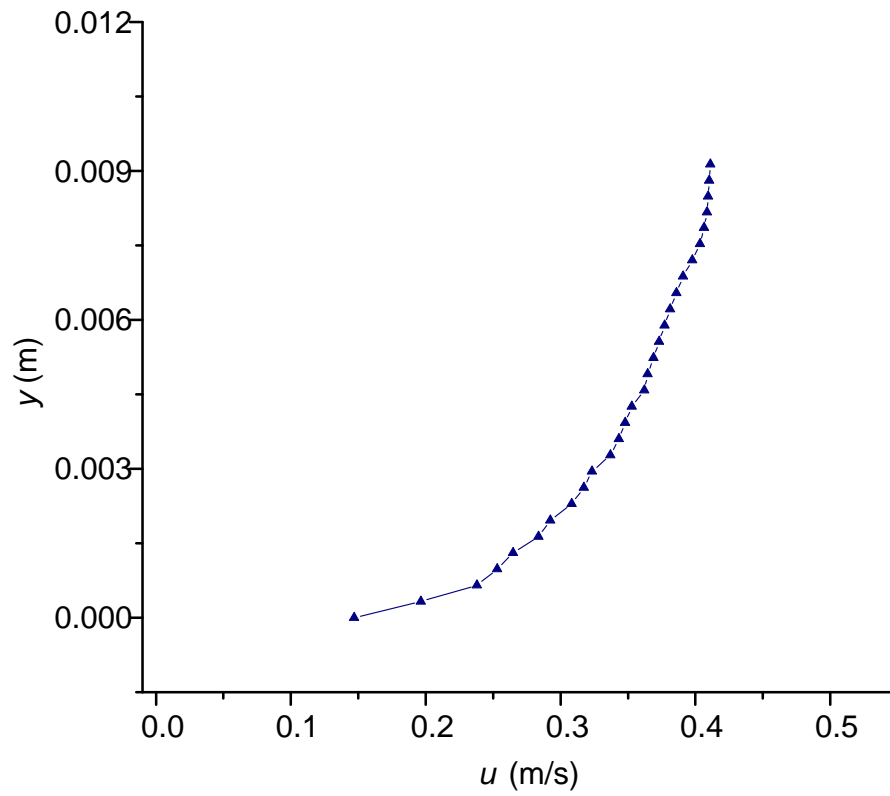
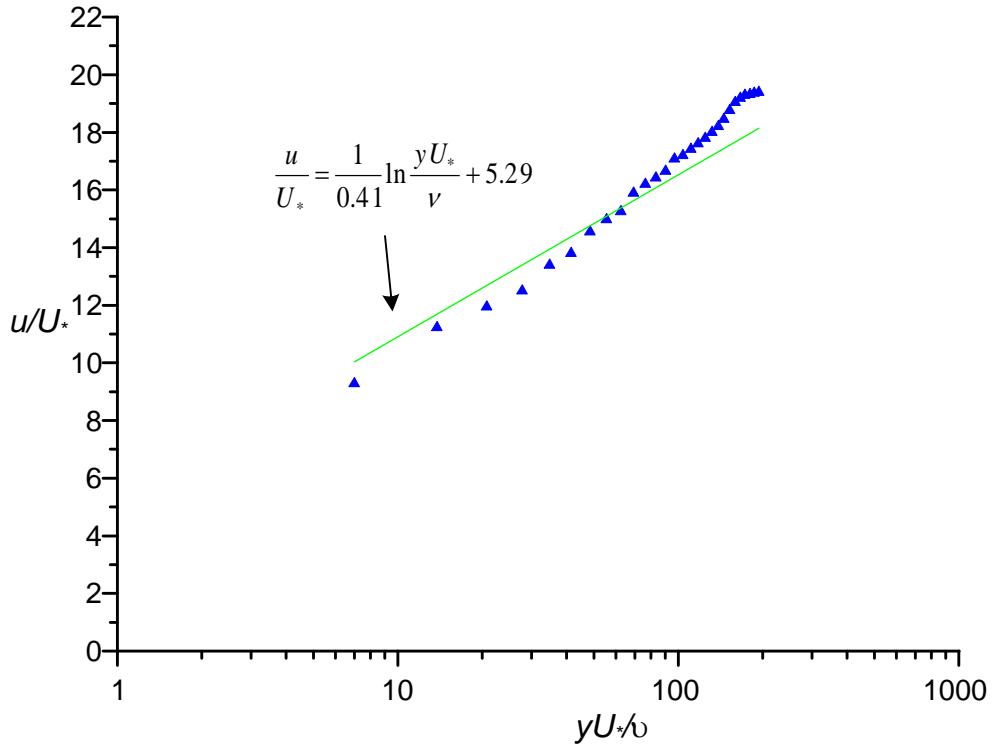


Figure 4-9. Velocity field computed from a set of double-frame image presented above



(a)



(b)

Figures 4-10. Streamwise flow velocity profile above the porous medium computed for a set of instantaneous velocity fields; (a), Streamwise flow velocity profile; (b), Comparison between streamwise flow velocity profile and logarithmic law

4.4 Conclusions

We have built an experimental system for the study of particle transport in an open channel with a porous medium. A high speed camera is used to capture the velocity of particles, and the flow velocity field is measured by the PIV system, the precision of the measurements is satisfied in our research. The experimental results will be compared with the numerical studies.

Chapter 5

Free Surface Flow over a Porous Bed in an Open Channel

5.1 Introduction

The flow phenomena and momentum transfer at the porous/fluid interface have also been studied by several investigators. However, few researchers studied the influences of the porous bed on the free surface flow.

In the present study, the characteristics of a free surface flow over a porous bed in an inclined open channel are studied numerically and experimentally. Effects of the dynamic characteristics of open channel and porous bed, such as channel slope, inflow rate, and seepage outflow rate, on the free surface flow are further investigated. Experiments are conducted by visualization. The numerical calculations are conducted using CFD-DEM coupling method.

The study methods and results of this chapter can be applied in industry and environmental analyses, for example, urban hydrology, river hydraulics, water treatment, etc.

5.1.1 Experimental setup

The experimental details for this chapter are similar to those outlined in chapter 4. Figure 5-1 is a schematic of the experimental setup.

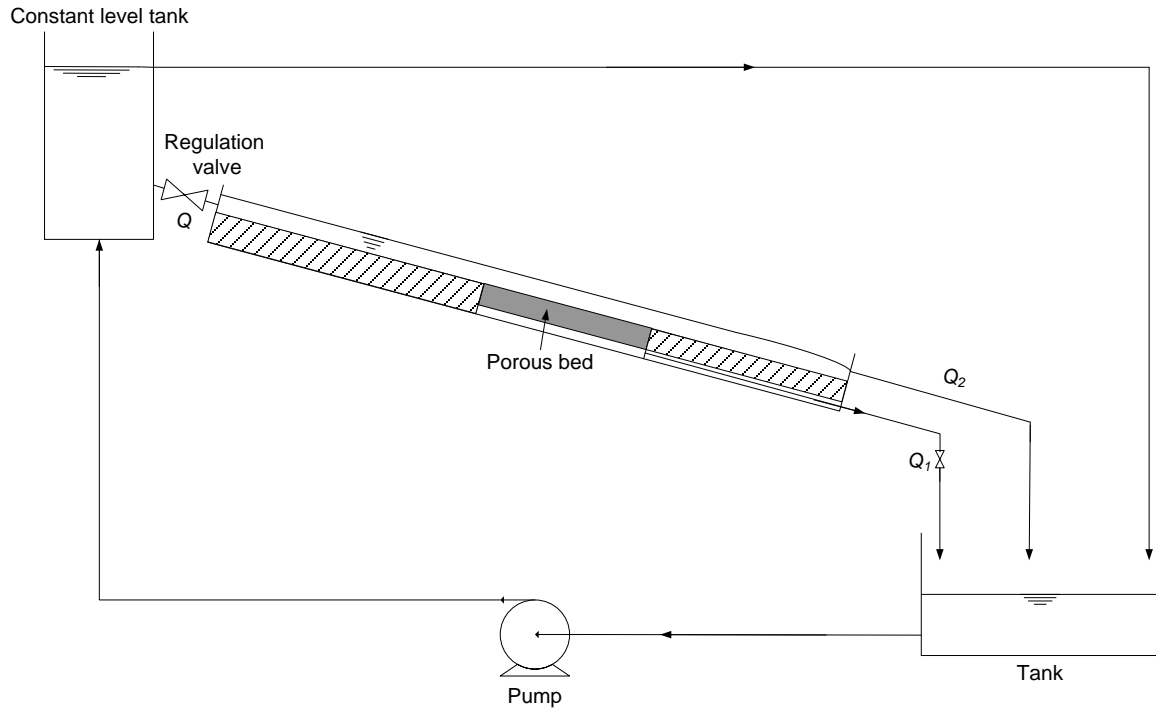


Figure 5-1. Schematic of experimental setup

5.1.2 Process of the experiment

1. Installing and setting the instrument

Install electronic balance and connect it with the computer, open the software for recording weight. Install high speed camera in the face of the porous bed and connect it with the computer, open the software for catching images.

2. Adjust the slope of channel

A motor is used to adjust the slope of channel to the conditions relevant to the experiment to be carried out.

3. Turn on the pump and adjust flow rate

Turn on the pump and fill constant level tank with water, open the regulation valve and electronic balance to adjust the inflow rate and the seepage outflow rate to the conditions relevant to the experiment.

4. Measure the flow depth and velocity field

After the flow is steady, measure approximately the flow depth over the porous bed with ruler, the depth is then measured with greater precision with images taken by camera. The flow velocity field is measured with a PIV system. The porous bed is 20 cm long, and the first 10

Chapter 5: Free Surface Flow over a Porous Bed in an Open Channel

cm is used to make the flow over the porous bed steady, so the second 10 cm is the zone of study.

5. Change parameters

Change the parameters, such as channel slope, inflow rate, seepage outflow rate and particle diameter, etc., and repeat the steps 1 - 4.

5.1.3 Numerical setup

Numerical simulations of one ball transport over the porous medium by the flow have also been carried out. The computational domain has dimensions equal to 0.03 m×0.025 m×0.30 m and a grid consisting of 30×50×600 points. Fixed solid particles with a diameter of 3 mm are used to assemble the porous media. The thickness of the porous medium is 9 mm and the inlet flow depth is 8 mm. The fixed particles have a density of 2500 kg/m³, a friction coefficient of 0.4 (Grigoriev et al., 1997), a stiffness coefficient of 1×10⁶ N/m, and a critical damping ratio of 0.04.

5.2 Parameters of the study

Table 5-1 presents the parameters studied in this work. Three parameters have been changed in our research as: channel slope, inflow rate, and seepage outflow rate. The porosity of the porous bed remains fixed to the value of 0.476 for all experiments.

1. Channel slope S_o varied from 0.0035 to 0.0244 (Angle of channel θ varied from 0.2° to 1.4°).
2. Inflow rate Q varied from 3.2 l/min to 6.8 l/min.
3. Seepage outflow rate Q_I varied from 0 to 10% of the inflow rate Q .

Table 5-1. Parameters used in the sensitivity analysis

Case	Slope S_o	Inflow rate Q (l/min)	Seepage outflow rate Q_I (l/min)
1	0.0035	6.00	0
2		6.00	0.30
3		6.00	0.40
4		6.00	0.60
5	0.0105	6.00	0
6		6.00	0.30
7		6.00	0.40
8		6.00	0.60
9	0.0175	6.00	0

Chapter 5: Free Surface Flow over a Porous Bed in an Open Channel

10		6.00	0.30
11		6.00	0.40
12		6.00	0.60
13	0.0244	6.00	0
14		6.00	0.30
15		6.00	0.40
16		6.00	0.60
17	0.0105	3.20	0
18		3.20	0.16
19		3.20	0.21
20		3.20	0.32
21	0.0105	4.50	0
22		4.50	0.23
23		4.50	0.30
24		4.50	0.45
25	0.0105	6.80	0
26		6.80	0.34
27		6.80	0.45
28		6.80	0.68

5.3 Results and analysis

5.3.1 Raw results

The experimental and numerical results of geometric and hydrodynamic characteristics of the flow are shown in Table 5-2.

Table 5-2. Experimental and numerical results of geometric characteristics of the free surface flow

Case	d (m)		Relative error of d	U_w (m/s)		Relative error of U_w	D_H (m)	
	simulation	experiment		simulation	experiment		simulation	experiment
1	0.01025	0.00979	0.0470	0.3039	0.3230	0.0591	0.0244	0.0237
2	0.00975	0.00847	0.1511	0.3205	0.3582	0.1052	0.0236	0.0217
3	0.00975	0.00817	0.1934	0.3286	0.3640	0.0973	0.0236	0.0212
4	0.00925	0.00726	0.2741	0.3412	0.3729	0.0850	0.0229	0.0196
5	0.00975	0.00913	0.0679	0.3335	0.3399	0.0188	0.0236	0.0227
6	0.00875	0.00816	0.0723	0.3547	0.3549	0.0006	0.0221	0.0211
7	0.00875	0.00781	0.1204	0.3634	0.3775	0.0374	0.0221	0.0205
8	0.00825	0.00713	0.1571	0.3753	0.3838	0.0221	0.0213	0.0193
9	0.00875	0.00831	0.0529	0.3749	0.3630	0.0328	0.0221	0.0214
10	0.00775	0.00767	0.0104	0.3921	0.3912	0.0023	0.0204	0.0203

Chapter 5: Free Surface Flow over a Porous Bed in an Open Channel

11	0.00775	0.00732	0.0587	0.3994	0.3848	0.0379	0.0204	0.0197
12	0.00725	0.00683	0.0615	0.4075	0.4074	0.0002	0.0196	0.0188
13	0.00775	0.00737	0.0516	0.4086	0.4316	0.0533	0.0204	0.0198
14	0.00725	0.00681	0.0646	0.4241	0.4398	0.0357	0.0196	0.0187
15	0.00725	0.00647	0.1206	0.4241	0.4405	0.0372	0.0196	0.0181
16	0.00675	0.00606	0.1139	0.4359	0.4392	0.0075	0.0186	0.0173
17	0.00675	0.00687	0.0175	0.2570	0.2377	0.0812	0.0186	0.0188
18	0.00625	0.00602	0.0382	0.2727	0.2639	0.0333	0.0176	0.0172
19	0.00575	0.00561	0.0250	0.2742	0.2718	0.0088	0.0166	0.0163
20	0.00575	0.00484	0.1880	0.2839	0.3032	0.0637	0.0166	0.0146
21	0.00825	0.00850	0.0294	0.3006	0.2813	0.0686	0.0213	0.0217
22	0.00725	0.00648	0.1188	0.3146	0.3315	0.0510	0.0196	0.0181
23	0.00725	0.00641	0.1310	0.3223	0.3409	0.0546	0.0196	0.0180
24	0.00675	0.00563	0.1989	0.3321	0.3562	0.0677	0.0186	0.0164
25	0.01075	0.00982	0.0947	0.3505	0.3629	0.0342	0.0250	0.0237
26	0.00975	0.00847	0.1511	0.3751	0.3963	0.0535	0.0236	0.0217
27	0.00925	0.00843	0.0973	0.3815	0.3947	0.0334	0.0229	0.0216
28	0.00875	0.00839	0.0429	0.3951	0.3832	0.0311	0.0221	0.0215

where d is the free flow depth; U_w is the mean flow velocity, $U_w = \frac{Q}{dB}$; D_H is the hydraulic diameter, $D_H = 4 \times \frac{\text{cross-sectional area}}{\text{wetted perimeter}}$; the relative error of the numerical result is calculated as: $\frac{|\text{experimental result} - \text{simulational result}|}{\text{experimental result}}$.

Table 5-3. Experimental and numerical results of hydrodynamic characteristics of the free surface flow

Case	Re		Fr		U_* (m/s)		U_w/U_*	
	simulation	experiment	simulation	experiment	simulation	experiment	simulation	experiment
1	7403	7654	0.959	1.043	0.0319	0.0339	9.53	9.52
2	7575	7755	1.037	1.243	0.0337	0.0382	9.52	9.38
3	7767	7701	1.063	1.286	0.0344	0.0391	9.55	9.31
4	7809	7297	1.133	1.398	0.0358	0.0402	9.53	9.27
5	7883	7716	1.079	1.136	0.0353	0.0368	9.45	9.24
6	7841	7502	1.211	1.255	0.0380	0.0379	9.32	9.37
7	8034	7756	1.241	1.365	0.0385	0.0404	9.45	9.35
8	7991	7419	1.320	1.452	0.0394	0.0411	9.53	9.34

Chapter 5: Free Surface Flow over a Porous Bed in an Open Channel

9	8287	7765	1.280	1.272	0.0407	0.0394	9.22	9.21
10	8014	7941	1.423	1.427	0.0414	0.0413	9.47	9.48
11	8163	7572	1.449	1.437	0.0421	0.0420	9.50	9.16
12	7967	7648	1.529	1.575	0.0434	0.0436	9.39	9.35
13	8352	8532	1.483	1.606	0.0436	0.0475	9.37	9.08
14	8291	8240	1.591	1.703	0.0454	0.0482	9.33	9.12
15	8291	7965	1.591	1.749	0.0454	0.0486	9.33	9.07
16	8117	7582	1.695	1.802	0.0470	0.0492	9.27	8.93
17	4786	4480	0.999	0.916	0.0306	0.0272	8.40	8.73
18	4812	4535	1.102	1.087	0.0328	0.0293	8.30	9.00
19	4558	4439	1.155	1.159	0.0335	0.0299	8.19	9.08
20	4720	4437	1.196	1.392	0.0345	0.0356	8.23	8.52
21	6399	6106	1.057	0.975	0.0337	0.0308	8.91	9.13
22	6151	6000	1.180	1.315	0.0359	0.0360	8.77	9.22
23	6300	6124	1.209	1.360	0.0367	0.0379	8.77	9.00
24	6184	5832	1.291	1.516	0.0382	0.0391	8.69	9.10
25	8779	8614	1.080	1.170	0.0362	0.0377	9.68	9.62
26	8866	8580	1.213	1.375	0.0386	0.0412	9.71	9.61
27	8730	8521	1.267	1.373	0.0392	0.0401	9.73	9.84
28	8735	8248	1.349	1.337	0.0401	0.0395	9.87	9.71

Where Re is Reynolds number, $Re = \frac{U_w D_H}{\nu}$; Fr is Froude number, $Fr = \frac{U_w}{\sqrt{gd}}$; U_* is shear velocity.

5.3.2 Reference case

Case No. 5 from the serial experiments is taken as the reference case; comparisons are made between reference case and the others cases, so case 5 should be investigated. This case is the open channel flow, has a porous bed at the channel bottom, but there is no seepage outflow in the vertical direction.

Figure 5-2 is the comparison of the velocity profile between numerical data and experiment measures. The results show good agreement between the measured data and those computed using CFD-DEM method. Table 5-2 shows the relative error of mean flow velocity in the clear water region is 0.0188 and the relative error of flow depth is 0.0679.

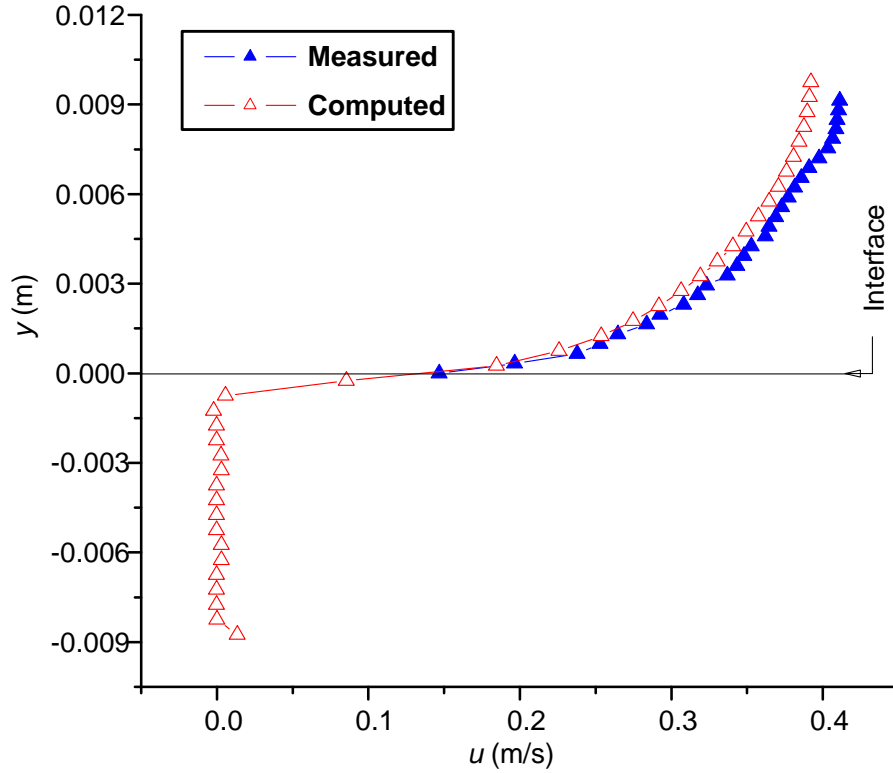


Figure 5-2. Comparison of the velocity profile between numerical data and experiment measures ($Q=6$ l/min, without seepage outflow)

Like the other experimental and numerical studies (e.g. Shimizu et al. 1990, and Prinos et al. 2003), at the interface of the clear water region and seepage flow region $y=0$, (summit of the particles that assemble the porous bed), the distribution of the streamwise velocity are significantly modified from law of the wall for impermeable beds, a non-zero slip velocity is about 0.14 m/s, that shows although there is no vertical seepage outflow at the channel bottom, there is a streamwise discharge in the porous bed, especially at the top layer of the bed because volume of pores increases near the interface. If we take the mean flow rate U_w , hydraulic diameter D_H and slope into the Manning equation (Equation 2-11 shown in Chapter 2) and Manning coefficient can be get. The simulated and experimental $n_{Manning}$ equals to 0.0100 and 0.00959, respectively. Compare to the typical values of shown in Table 2-1, the value of Manning coefficient of the porous bed assembled by 3 mm spherical particles without vertical seepage outflow is between the value of Perspex and mortar in the laboratory channel models, which means because of the slip velocity the energy losses at the interface is less than that at impermeable rough surface boundary.

5.3.3 Flow regimes

The flow of water is described by several complementary characterizations: steady and unsteady, uniform and non-uniform, laminar and turbulent, and supercritical and subcritical.

Chapter 5: Free Surface Flow over a Porous Bed in an Open Channel

The measures are taken after the flow is steady. As analyzed in Chapter 4 because the maximum downward seepage velocity is about 1% of the mean flow velocity in the clear water region, so the flow in our research can be considered as uniform flow.

The plots of Reynolds number against Froude number are shown in Figure 5-3. Re is between 4000 and 9000, while Fr is between 0.9 and 1.8, so the flows in our research are near-critical (i.e. $0.7 < Fr < 1.5$) or supercritical turbulent flows.

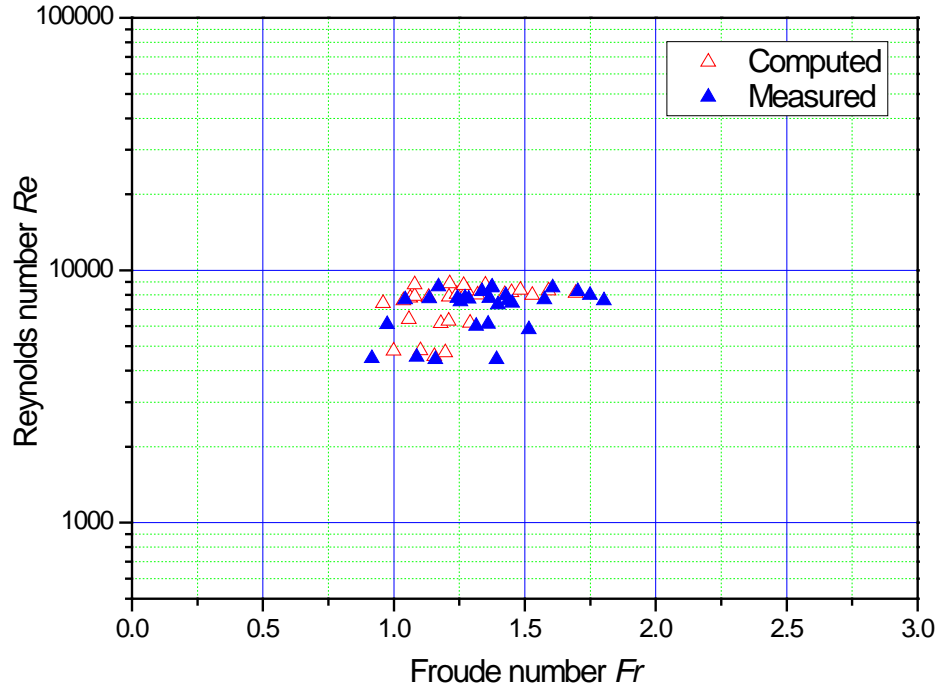


Figure 5-3. Reynolds number - Froude number of the computed and measured data

5.3.4 Flow depth

5.3.4.1 Influence of channel slope

Figure 5-4 shows the variation of the flow depth with different channel slopes. As expected both experimental and simulation flow depth lowered with higher slope. With the same channel slope flow depth slightly decreases when the seepage outflow rate Q_I increases. There are small differences in velocities between computed and measured data, but that is in the range of tolerance.

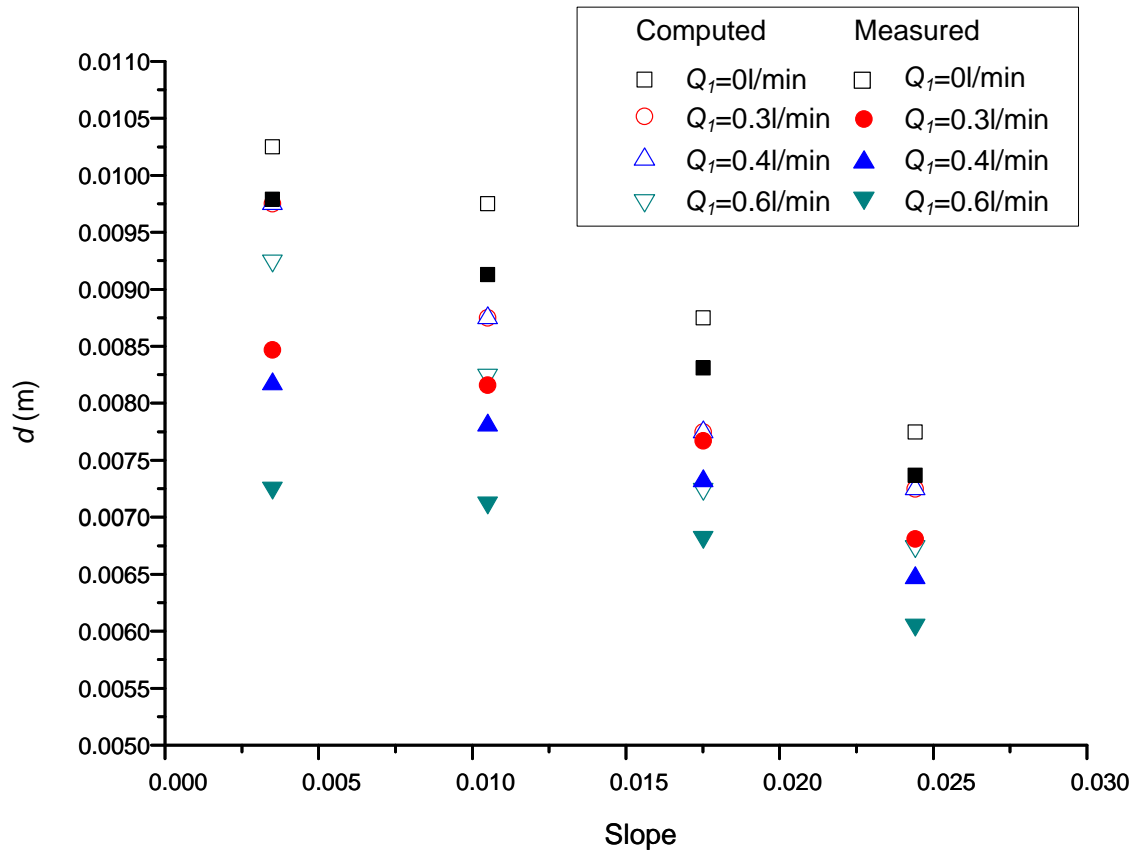


Figure 5-4. Influence of channel slope on flow depth (inflow rate $Q=6$ l/min)

5.3.4.2 Influence of flow rate

Figure 5-5 shows the variation of flow depth with different inflow rate. As expected both experimental and simulation data significantly goes up when inflow rate increases. With the same inflow rate, the flow depth slightly decreases when the seepage outflow rate Q_1 increases. There are small differences in velocities between computed and measured data, but the differences are acceptable.

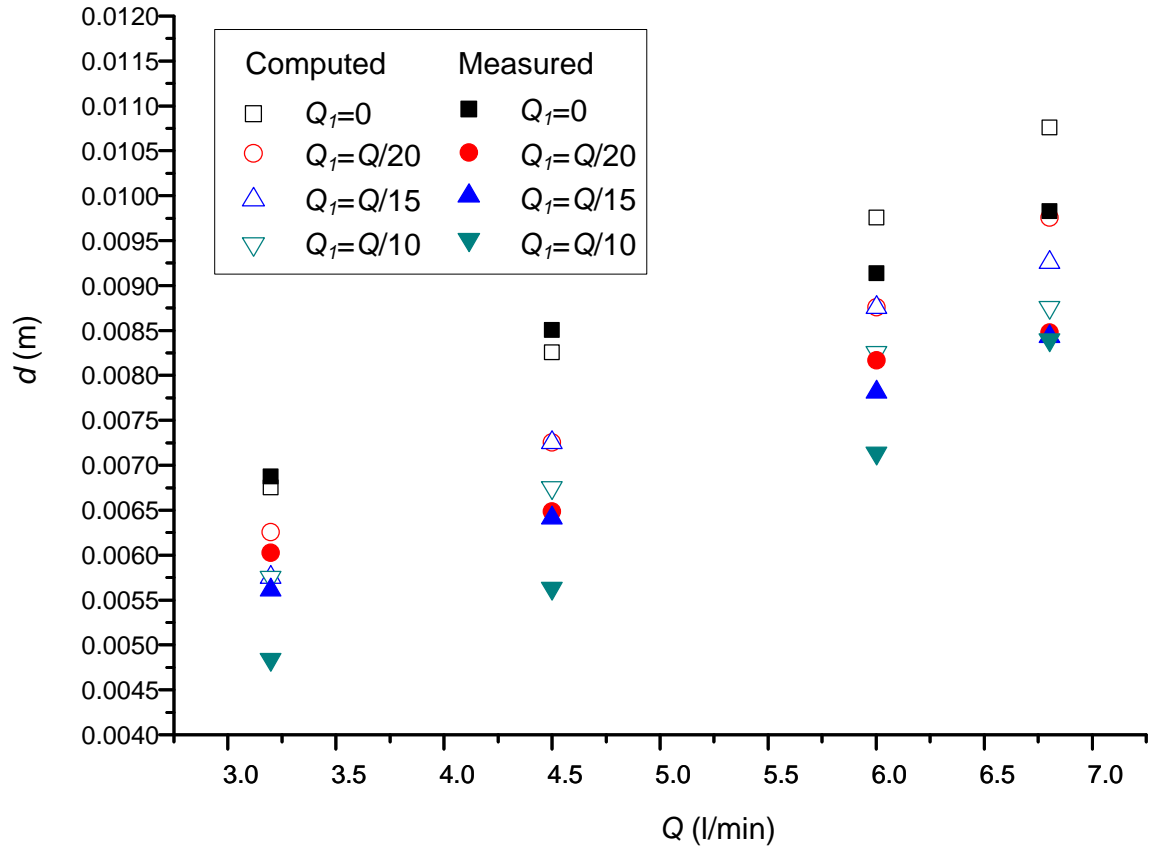


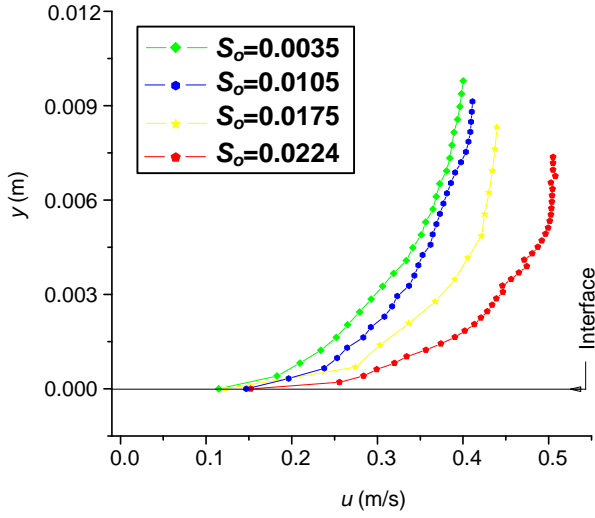
Figure 5-5. Influence of inflow rate on flow depth (channel slope $S_0=0.0105$)

5.3.5 Velocity distributions above and within the porous region

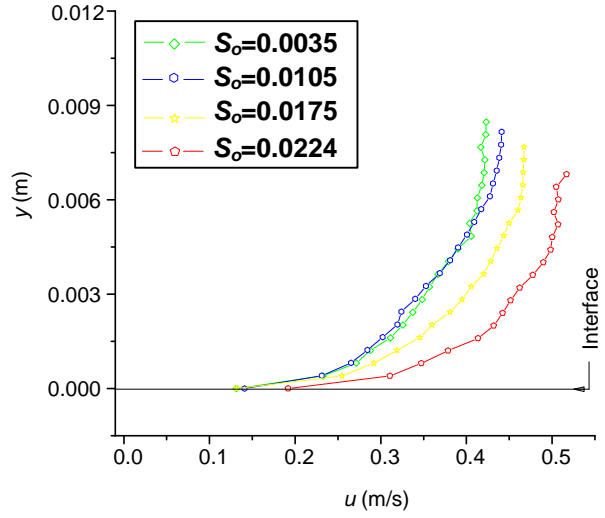
5.3.5.1 Influence of channel slope

Figure 5-6 presents the corresponding variation of the computed velocity profiles. Evidently, the greater channel slope causes a higher flow velocity around the fluid/porous interface and within free-fluid region, and the increases of seepage outflow also cause higher flow velocity. Though the experiment doesn't permit to measure the velocity within the porous medium, the numerical simulation has the advantage that the velocity inside the porous medium could be known as well.

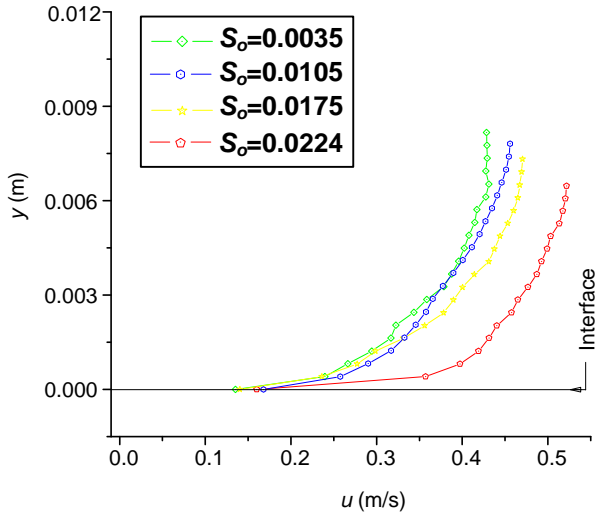
Chapter 5: Free Surface Flow over a Porous Bed in an Open Channel



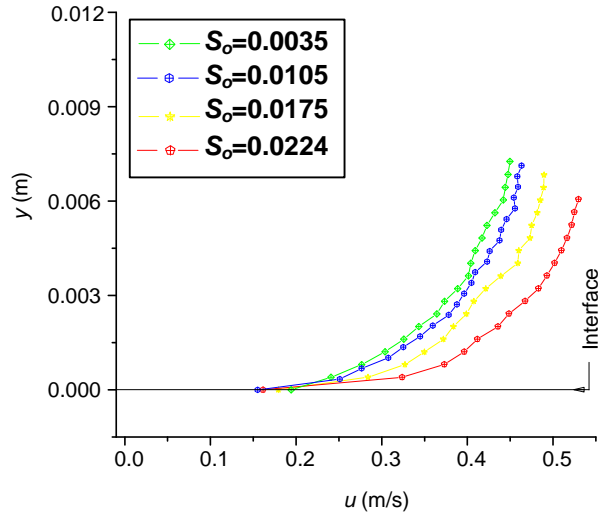
(a)



(b)

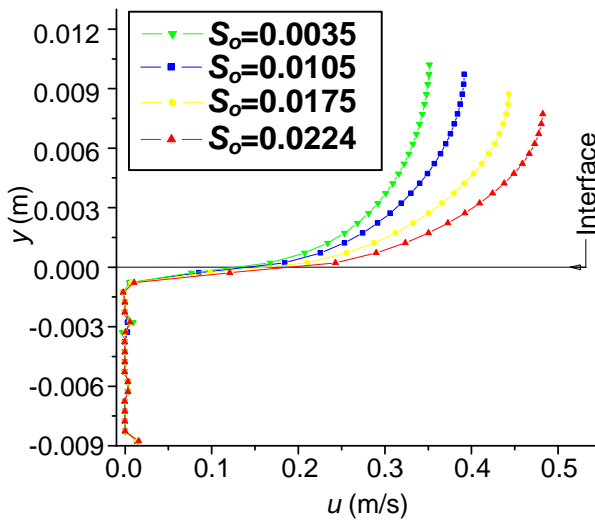


(c)

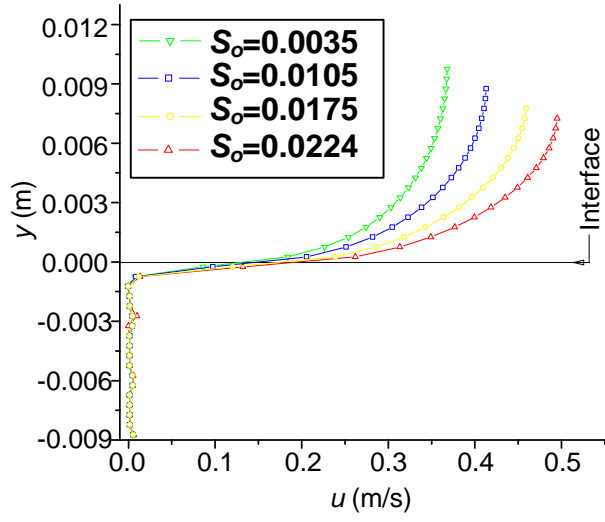


(d)

(A)



(a)



(b)

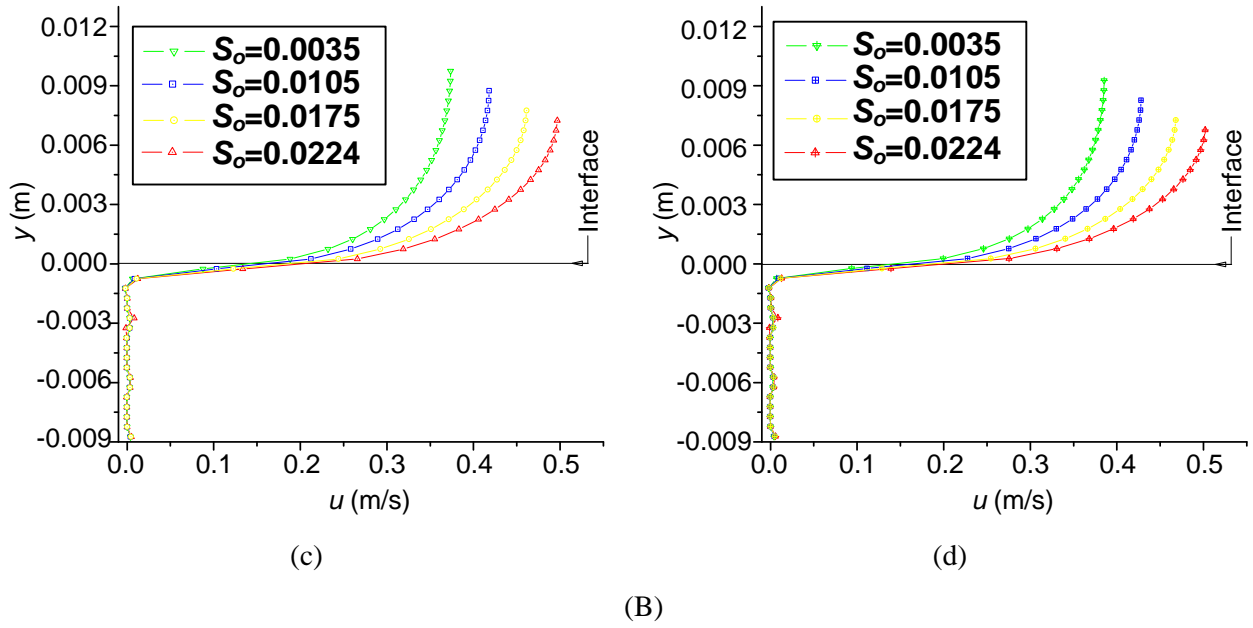
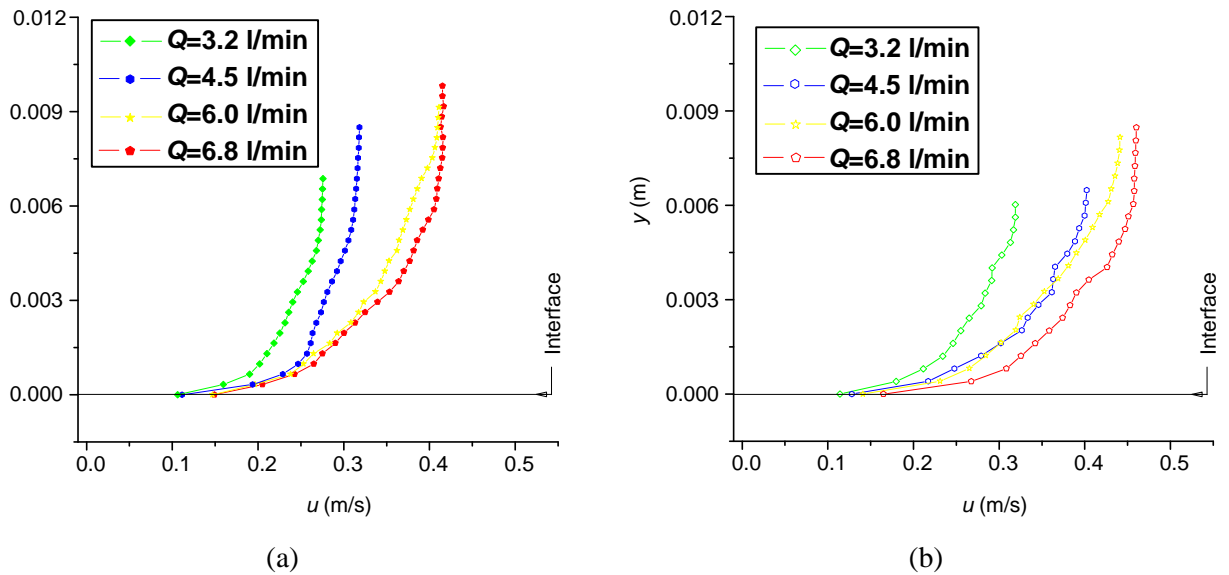


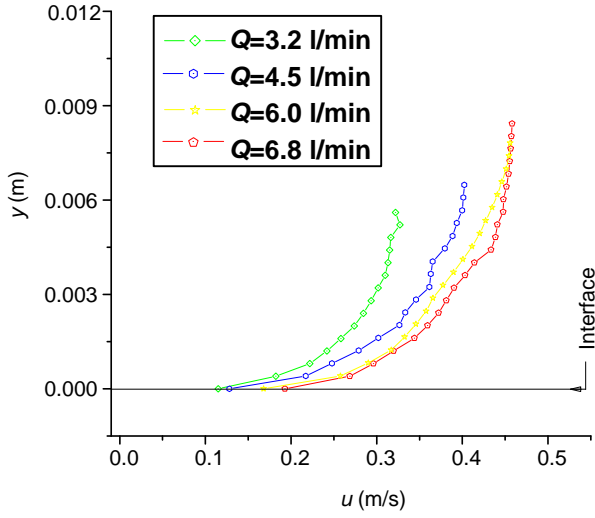
Figure 5-6. Flow velocity profiles above and within the porous region for different channel slopes, in different infiltration conditions. (A), measured data for four different seepage outflow rates; (B), simulated data for four different seepage outflow rates

5.3.5.2 Influence of flow rate

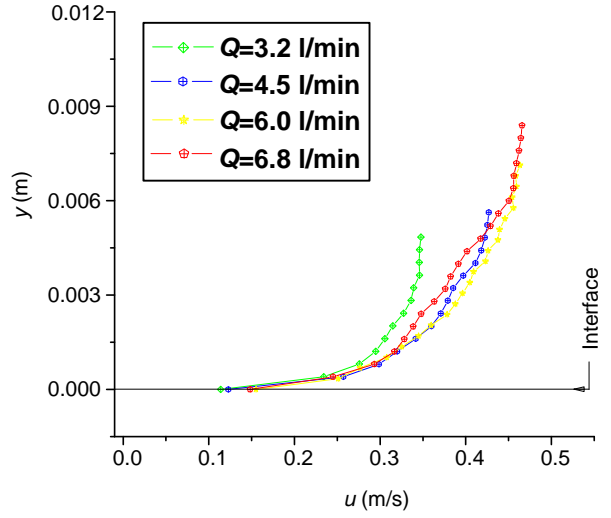
Figure 5-7 shows flow velocity profile above and within the porous region, and velocity is augment with higher inlet flow rate, while the increase of seepage outflow rate also increases flow velocity.



Chapter 5: Free Surface Flow over a Porous Bed in an Open Channel

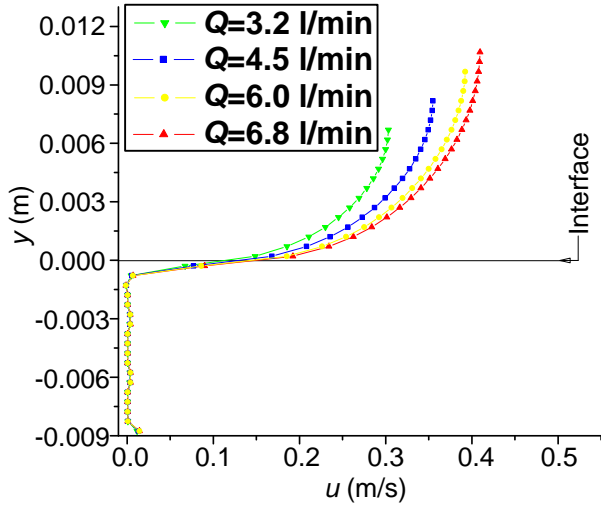


(c)

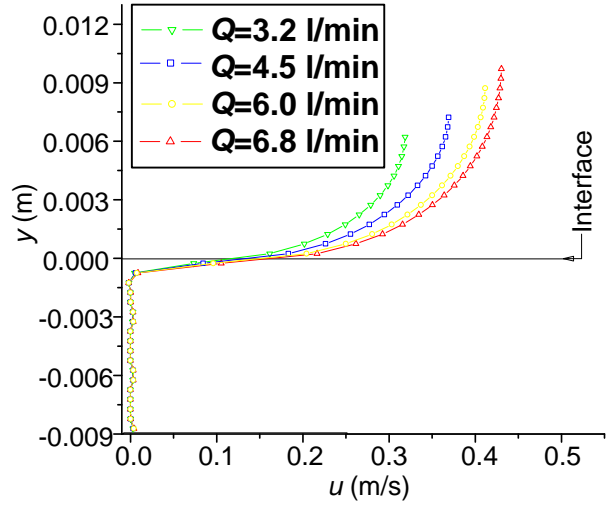


(d)

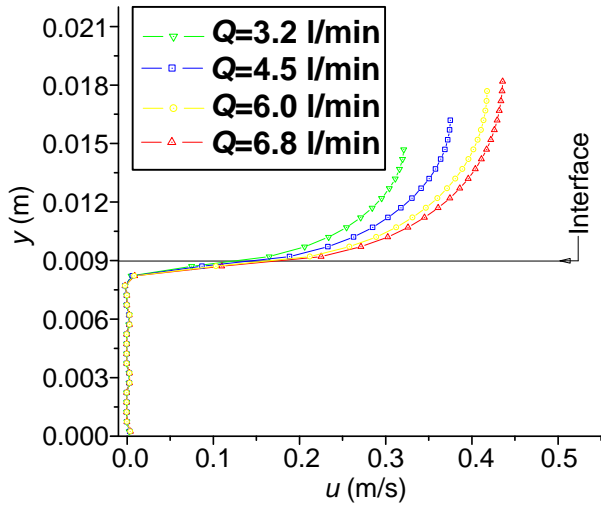
(A)



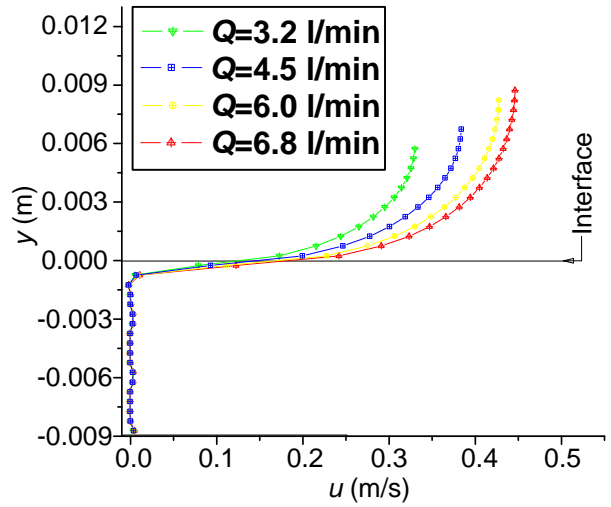
(a)



(b)



(c)



(d)

(B)

Figure 5-7. Flow velocity profiles above and within the porous region for different inflow rate, with different infiltration rates. (A), measured data for four different seepage outflow rates; (B), simulated data for four different seepage outflow rates

5.3.6 Shear velocity

The shear velocity is a measure of shear stress and velocity gradient near the boundary, a large shear velocity U_* implies large shear stress and large velocity gradient.

Generally, there are four methods to estimate the shear velocity: Reynolds stress, logarithmic law, parabolic law and a global approach.

The simplest one, derived for steady uniform flow in wide channels, estimates U_* as $U_* = \sqrt{g \frac{D_H}{4} S_o}$, in which g is the gravitational acceleration, and S_o is the slope of the channel bed (for uniform flow the slope of the channel bed, the friction slope, and the water-surface slope are all equal). In the case of steady non-uniform flow, the energy slope replaces S_o . In our study, the seepage outflow rate would influence the energy slope. So accurate estimation of U_* by this method is difficult, therefore, U_* must be estimated with other methods.

The logarithmic law method is based on the velocity distribution in the region $y/d < 0.6$, can be described by the logarithmic law: $\frac{u}{U_*} = \frac{1}{\kappa} \ln\left(\frac{y}{k_s}\right) + C$, where κ is the von Karman constant (equal to 0.41), and C is a constant. Einstein and El-Samni (1949) proposed a modified logarithmic law for the flow over a surface with large roughness: $\frac{u}{U_*} = \frac{1}{\kappa} \ln\left(\frac{y+y_0}{k_s}\right) + C$, where y_0 is the distance of the theoretical wall below the top of the spheres whose diameter is k_s , (Figure 5-8), they chose a value of $y_0 = 0.2k_s$.

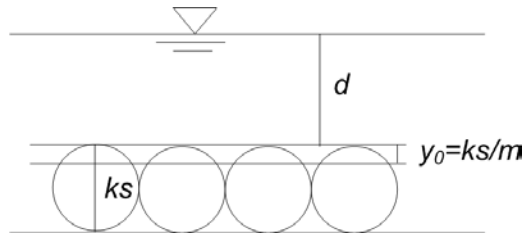


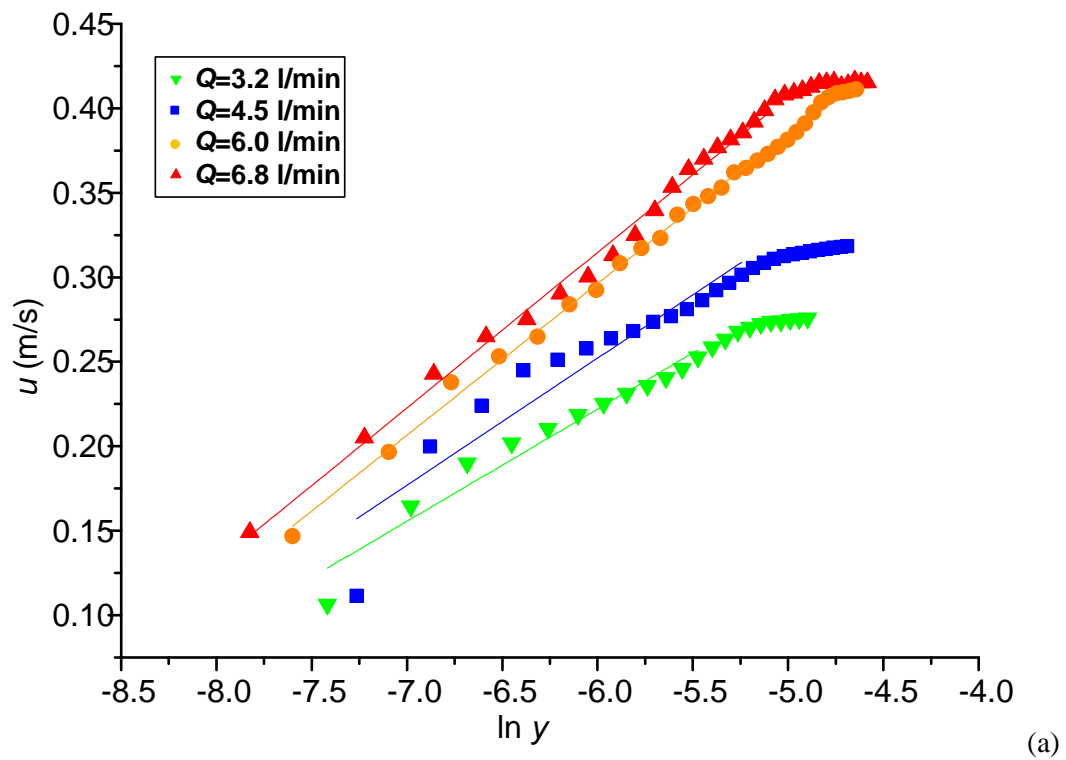
Figure 5-8. The position of y_0

Cheng and Chiew (1998) suggested a modified logarithmic law for the influence of vertical seepage flow: $\frac{u}{U_*} = \frac{1}{\kappa} \ln\left(\frac{y}{y_0}\right) + \frac{V_s}{4U_*} \left(\frac{1}{\kappa} \ln\left(\frac{y}{y_0}\right)\right)^2$, where V_s is the vertical mean seepage flow rate due to the injection or suction.

Chapter 5: Free Surface Flow over a Porous Bed in an Open Channel

In our study, we employed all these three logarithmic laws to calculate the U_* , based on the results we find that the most convenient and accurate method is the modified logarithmic law proposed by Einstein and El-Samni (1949).

In Figure 5-9 to 5-11 u - $\ln y$ are plotted to derive shear velocity U_* from slope of the line in the region $y/d < 0.6$ which equals to U_*/κ . In our study, the value of U_* for 28 cases are estimated by fitting the measured velocity profiles to the logarithmic law proposed by Einstein and El-Samni (1949), results are shown in Table 5-3. From the figures and Table 5-3, we can find that shear velocity increases as inflow rate, slope, and seepage outflow rate increase.



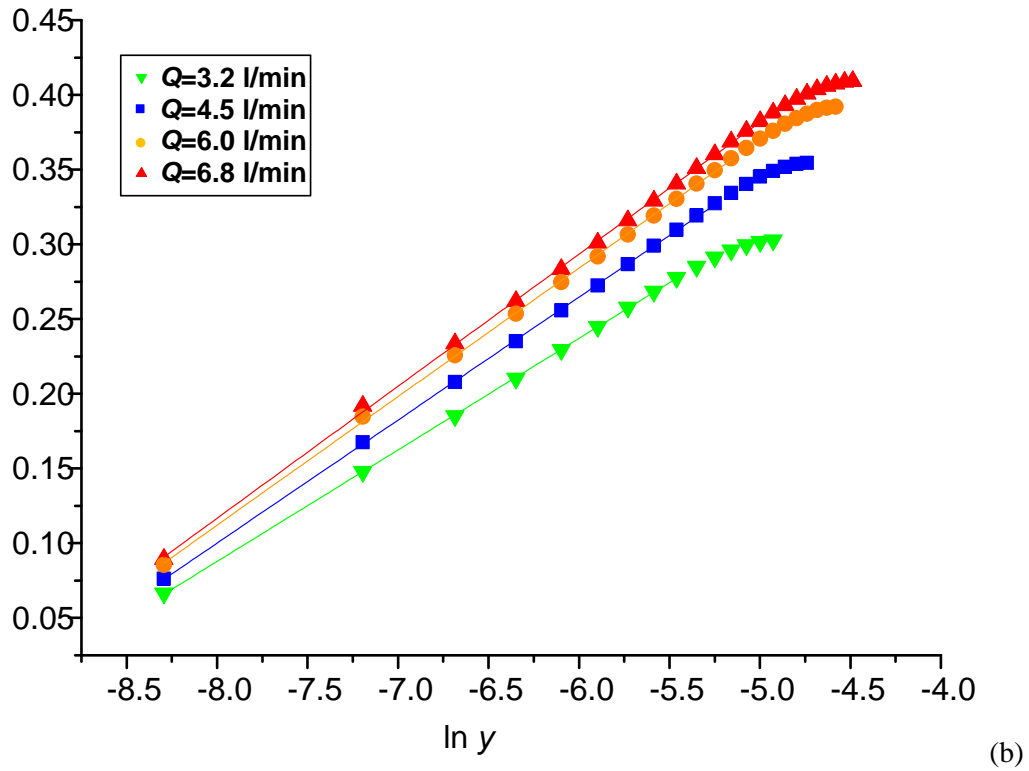
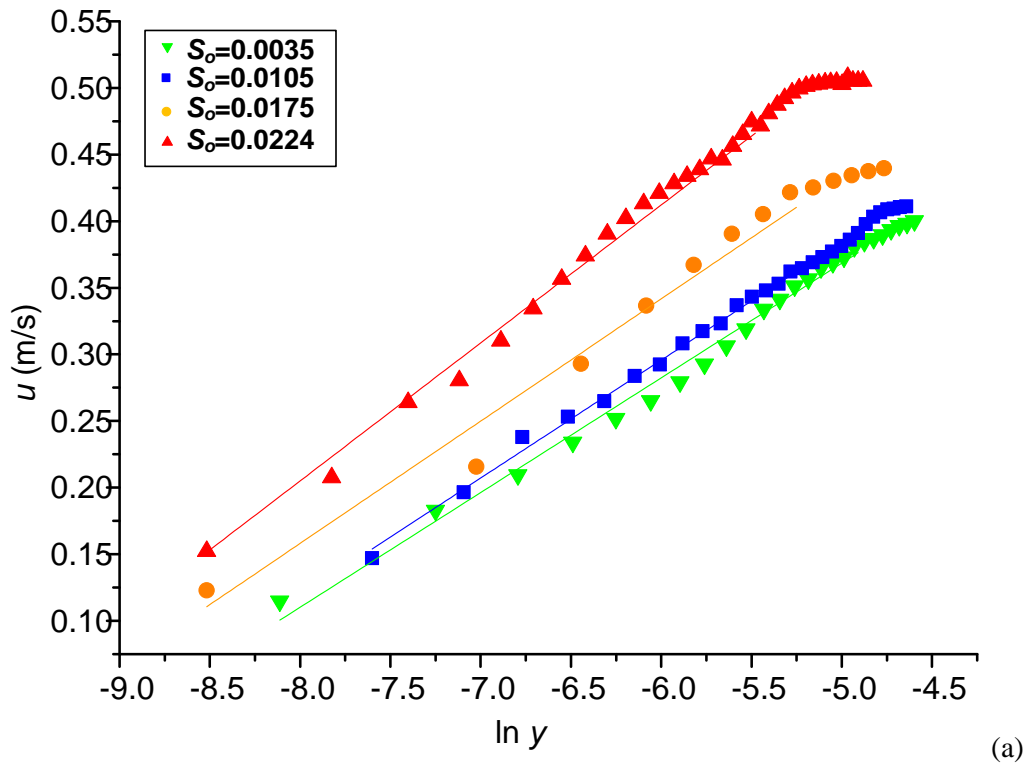


Figure 5-9. Velocity profiles against $\ln y$ for different inflow rate (channel slope $S_o=0.0105$, without seepage outflow). (a) Experimental result; (b) Computed result



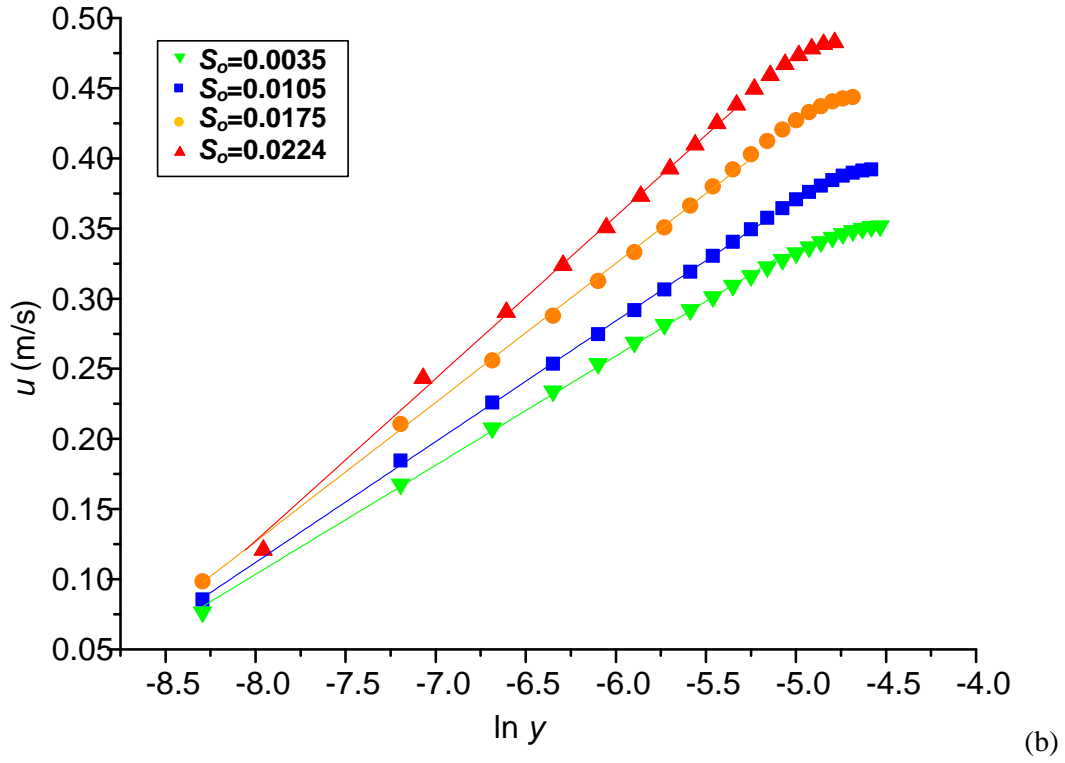
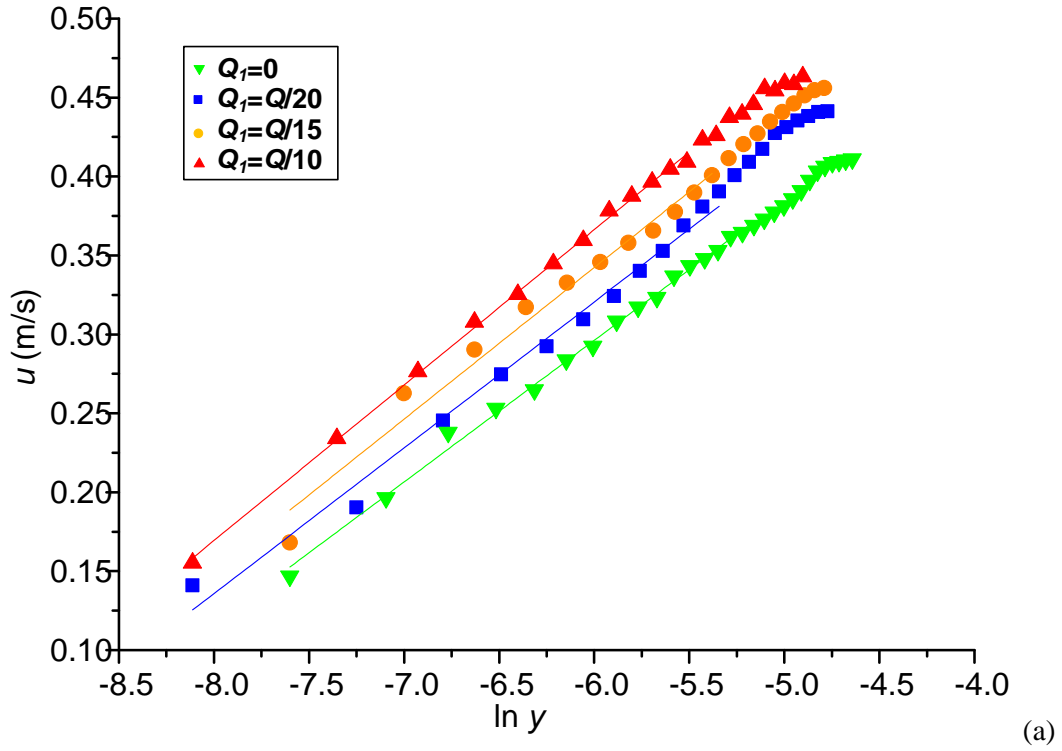


Figure 5-10. Velocity profiles against $\ln y$ for different channel slope (inflow rate $Q=6.0$ l/min, without seepage outflow). (a) Experimental result; (b) Computed result



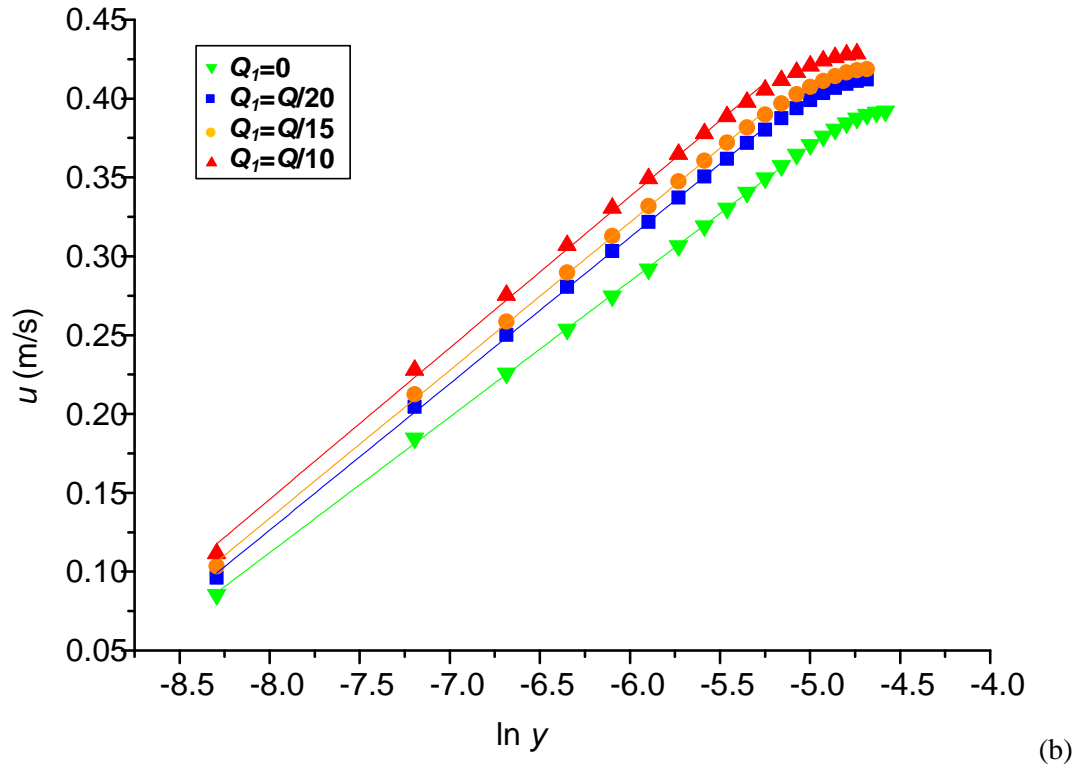
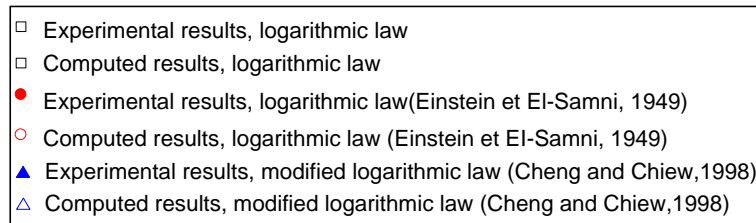
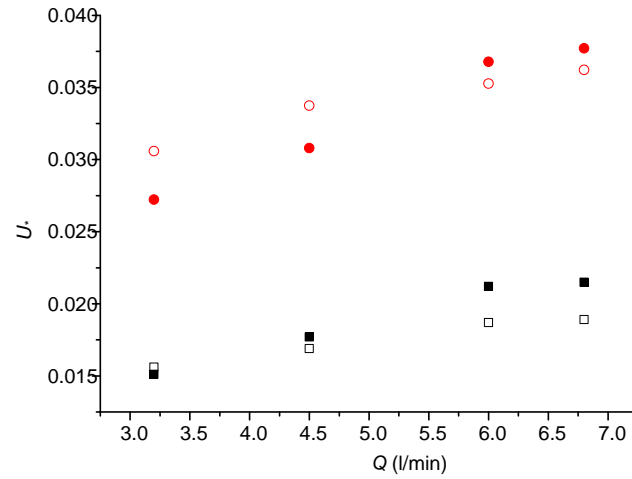


Figure 5-11. Velocity profiles against $\ln y$ for different seepage outflow rate (inflow rate $Q=6.0$ l/min, channel slope $S_o=0.0105$). (a) Experimental result; (b) Computed result

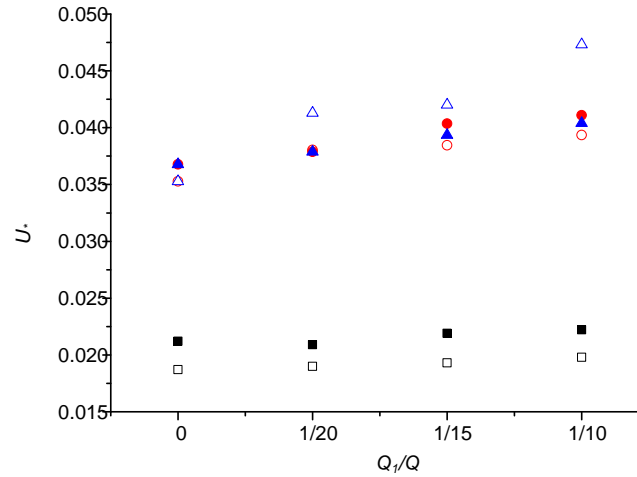
The comparisons of the values of U_* got from different methods are plotted in Figure 5-12.



(a)



(b)



(c)

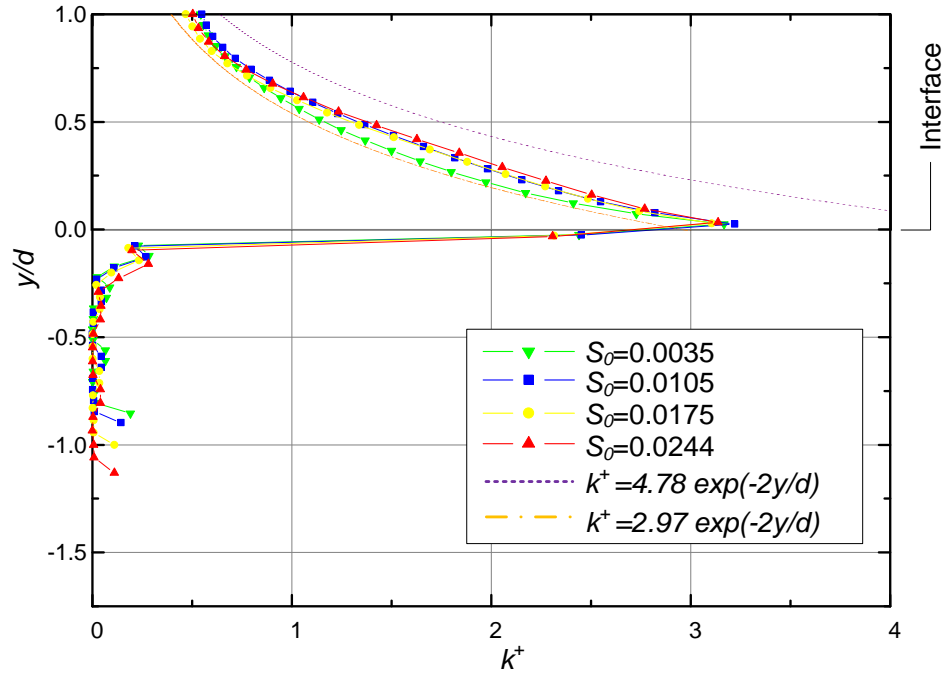
Figure 5-12. The comparisons of the values of U_* got from different methods

From these figures we can find that the U_* calculated by the modified logarithmic law proposed by Einstein and El-Samni (1949) and Cheng and Chiew (1998) are located near each other but about twice larger than the results calculated by the original logarithmic law.

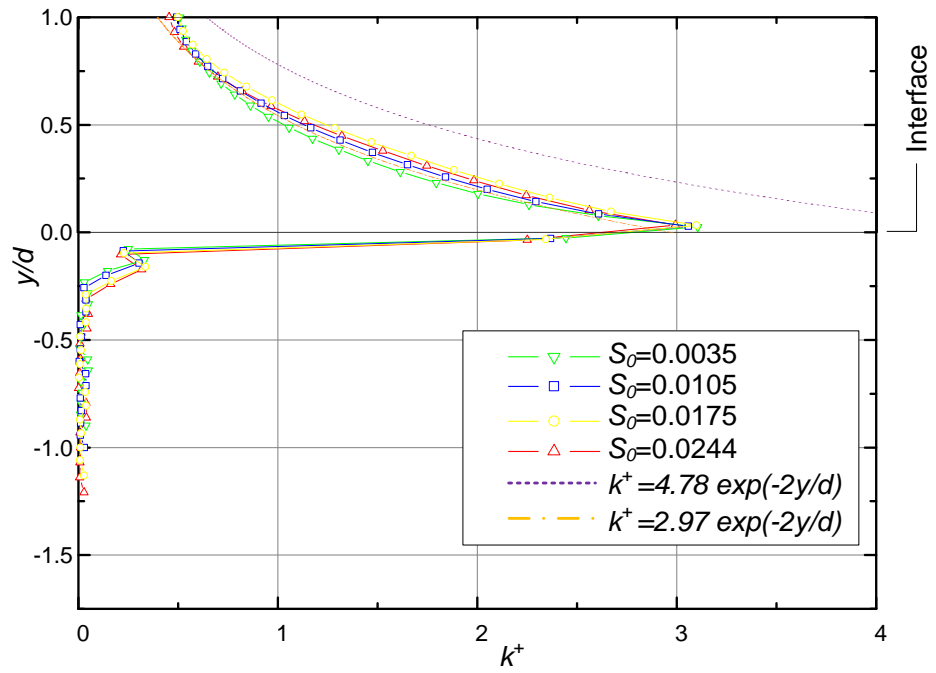
5.3.7 Turbulent kinetic energy above and within the porous region

5.3.7.1 Influence of channel slope

Figure 5-13 presents the effect of channel slope on the normalized turbulent kinetic energy. After normalization little differences can be found for the different channel slopes, all the profiles of k^+ ($= k/U_*^2$) are overlapped. The largest value of k^+ is in the region around the interface of free flow and porous medium. The penetration of the turbulent kinetic energy into the porous region also remains considerable.



(a)



(b)

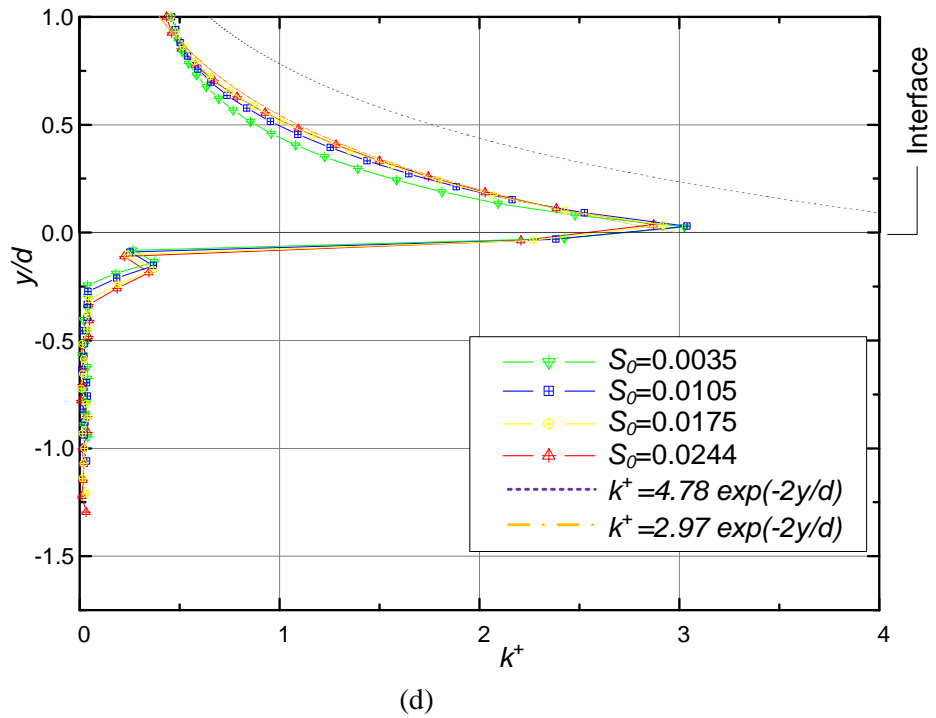
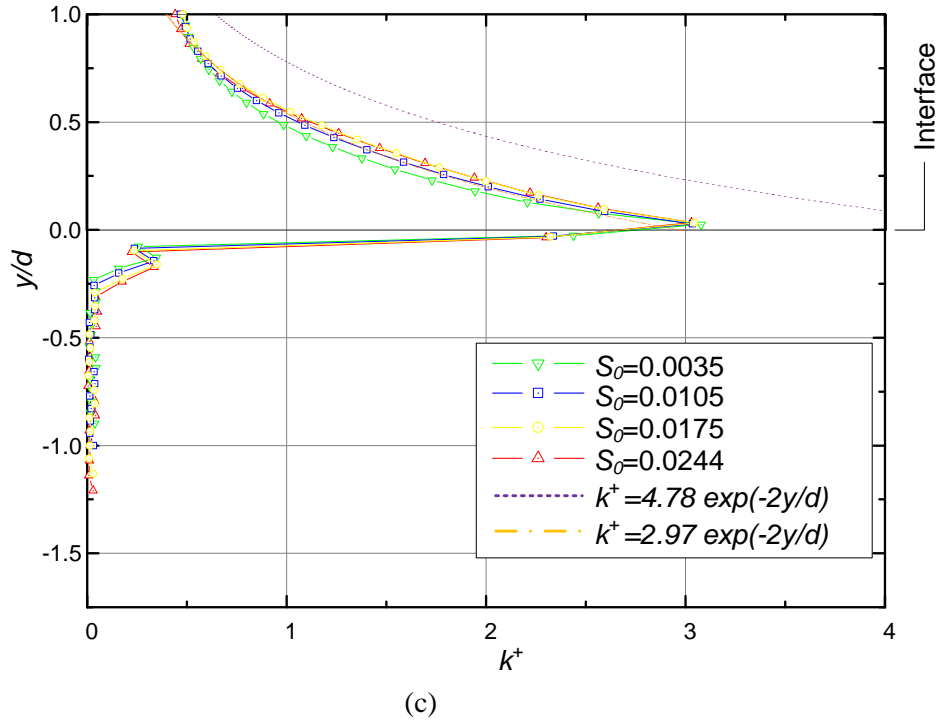


Figure 5-13. Variation of k/U_*^2 above and within porous bed for different channel slopes; (a) inflow rate $Q=6$ l/min, no seepage outflow rate; (b) inflow rate $Q=6$ l/min, seepage outflow rate $Q_I=0.3$ l/min; (c) inflow rate $Q=6$ l/min, seepage outflow rate $Q_I=0.4$ l/min; (d) inflow rate $Q=6$ l/min, seepage outflow rate $Q_I=0.6$ l/min

5.3.7.2 Influence of flow rate

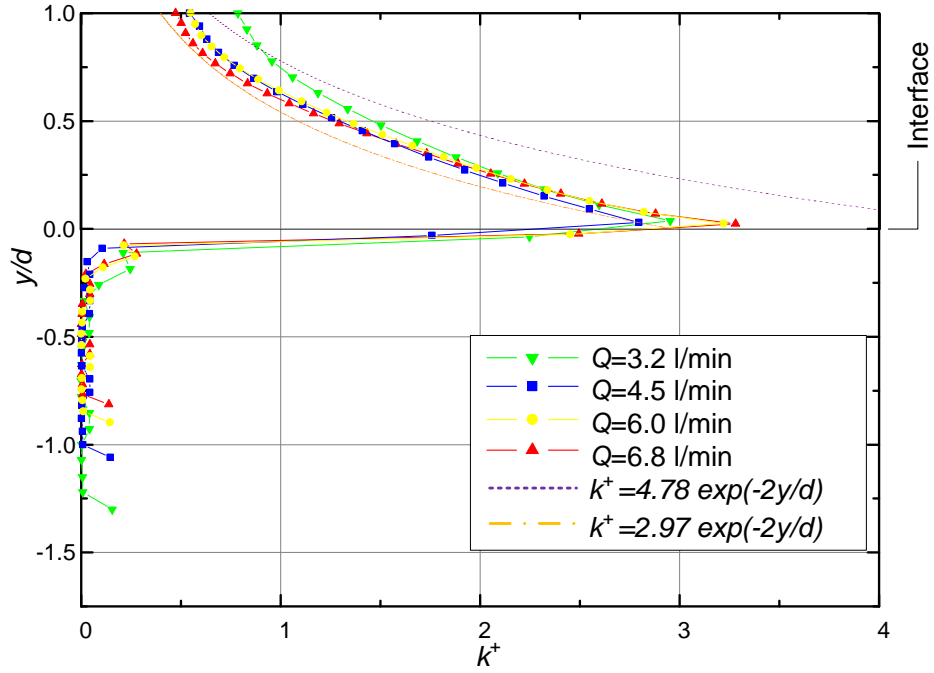
Chapter 5: Free Surface Flow over a Porous Bed in an Open Channel

Figure 5-14 shows the normalized turbulent kinetic energy k^+ profiles of the fully developed flow for inflow rate Q varying from 3.2 l/min to 6.8 l/min, with the seepage outflow rate Q_I varying from 0 to $Q/10$ for each inflow rate, and the channel slope is fixed to 0.0105.

After normalization little differences can be found for the different channel slopes, all the profiles of k^+ ($= k/U_*^2$) are overlapped.

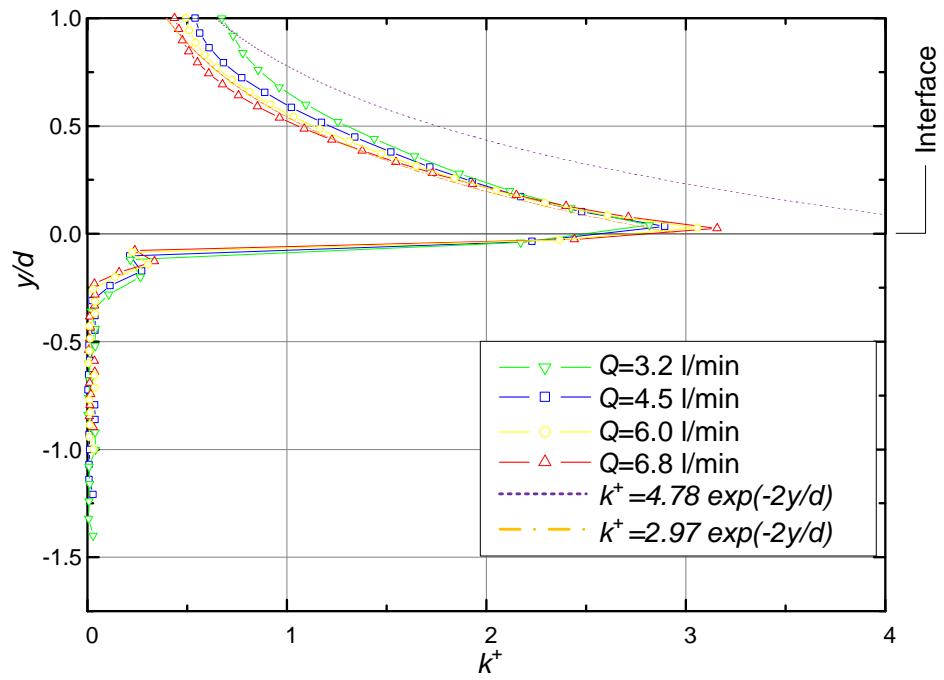
It is shown that the k^+ distribution in the free flow region is more uniform than empirical relationship for flow over impermeable beds developed by Nezu and Nakagawa (1993), $k^+ = 4.78 \exp(-2y/d)$. This is due to the penetration of turbulence to the upper part of porous region in significant levels. The empirical relationship for the range of these simulations is as follow:

$$k^+ = 2.97e^{(-2y/d)} \quad (5-9)$$

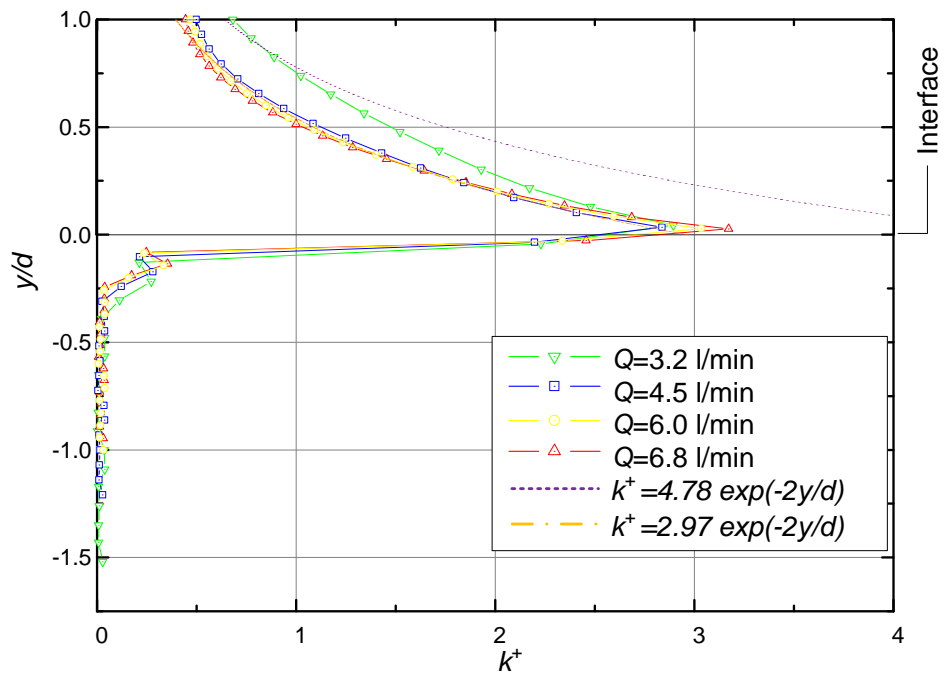


(a)

Chapter 5: Free Surface Flow over a Porous Bed in an Open Channel



(b)



(c)

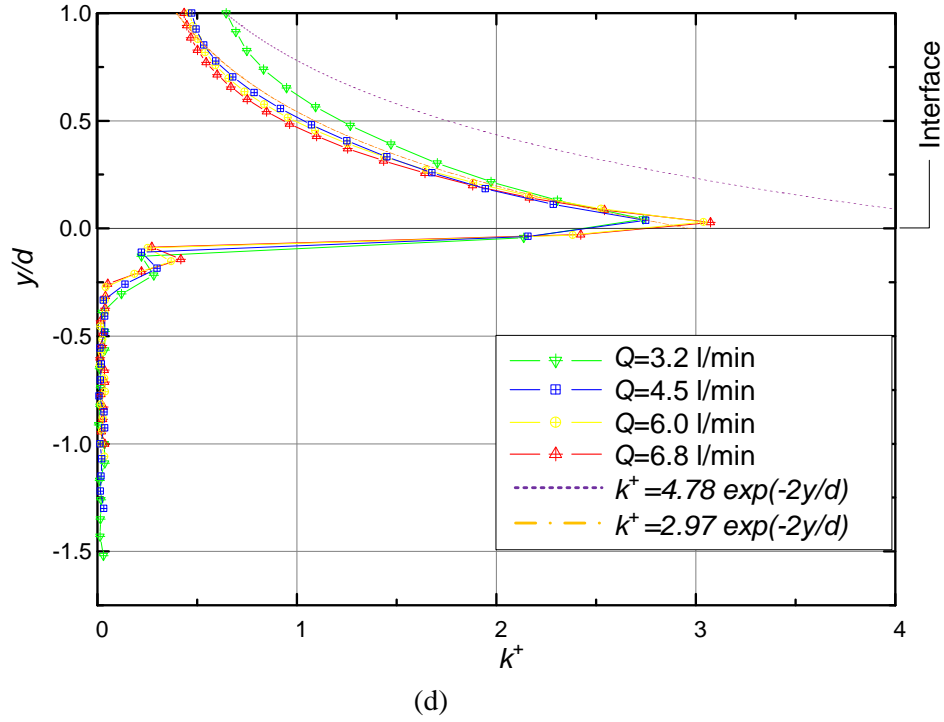


Figure 5-14. Variation of k/U_*^2 above and within porous bed for different inflow rate; (a) inflow rate $Q=6$ l/min, no seepage outflow rate; (b) inflow rate $Q=6$ l/min, seepage outflow rate $Q_I=0.3$ l/min; (c) inflow rate $Q=6$ l/min, seepage outflow rate $Q_I=0.4$ l/min; (d) inflow rate $Q=6$ l/min, seepage outflow rate $Q_I=0.6$ l/min

5.4 Conclusions

A turbulent 3D free surface flow in an open channel with a porous bed has been studied numerically and experimentally for channel slope S_0 varied from 0.0035 to 0.0244; inflow rate Q varied from 3.2 l/min to 6.8 l/min; and seepage outflow rate Q_I varied from 0 to 10% of the inflow rate Q . The characteristics of the interaction of flow over and within the porous region were simulated using a CFD-DEM approach, while in the experiments the turbulence flow parameters over the permeable region were measured with PIV system.

The following conclusions can be derived:

1. The average flow velocity within the free-fluid region increases with increasing angle of inclination, inflow rate and seepage outflow rate; simultaneously, the flow depth increases with increasing inflow rate and it decreases with increasing angle of inclination and seepage outflow rate.

Chapter 5: Free Surface Flow over a Porous Bed in an Open Channel

2. In the range of our experiments, the friction factor f decreases as inflow rate Q , slope S_o , seepage outflow rate Q_I , and Reynolds number Re increase. In most of our cases the friction factors are smaller than that of the flow with rough surface.
3. The k^+ distribution in the free flow region is more uniform than empirical relationship for flow over impermeable beds developed by Nezu and Nakagawa (1993), $k^+ = 4.78 \exp(-2y/d)$. This is due to the penetration of turbulence to the upper part of porous region in significant levels. The empirical relationship for k^+ above the porous region in the range of these simulations is as:

$$k^+ = 2.97e^{(-2y/d)}$$

Chapter 6

Particle Incipient Motion over a Porous Bed

6.1 Introduction

It is important to understand the flow conditions and boundary conditions for which the transport of sediment starts to occur when investigating sediment transport. In this chapter we try to look into some aspects of the particle incipient motion over a porous bed both experimentally and numerically. The experiment is conducted by visualization. The numerical calculations are conducted with using the CFD-DEM coupling method.

6.1.1 Experimental setup

The experimental details for this chapter are similar to those outlined in chapter 4, but have been modified slightly to allow for capture the particle incipient motions over the porous bed. Figure 6-1 is a sketch of the experimental setup.

A high speed camera was placed overhead the interested area to record the particle incipient motion, another (high speed) camera captured the motion of particles and flow depth from the side. An electronic balance was used to record the weight of the tank which collects the flume runoff Q_2 .

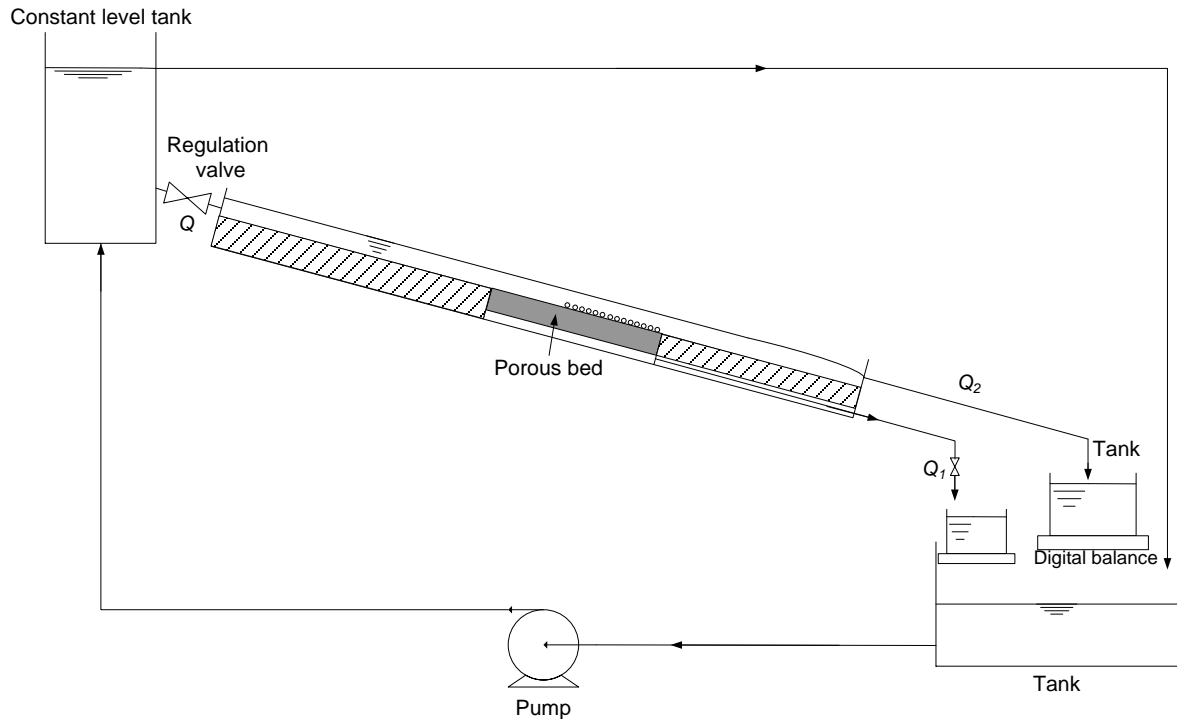


Figure 6-1. Sketch of experimental setup

6.1.2 Process of the experiment

1. Installing and setting the instrument

Install electronic balance and connect it with the computer, open the software for recording weight. Install high speed cameras in both horizontal and vertical direction of the porous bed and connect them with the computer, open the software for catching images.

2. Adjust the slope of channel

A motor is used to adjust the slope of the channel to the conditions relevant to the experiment will be carried out.

3. Put particles on the surface of porous bed

100 glass particles are placed over the surface of porous bed. Four diameters are studied (see in Table 6-1).

4. Turn on the pump and measure flow rate

Turn on the pump and fill constant level tank with water, open the regulation valve and increase the flow rate slowly, meanwhile, use high speed cameras to catch images of both

particles that have been picked up by the flow and the corresponding flow depth, use electronic balance to measure the channel outflow rate and seepage outflow rate.

5. Change parameters

Change the parameters, include channel slope, particle diameter, and seepage outflow rate, etc., and repeat the steps 1 - 4.

6.1.3 Numerical setup

Numerical simulations of particle incipient motion over the porous medium by the flow have also been carried out. The computational domain having dimensions equal to 0.03 m×0.025 m×0.30 m, a grid consisting of 30×50×600 points for the computation domain. The samples are from 100 spherical particles which have been added over the surface of fixed porous bed before the coupling calculation with fluid. The particles have a diameter of 2 mm and density of 2500 kg/m³, friction coefficient of 0.4 (Grigoriev et al., 1997), stiffness coefficient of 1×10⁶ N/m, and the critical damping ratio is 0.04. Fixed solid particles with a diameter of 3 mm are used to assemble the porous media. The thickness of porous medium is 9 mm and the inlet flow thickness is 8 mm. The coupling will be started after all particles stopped moving, and the inflow velocity is augmented from 0 at regular intervals.

6.2 Parameters of the study

Table 6-1 presents the parameters studied in this work. Three parameters have been changed in our research as: channel slope, particle diameter, and seepage outflow rate. The Reynolds number for each particle incipient motion test ranges from 100 to 8900, based on the range of inflow rate and channel slope. The porosity of the porous bed remains fixed to the value of 0.476 for all experiments.

1. Channel slope S_o varied from 0.0035 to 0.0244 (Angle of channel θ varied from 0.2° to 1.4°).
2. Particle diameter d_s varied from 1 mm to 4 mm.
3. With or without seepage outflow rate.

Table 6-1. Parameters used in the sensitivity analysis

Case	Slope S_o	Seepage outflow rate Q_I (l/min)	Particle diameter d_s (mm)
1	0.0035	0	2
2		0.43	2
3	0.0105	0	2

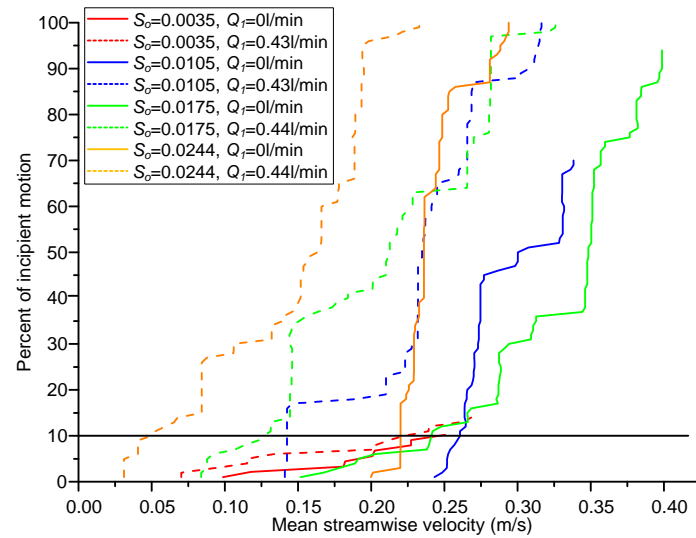
4		0.43	2
5	0.0175	0	2
6		0.44	2
7	0.0244	0	2
8		0.44	2
9	0.0105	0	1
10		0.43	1
11	0.0105	0	3
12		0.43	3
13	0.0105	0	4
14		0.43	4

6.3 Results and analysis

The probability of incipient motion is determined by counting the number of the particles (total 100 piece particles) leaving their original position and the transport starts to occur. The probability of incipient motion is plotted on function with the corresponding mean streamwise velocity and shear velocity.

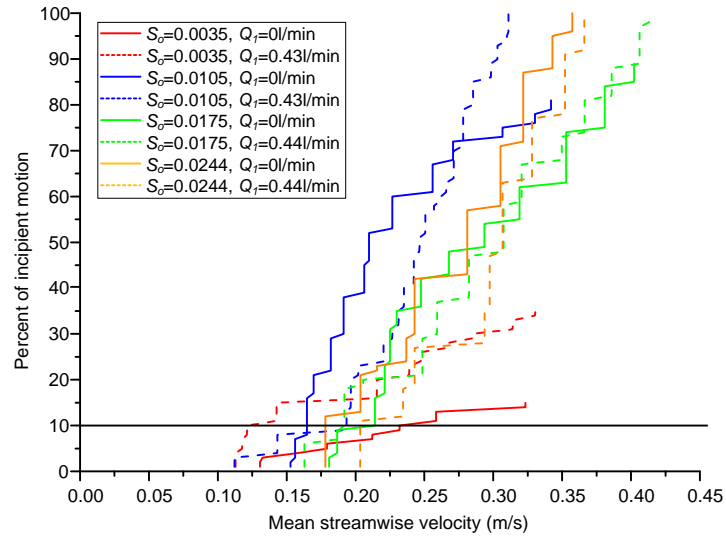
6.3.1 Influence of channel slope

The experimental and simulation probability distributions of incipient motion at different mean streamwise velocities influenced by channel slope are shown in Figure 6-2, and the cumulative incipient motion distribution curves for different shear velocities are shown in Figure 6-3. The threshold of the incipient motion is set to 40%.

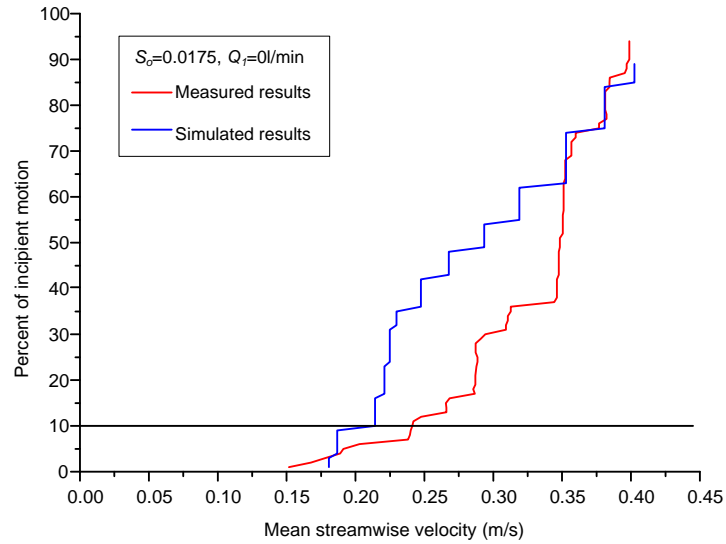


(a)

Chapter 6: Particle Incipient Motion over a Porous Bed

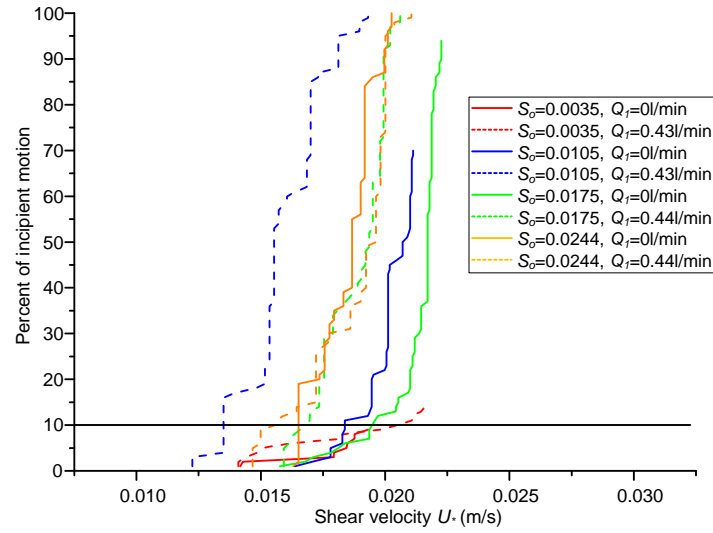


(b)

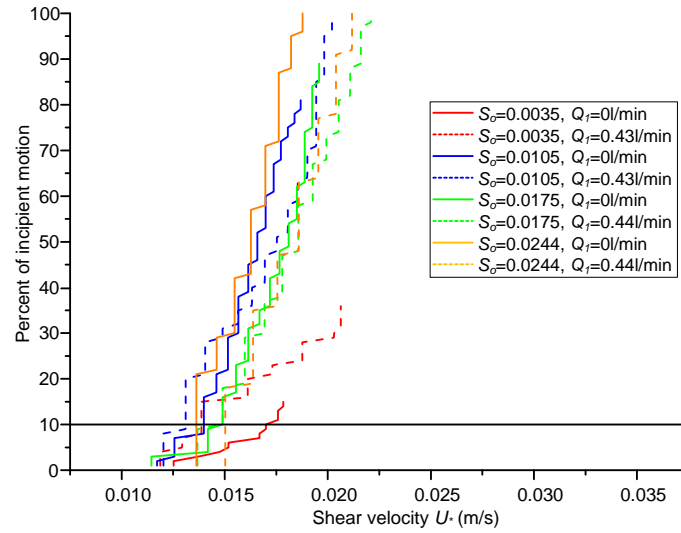


(c)

Figure 6-2. Probability distributions of incipient motion at different mean streamwise velocities, based on the measurements of 100 particles. (a), Measured results; (b), Simulated results; (c), Comparison between measured and simulated results for the case $S_o=0.0175$ without seepage outflow



(a)



(b)

Figure 6-3. Cumulative incipient motion distribution curves for different shear velocities. (a), Measured results; (b), Simulated results

The figures show that simulated results correspond well with measured results. For the case shown in Figure 6-2 (c), the maximum difference between the experimental and simulated results is less than 29%. Not all the 100 particles can be picked up within the range of inflow rate used in our experiment. The percentage of particle incipient motion is increased when mean streamwise velocity or shear velocity is increased. A larger percentage of particle incipient motion can be observed when the channel slope is increased. While comparing the rates of particles get into incipient motion with or without seepage outflow rate, we observed that greater of incipient motion occurred with a seepage outflow rate.

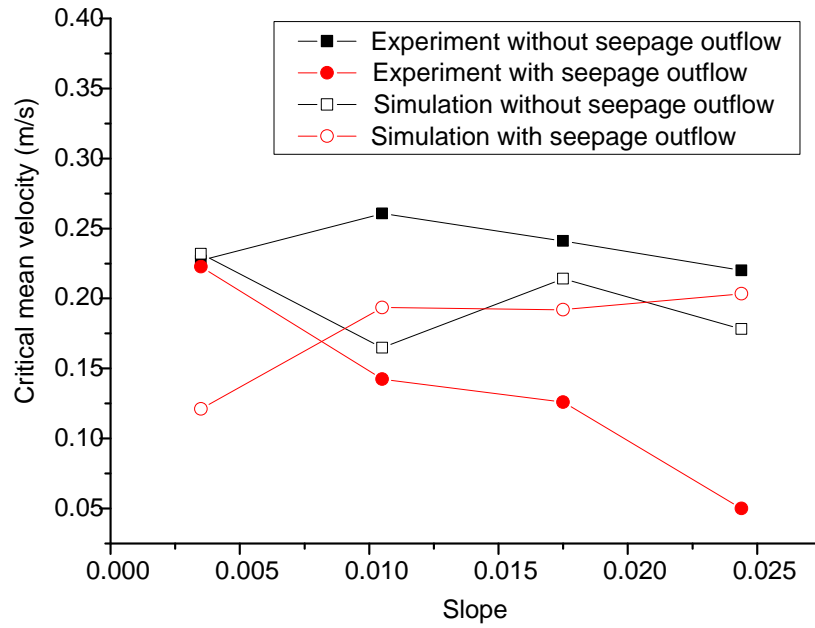


Figure 6-4. Critical mean flow velocity of the incipient motion for different channel slopes

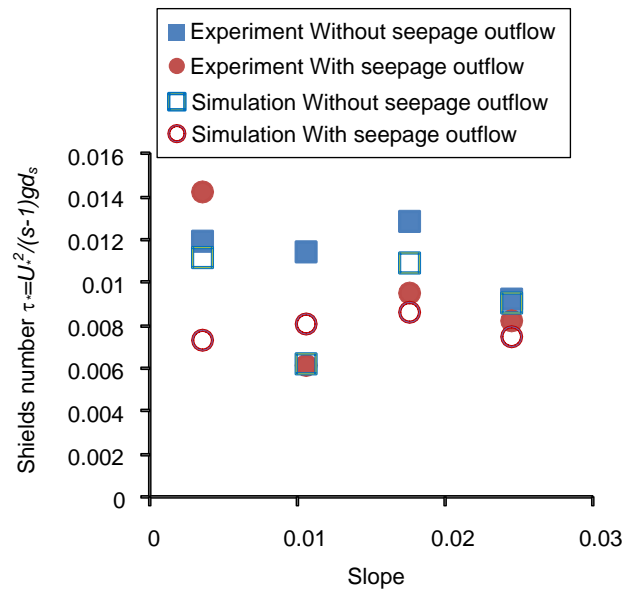


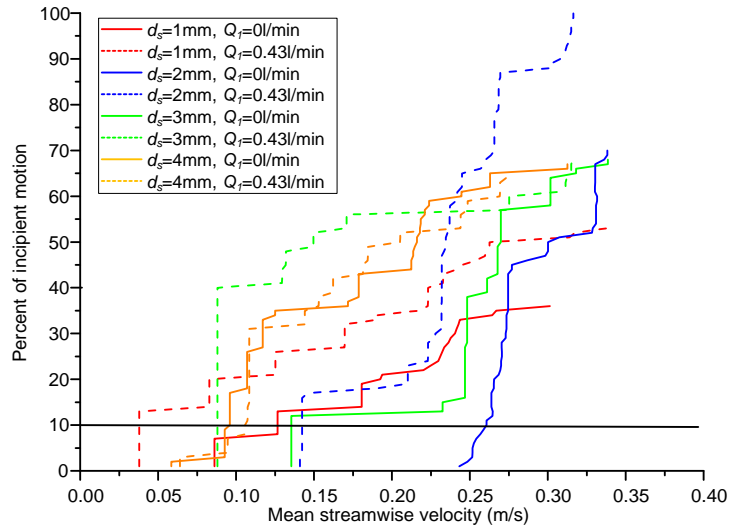
Figure 6-5. The influence of channel slopes on the Shields number

If we set a threshold of 10% particles getting into motion, then the critical mean flow velocity can be got, the results are shown in Figure 6-4, we can see that there are many uncertainties, and little influence of slope on the critical mean flow velocity. The Shields number is plotted in Figure 6-5 and little influence of slope on the Shields number can be found.

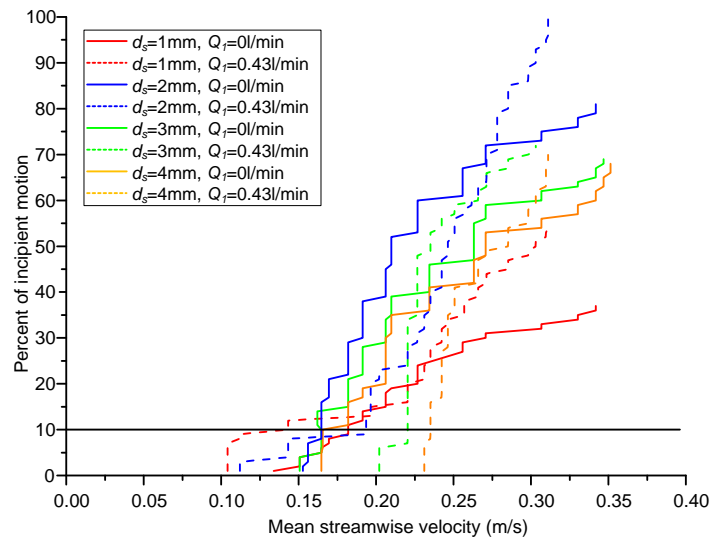
6.3.2 Influence of particle diameter

Chapter 6: Particle Incipient Motion over a Porous Bed

The experimental and simulation probability distributions of incipient motion at different mean streamwise velocities influenced by particle diameter are shown in Figure 6-6, and the cumulative incipient motion distribution curves for different shear velocities are shown in Figure 6-7. For these cases, the channel slope is fixed, $S_o = 0.0105$. The threshold of the incipient motion is set to 40%.

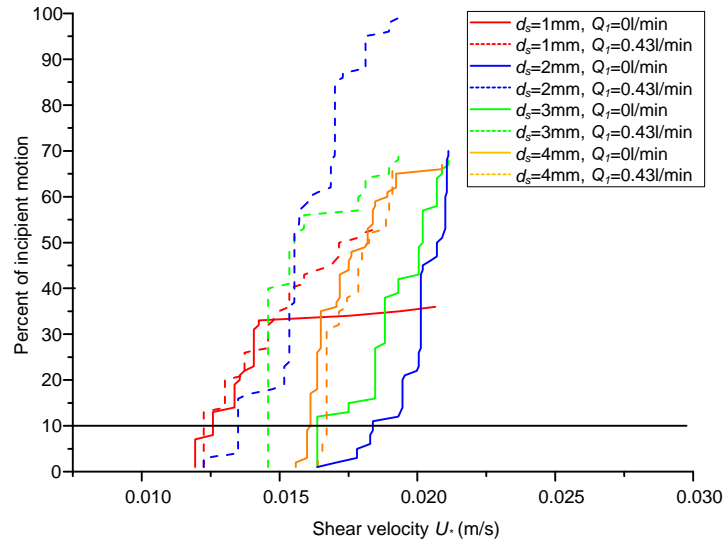


(a)

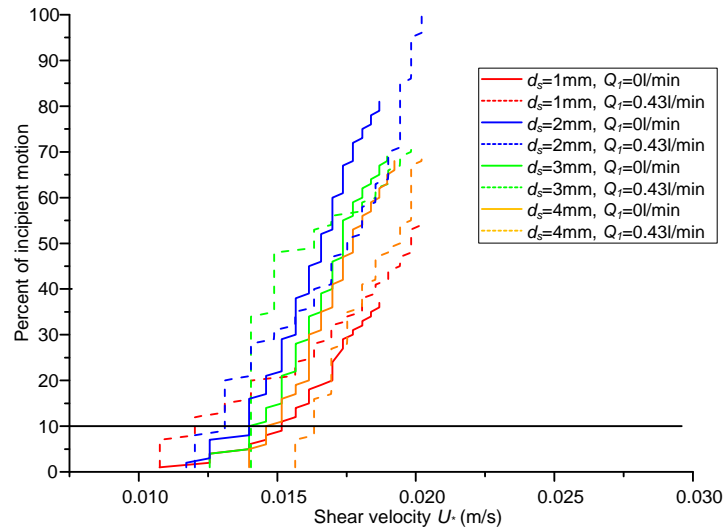


(b)

Figure 6-6. Probability distributions of incipient motion at different mean streamwise velocities, based on the measurements of 100 particles. (a), Measured results; (b), Simulated results



(a)



(b)

Figure 6-7. Cumulative incipient motion distribution curves for different shear velocities. (a), Measured results; (b), Simulated results

The figures show that a larger percentage of particle incipient motion can be observed when the particle diameter is increased from 1mm to 2mm, but fewer particles got an incipient motion when particle diameter is increased from 2mm to 4mm. While comparing the rates of particles get into incipient motion with or without seepage outflow rate, we observed that greater of incipient motion occurred with a seepage outflow rate.

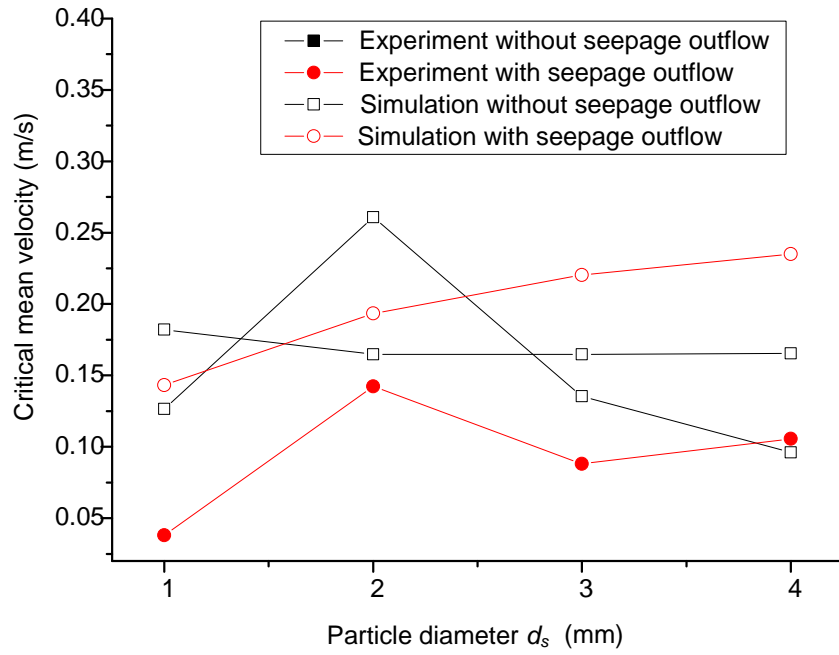


Figure 6-8. Critical mean flow velocity of the incipient motion for different particle diameters

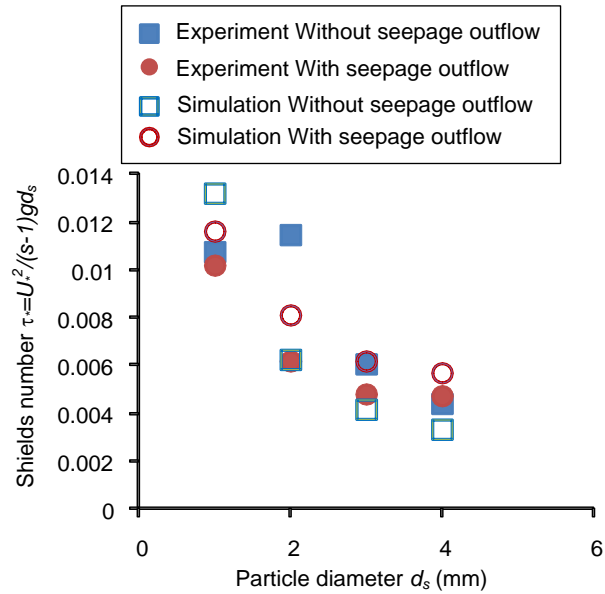


Figure 6-9. The influence of particle diameter on the Shields number

A threshold of 10% particles getting into motion has been set, then the critical mean flow velocity can be got, the results are shown in Figure 6-8, we can see that there are many uncertainties, and little influence of particle diameter on the critical mean flow velocity. The Shields number is plotted in Figure 6-9, the Shields number is diminishing with the increasing particle diameter. The explanation is that the fixed particles consisting the porous bed will

‘protect’ small particles get into motion, so for the small particles the Shields number is larger compared with the big particles.

6.4 Conclusions

The particle incipient motion over a porous bed is studied both experimentally and numerically for channel slope S_o varied from 0.0035 to 0.0244; particle diameter d_s varied from 1 mm to 4 mm; with or without seepage outflow rate Q_I . Based on the range of inflow rate and channel slope, the Reynolds number for each particle incipient motion test ranges from 100 to 8900. 100 pieces glass particles are placed over the surface of porous bed. The probability of incipient motion is determined by counting the number of the particles leaving their original position and the transport starts to occur. The particle incipient motion over a porous bed has been studied numerically using a CFD-DEM coupling method, and has also been studied experimentally with high speed camera.

The following conclusions can be derived:

1. The numerical simulated results correspond well with measured results.
2. In the range of tested Reynolds number, a larger percentage of particle incipient motion can be observed when the channel slope is increased.
3. A larger percentage of particle incipient motion can be observed when the particle diameter is increased from 1mm to 2mm, but fewer particles got an incipient motion when particle diameter is increased from 2mm to 4mm.
4. More incipient motion occurs with a seepage outflow rate than without outflow rate.
5. Little influence of channel slope and particle diameter on the critical mean flow velocity. The Shields number is diminishing with the increasing particle diameter.

Chapter 7

Particle Transport over a Porous Bed

7.1 Introduction

In this chapter particle transport in open channel over a porous bed will be studied both experimentally and numerically. Effects of the dynamic characteristics of open channel and porous bed, such as channel slope, inflow rate, seepage outflow rate and particle size, on the the solid grains transport are investigated. Experiments are conducted by visualization. The numerical calculations are conducted using CFD-DEM coupling method.

The study methods and results of this chapter can be applied in industry and environmental analyses, for example, urban hydrology, river hydraulics, water treatment, etc.

7.1.1 Experimental setup

The experimental details for this chapter are similar to those outlined in chapter 5. Figure 7-1 is a schematic of the experimental setup.

As it was described in chapter 4, a particle adding device was placed at the middle point of the porous bed allowed the particles to be added into the flow. A particle collection device constituted on a filter is placed after the outflow of the channel allowed the particles to be separated from the water via gravitational settling. The porous bed is 20 cm long, and the first

10 cm is used to make the flow over the porous bed steady, so the second 10 cm is the zone of study.

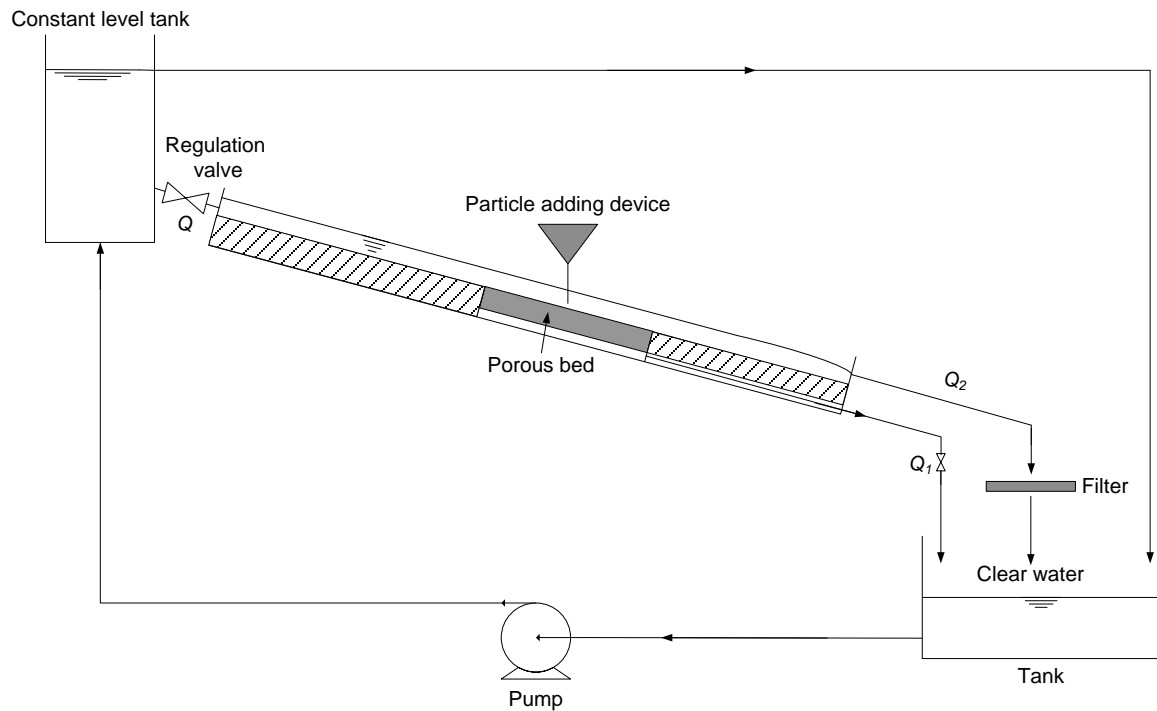


Figure 7-1. Schematic of experimental setup

7.1.2 Process of the experiment

1. Installing and setting the instrument

Install electronic balance and connect it with the computer, open the software for recording weight. Install high speed camera in the face of the porous bed and connect it with the computer, open the software for catching images.

2. Adjust the slope of channel

A motor is used to adjust the slope of channel to the conditions relevant to the experiment to be carried out.

3. Turn on the pump and adjust flow rate

Turn on the pump and fill constant level tank with water, open the regulation valve and electronic balance to adjust the inflow rate and the seepage outflow rate to the conditions relevant to the experiment.

4. Measure the flow depth and velocity field

Chapter 7: Particle Transport over a Porous Bed

After the flow is steady, measure approximately the flow depth over the porous bed with ruler, the depth is then measured with greater precision with images taken by camera. The flow velocity field is measured with a PIV system.

5. Add particles and measure weight changing

Fifty particles are added one by one 5 mm over the middle point of the porous bed surface. In the meantime, catch images of the particles transported over the porous bed with high speed camera.

6. Change parameters

Change the parameters, such as channel slope, inflow rate, seepage outflow rate and particle diameter, etc., and repeat the steps 1 - 5.

7.1.3 Numerical setup

Numerical simulations of one ball transport over the porous medium by the flow have also been carried out. The computational domain has dimensions equal to 0.03 m×0.025 m×0.30 m and a grid consisting of 30×50×600 points. Like the laboratory experiment did, the samples are from fifty particles which are added to the flow field one by one, a particle is deleted if it reaches the edge of the area of interest, in the meantime, the next particle is added in the middle of the flow field over the surface of the porous media, without initial velocity. The average velocity of a particle is calculated over a distance along the channel of 100 mm. The injected particle has a diameter of listed in Table 7-1. Fixed solid particles with a diameter of 3 mm are used to assemble the porous media. The thickness of the porous medium is 9 mm and the inlet flow depth is 8 mm. All the particles include movable or fixed, have a density of 2500 kg/m³, a friction coefficient of 0.4 (Grigoriev et al., 1997), a stiffness coefficient of 1×10⁶ N/m, and a critical damping ratio of 0.04.

7.2 Parameters of the study

Table 7-1 presents the parameters studied in this work. Four parameters have been changed in our research as: channel slope, inflow rate, seepage outflow rate, and particle diameter. The porosity of the porous bed remains fixed to the value of 0.476 for all experiments.

1. Channel slope S_o varied from 0.0035 to 0.0244 (Angle of channel θ varied from 0.2° to 1.4°).
2. Inflow rate Q varied from 3.2 l/min to 6.8 l/min.
3. Seepage outflow rate Q_I varied from 0 to 10% of the inflow rate Q .

Chapter 7: Particle Transport over a Porous Bed

4. Particle diameter d_s varied from 1 mm to 4 mm.

Table 7-1. Parameters used in the sensitivity analysis

Case	Slope S	Inflow rate Q (l/min)	Seepage outflow rate Q_I (l/min)	Particle diameter d_s (mm)
1	0.0035	6.00	0	2
2		6.00	0.30	2
3		6.00	0.40	2
4		6.00	0.60	2
5	0.0105	6.00	0	2
6		6.00	0.30	2
7		6.00	0.40	2
8		6.00	0.60	2
9	0.0175	6.00	0	2
10		6.00	0.30	2
11		6.00	0.40	2
12		6.00	0.60	2
13	0.0244	6.00	0	2
14		6.00	0.30	2
15		6.00	0.40	2
16		6.00	0.60	2
17	0.0105	3.20	0	2
18		3.20	0.16	2
19		3.20	0.21	2
20		3.20	0.32	2
21	0.0105	4.50	0	2
22		4.50	0.23	2
23		4.50	0.30	2
24		4.50	0.45	2
25	0.0105	6.80	0	2
26		6.80	0.34	2
27		6.80	0.45	2
28		6.80	0.68	2
29	0.0105	6.00	0	1
30		6.00	0.30	1
31		6.00	0.40	1
32		6.00	0.60	1
33	0.0105	6.00	0	3
34		6.00	0.30	3
35		6.00	0.40	3
36		6.00	0.60	3
37	0.0105	6.00	0	4
38		6.00	0.30	4
39		6.00	0.40	4
40		6.00	0.60	4

7.3 Results and analysis

7.3.1 Raw results

The experimental and simulation geometric and hydrodynamic characteristics are shown in Table 5-2 in chapter 5, particle mean streamwise velocity and properties are shown in Table A-1 in the appendix.

7.3.2 Particle transport velocity

The analytical results show that the velocity distributions of particles in different cases (Figure A-1, A-2, and A-3, in the Appendix) follow a Gaussian distribution with a high correlation coefficient. The corresponding probability can be expressed into the following correlation:

$$Pr(U_{px}) = \frac{A}{\sigma\sqrt{2\pi}} \exp\left(-\frac{(U_{px}-\mu)^2}{2\sigma^2}\right) \quad (7-1)$$

where Pr represents the probability distribution of horizontal component of the particle velocity; A, μ, σ are the parameters of the Gaussian equation. Table 7-3 gives the value of the parameters and the correlation coefficient R^2 .

Table 7-3. Fitting parameters of Gaussian distribution

Case	A		μ		σ		R^2	
	simulation	experiment	simulation	experiment	simulation	experiment	simulation	experiment
1	0.311	1.030	0.148	0.140	0.007	0.025	0.899	0.981
2	0.196	0.921	0.178	0.182	0.004	0.022	0.896	0.974
3	0.256	0.814	0.183	0.195	0.007	0.020	0.928	0.908
4	0.294	1.383	0.208	0.210	0.006	0.022	0.912	0.971
5	0.312	0.833	0.173	0.144	0.010	0.019	0.938	0.958
6	0.334	0.707	0.215	0.184	0.007	0.014	0.976	0.970
7	0.288	0.687	0.225	0.203	0.006	0.015	0.907	0.885
8	0.358	0.775	0.245	0.225	0.007	0.015	0.955	0.943
9	0.256	0.920	0.226	0.215	0.007	0.023	0.968	0.876
10	0.325	1.030	0.260	0.244	0.009	0.018	0.916	0.988
11	0.299	1.201	0.268	0.267	0.008	0.025	0.936	0.892
12	0.281	0.707	0.279	0.285	0.008	0.015	0.874	0.980
13	0.295	1.756	0.265	0.311	0.007	0.026	0.995	0.947
14	0.308	1.348	0.291	0.313	0.006	0.022	0.903	0.972

Chapter 7: Particle Transport over a Porous Bed

15	0.249	1.139	0.299	0.322	0.008	0.021	0.961	0.943
16	0.303	1.528	0.311	0.327	0.008	0.021	0.848	0.995
17	0.307	0.995	0.108	0.113	0.009	0.019	0.963	0.993
18	0.244	0.611	0.166	0.155	0.005	0.014	0.964	0.930
19	0.356	0.633	0.169	0.165	0.007	0.009	0.960	0.967
20	0.265	0.609	0.182	0.194	0.008	0.012	0.881	0.949
21	0.383	0.881	0.144	0.170	0.011	0.017	0.885	0.978
22	0.257	0.716	0.178	0.221	0.007	0.017	0.974	0.960
23	0.256	1.099	0.192	0.242	0.008	0.020	0.932	0.990
24	0.281	0.720	0.210	0.269	0.005	0.013	0.881	0.901
25	0.598	1.394	0.189	0.186	0.014	0.023	0.919	0.998
26	0.273	1.024	0.235	0.221	0.007	0.020	0.870	0.927
27	0.265	0.718	0.244	0.247	0.006	0.016	0.808	0.879
28	0.293	1.163	0.262	0.274	0.008	0.023	0.870	0.952
29	0.509	1.737	0.126	0.169	0.013	0.028	0.874	0.948
30	0.413	1.299	0.183	0.213	0.011	0.027	0.878	0.967
31	0.347	0.942	0.226	0.224	0.010	0.026	0.947	0.924
32	0.325	1.376	0.240	0.227	0.010	0.025	0.967	0.988
33	0.475	0.695	0.177	0.194	0.013	0.012	0.867	0.989
34	0.266	1.445	0.218	0.255	0.006	0.034	0.927	0.955
35	0.186	1.134	0.233	0.266	0.005	0.020	0.960	0.941
36	0.233	1.566	0.251	0.268	0.005	0.031	0.940	0.924
37	0.508	0.703	0.174	0.178	0.012	0.013	0.821	0.981
38	0.131	0.930	0.223	0.228	0.004	0.020	0.899	0.947
39	0.137	0.713	0.233	0.229	0.003	0.015	0.980	0.962
40	0.155	0.828	0.248	0.236	0.004	0.019	0.948	0.937

7.3.2.1 Influence of channel slope

Figure 7-2 shows the influence of channel slope on particle velocity. Figure A-1 in Appendix illustrates the channel slope influence on the distribution of average horizontal component of the particle velocity, in different infiltration conditions. As shown in Figures 7-2 and A-1 a greater channel slope corresponds to larger average particle speed; with the same channel slope, the higher infiltration flow rate leads to faster particle speed. Higher flow velocity near the interface together with down slope component of gravity causes the increase in particle velocity.

7.3.2.2 Influence of flow rate

Figure 7-3 shows the influence of inflow rate on particle velocity. Figure A-2 in Appendix presents the inflow rate influence on the distribution of average horizontal component of the particle velocity, with different infiltration rates. As depicted in Figures 7-3 and A-2, the average particle velocity increases with increasing inflow rate and seepage flow rate.

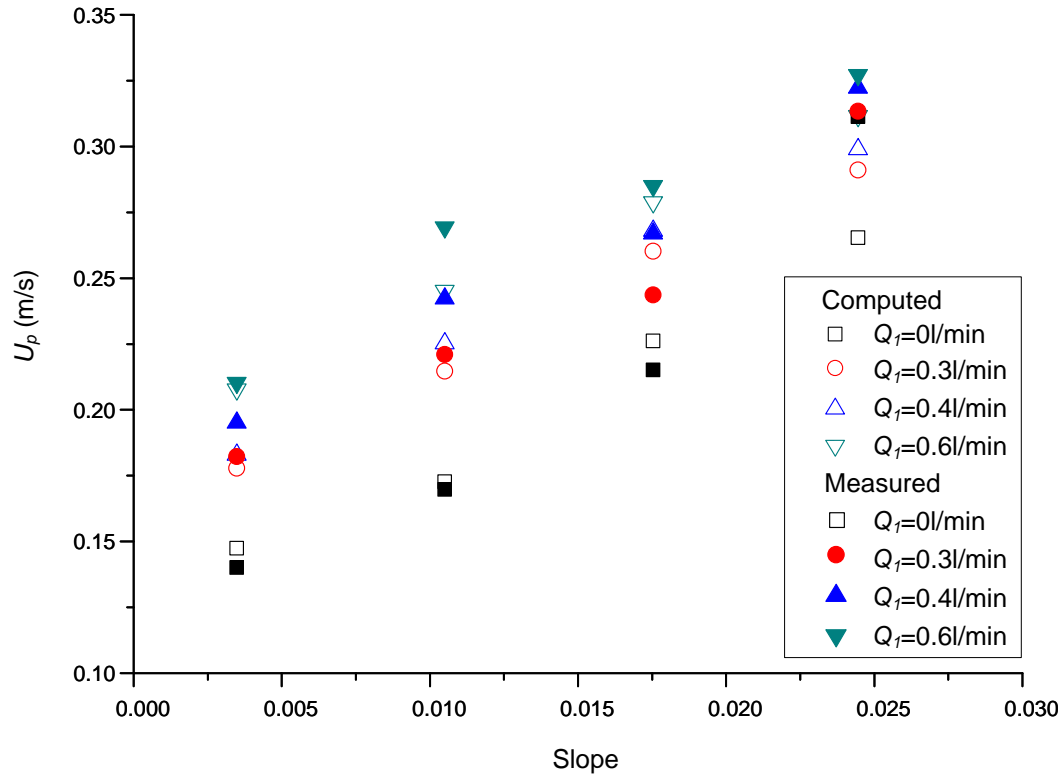


Figure 7-2. Influence of channel slope on particle velocity (inflow rate $Q=6$ l/min)

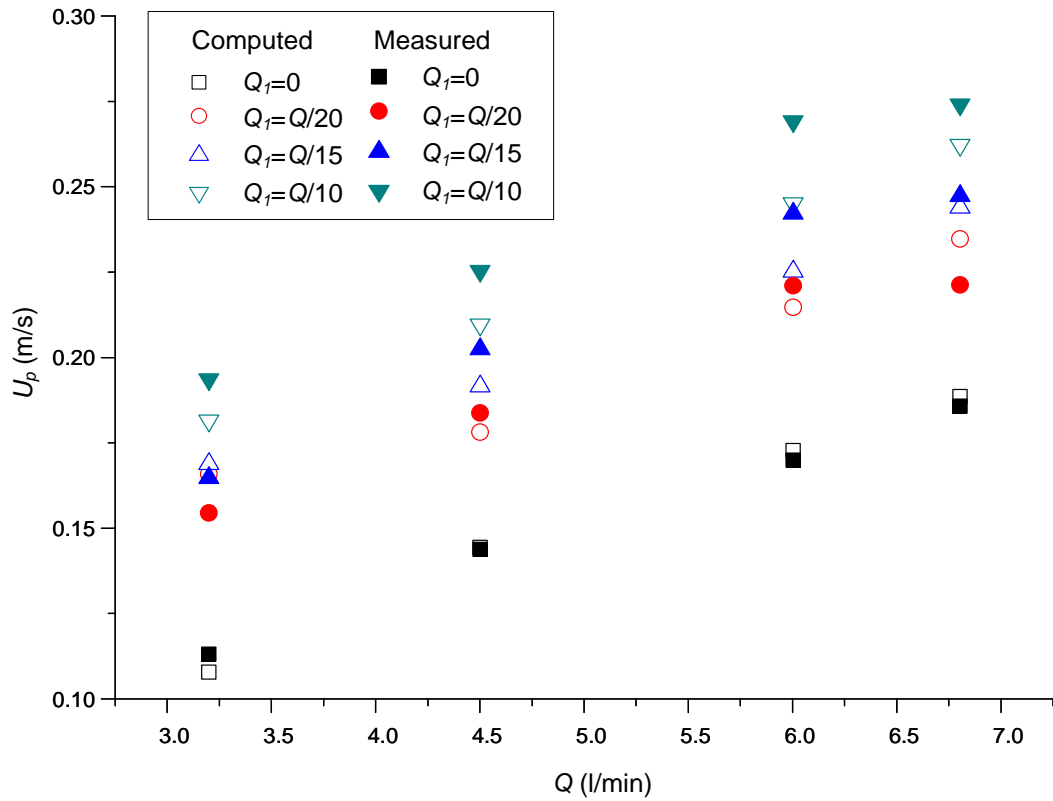


Figure 7-3. Influence of inflow rate on particle velocity (channel slope $S_o=0.0105$)

7.3.2.3 Influence of particle diameter

Figures 7-4 and A-2 in Appendix investigate particle size influence on the distributions of average particle velocity. The average particle velocity significantly increases when the particle diameter is increased from 1 mm to 2 mm, however, with diameters of 2 mm, 3 mm and 4 mm the effect is not so obvious, and velocity of particles with a diameter of 4 mm even a little slower than 3 mm particles.

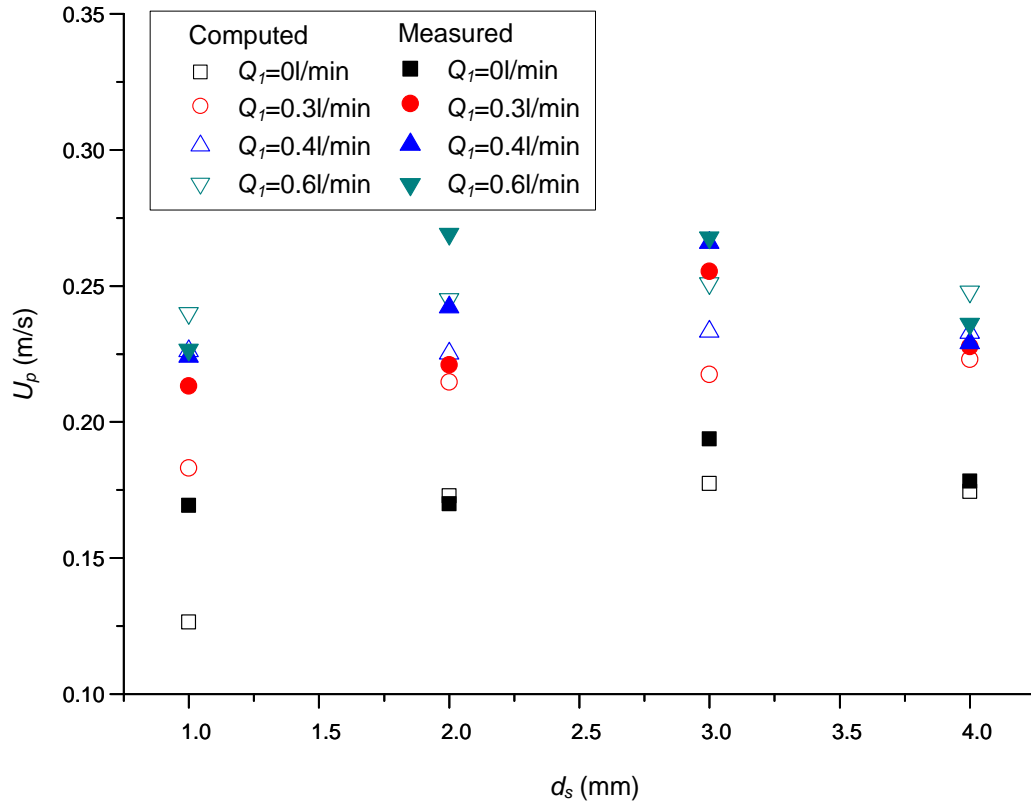


Figure 7-4. Influence of particle diameter on particle velocity (channel slope $S_o=0.0105$, inflow rate $Q=6$ l/min)

7.3.3 Analysis of particle velocity distribution along the vertical direction

For the study on movement characteristics of particles, we separate the clear water flow zone into several sub-zones by their flow depth. The positions of each sub-zone are given by Table 7-4 and Figure 7-5.

Table 7-4. The position of subzones for analysis of particle velocity

Sub-zones	1	2	3	4	5	6	7	8	9	10	11	12	
y/D	0.00	0.17	0.33	0.50	0.67	0.83	1.00	1.17	1.33	1.50	1.67	1.83	2.00

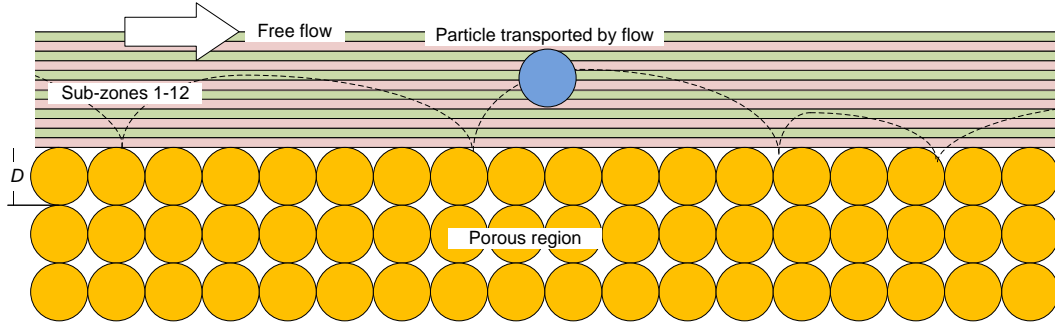


Figure 7-5. Sketch of sub-zones for analysis of particle velocity

In order to know in which sub-zone a particle is located, we seek the position of its center. Then calculate the average particle velocity of each sub-zone with calculating the mean value of all the instantaneous particle velocity in this sub-zone.

The average horizontal and vertical component of particle velocity in a sub-zone can be calculated as:

$$U_{pj} = \frac{1}{N_j} \sum_{i=1}^{N_j} U_i \quad (7-2)$$

$$V_{pj} = \frac{1}{N_j} \sum_{i=1}^{N_j} V_i \quad (7-3)$$

where U_i is the instantaneous horizontal component of particle velocity within the sub-zone j ; V_i is the instantaneous vertical component of particle velocity within the sub-zone j ; N_j is the total number of the instantaneous particle velocity located in the sub-zone j .

7.3.3.1 Influence of channel slope

Figure 7-6, 7-7, 7-8 and 7-9 are the horizontal component of particle velocity distribution, normalized with shear velocity U_* , for different channel slopes. The horizontal component of flow velocity for each flow condition has been also plotted in these figures.

Every comparison in the same figure has the same particle diameter, inflow rate and seepage outflow rate, but different channel slopes, which cause variation of the flow depth.

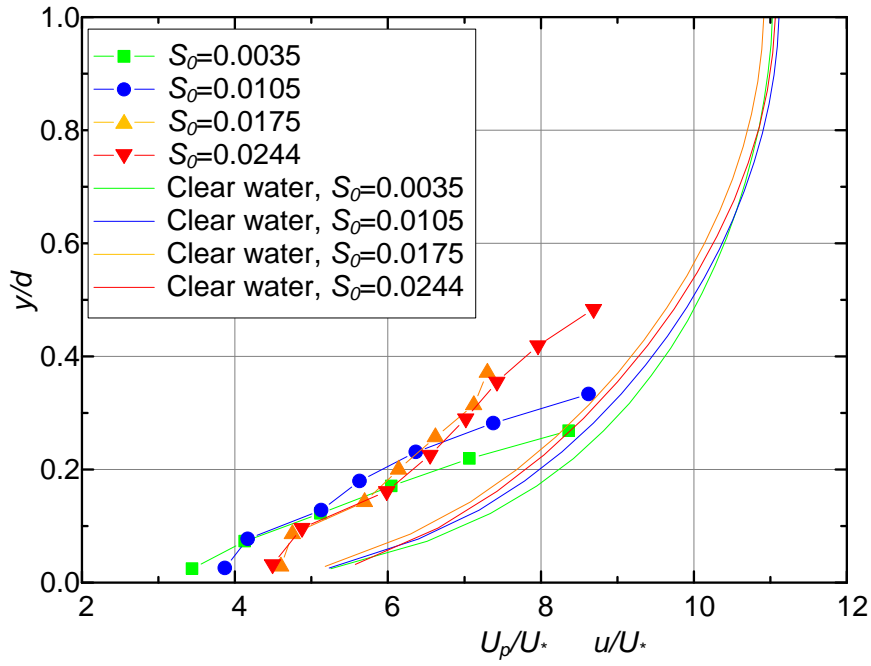


Figure 7-6. The horizontal component of particle velocity distribution for different channel slopes (flow conditions: inflow rate $Q=6$ l/min, no seepage outflow rate, four channel slopes together with their flow depths: 1, $S=0.0035$ with $d=10.25$ mm; 2, $S=0.0105$ with $d=9.75$ mm; 3, $S=0.0175$ with $d=8.75$ mm; 4, $S=0.0244$ with $d=7.75$ mm)

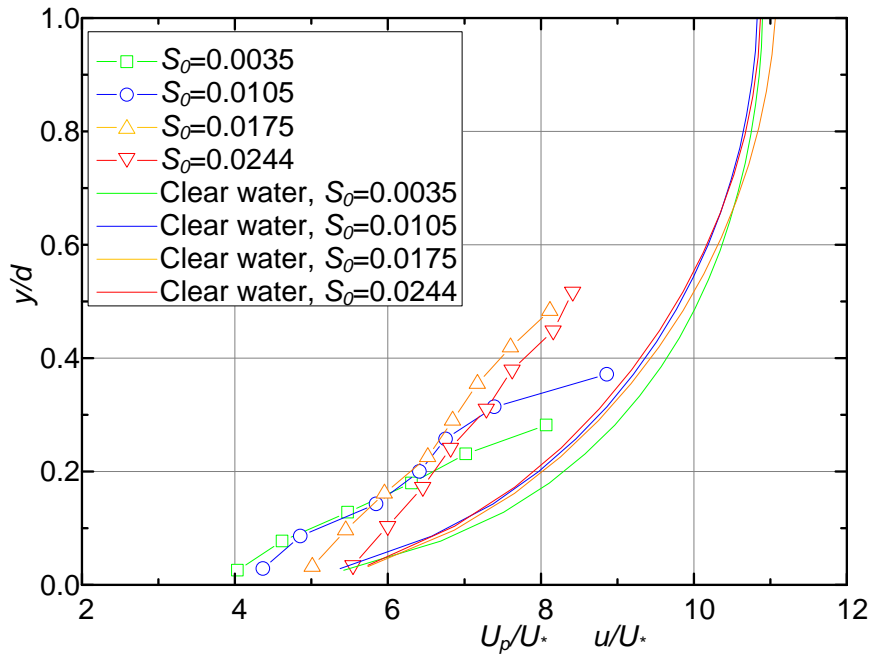


Figure 7-7. The horizontal component of particle velocity distribution for different channel slopes (flow conditions: inflow rate $Q=6$ l/min, seepage outflow rate $Q_I=0.3$ l/min, four channel slopes together with their flow depths: 1, $S=0.0035$ with $d=9.75$ mm; 2, $S=0.0105$ with $d=8.75$ mm; 3, $S=0.0175$ with $d=7.75$ mm; 4, $S=0.0244$ with $d=7.25$ mm)

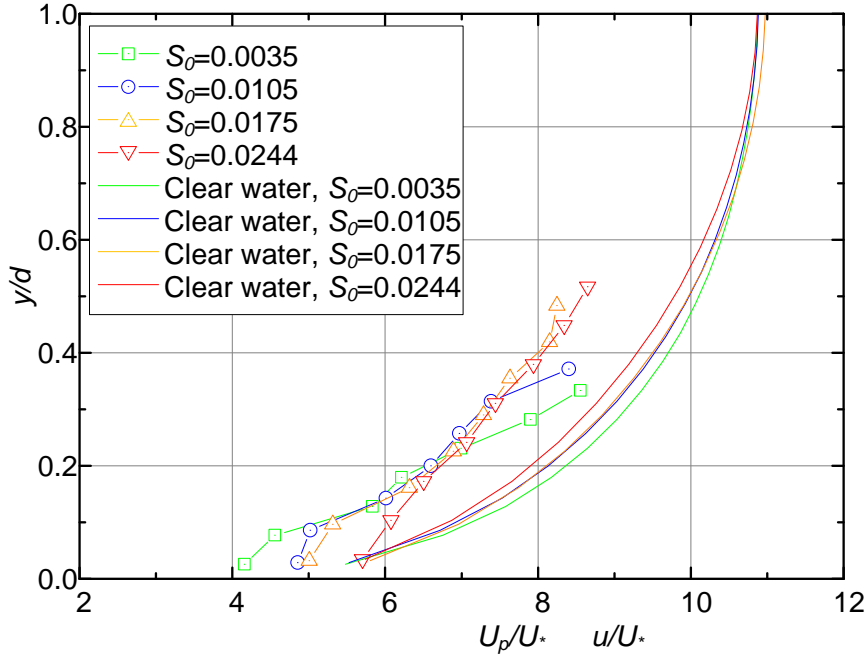


Figure 7-8. The horizontal component of particle velocity distribution for different channel slopes (flow conditions: inflow rate $Q=6$ l/min, seepage outflow rate $Q_I=0.4$ l/min, four channel slopes together with their flow depths: 1, $S=0.0035$ with $d=9.75$ mm; 2, $S=0.0105$ with $d=8.75$ mm; 3, $S=0.0175$ with $d=7.75$ mm; 4, $S=0.0244$ with $d=7.25$ mm)

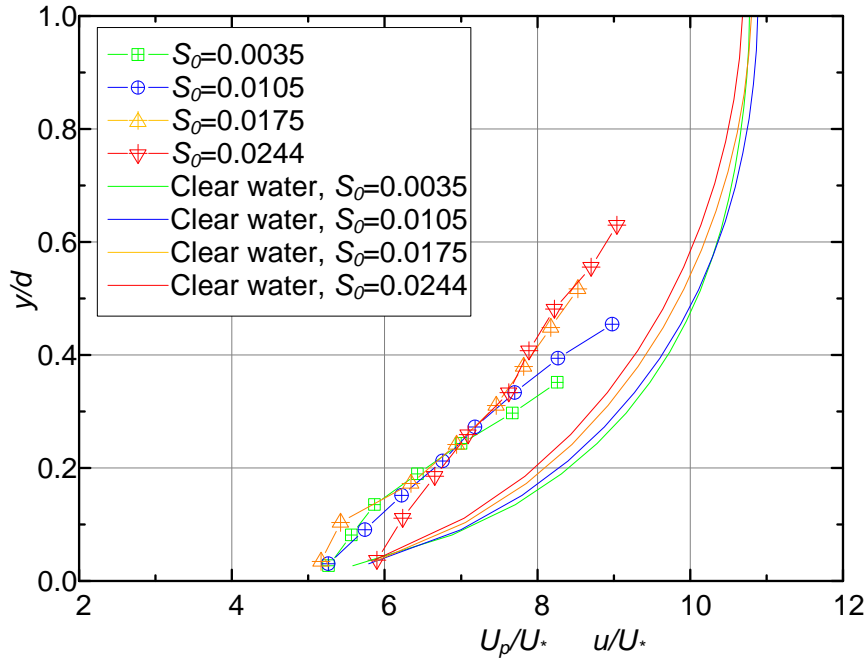


Figure 7-9. The horizontal component of particle velocity distribution for different channel slopes (flow conditions: inflow rate $Q=6$ l/min, seepage outflow rate $Q_I=0.6$ l/min, four channel slopes together with their flow depths: 1, $S=0.0035$ with $d=9.25$ mm; 2, $S=0.0105$ with $d=8.25$ mm; 3, $S=0.0175$ with $d=7.25$ mm; 4, $S=0.0244$ with $d=6.75$ mm)

These figures show that the particle velocity increases with the height of the particle position. The particle velocity increases with the increasing channel slope.

The velocity distribution for different seepage outflow rates shown in different figures demonstrate the particle velocities in bottom sub-zone are generally increasing for increasing seepage outflow, this trend agrees with the variation of flow velocity.

7.3.3.2 Influence of inflow rate

Figure 7-10, 7-11, 7-12 and 7-13 are the horizontal component of particle velocity distribution, normalized with U_* , for different inflow rates. The horizontal component of flow velocity for each flow condition has been also plotted in these figures.

Every comparison in the same figure has the same particle diameter, seepage outflow rate, but different inflow rates and the different flow depths caused by the change of inflow rates.

These figures show that with larger inflow rate the particle can move higher and faster. Like respective flow velocity profile. In addition, differences between the maximum particle velocity and the flow velocity in the same level are smaller with larger inflow rate.

The velocity distribution for different seepage outflow rates shown in different figures demonstrate the particle velocities in bottom sub-zone are generally increasing for seepage outflow rate increasing, this trend agrees with the variation of flow velocity.

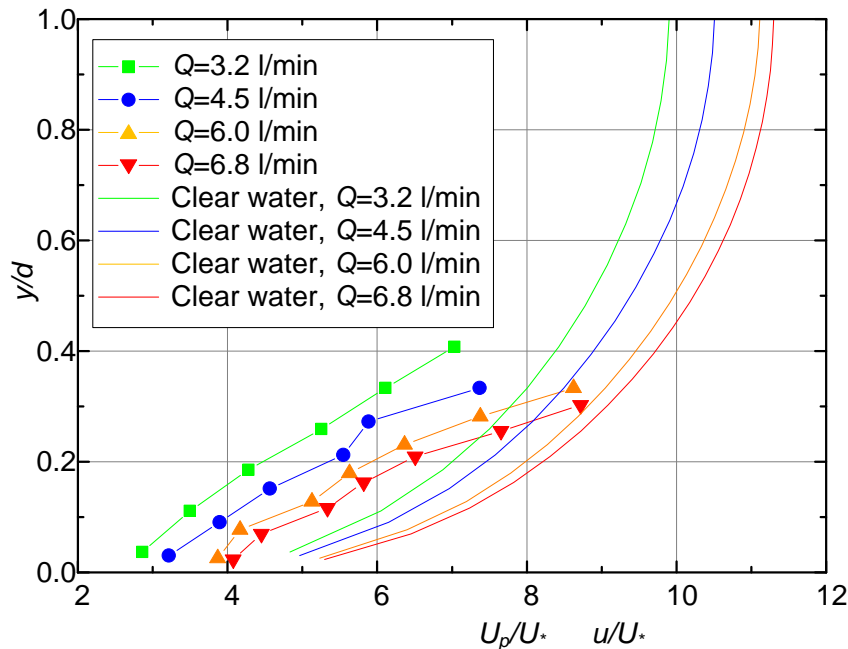


Figure 7-10. The horizontal component of particle velocity distribution for different inflow rates (flow conditions: 1, $Q=3.2$ l/min, $Q_I=0$ l/min, $d=6.75$ mm; 2, $Q=4.5$ l/min, $Q_I=0$ l/min,

$d=8.25$ mm; 3, $Q=6.0$ l/min, $Q_I=0$ l/min, $d=9.75$ mm; 4, $Q=6.8$ l/min, $Q_I=0$ l/min, $d=10.75$ mm)

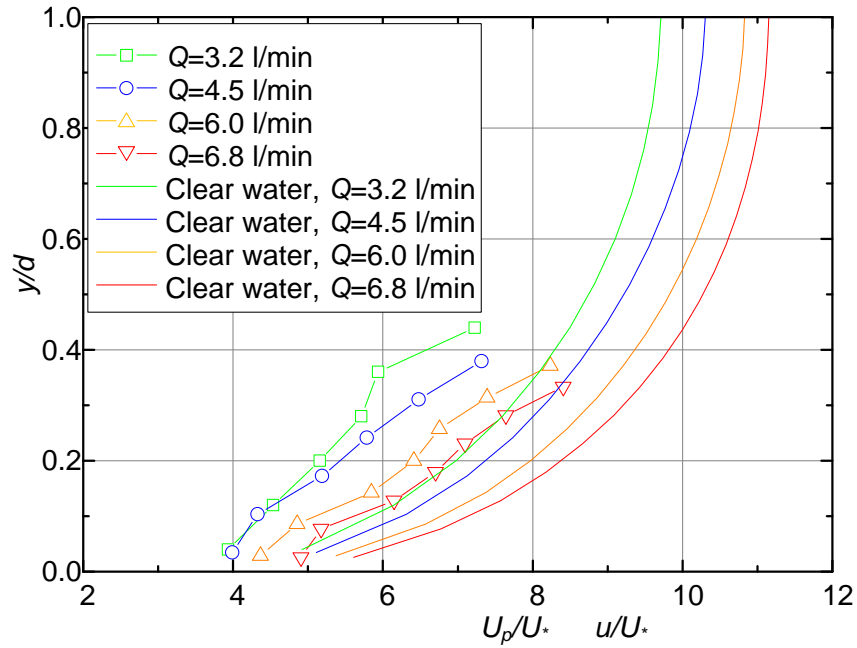


Figure 7-11. The horizontal component of particle velocity distribution for different inflow rates (flow conditions: 1, $Q=3.2$ l/min, $Q_I=0.16$ l/min, $d=6.25$ mm; 2, $Q=4.5$ l/min, $Q_I=0.23$ l/min, $d=7.25$ mm; 3, $Q=6.0$ l/min, $Q_I=0.3$ l/min, $d=8.75$ mm; 4, $Q=6.8$ l/min, $Q_I=0.34$ l/min, $d=9.75$ mm)

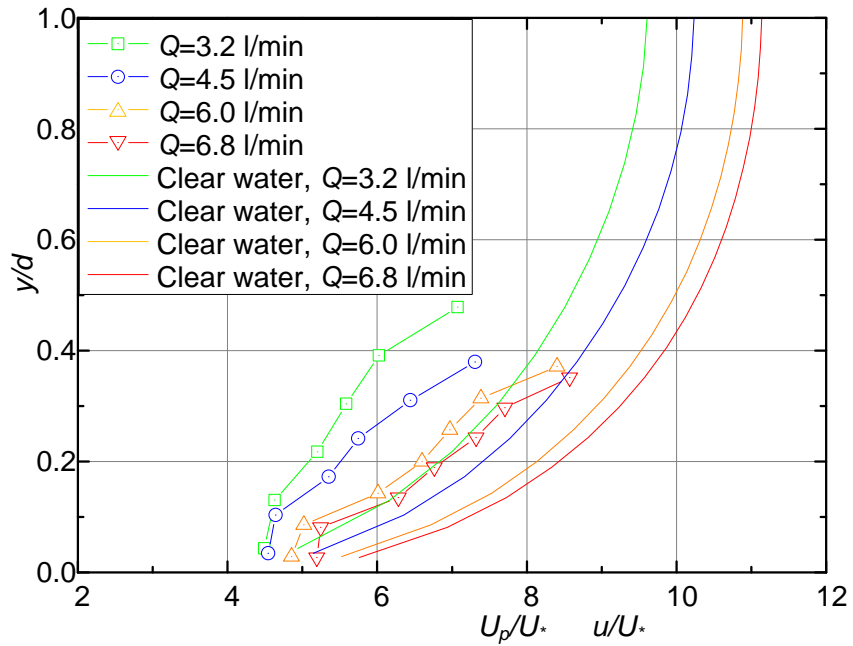


Figure 7-12. The horizontal component of particle velocity distribution for different inflow rates (flow conditions: 1, $Q=3.2$ l/min, $Q_I=0.21$ l/min, $d=5.75$ mm; 2, $Q=4.5$ l/min, $Q_I=0.3$

l/min, $d=7.25$ mm; 3, $Q=6.0$ l/min, $Q_I=0.4$ l/min, $d=8.75$ mm; 4, $Q=6.8$ l/min, $Q_I=0.45$ l/min, $d=9.25$ mm)

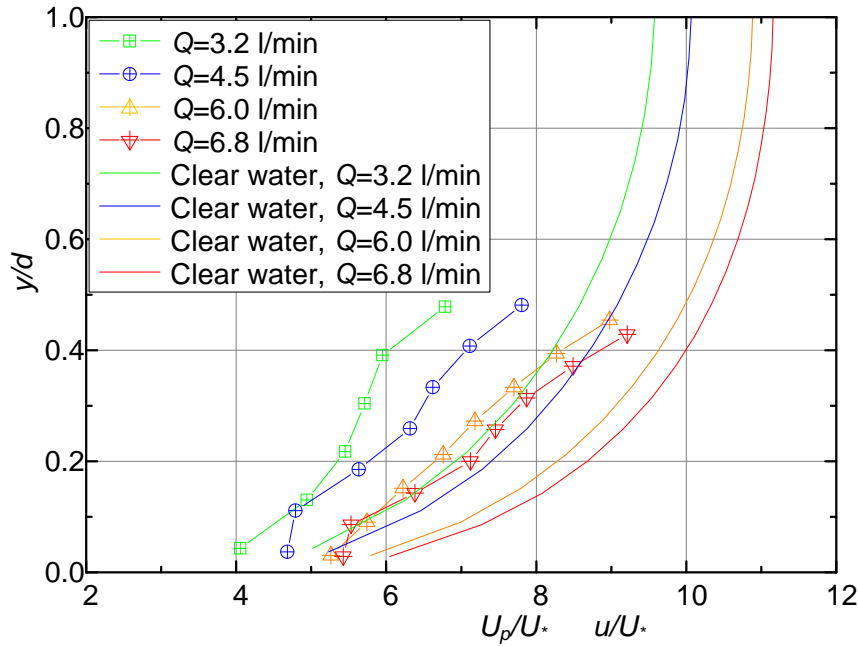


Figure 7-13. The horizontal component of particle velocity distribution for different inflow rates (flow conditions: 1, $Q=3.2$ l/min, $Q_I=0.32$ l/min, $d=5.75$ mm; 2, $Q=4.5$ l/min, $Q_I=0.45$ l/min, $d=6.75$ mm; 3, $Q=6.0$ l/min, $Q_I=0.6$ l/min, $d=8.25$ mm; 4, $Q=6.8$ l/min, $Q_I=0.68$ l/min, $d=8.75$ mm)

7.3.3.3 Influence of particle diameter

Figure 7-14, 7-15, 7-16 and 7-17 are the horizontal component of particle velocity distribution, normalized with U_* , for different particle diameters in different seepage outflow rate conditions. The horizontal component of flow velocity for each flow condition is also plotted in these figures.

From these figures, the horizontal component of particle velocity keeps arising in vertical direction, like the flow velocity, this trend indicates that the movement of particles in horizontal direction is mainly controlled by flow. But for particles diameter $d_s=4$ mm, the velocity decreases at the top of their movements, this may be caused by the ratio of particle diameter and flow depth is too large. These figures also show that, as the particle diameter increase, the height of particle body center increases in vertical direction, and the flow velocity around the particle keeps arising; and generally, the velocity in bottom sub-zone of each size particle tends to increase, this trend agrees with the variation of particle pick-up velocity. In addition these figures present that within the same flow depth, the particle velocity tends to increase with the particle size diminishing.

Chapter 7: Particle Transport over a Porous Bed

With increasing seepage outflow rates, the particle velocities in bottom sub-zone for every case are generally increasing, this trend agrees with the variation of flow velocity, which means the seepage outflow helps to increase the horizontal component of particle velocity.

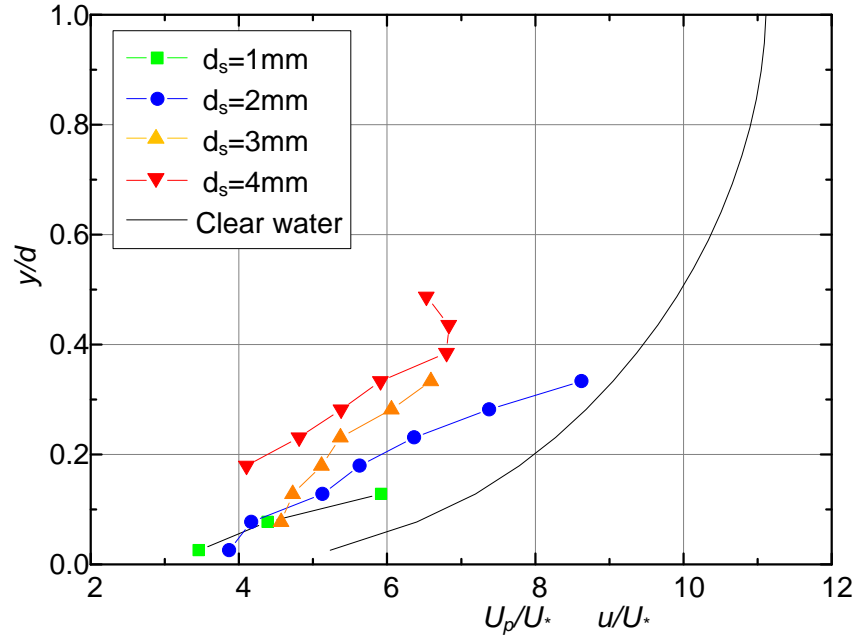


Figure 7-14. The horizontal component of particle velocity distribution for different particle diameters in same flow condition (inflow rate $Q=6$ l/min, no seepage outflow rate, flow depth $d=9.75$ mm, channel slope $S=0.0105$)

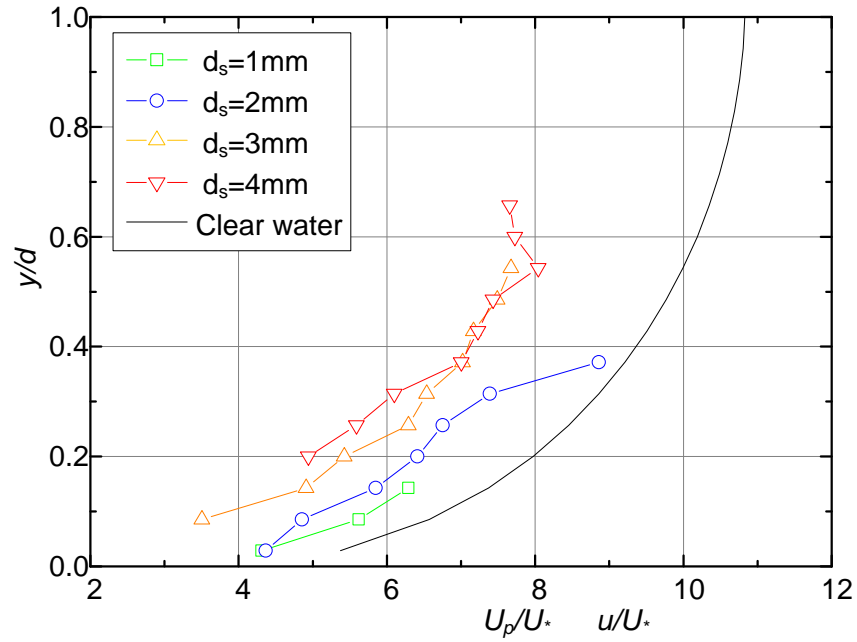


Figure 7-15. The horizontal component of particle velocity distribution for different particle diameters in same flow condition (inflow rate $Q=6$ l/min, seepage outflow rate $Q_I=0.3$ l/min, flow depth $d=8.75$ mm, channel slope $S=0.0105$)

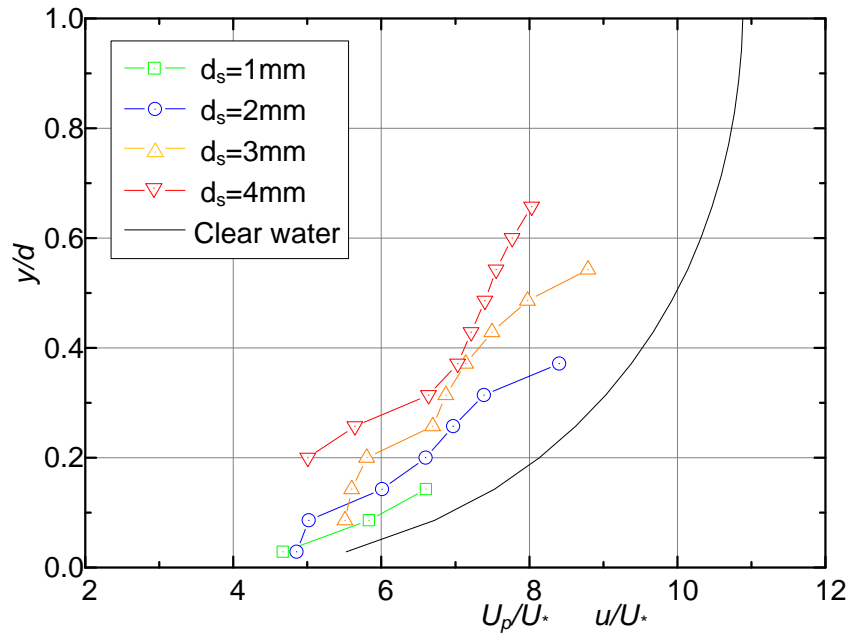


Figure 7-16. The horizontal component of particle velocity distribution for different particle diameters in same flow condition (inflow rate $Q=6$ l/min, seepage outflow rate $Q_I=0.4$ l/min, flow depth $d=8.75$ mm, channel slope $S=0.0105$)

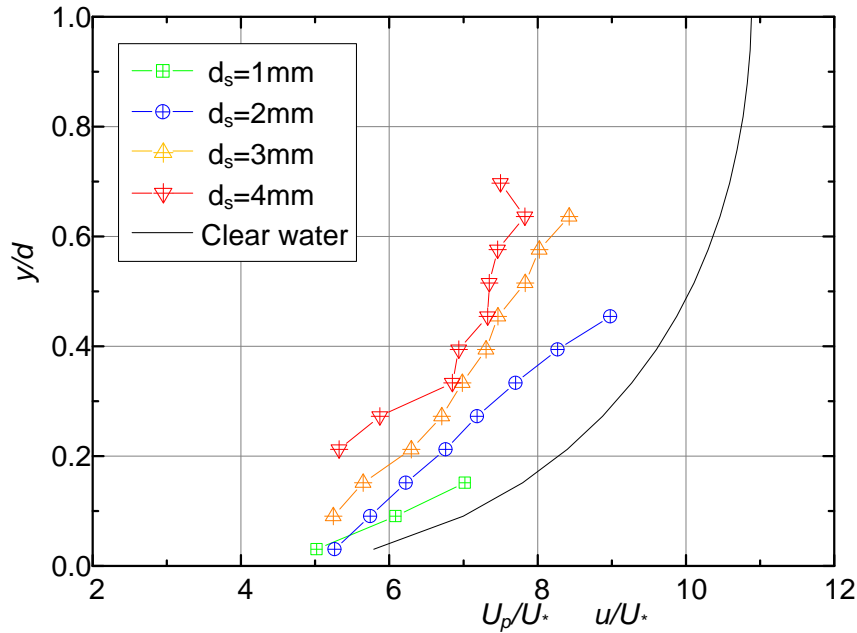


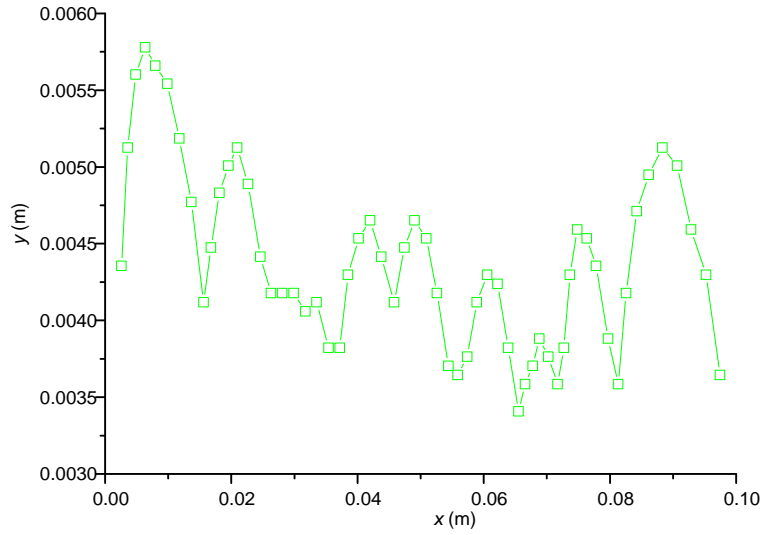
Figure 7-17. The horizontal component of particle velocity distribution for different particle diameters in same flow condition (inflow rate $Q=6$ l/min, seepage outflow rate $Q_I=0.6$ l/min, flow depth $d=8.25$ mm, channel slope $S=0.0105$)

7.3.4 Analysis of particle motion in flow

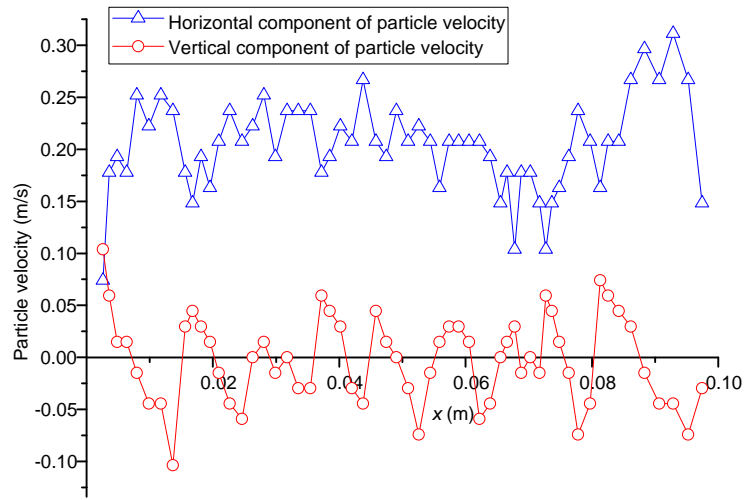
When studying the movement of particles caused by flow there is a need to analyze the typical motion of particle. Here we take one example of the particle transport inflow we have studied both experimentally and numerically. The flow condition for this example is as, inflow rate $Q=6.8$ l/min, seepage outflow rate $Q_I=0.34$ l/min, flow depth $d=8.47$ mm, particle diameter $d_s=2$ mm. In laboratory experiment the particle is added 5 mm above the surface of porous bed by particle adding device motioned in Chapter 4, and the high speed camera is used to record the trajectory of the particle, a frame rate of 250 frames/s has been used, the first collision between the particle and the bed surface is considered as the start point of the transport. In the corresponding numerical simulation the particle is generated on the surface of porous bed without initial velocity, once the particle is generated, the transport starts.

The coordinate data are plotted (Figure 7-18a for experiment and Figure 7-19a for simulation) for the complete trajectory of the particle transport over porous bed within the first 10 cm distance. The trajectory got from numerical simulation agrees well with the experimental trajectory, because the particle adding method is different between the experiment and the numerical simulation, there is a little difference of the trajectory at the beginning stage, but the range of particle saltation is the same, the vertical coordinate of the particle center y varies mainly from 3.5 mm to 5.5 mm. In a trajectory, the particle keeps jumping along the streamwise direction, when the particle impacts the surface of porous bed, immediately it starts a new saltation. From Figures 7-18 and 7-19 we can find that, during the saltation, the horizontal component of particle velocity varies mainly from 0.10 m/s to 0.30 m/s, it increases when the particle is climbing, it decreases when particle is descending, then it losses a lot because of collision. While during the saltation, the vertical component of particle velocity varies from -0.10 m/s to 0.10 m/s, it decreases when the particle is climbing, and changes the direction into downward after the particle starts descending from the top of the jumping, because of the negative composition of forces (include gravitational force, buoyant force and drag force etc.), its magnitude increases, then it changes the direction upward after the collision.

Chapter 7: Particle Transport over a Porous Bed



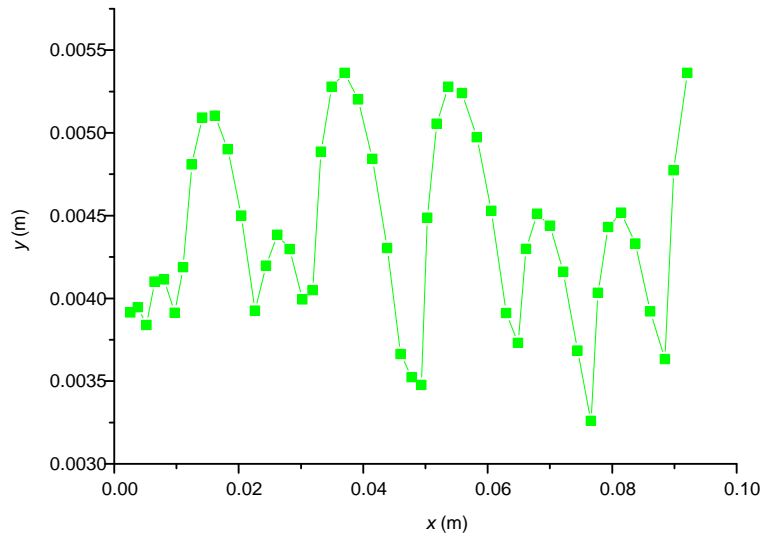
(a)



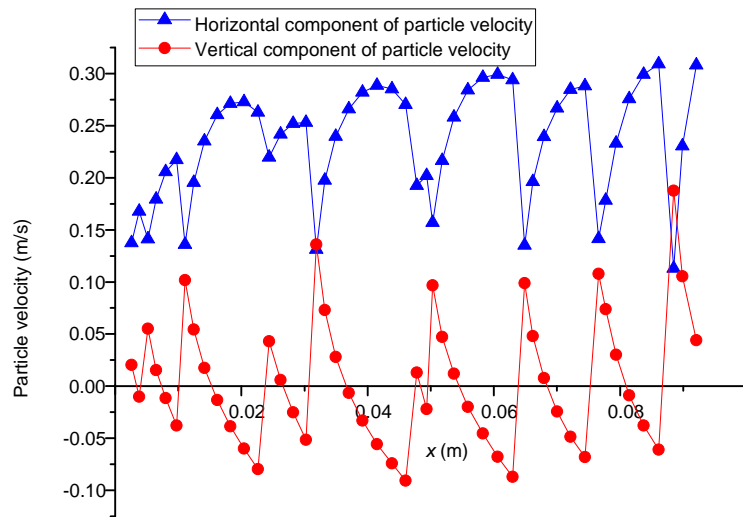
(b)

Figure 7-18. Experimental variations processes of particle velocity along saltation trajectory (one of the fifty particles simulated for inflow rate $Q=6.8$ l/min, seepage outflow rate $Q_I=0.34$ l/min, $d=8.47$ mm). (a), particle saltation trajectory; and (b), variation of particle velocity

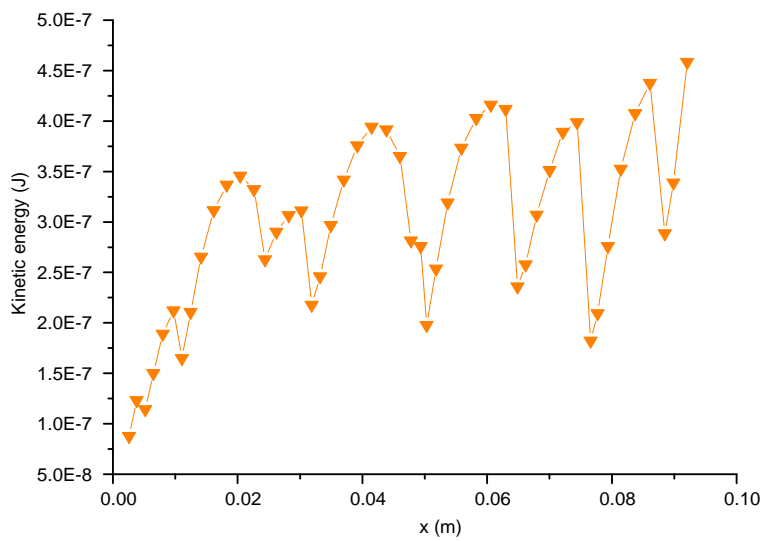
Chapter 7: Particle Transport over a Porous Bed



(a)



(b)



(c)

Figure 7-19. Variations processes of particle velocity and kinetic energy along saltation trajectory (one of the fifty particles simulated for inflow rate $Q=6.8$ l/min, seepage outflow rate $Q_I=0.34$ l/min, $d=9.75$ mm). (a), particle saltation trajectory; (b), variation of particle velocity; and (c), variation of particle energy

7.3.5 Analysis of horizontal component of particle velocity distribution in ascent and descent motion

The movement of particle can be regard as the combination of ascent motions (i.e. $V_p > 0$, note as V_{p+}) and descent motions (i.e. $V_p < 0$, note as V_{p-}).

Take $Q=6.8$ l/min with four different seepage outflow conditions (i.e. $Q_I=0$ l/min, $Q_I=0.34$ l/min, $Q_I=0.45$ l/min, $Q_I=0.68$ l/min) for instance. The results given by figure 7-20, 7-21, 7-22, 7-23. The mean horizontal component of particle velocity distribution in ascent motion and descent motion has the relation as follow:

$$U_{pd} > U_{pa} \quad (7-2)$$

where U_{pd} is the mean horizontal component of particle velocity in descent motion; U_{pa} is the mean horizontal component of particle velocity in ascent motion, Equation (7-2) shows that the horizontal component of particle velocity of descent motion is larger than that of ascent motion. Sumer and Deigaard (1981) search the particle motions near the bottom in turbulent flow also found this phenomenon, they suggested explaining this as the bursting process, in turbulent boundary layers a significant part of the momentum transfer is related to large coherent fluid motions, which can cause a vertical convection of suspended sediment.

Actually, the last analysis show that the motion of particles in horizontal direction is mainly controlled by flow, and in the open channel flow velocity is increasing from the bottom to the surface in vertical direction, so within the same level, the particle ascent from a lower position has the smaller horizontal velocity component than the particle descent from a higher position. Obviously, this explication can fit the whole clear flow region. Moreover, the bursting process also influences the particle motion at the bottom.

These figures also present that the differences for ascent motion and descent motion at the bottom are much larger than that at the top of particle motion, this is because, at the top the motion direction has just been changed from ascent to descent, the drag force between the particle and the fluid cannot affect too much to the horizontal component of particle velocity, but at the bottom because of the shock between the particle and the porous bed, the horizontal component of particle velocity has been lost badly.

From these figures we can also find that the mean horizontal component of particle velocity increases with the increasing seepage outflow rate both in ascent motion and descent motion.

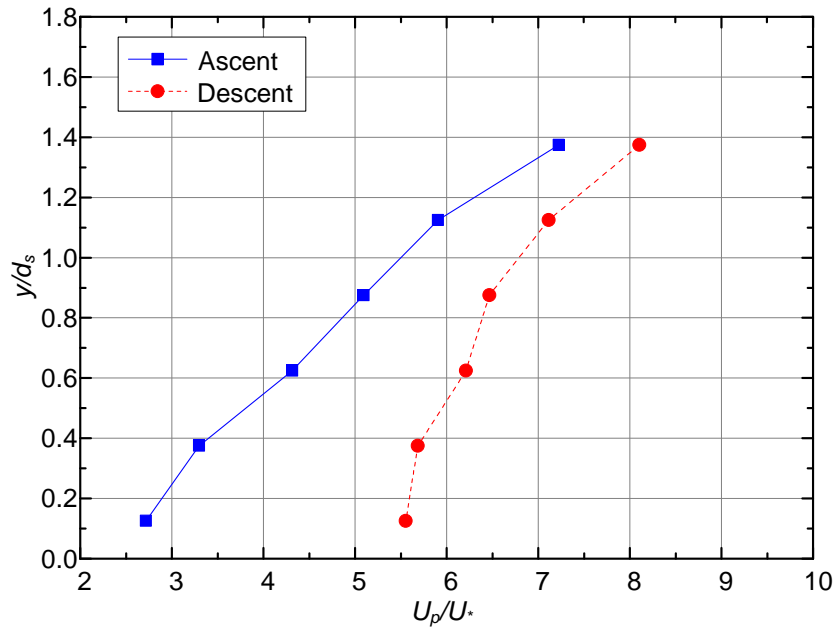


Figure 7-20. Comparison of horizontal component of particle velocity distribution for ascent motion and descent motion (flow condition: inflow rate $Q=6.8$ l/min, no seepage flow, $d=10.75$ mm)

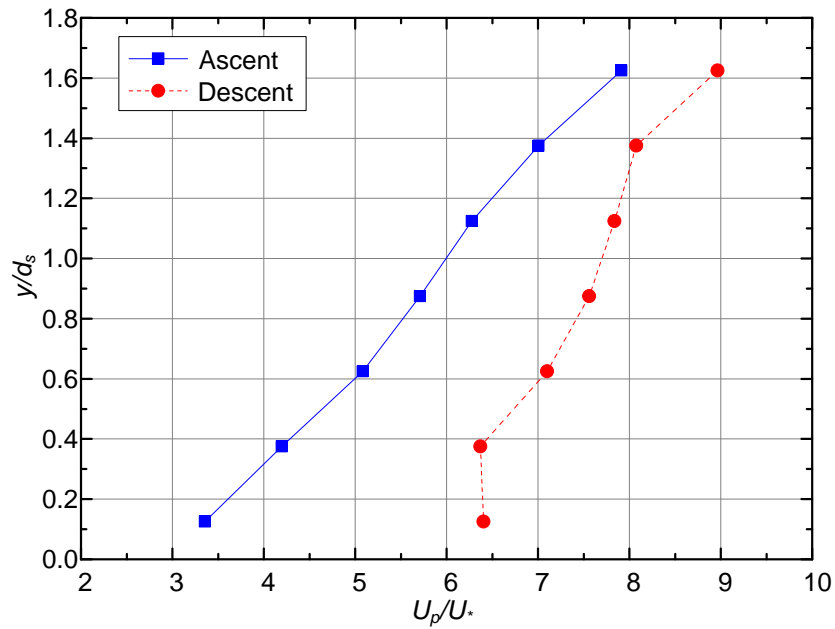


Figure 7-21. Comparison of horizontal component of particle velocity distribution for ascent motion and descent motion (flow condition: inflow rate $Q=6.8$ l/min, seepage outflow rate $Q_I=0.34$ l/min, $d=9.75$ mm)

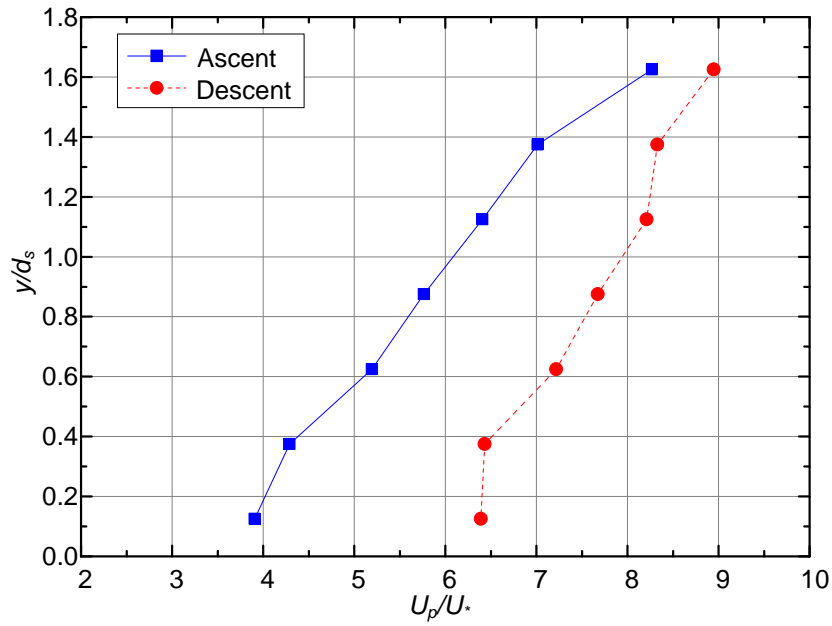


Figure 7-22. Comparison of horizontal component of particle velocity distribution for ascent motion and descent motion (flow condition: inflow rate $Q=6.8$ l/min, seepage outflow rate $Q_I=0.45$ l/min, $d=9.25$ mm)

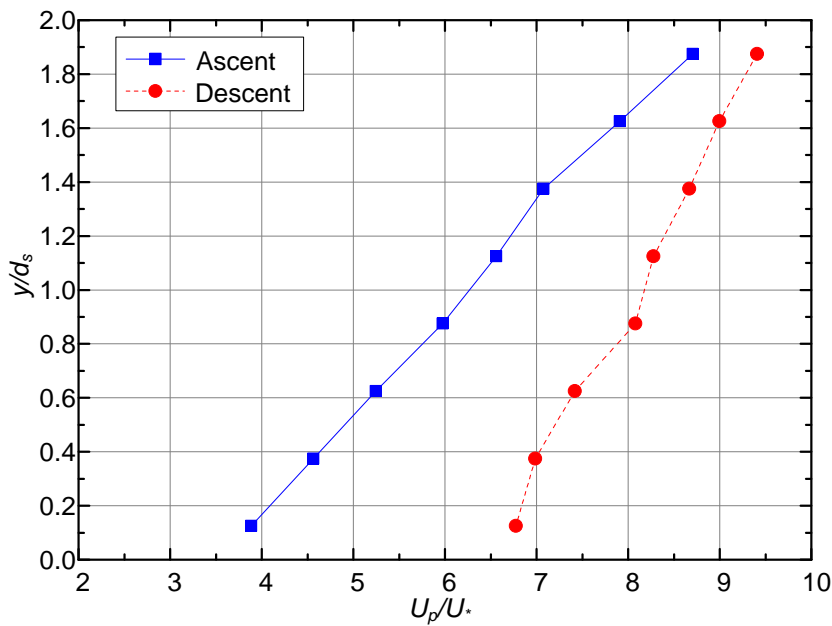


Figure 7-23. Comparison of horizontal component of particle velocity distribution for ascent motion and descent motion (flow condition: inflow rate $Q=6.8$ l/min, seepage outflow rate $Q_I=0.68$ l/min, $d=8.75$ mm)

7.3.6 The mean vertical component of particle velocity distribution in ascent and descent motion

We also take $Q=6.8$ l/min with four different seepage outflow conditions (i.e. $Q_I=0$ l/min, $Q_I=0.34$ l/min, $Q_I=0.45$ l/min, $Q_I=0.68$ l/min) for example to compare the averaged vertical component of particle velocity. Figure 7-24, 7-25, 7-26 and 7-27 show that the maximum mean velocity is located near the surface of porous bed, while the minimum mean velocity appears at the top of particle motion. When the particle goes up the composition of forces (include gravitational force, buoyant force and drag force etc.) reduce the velocity in vertical direction continuously, until it reaches zero and begin to descent, and then the vertical velocity is accelerating until the particle meets the surface of porous bed after collision it shifts direction. The particle never reaches a constant terminal fall velocity during its downward motion (which equals to 0.232 m/s for 2mm glass particle settling in still water) shown in the left side of the figures means the distance between the top of particle motion and the surface of porous bed is too short to reach the terminal velocity for gravitational settling.

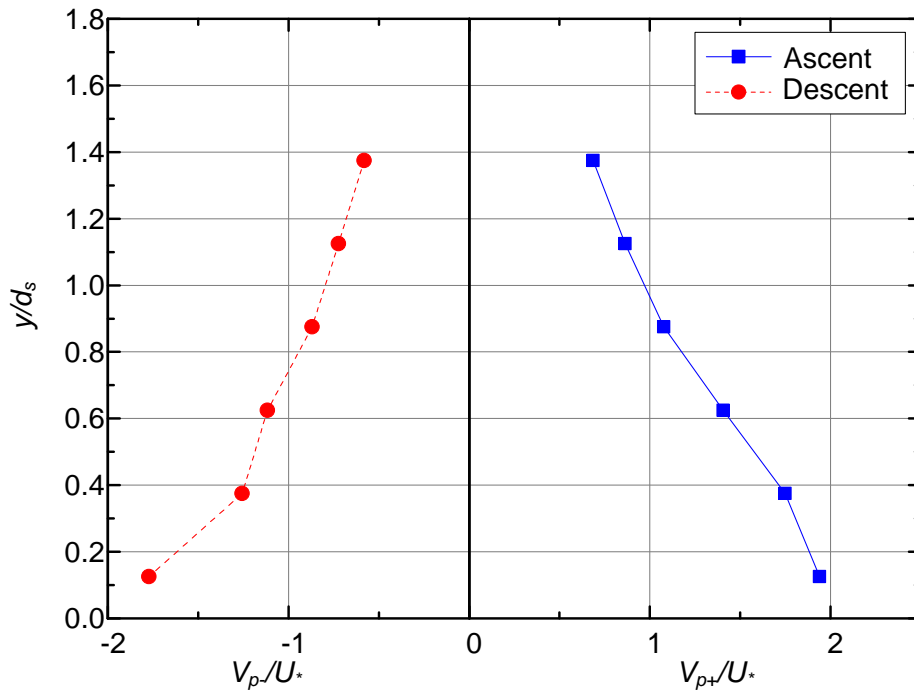


Figure 7-24. Comparison of vertical component of particle velocity distribution for ascent motion and descent motion (flow condition: inflow rate $Q=6.8$ l/min, no seepage flow, $d=10.75$ mm)

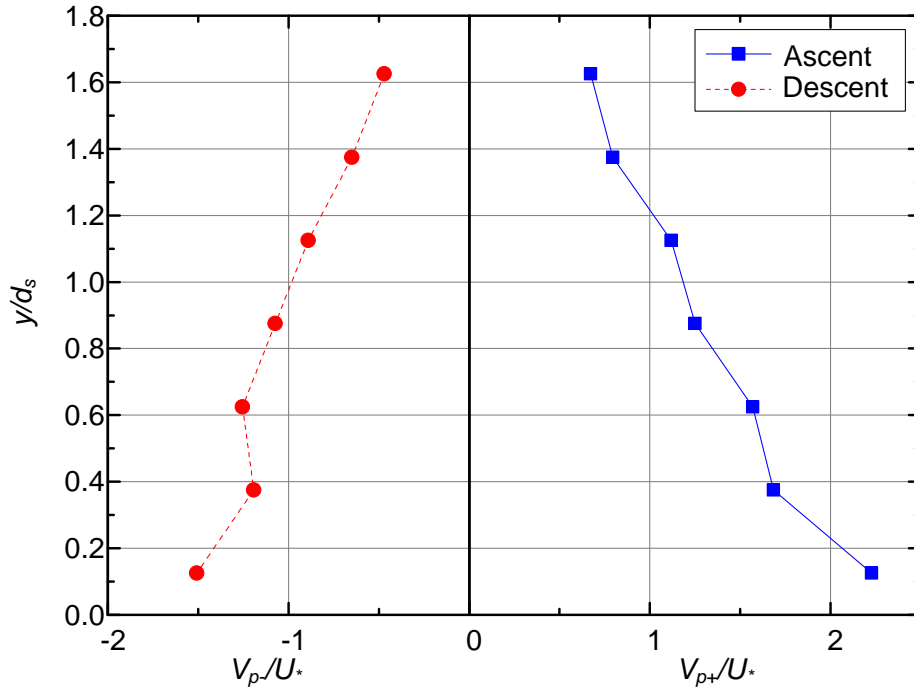


Figure 7-25. Comparison of vertical component of particle velocity distribution for ascent motion and descent motion (flow condition: inflow rate $Q=6.8$ l/min, seepage outflow rate $Q_I=0.34$ l/min, $d=9.75$ mm)

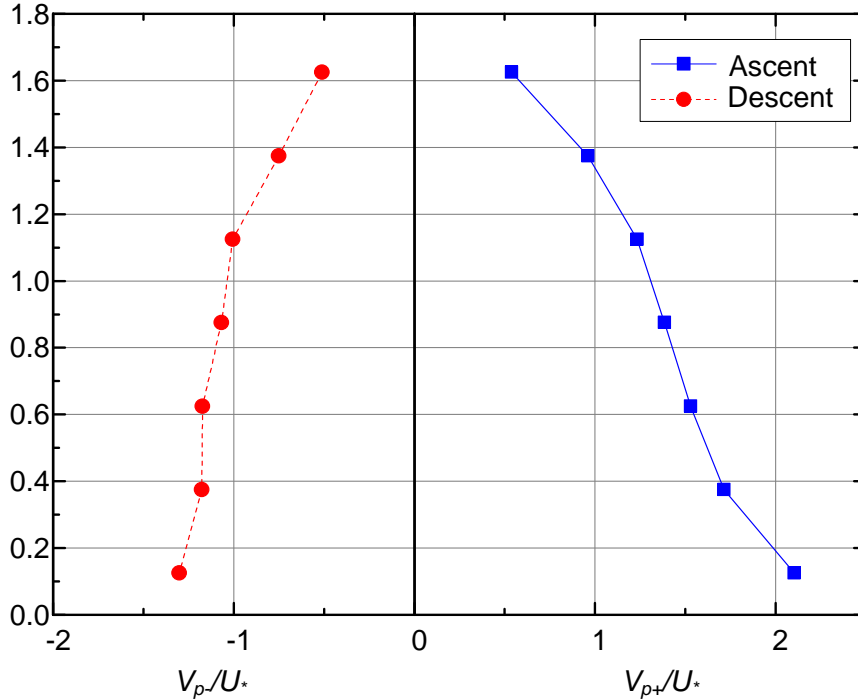


Figure 7-26. Comparison of vertical component of particle velocity distribution for ascent motion and descent motion (flow condition: inflow rate $Q=6.8$ l/min, seepage outflow rate $Q_I=0.45$ l/min, $d=9.25$ mm)

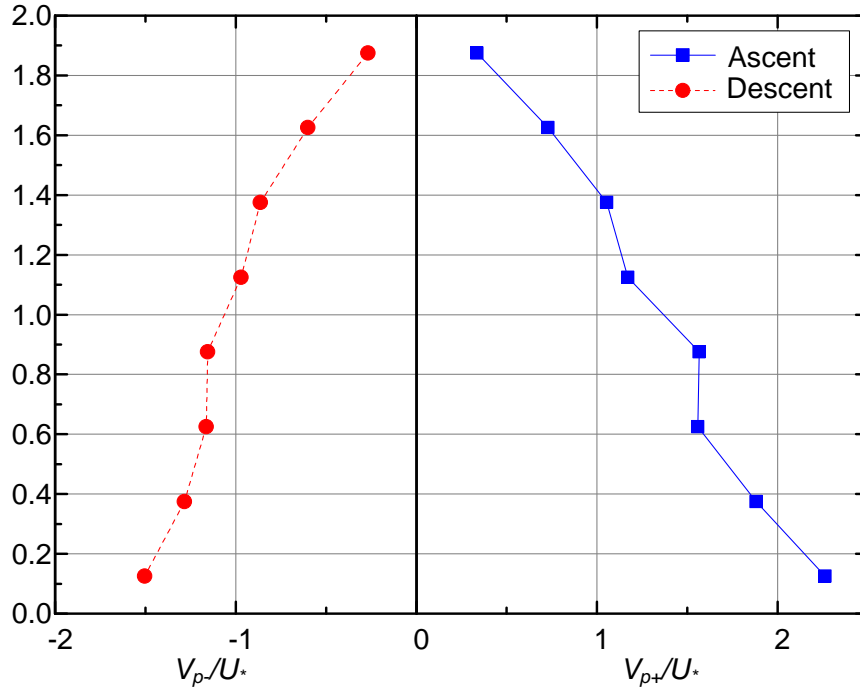


Figure 7-27. Comparison of vertical component of particle velocity distribution for ascent motion and descent motion (flow condition: inflow rate $Q=6.8$ l/min, seepage outflow rate $Q_I=0.68$ l/min, $d=8.75$ mm)

From these figures we can also find that at the bottom sub-zone the magnitude of mean vertical velocity in descent motion is smaller than that in ascent motion, while at the other sub-zones the vertical velocity component is almost the same in the ascent motion as in the descent motion. To explain this phenomenon, we look at the example of variations processes of particle velocity and kinetic energy along saltation trajectory plotted in figure 7-19. we can deduce during the collision of the particle and the porous bed surface, the particle is losing its horizontal component of particle velocity badly, some horizontal momentum convert into vertical momentum because of the impact angle, the kinetic energy also diminishes, but a part of the lost energy transformed to the turbulent energy which has a counteraction to the particle and enhances the particle vertical velocity after it shift direction upwards.

7.3.7 Formula for determining the velocity of particle

The results show that the horizontal average velocities of the particles neither agree with the law suggested by Einstein (1950) nor obey the law assumed by Bagnold (1973). The Einstein's law is that the particle velocity is equal to 11.6 times of shear velocity ($U_p=11.6U_*$) and the Bagnold's law assumes the velocity equals to the difference between flow velocity at corresponding water depth and settling velocity of particle ($U_p=U-w_0$).

Chapter 7: Particle Transport over a Porous Bed

Based on Bagnold's law, use ζ as the relative particle movement velocity, and ζ has a negative relative relation with particle diameter d_s and channel slope S , so ζ must have a relation with Re_p ,

$$\zeta = f(Re_p) = f\left(\frac{U_* d_s}{\nu}\right) \quad (7-3)$$

Based on the simulation results plotted in Figure 7-28, the fit curve can be given as:

$$\zeta = \frac{U_w - U_p}{w_0} = \frac{44}{Re_p} - \frac{Q_1}{Q} + 0.0734 \quad (7-4)$$

The particle transport velocity over porous bed can be written as:

$$U_p = U_w - w_0 \left(\frac{44}{Re_p} - \frac{Q_1}{Q} + 0.0734 \right) \quad (7-5)$$

where Q_1/Q present the proportion of seepage outflow rate to inflow rate. We can find that there is little influence of seepage outflow on the mean particle transport velocity. When $Re_p \approx 44$, Equation (7-5) becomes Bagnold's law; when $Re_p > 44$, $\zeta (= (U_w - U_p)/w_0) < 1$, it diminishes as Re_p increases.

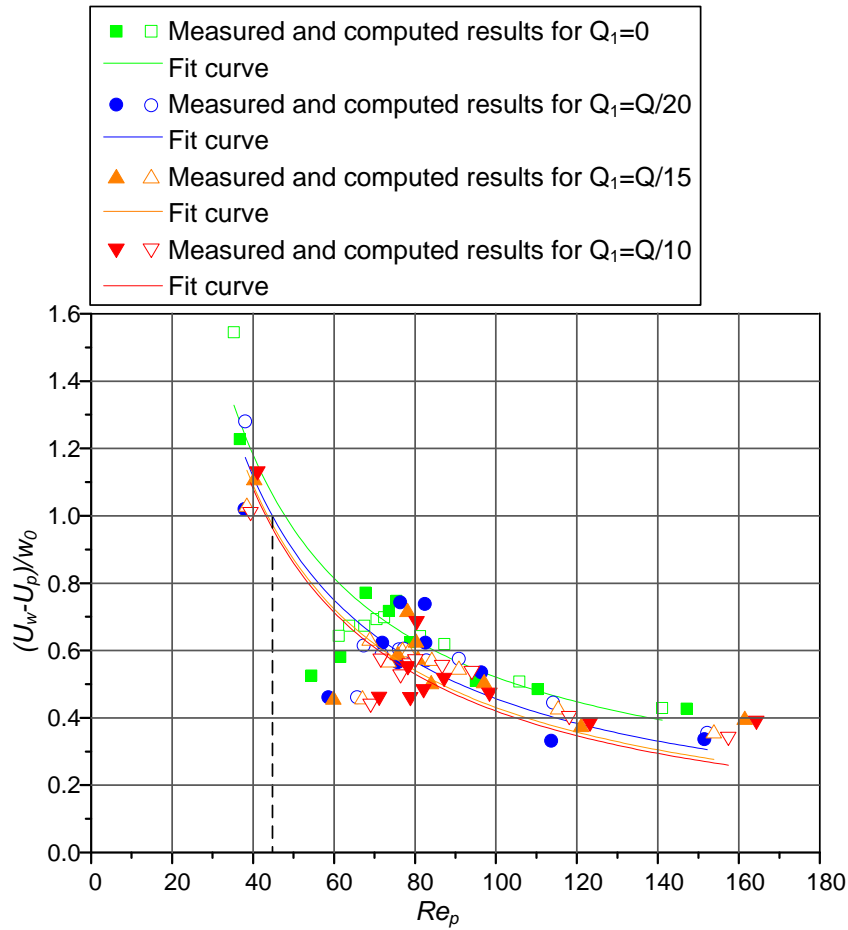


Figure 7-28. The relation between $\zeta (= (U_w - U_p)/w_0)$ and Re_p

7.4 Conclusions

Particle transport in a turbulent 3D flow in an open channel with a porous bed has been studied numerically and experimentally for channel slope S_o varied from 0.0035 to 0.0244; inflow rate Q varied from 3.2 l/min to 6.8 l/min; seepage outflow rate Q_I varied from 0 to 10% of the inflow rate Q ; and glass particle diameter d_s varied from 1 mm to 4 mm. 50 particles are added one by one 5 mm over the middle point of the porous bed surface. The characteristics of the interaction of flow over and within the porous region and the particles were simulated using a CFD-DEM approach, while turbulence flow parameters over the permeable region were measured with PIV system, and particle velocities were measured with high speed camera.

The following conclusions can be derived:

1. The statistical results demonstrate that average horizontal component of the particle velocity follows a Gaussian distribution for each case. The average particle velocity increase with increasing angle of inclination, inflow rate and seepage flow rate but there is not a positive correlation between the particle velocity and size.
2. The movement of particles in horizontal direction is mainly controlled by flow. Within the same flow depth, the normalized horizontal component of particle velocity increases with increasing inflow rate and channel slope; generally increases with the particle size diminishing. With larger inflow rate and channel slope the particle can move higher. The particle velocity near the surface of porous bed for is generally increasing for seepage outflow rate increasing, this trend agrees with the variation of flow velocity.
3. The mean horizontal component of particle velocity in ascent motion or in descent motion increases with the particle height. The mean horizontal component of particle velocity in ascent motion is smaller than that in descent motion. This is because within the same level of flow depth, the particle ascent from a lower position has the smaller horizontal velocity component than the particle descent from a higher position.
4. Because the distance between the top of particle motion and the surface of porous bed is too short, the particle vertical velocity is accelerating until the particle meets the surface of porous bed and never reaches a constant terminal fall velocity during its downward motion in our range of experiments.
5. There is little influence of seepage outflow on the particle transport velocity. The particle transport velocity over porous bed can be written with a new formula as:

Chapter 7: Particle Transport over a Porous Bed

$$U_p = U_w - w_0 \left(\frac{44}{Re_p} - \frac{Q_1}{Q} + 0.0734 \right)$$

When $Re_p \approx 44$, the formula becomes Bagnold's law; when $Re_p > 44$, $\zeta (= (U_w - U_p)/w_0) < 1$, it diminishes as Re_p increases.

Chapter 8

Sediment Clogging Phenomenon in an Open Channel with a Porous Bed

8.1 Introduction

Sometimes the sediment transport capacity of the flow is limited, the sediment transported by fluid will deposit and some of the small particles attempt to percolate through the porous medium. If the size or concentration of small percolating particles is large enough, clogging of pores can occur which can modify the permeability of the crossed medium. Although the transport of small spherical particles through packings of larger spheres in vertical system has already been studied both experimentally and numerically, the literatures on studies of sediment clogging phenomenon of porous bed in an open channel with seepage outflow is hard to find.

In this chapter we try to look into some aspects of the sediment transport in an open channel and clogging phenomenon of the porous bed within the channel, it will be studied experimentally.

8.1.1 Experimental setup

The experimental apparatus used to study the behavior of individual particles in chapter 6, and is modified slightly to allow for weighting small particles transported run over the porous bed. Figure 8-1 is a schematic of this experimental setup.

Chapter 8: Sediment Clogging Phenomenon in an Open Channel with a Porous Bed

A particle adding device is placed at the upstream of the porous bed allowing the particles to be added into the flow. A particle collection device is placed after the outflow of the channel allowing the particles to be separated from the water via gravitational settling. An electronic balance placed under the particle collection device records the weight of sediment transported by flow arrive at the end of the channel.

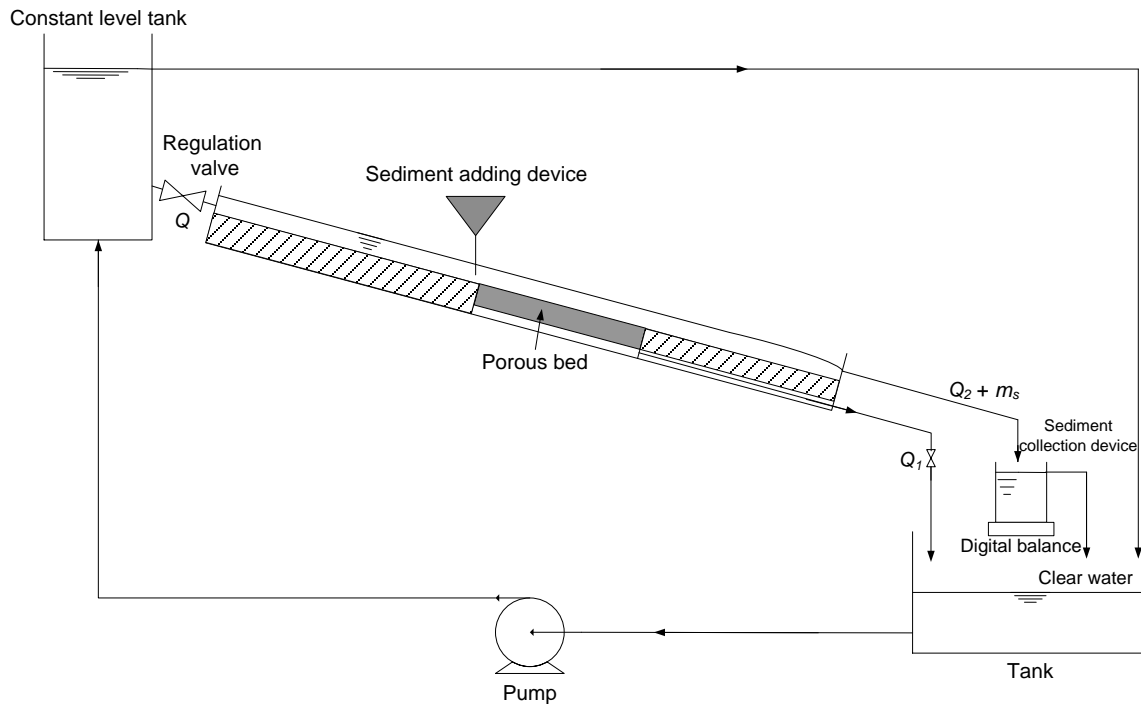


Figure 8-1. Schematic of experimental setup

8.1.2 Process of the experiment

1. Installing and setting the instrument

Install electronic balance and connect it with the computer, open the software for recording weight.

2. Adjust the slope of channel

A motor is used to adjust the slope of channel to the conditions relevant to the experiment to be carried out.

3. Turn on the pump and adjust flow rate

Chapter 8: Sediment Clogging Phenomenon in an Open Channel with a Porous Bed

Turn on the pump and fill constant level tank with water, open the regulation valve and electronic balance to adjust the inflow rate and the seepage outflow rate to the conditions relevant to the experiment to be carried out.

4. Measure the flow depth

After the flow is steady, measure the flow depth over the porous bed with ruler.

5. Add glass sediment and measure weight changing

Use the particle adding device adding 50 g glass sediment in a constant rate of 1 g/s, just over the start part of porous bed (201 mm long). Measure the mass changing of particle collection device with electronic balance until the weight is not changing.

6. Collect the sediment clogged in the porous bed

After the weight of particle collection device get into constant, close the regulation valve and the pump. Wash the porous medium and collect the sediment clogged in it. Dry the sediment and measure its weight.

7. Change parameters

Change the parameters, including channel slope, inflow rate, seepage outflow rate and sediment diameter, etc., and repeat the steps 1 - 6.

8.2 Parameters of the study

Table 8-1 presents the parameters used in this work. Four parameters have been changed in our research as: channel slope, inflow rate, seepage outflow rate, and particle diameter. The porosity of the porous bed remains fixed to the value of 0.476 for all experiments.

1. Channel slope S_o varied from 0.0035 to 0.0244 (Angle of channel θ varied from 0.2° to 1.4°).
2. Inflow rate Q varied from 3.2 l/min to 6.8 l/min.
3. Seepage outflow rate Q_I varied from 0 to 10% of the inflow rate Q .
4. Particle diameter d_s varied from 630 μm to 1250 μm .

Table 8-1. Parameters used in the sensitivity analysis

Case	Slope S_o	Inflow rate Q (l/min)	Seepage outflow rate Q_I (l/min)	Sediment diameter d_s (μm)
1	0.0035	6.00	0	630-800
2		6.00	0.30	630-800
3		6.00	0.40	630-800
4		6.00	0.60	630-800
5	0.0105	6.00	0	630-800
6		6.00	0.30	630-800
7		6.00	0.40	630-800
8		6.00	0.60	630-800
9	0.0175	6.00	0	630-800
10		6.00	0.30	630-800
11		6.00	0.40	630-800
12		6.00	0.60	630-800
13	0.0244	6.00	0	630-800
14		6.00	0.30	630-800
15		6.00	0.40	630-800
16		6.00	0.60	630-800
17	0.0105	3.20	0	630-800
18		3.20	0.16	630-800
19		3.20	0.21	630-800
20		3.20	0.32	630-800
21	0.0105	4.50	0	630-800
22		4.50	0.23	630-800
23		4.50	0.30	630-800
24		4.50	0.45	630-800
25	0.0105	6.80	0	630-800
26		6.80	0.34	630-800
27		6.80	0.45	630-800
28		6.80	0.68	630-800
29	0.0105	6.00	0	1000-1250
30		6.00	0.30	1000-1250
31		6.00	0.40	1000-1250
32		6.00	0.60	1000-1250

8.3 Results and analysis

8.3.1 Sediment clogging

The experimental results of the clogging of pores, including mass of clogged sediment trapped inside the porous bed (which can be got from wash the sediment out of porous bed, dry and measure it), the ratio of volume of trapped sediment to volume of pores for each case and the

Chapter 8: Sediment Clogging Phenomenon in an Open Channel with a Porous Bed

porosity of porous bed after clogging of pores are shown in Table 8-2. The corresponding hydrodynamic characteristics of each case have been shown in Table 5-2 of chapter 5.

Table 8-2. The experimental results of the clogging of pores

Case	Weight of sediment trapped inside the porous bed (g)	V_s/V_p	porosity of porous bed after clogging	Case	Weight of sediment trapped inside the porous bed (g)	V_s/V_p	porosity of porous bed after clogging
1	9.95	0.154	0.403	17	10.89	0.168	0.396
2	10.75	0.166	0.397	18	12.02	0.185	0.388
3	10.86	0.168	0.396	19	12.05	0.186	0.388
4	10.98	0.170	0.396	20	12.92	0.200	0.381
5	7.57	0.117	0.421	21	10.12	0.157	0.402
6	9.21	0.142	0.409	22	11.05	0.171	0.395
7	9.45	0.146	0.407	23	11.14	0.172	0.394
8	9.81	0.151	0.404	24	11.67	0.181	0.390
9	7.31	0.113	0.423	25	7.16	0.111	0.424
10	9.09	0.141	0.409	26	9.08	0.140	0.409
11	9.00	0.139	0.410	27	9.14	0.141	0.409
12	9.32	0.144	0.408	28	9.46	0.146	0.407
13	7.16	0.111	0.424	29	5.92	0.092	0.433
14	9.08	0.140	0.409	30	6.42	0.099	0.429
15	9.00	0.139	0.410	31	6.45	0.100	0.429
16	9.18	0.142	0.409	32	6.77	0.105	0.427

V_s/V_p : the ratio of volume of trapped sediment to volume of pores.

Measurements in the above table shows that although the clogged sediment in porous bed changes not too much from case to case, it generally decreases with increasing channel angle, inflow rate and sediment diameter, but the clogged sediment increases with increasing seepage outflow rate. The maximum mass of sediment clogged in porous bed appears at case 20, which has an inflow rate of 3.2 l/min and seepage outflow rate of 0.32 l/min, and the volume of clogged sediment is about 20% of the volume of pores, which causes the porosity of the porous bed has decreased to 0.381.

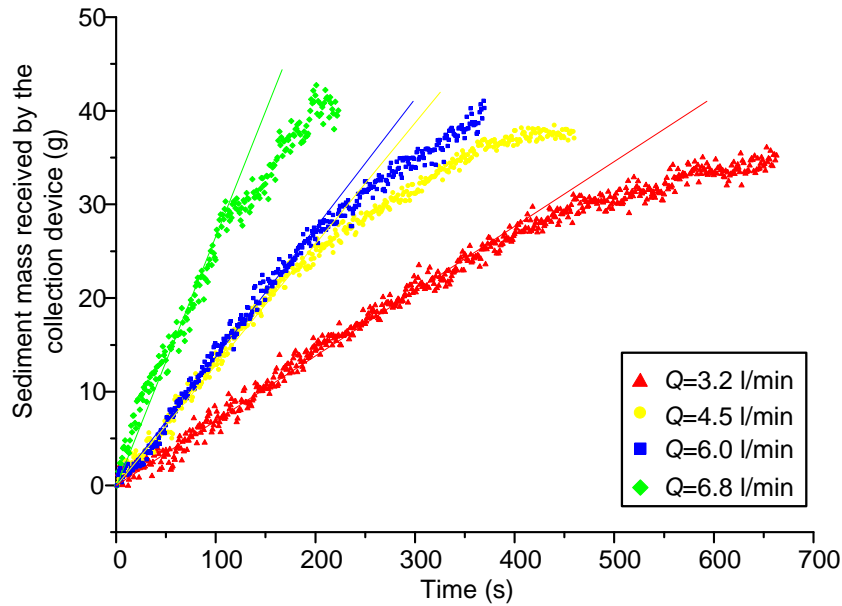
8.3.2 Sediment transport rate over porous bed

8.3.2.1 Influence of inflow rate

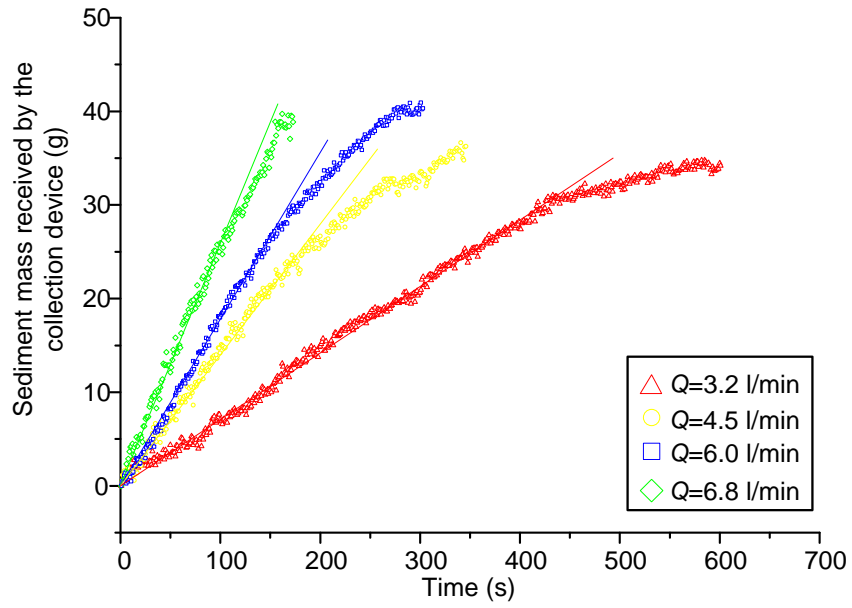
The sediment transported by open channel flow over the porous bed was received by the sediment collection device. The electronic balance placed under the collection device is used to record the mass of sediment be collected. The results are presented as a function of time and $t=0$ corresponds to the moment of the first sediment arrive to the collection device.

The influence of inflow rate on sediment mass received by the collection device as a function of time is shown in Figure 8-2. The accumulation of sediment in the collection device which placed after the flume demonstrates the sediment transported by open channel flow over the porous bed without clogging. And the mass sediment transport rates can be got from these measurements, they are presented in Figure 8-3.

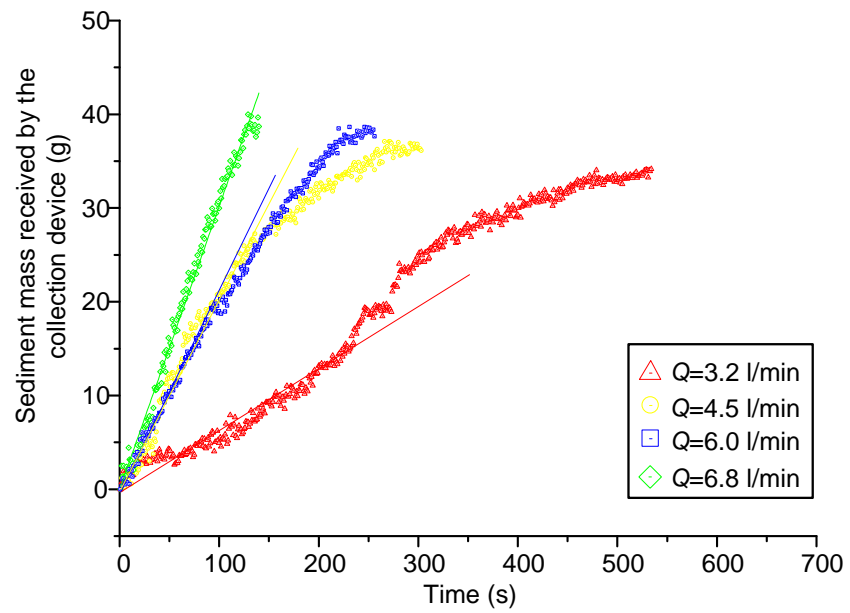
From Figure 8-2 we can also find that with a bigger flow rate more sediment could be transported to the end of the channel, so less sediment would be captured by porous bed. Figure 8-3 shows that with larger inflow rate, the sediment transport rate over the porous bed is larger. This agrees with the results single particle transport velocity studied in Chapter 6.



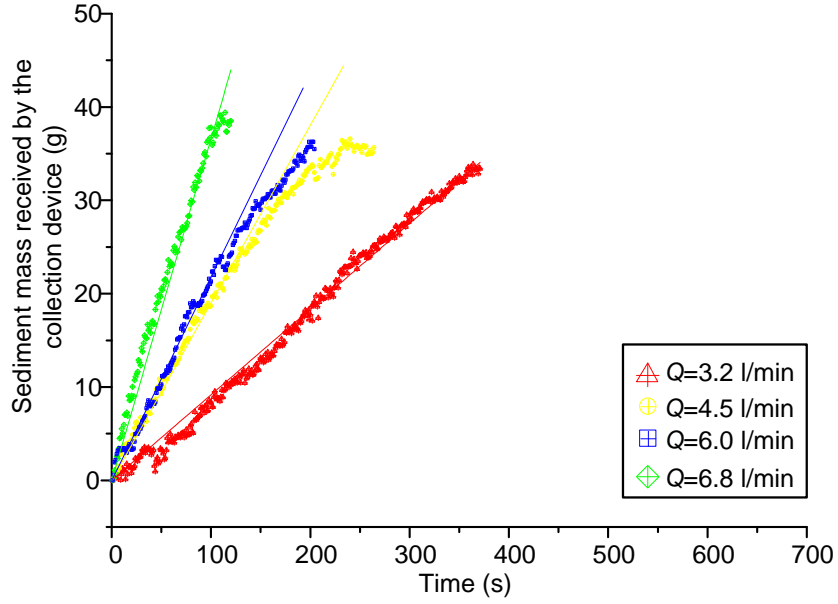
(a)



(b)



(c)



(d)

Figure 8-2. Influence of inflow rate on sediment mass received by the collection device as a function of time (channel slope $S_o=0.0105$). (a) without seepage outflow; (b) seepage outflow rate $Q_I=Q/20$; (c) seepage outflow rate $Q_I=Q/15$; and (d) seepage outflow rate $Q_I=Q/10$

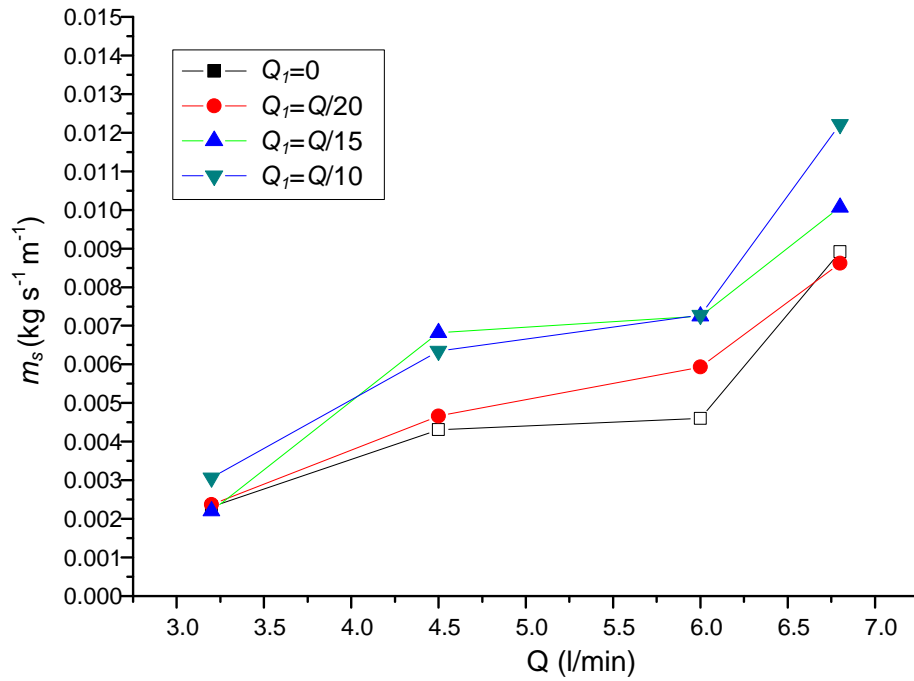
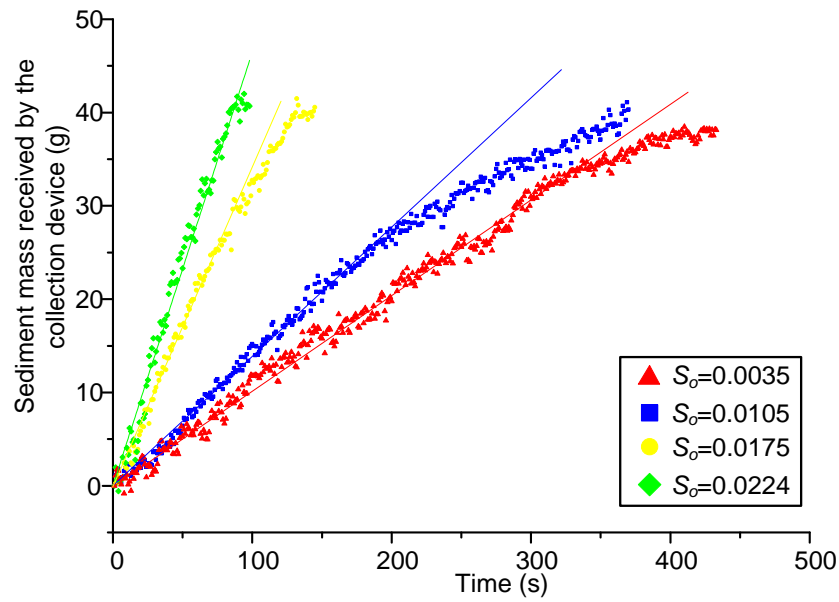


Figure 8-3. Influence of inflow rate on the mass sediment transport rate per unit width

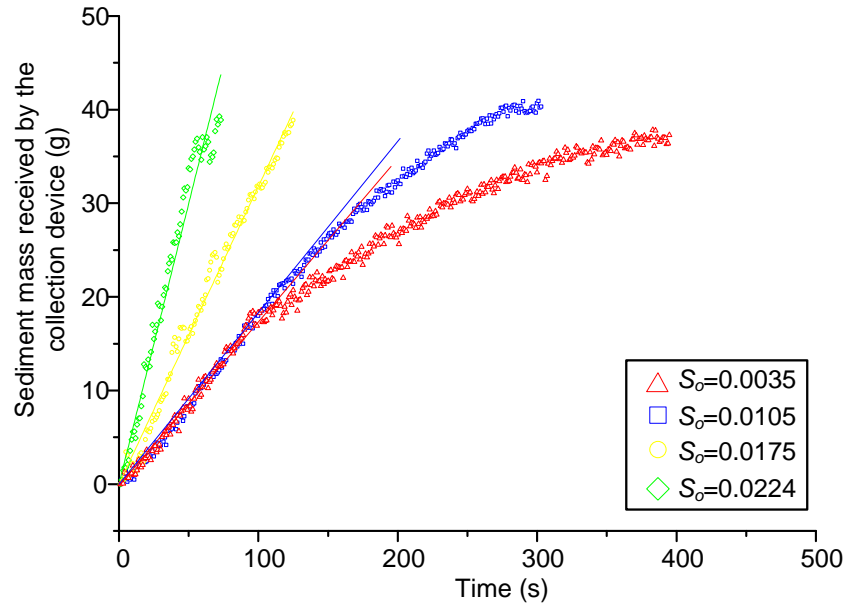
8.3.2.2 Influence of channel slope

The influence of channel slope on sediment mass received by the collection device as a function of time is shown in Figure 8-4. And the mass sediment transport rates with different channel slopes are presented in Figure 8-5.

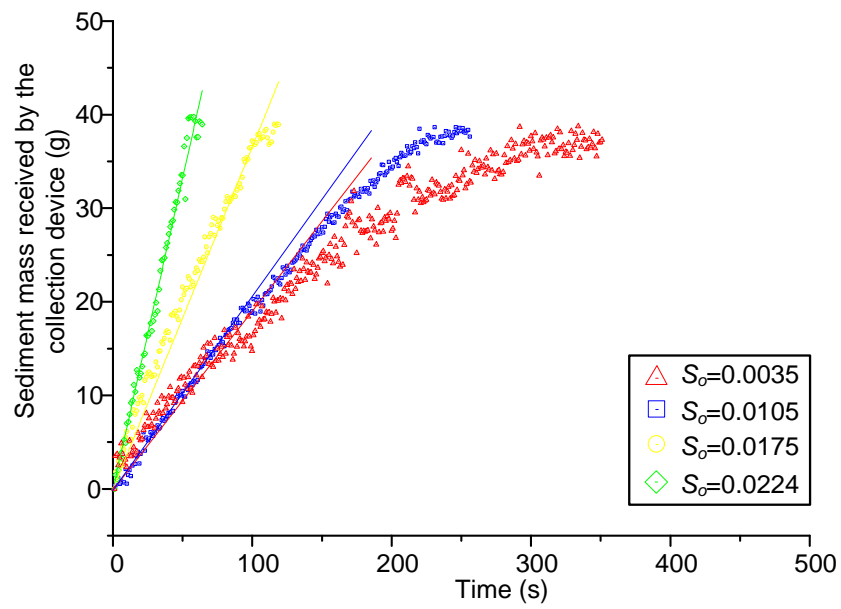
From Figure 8-4 we can also find that with a bigger channel slope more sediment could be transported to the end of the channel, so less sediment would be captured by porous bed. Figure 8-5 shows that with larger channel slope, the sediment transport rate over the porous bed is larger. This agrees with the results single particle transport velocity studied in Chapter 6.



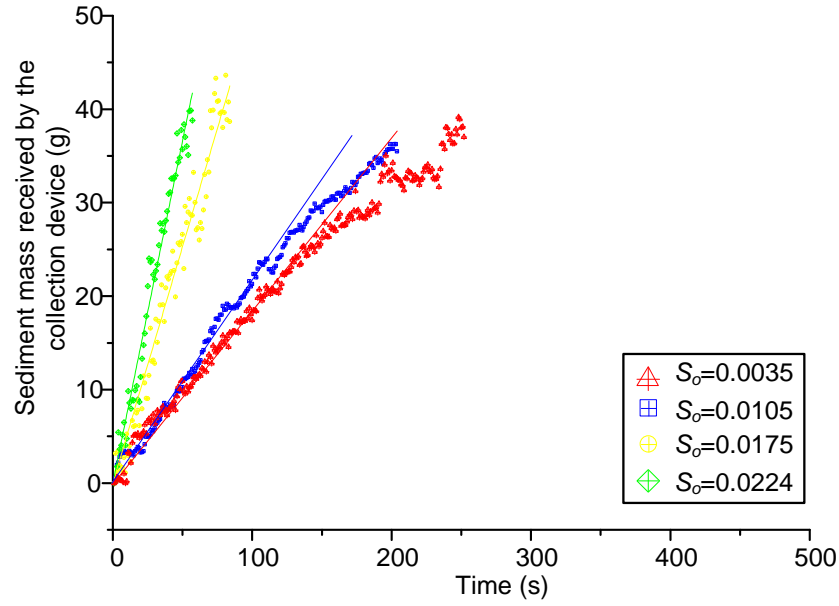
(a)



(b)



(c)



(d)

Figure 8-4. Influence of channel slope on sediment mass received by the collection device as a function of time (inflow rate $Q=6$ l/min). (a) without seepage outflow; (b) seepage outflow rate $Q_i=0.30$ l/min; (c) seepage outflow rate $Q_i=0.4$ l/min; and (d) seepage outflow rate $Q_i=0.6$ l/min

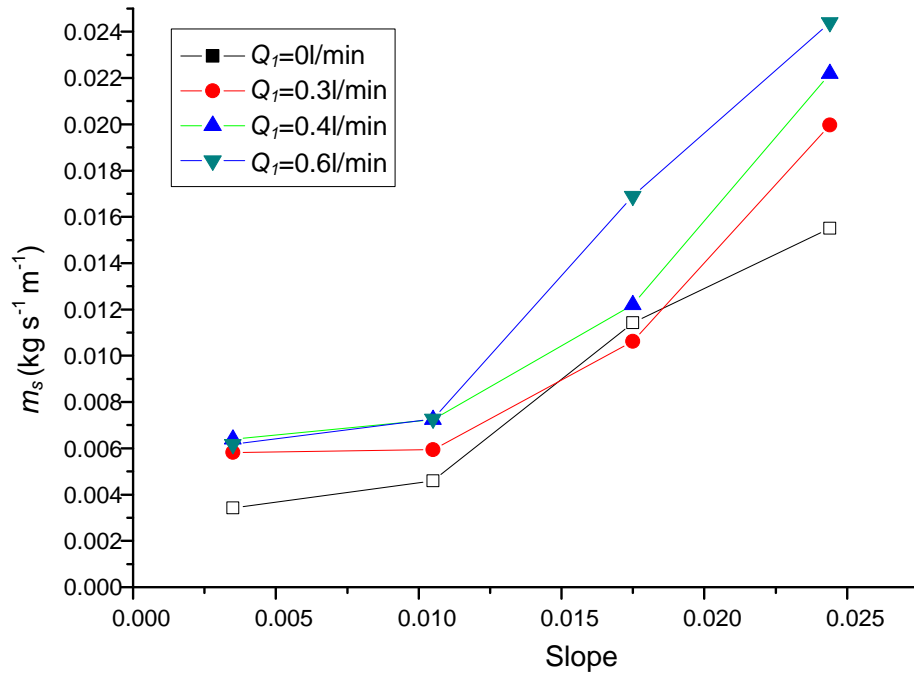
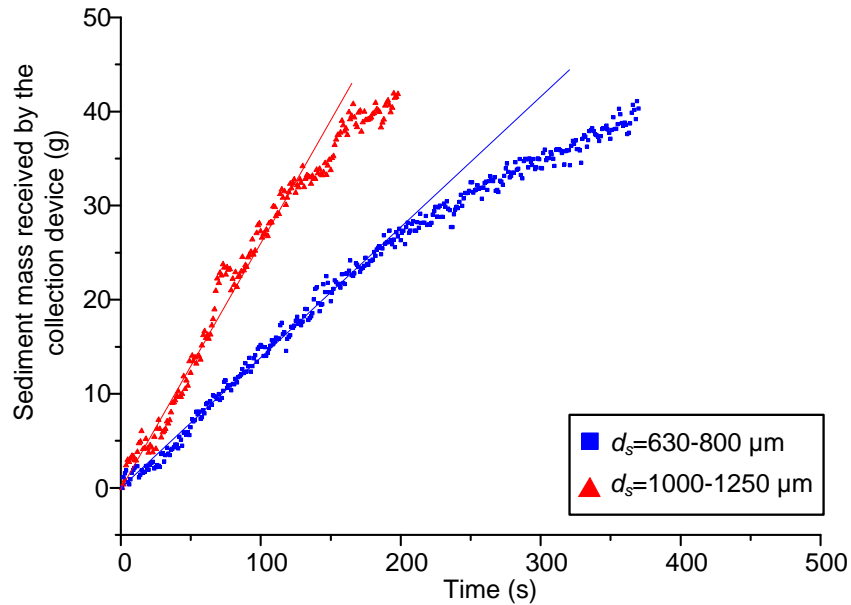


Figure 8-5. Influence of channel slope on the mass sediment transport rate per unit width

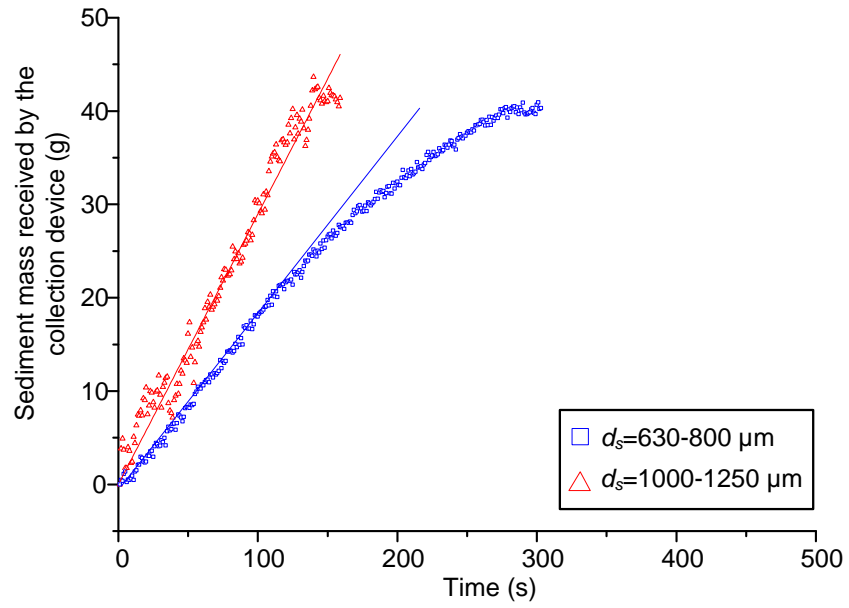
8.3.2.3 Influence of particle diameter

The influence of inflow rate on sediment mass received by the collection device as a function of time is shown in Figure 8-6. And the mass sediment transport rates with different sediment size are presented in Table 8-3.

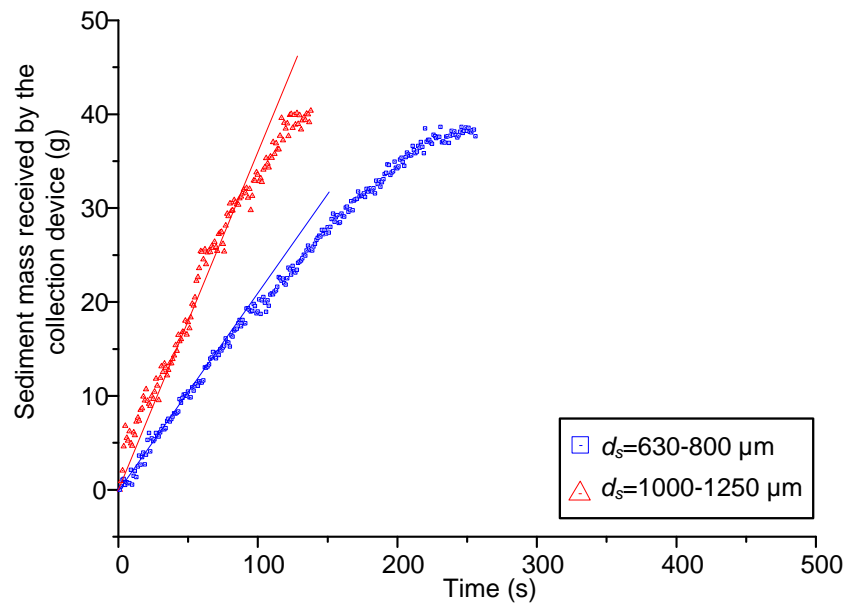
Table 8-3 shows that within the range of sediment sizes used in our experiments, with larger sediment size, the sediment transport rate over the porous bed is larger. This agrees with the results single particle transport velocity studied in Chapter 6. From Figure 8-6 we can also find that with a bigger size more sediment could be transported to the end of the channel, so less sediment would be captured by porous bed. The reason why bigger size sediment could have a larger transport rate in the same flow condition in our experiment is because the particle diameter assembling the porous bed is 3 mm, but the small sediment used in the experiment has a diameter of 630-800 μm , after the initial sediment above the porous bed have been taken away by flow, the big particle of the porous bed will act as an armor preventing further transport of sediment, and this effect is much greater with smaller sediment size.



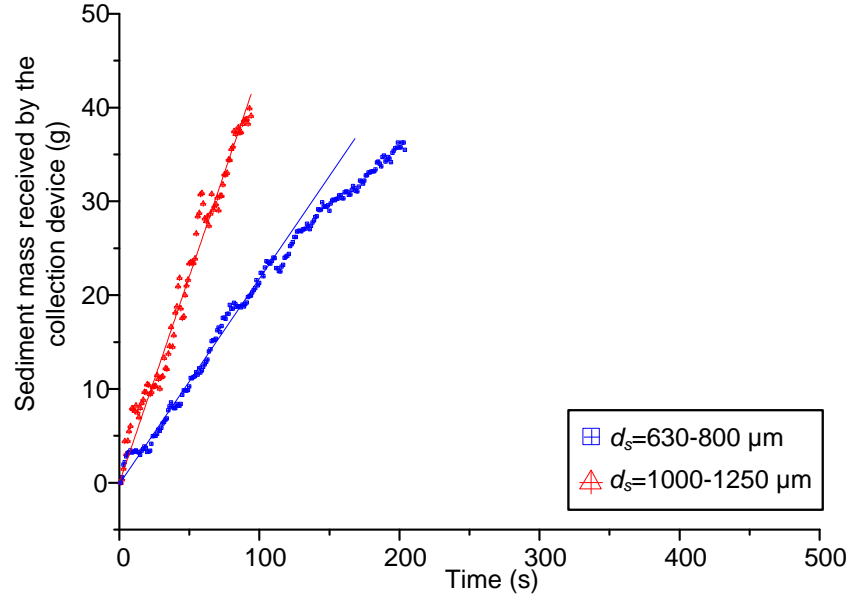
(a)



(b)



(c)



(d)

Figure 8-6. Influence of sediment diameter on sediment mass received by the collection device as a function of time (inflow rate $Q=6$ l/min, channel slope $S_o=0.015$). (a) without seepage outflow; (b) seepage outflow rate $Q_I=0.30$ l/min; (c) seepage outflow rate $Q_I=0.4$ l/min; and (d) seepage outflow rate $Q_I=0.6$ l/min

Table 8-3. Influence of sediment diameter on the mass sediment transport rate per unit width

Sediment diameter d_s (μm)	Transport rate without seepage outflow (kg s ⁻¹ m ⁻¹)	Transport rate with seepage outflow $Q_I=0.3$ l/min (kg s ⁻¹ m ⁻¹)	Transport rate with seepage outflow $Q_I=0.4$ l/min (kg s ⁻¹ m ⁻¹)	Transport rate with seepage outflow $Q_I=0.6$ l/min (kg s ⁻¹ m ⁻¹)
630-800	0.0046	0.0059	0.0072	0.0073
1000-1250	0.0087	0.0097	0.0120	0.0147

8.3.2.4 Influence of seepage outflow rate

From the figures 8-2 to 8-6 and Table 8-3, we can also find that with larger seepage outflow rate the mass sediment transport rate would be larger, but more sediment might be captured by porous bed. The reason might be the increasing seepage flow rate causes more sediment get inside the porous bed with seepage flow, and the increasing seepage outflow rate also makes sediment at the bed surface more easily to start moving (analyzed in Chapter 5), that could keeps passages at the

superficial of porous bed clean, and allows more sediment get into the deeper part of porous medium.

8.3.2.5 Empirical bed-load transport relation

The bed-load transport rate has been predicted by many researchers. The correlation of Meyer-Peter (1949) is considered most appropriate for wide channels and coarse material. Equation by Meyer-Peter (1949) can be written as:

$$\frac{q_s}{\sqrt{(s-1)gd_s^3}} = \left(\frac{4\tau_0}{\rho(s-1)gd_s} - 0.188 \right)^{3/2} \quad (8-1)$$

where q_s is the volumetric sediment flow rate per unit width; ρ is the fluid density, τ_0 is shear stress: $\tau_0 = U_* \rho$, s is relative density of sediment: $s = \rho_s / \rho$, d_s is the sediment diameter.

The Einstein's (1950) bed-load equation is derived from the concept of probabilities of particle motion:

$$1 - \frac{1}{\sqrt{\pi}} \int_{-B_* \Psi_* - 1/\eta_0}^{+B_* \Psi_* - 1/\eta_0} e^{-t^2} dt = \frac{A_* \Phi_*}{1 + A_* \Phi_*} \quad (8-2)$$

where A_* , B_* , and η_0 are universal constants to be determined from experiment data; t is only a variable of integration; Ψ_* , Φ_* are flow intensity and bed-load transport intensity, respectively. With uniform grain size, they are as:

$$\Psi_* = \frac{\rho(s-1)gd_s}{\tau_0} \quad (8-3)$$

$$\Phi_* = \frac{q_s}{\sqrt{(s-1)gd_s^3}} \quad (8-4)$$

Both the Meyer-Peter and Einstein correlations give close results. These two bed-load equations are widely used. Our experimental results of sediment transport rate after dimensionless transformation are presented in Figure 8-7 to compare with the equations of Meyer-Peter (1949) and Einstein (1950).

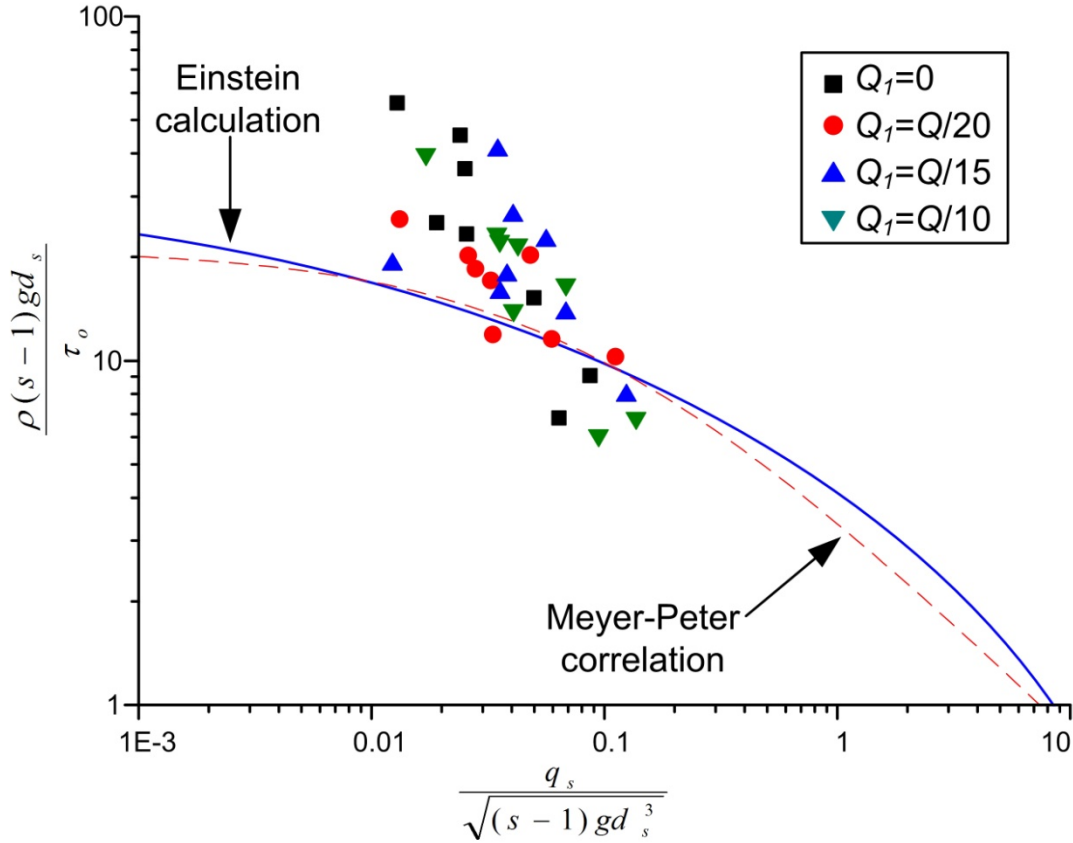


Figure 8-7. Sediment transport rate: comparison between Meyer-Peter formula, Einstein calculation and our laboratory data (Meyer-Peter *et al.*, 1934; Chien, 1954)

From this figure we can find that a large number of our experimental points are concentrated near the empirical curves whereas others scatter rather widely. This may be caused by flow conditions are different, their empirical equations were got based on the experiments have been done over a bed composed mainly of unconsolidated sand with large flow depth, while ours is opposite, we use fixed porous bed and small flow depth, as our main interest is to study surface runoff in the urban area.

8.4 Conclusions

Sediment transport and clogging phenomenon in a turbulent flow in an open channel with a porous bed has been studied experimentally for channel slope S_o varied from 0.0035 to 0.0244; inflow rate Q varied from 3.2 l/min to 6.8 l/min; seepage outflow rate Q_1 varied from 0 to 10% of the inflow rate Q ; and particle diameter d_s varied from 630 μm to 1250 μm . Total 50 g glass

Chapter 8: Sediment Clogging Phenomenon in an Open Channel with a Porous Bed

sediment is added at the start part of the porous bed (201 mm long) in a constant rate of 1 g/s using the particle adding device.

The following conclusions can be derived:

1. The mass of sediment clogged in the porous bed generally decreases with increasing channel angle, inflow rate and sediment diameter, but the clogging risk increases with increasing seepage outflow rate.
2. Greater sediment transport rate over the porous bed is observed if the channel angle, inflow rate, sediment diameter or seepage outflow rate is larger.
3. Our experiment results have been compared with Meyer-Peter and Einstein correlations. Most of the scatters are concentrated near the empirical curves, but the deviation from these empirical could be important because of the flow conditions are different compared with theirs.

Chapter 9

General Conclusions

In this study, experiment and numerical researches have been carried out to study multiphase flow in urban area. A series laboratory experiments were designed with PIV system and high speed camera. A numerical method has been conducted with the CFD-DEM coupling method. A comparison with the experimental data available in the literature validates this numerical tool. Both experimental and numerical methods were used to investigate the characteristics of open channel flow over a porous bed, particle transport, incipient motion, and clogging phenomenon in this kind of flow.

9.1 Free surface flow over a porous bed in an open channel

A turbulent 3D free surface flow in an open channel with a porous bed has been studied numerically and experimentally for channel slope S_o varied from 0.0035 to 0.0244; inflow rate Q varied from 3.2 l/min to 6.8 l/min; and seepage outflow rate Q_f varied from 0 to 10% of the inflow rate Q . The characteristics of the interaction of flow over and within the porous region were simulated using a CFD-DEM approach, while in the experiments the turbulence flow parameters over the permeable region were measured with PIV system.

The following conclusions can be derived:

4. The average flow velocity within the free-fluid region increases with increasing angle of inclination, inflow rate and seepage outflow rate; simultaneously, the flow depth

Chapter 9: General Conclusions

increases with increasing inflow rate and it decreases with increasing angle of inclination and seepage outflow rate.

5. In the range of our experiments, the friction factor f decreases as inflow rate Q , slope S_o , seepage outflow rate Q_I , and Reynolds number Re increase. In most of our cases the friction factors are smaller than that of the flow with rough surface.
6. The k^+ distribution in the free flow region is more uniform than empirical relationship for flow over impermeable beds developed by Nezu and Nakagawa (1993), $k^+ = 4.78 \exp(-2y/d)$. This is due to the penetration of turbulence to the upper part of porous region in significant levels. The empirical relationship for k^+ above the porous region in the range of these simulations is as:

$$k^+ = 2.97e^{(-2y/d)}$$

9.2 Particle incipient motion over a porous bed

The particle incipient motion over a porous bed has been studied both experimentally and numerically for channel slope S_o varied from 0.0035 to 0.0244; particle diameter d_s varied from 1 mm to 4 mm; with or without seepage outflow rate Q_I . Based on the range of inflow rate and channel slope, the Reynolds number for each particle incipient motion test ranges from 100 to 8900. 100 pieces glass particles are placed over the surface of porous bed. The probability of incipient motion is determined by counting the number of the particles leaving their original position and the transport starts to occur. The particle incipient motion over a porous bed has been studied numerically using a CFD-DEM coupling method, and has also been studied experimentally with high speed camera. The main conclusions are:

6. The numerical simulated results correspond well with measured results.
7. In the range of tested Reynolds number, a larger percentage of particle incipient motion can be observed when the channel slope is increased.
8. A larger percentage of particle incipient motion can be observed when the particle diameter is increased from 1mm to 2mm, but fewer particles got an incipient motion when particle diameter is increased from 2mm to 4mm.
9. More incipient motion occurs with a seepage outflow rate than without outflow rate.
10. Little influence of channel slope and particle diameter on the critical mean flow velocity. The Shields number is diminishing with the increasing particle diameter.

9.3 Particle transport over a porous bed

Particle transport in a turbulent 3D flow in an open channel with a porous bed has been studied numerically and experimentally for channel slope S_o varied from 0.0035 to 0.0244; inflow rate Q varied from 3.2 l/min to 6.8 l/min; seepage outflow rate Q_I varied from 0 to 10% of the inflow rate Q ; and glass particle diameter d_s varied from 1 mm to 4 mm. 50 particles are added one by one 5 mm over the middle point of the porous bed surface. The characteristics of the interaction of flow over and within the porous region and the particles were simulated using a CFD-DEM approach, while turbulence flow parameters over the permeable region were measured with PIV system, and particle velocities were measured with high speed camera.

The following conclusions can be derived:

1. The statistical results demonstrate that average horizontal component of the particle velocity follows a Gaussian distribution for each case. The average particle velocity increase with increasing angle of inclination, inflow rate and seepage flow rate but there is not a positive correlation between the particle velocity and size.
2. The movement of particles in horizontal direction is mainly controlled by flow. Within the same flow depth, the normalized horizontal component of particle velocity increases with increasing inflow rate and channel slope; it generally increases with the particle size diminishing. With larger inflow rate and larger channel slope the particle can move higher. The particle velocity near the surface of porous bed for is generally increasing for seepage outflow rate increasing, this trend agrees with the variation of flow velocity.
3. The mean horizontal component of particle velocity in ascent motion or in descent motion increases with the particle height. The mean horizontal component of particle velocity in ascent motion is smaller than that in descent motion. This is because in the open channel flow velocity is increasing from the bottom to the surface in vertical direction, so within the same level, the particle ascent from a lower position has the smaller horizontal velocity component than the particle descent from a higher position.
4. Because the distance between the top of particle motion and the surface of porous bed is too short, the particle vertical velocity is accelerating until the particle meets the surface of porous bed and never reaches a constant terminal fall velocity during its downward motion in our range of experiments.
5. The particle transport velocity over porous bed can be written with a new formula as:

$$U_p = U_w - w_0 \left(\frac{44}{Re_p} - \frac{Q_1}{Q} + 0.0734 \right)$$

Chapter 9: General Conclusions

When there is no seepage flow and $Re_p \approx 44$, becomes Bagnold's law; when $Re_p > 44$, $\zeta (= (U_w - U_p)/w_0) < 1$, it diminishes as Re_p increases.

9.4 Sediment clogging phenomenon in an open channel with a porous bed

Sediment transport and clogging phenomenon in a turbulent flow in an open channel with a porous bed has been studied experimentally for channel slope S_o varied from 0.0035 to 0.0244; inflow rate Q varied from 3.2 l/min to 6.8 l/min; seepage outflow rate Q_I varied from 0 to 10% of the inflow rate Q ; and particle diameter d_s varied from 630 μm to 1250 μm . Total 50 g glass sediment is added at the start part of the porous bed (201 mm long) in a constant rate of 1 g/s using the particle adding device. The main conclusions are:

1. The mass of sediment clogged in the porous bed generally decreases with increasing channel angle, inflow rate and sediment diameter, but the clogging risk increases with increasing seepage outflow rate.
2. Greater sediment transport rate over the porous bed is observed if the channel angle, inflow rate, sediment diameter or seepage outflow rate is larger.
3. Our experiment results have been compared with Meyer-Peter and Einstein correlations. Most of the scatters are concentrated near the empirical curves, but the deviation from these empirical could be important because of the flow conditions are different compared with theirs.

9.5 Suggestions for further research

This thesis has presented a detailed study on the particle transport in open channel flow over a porous bed using both experimental and numerical methods. Several areas that are worthy of further research can be pointed out:

9.5.1 From experimental point of view

1. The ratio of channel width / depth of flow used in our experiment sometimes is less than 5, therefore the influence of width can't be ignored and for this reason we have analyzed the results with the hydraulic diameter instead of the flow depth. It's interesting for engineering applications to use the depth only. Thus experiments with wide channel could be considered in the future works.

Chapter 9: General Conclusions

2. Preliminary investigations used a porous bed with the same porosity which is 0.476, although this setting is ideal when comparing the results got in experiment with the numerical results, but for further research, the influence of different porosities should be compared.
3. The porous bed made up by other kinds of materials beside magnetic particles may be used, like the materials of pavement, soil and bottom of rivers could be employed.
4. For the study of clogging, the sediment with a diameter much smaller could be used for comparison.
5. The influence of rain to the particle transport could be added and studied in further research.

9.5.2 From numerical point of view

1. The coupling PFC-DEM has been validated in many situations by our experiments. Thus it is worth to use it to simulate the experiments noted above. This way offers possibility to vary parameters easily.
2. The parallel calculation could be developed for faster calculation.

Chapter 9: General Conclusions

References

-
- Ashgriz, N. and Poo, J. Y. (1991) FLAIR: flux line segment model for advection and interface reconstruction. *J. Comp. Phys.*, 93, pp. 449-468.
- Ball J.E., Wojcik A. and Tilley J. (2000) Stormwater Quality from Road Surfaces-Monitoring of the Hume Highway at South Strathfield, University of New South Wales.
- Beavers. G. S., and Joseph, D. D. (1967) Boundary conditions at a naturally permeable wall. *J. Fluid Mech.*, 30(1), 197-207.
- Bigillon, F. (2001) Etude du mouvement bidimensionnel d'une particule dans un courant d'eau sur forte pente. Ph. D. thesis, Universite Grenoble 1- Joseph Fourier, U.F.R de Mechanique.
- Brackbill, J.U., Kothe, D. B., and C. Zemach. (1992) Acontinuum method for modeling surface tension. *J. comp. Phys*, 100, pp. 335-354.
- Chan H.C., Huang W.C., Leu J.M., Lai C.J., (2007) Macroscopic modeling of turbulent flow over a porous medium. *Int. J. Heat and Fluid Flow*, 28, pp. 1157-1166.
- Chang M. and Crowley C.M. (1993) Preliminary observations on water quality of storm runoff from four selected residential roofs. *Water Res. Bull.*, 295.
- Chanson H. (2004) *The Hydraulics of Open Channel Flow: An Introduction*. 2nd edition Linacre House, Jordan Hill, Oxford, pp.73.
- Chien, N. (1954) Meyer-Peter formula for bed-load transport and Einstein bed-load function. *Research Report No. 7*, University California Institute of Engineering, USA.
- Choi, C. Y. and Waller. P. M. (1997) Momentum transport mechanism for water flow over porous media. *J. Environ. Eng.*, 123(8). 792-799.
- Chu, Y. H., and Gelhar. L. W. (1972) Turbulent pipe flow with granular permeable boundaries. *Rep. No. 148*, Ralph M. Parsons Laboratory for Water Resources and Hydrodynamics, Dept. of Civil Engineering. Massachusetts Institute of Technology (M.I.T.), Cambridge, Mass.
- Clauser, F. H. (1956) The turbulent boundary layer. *Adv. App. Mech.*, 4, pp. 1-51.

References

- Colebrook, C.F. (1939) Turbulent flow in pipes with particular reference to the transition region between the smooth and rough pipe laws. *Journal Institute Civil Engineering*, 1938–1939, No. 4, 133–156.
- Cundall, P. A. (1971) A Computer Model for Simulating Progressive Large Scale Movements in Blocky Rock Systems, in *Proceedings of the Symposium of the International Society of Rock Mechanics* (Nancy, France), Vol. 1, Paper No. II-8.
- Cundall, P. A. and Strack, O. D. L. (1979) A discrete numerical model for granular assemblies. *Geotechniques*. Storming Media.
- Dallavalle, J.M. (1948) *Micromeritics: the Technology of Fine Particles*, 2nd edn., Pitman, London, pp. 14-40.
- Di Felice, R., (1994) The voidage function for fluid-particle interaction systems. *Int. J. Multiphase Flow*, 20, pp. 153-159.
- Einstein, H.A. (1950) The bed-load function for sediment transportation in open channel flows. *US Department of Agriculture Technical Bulletin No. 1026* (Soil Conservation Service, Washington DC, USA).
- Francis, J. R. D. (1973) Experiments on the motion of solitary grains along the bed of a water stream. *Proc. Roy. Soc., London A* 332: pp. 443-471.
- Grigoriev I. S., Meilikhov E. Z., Radzig A. A., (1997) *Handbook of Physical Quantities*, CRC Press.
- Hahn, S., Je, J. and Choi, H. (2002) Direct numerical simulation of turbulent channel flow with permeable walls. *J. Fluid Mech.*, 450, 259-285.
- Hansen, D. (1992) The behavior of follow-through rockfill dams. Ph. D. thesis, Dept. Of Civ. Engrg., University of Ottawa, Ont. Canada.
- Haselbach, L.M., Valavala, S., Montes, F., (2006) Permeability predictions for sand-clogged Portland cement pervious concrete pavement systems, *Journal of Environmental Management*, 81, pp. 42-49.
- Henderson, F.M. (1966) *Open Channel Flow*. (MacMillan Company: New York, USA). pp 91-96.
- Hirt, C. R. and Nichols, B. D. (1981) Volume of Fluid (VOF) method for the dynamics of free boundaries. *Journal of Computational Physics*, 39, pp. 201-225.

References

- Ikeda, S. (1971) Some studies on the mechanics of bed load transport. *Proc. Jpn. Soc. Civ. Eng.*, 185, pp. 61-69.
- Ippen, A. T. and Verma, R. P. (1955) Motion of particles on bed of a turbulent stream. *Trans. Am. Soc. Civ. Eng.*, pp. 921-938.
- ITASCA Consulting Group, Inc., (2007) *PFC3D 4.0 theory and background manual*, Itasca Consulting Group Inc, Minneapolis.
- ITASCA Consulting Group, Inc., (2008) *PFC3D 4.0 User Guide CCFD add-on*, Itasca Consulting Group Inc, Minneapolis.
- James. D. F. and Davis, A.M. (2001). Flow at the interface of a model fibrous porous medium. *J. Fluid Mech.*, 426.47-72.
- Jan, C. D. (1992) Movement of a sphere moving over smooth and rough inclines. Ph. D. thesis, University of California at Berkeley, California.
- Kalinske, A. A. (1942) Discussion of "Settling velocity and flume behavior of non-spherical particles" by Krumbein, W. C., *EOS Trans.*, AGU 23, pp. 632-633.
- Kawaguchi, T., (1992) Numerical simulation of fluidized bed using the discrete element method (the Case of Spouting Bed), *JSME (B)*, 58(551), pp. 79-85.
- Kothe, D. B. and Mjolsness, R. C. (1992) RIPPLE: a new model for incompressible flows with free surfaces. *AIAA J.*, 30(11), pp. 2692-2700.
- Krumbein, W. C. (1942) Settling velocities and flume behavior of non-spherical particles. *EOS Trans.* AGU 23: pp. 621-632.
- Li. B., and Garga. Y. K. (1998) Theoretical solution for seepage flow in overtopped rockfill. *J. Hydraul. Eng.*, 124(2). pp. 213-217.
- Liang, P. Y. (1991) Numerical method for calculation of surface tension flows in arbitrary grids. *AIAA J.*, 29, pp. 161-167.
- Meland, N. and Norrman, J. O. (1966) Transport velocities of single particles in bed load motion. *Geografiska Annaler*, 48 A (4), pp.165-182.
- Mendoza, C., and Zhou, D., (1992) Effect of porous bed on turbulent stream flow above bed. *J. Hydraul. Engrg.*, 118 (9), pp. 1222-1240.

References

- Meyer-Peter, E., and Müller, R. (1948) Formulas for Bedload Transport. *Proc., 2nd Meeting, IAHR*, Stockholm, Sweden, pp.39-64.
- Moody, L.F. (1944) Friction factors for pipe flow. *Transactions, ASME*, 66, pp. 671–684.
- Munoz-Goma, R. J. and Gelhar, L. W. (1968) Turbulent pipe flow with rough and porous walls. *Rep. No. 109*. Hydrodynamics Laboratory. Dept. of Civil Engineering. M.I.T., Cambridge, Mass.
- Nezu, I. (1977) Turbulent structure in open-channel flows. Ph. D. thesis. Dept. of Civil Engineering, Kyoto Univ., Japan.
- Nezu, I. and Rodi, W. (1986) Open-channel flow measurements with a Laser Doppler anemometer. *Journal of Hydraulic Engineering, ASCE*, 112(5), pp. 335-355.
- Nguyen, T. (2007) Contribution à l'étude du transport de particules denses liquides ou solides dans un matériau poreux. Ph. D. thesis, LGCGM, National Institute for Applied Sciences of Rennes.
- Nikuradse, J. (1933) *Strömungsgesetze in rauhen Rohren. (Laws of Turbulent Pipe Flow in Rough Pipes.)* (VDI-Forschungsheft, No. 361).
- Ochoa-Tapia, A. J. and Whitaker, S. (1995b) Momentum transfer at the boundary between a porous medium and a homogeneous fluid. II: Comparison with experiment. *Int. J. Heat Mass Transfer*, 38(14), pp. 2647-2655.
- Ochoa-Tapia, A. J. and Whitaker, S. (1995a) Momentum transfer at the boundary between a porous medium and a homogeneous fluid. 1: Theoretical development. *Int. J. Heat Mass Transfer*, 38(14), pp. 2635-2646.
- Patankar, S. V. (1980) *Numerical heat transfer and fluid flow*, Hemisphere Publishing Corp., New York.
- Pedras, M.H.J., & de Lemos, M.J.S., (2000) On the definition of turbulent kinetic energy for flow in porous media. *Int. Commun. Heat Mass Transfer*, 27 (2), pp. 211-220.
- Poulikakos, D., and Kazmierczak, M. (1987) Forced convection in a duct partially filled with a porous material. *J. Heat Transfer*, 109, pp. 653-662.
- Prinos, P., Sofialidis, D., Keramaris, E., (2003) Turbulent flow over and within a porous bed. *J. Hydraul. Engrg.*, 129 (9), pp. 720-733.

References

- Raudkivi, A.J., and Callander, R.A. (1976) *Analysis of Groundwater Flow*. Edward Arnold Publisher: London, UK.
- Remond, S. (2010) DEM simulation of small particles clogging in the packing of large beads, *Physica A*, 389, pp. 4485-4496.
- Rider, W. J. and Kothe, D. B. (1998) Reconstructing volume tracking. *J. Comp. Phys.*, 141, pp. 112-152.
- Van Rijn, L.C. (1993) *Principles of Sediment Transport in Rivers, Estuaries and Coastal Seas*. Aqua Publications, Amsterdam, Netherlands.
- Rudraiah, N. (1985) Coupled parallel flows in a channel and a bounding porous medium of finite thickness. *J. Fluids Eng.*, 107, pp. 322-329.
- Ruff, J. F. and Gelhar, L W (1970) Porous boundary effects in turbulent shear flow. *Rep. No. 126*, Water Resources and Hydrodynamics Laboratory, Dept. of Civil Engineering. M.I.T., Cambridge, Mass.
- Sahraoui, M., and Kaviany, M. (1992) Slip and no-slip velocity boundary conditions at interface of porous, plain media. *Int. J. Heat Mass Transfer*, 35, pp. 927-943.
- Scardovelli, R. and Zaleski, S. (1999) Direct numerical simulation of free-surface and interfacial flow. *Annu. Rev. Fluid Mech.*, 31, pp. 567-603.
- Schlichting, H. (1968) *Boundary-Layer Theory*, sixth edition. McGraw-Hill Book Co. New York.
- Shields, A. (1936) *Anwendung der Aehnlichkeitsmechanik und der Turbulenz Forschung auf die Geschiebebewegung*. (Mitt. der Preussische Versuchanstalt für Wasserbau und Schiffbau: Berlin, Germany), No. 26.
- Shimizu, Y., Tsujimoto, T., Nakagawa, H., (1990) Experimental and macroscopic modeling of flow in highly porous medium under free surface flow. *J. Hydrosoci. Hydraul. Engrg.*, 8 (1), pp. 69-78.
- Streeter, V.L., and Wylie, E.B. (1981) *Fluid Mechanics*, 1st SI metric edition (McGraw-Hill: Singapore). pp. 236.
- Vafai, K., and Thiyagaraja, R. (1987) Analysis of flow and heat transfer at the interface region of a porous medium. *Int. J. Heat Mass Transfer*, 30, pp. 1391-1405.
- White F.M. (2003) *Fluid Mechanics*, 5th Ed., McGraw Hill International.

References

White, H. E. Walton, S. F. (1937) Particle Packing and Particle Shape, *J. Am Ceram. Soc.*, 20 pp. 155-166.

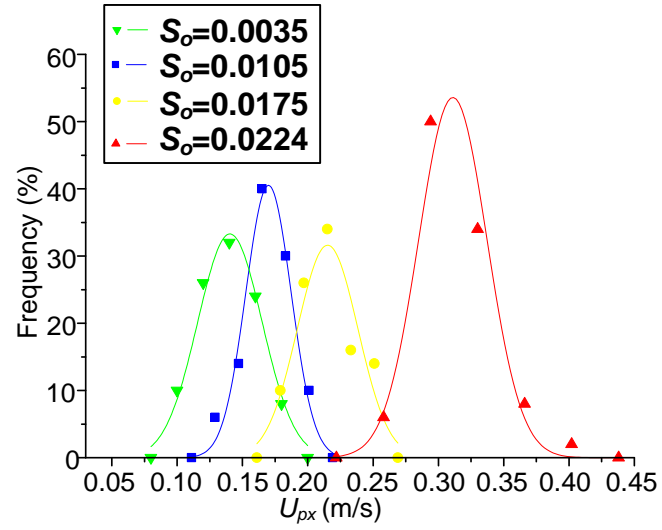
Xu, B. H., Yu, A. B., (1997) Numerical simulation of the gas-solid flow in a fluidized bed by combining discrete particle method with computational fluid dynamics. *Chem. Eng. Sci*, 52, pp. 2786-2809.

Youngs, D.L. (1982) Time-dependent multi-material flow with large fluid distortion. *Numerical Methods for Fluid Dynamics*, edited by K. W. Morton and M. J. Baines, Academic Press, New York, pp. 273-285.

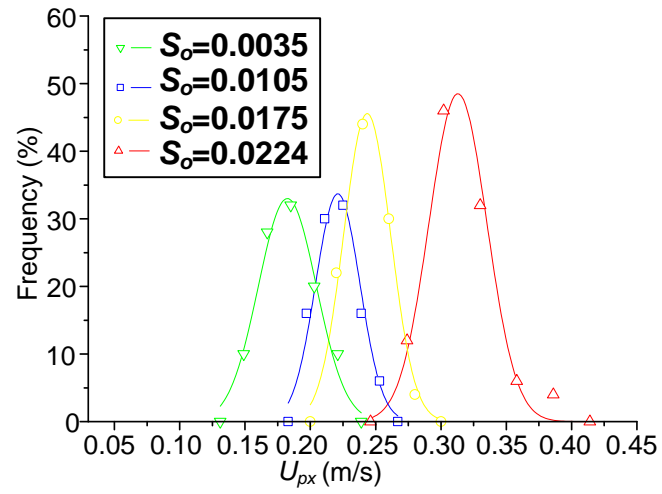
Zhou, D., & Mendoza, C., (1993) Flow through porous bed of turbulent stream. *J. Engrg. Mech.*, 119 (2), pp. 365-383.

Zippe, H. J., and Graf, W. H. (1983) Turbulent boundary-layer flow over permeable and nonpermeable rough surfaces. *J. Hydraul. Res.*, 21(1). pp. 51-65.

Appendix

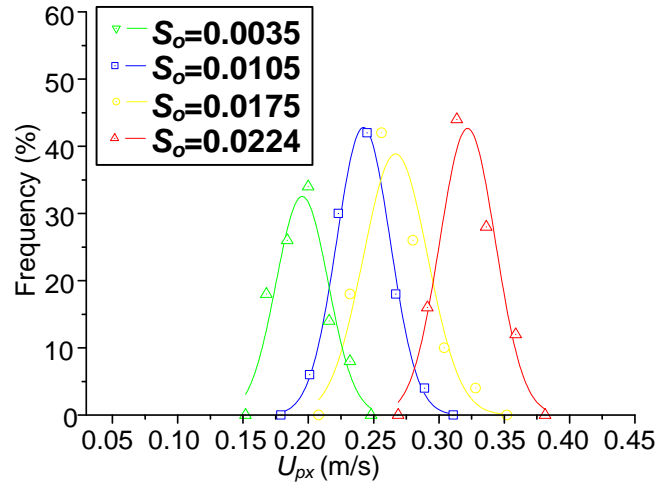


(a1) Inflow rate $Q=6$ l/min, seepage outflow rate $Q_I=0$ l/min

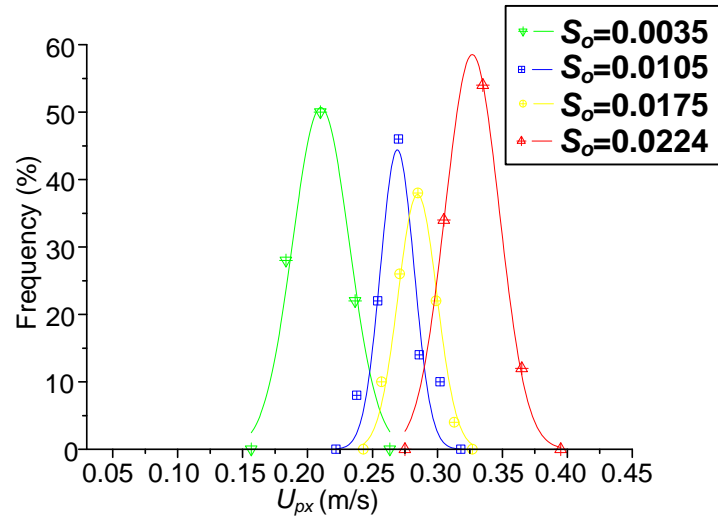


(a2) Inflow rate $Q=6$ l/min, seepage outflow rate $Q_I=0.3$ l/min

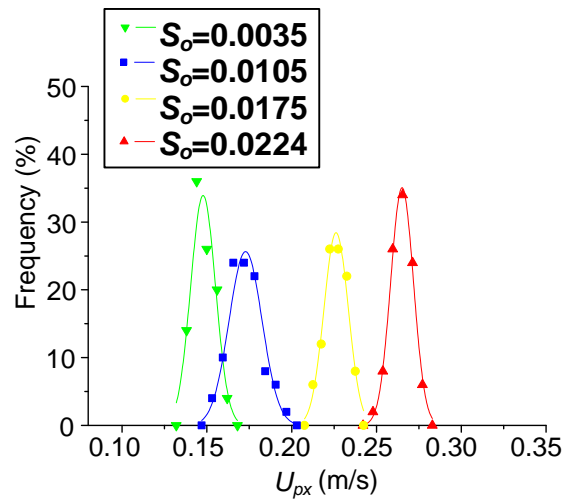
Appendix



(a3) Inflow rate $Q=6$ l/min, seepage outflow rate $Q_I=0.4$ l/min

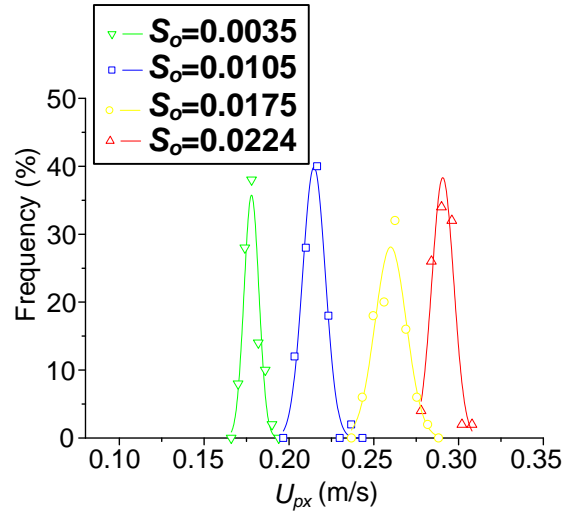


(a4) Inflow rate $Q=6$ l/min, seepage outflow rate $Q_I=0.6$ l/min

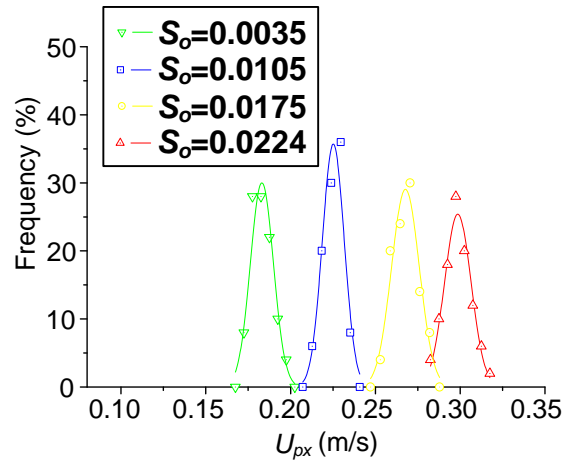


(b1) Inflow rate $Q=6$ l/min, seepage outflow rate $Q_I=0$ l/min

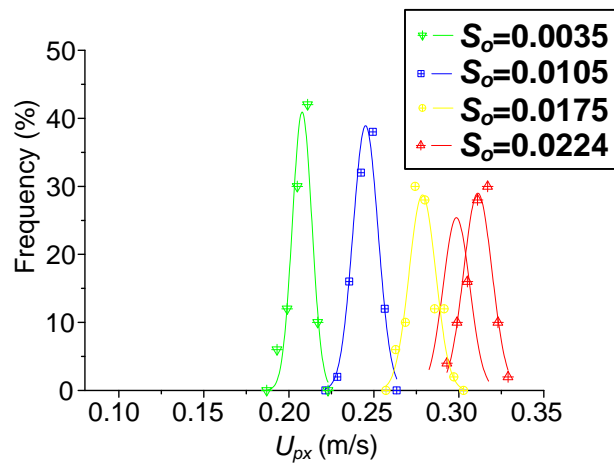
Appendix



(b2) Inflow rate $Q=6$ l/min, seepage outflow rate $Q_I=0.3$ l/min



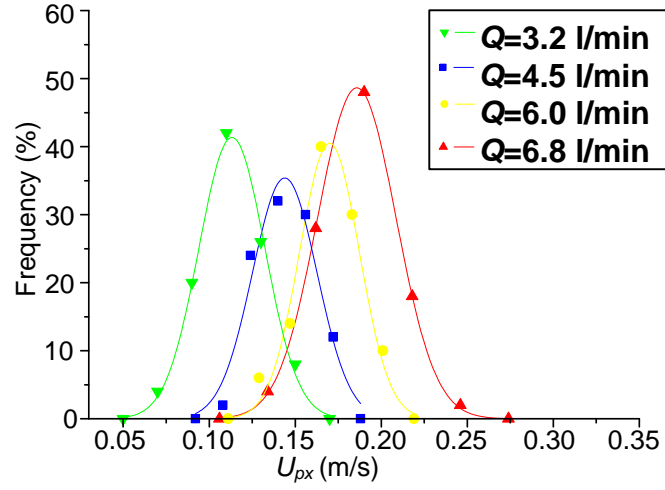
(b3) Inflow rate $Q=6$ l/min, seepage outflow rate $Q_I=0.4$ l/min



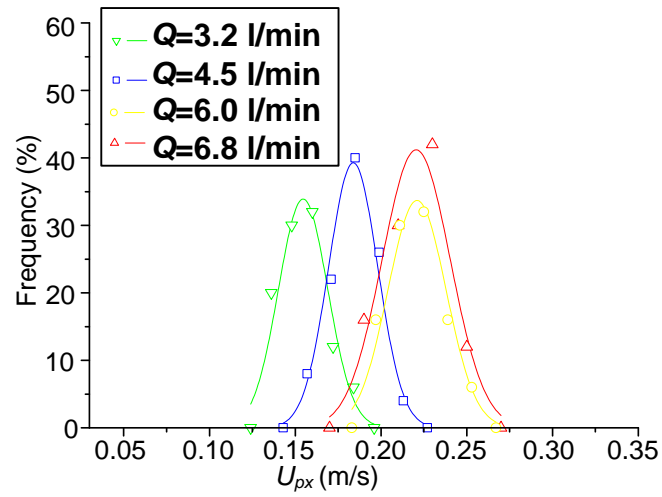
(b4) Inflow rate $Q=6$ l/min, seepage outflow rate $Q_I=0.6$ l/min

Appendix

Figure A-1. Distributions of average horizontal component of the particle velocity for different channel slopes, in different infiltration conditions, lines correspond to Gaussian distribution. (a), measured data; (b), simulated data

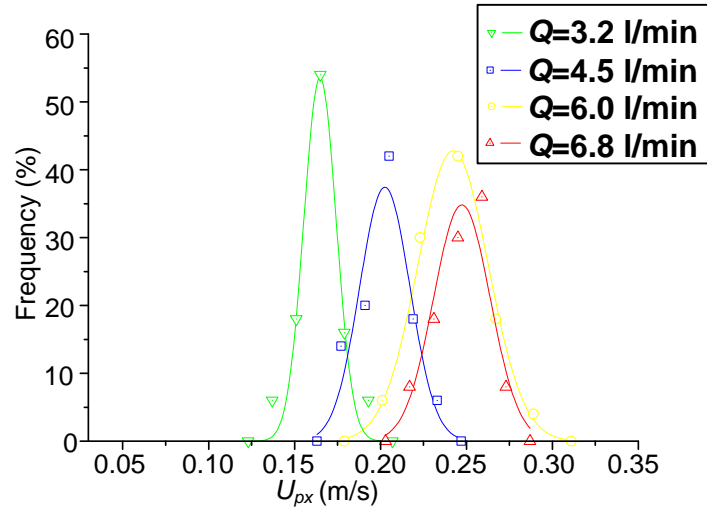


(a1) Channel slope $S_o=0.0105$, seepage outflow rate $Q_I=0$ l/min

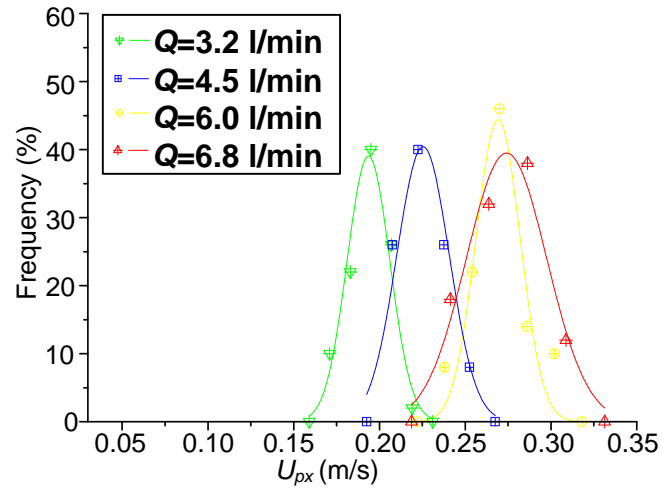


(a2) Channel slope $S_o=0.0105$, seepage outflow rate $Q_I=Q/20$ l/min

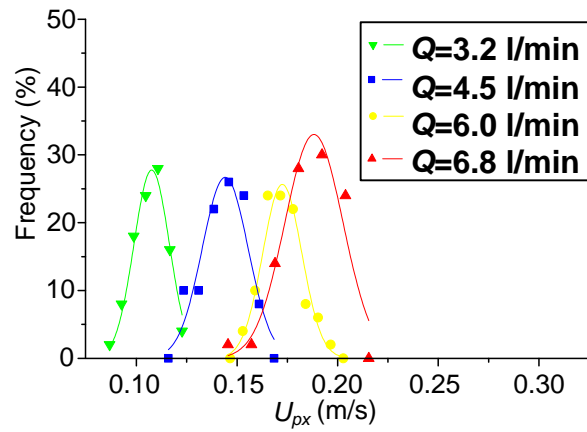
Appendix



(a3) Channel slope $S_o=0.0105$, seepage outflow rate $Q_I=Q/15$ l/min

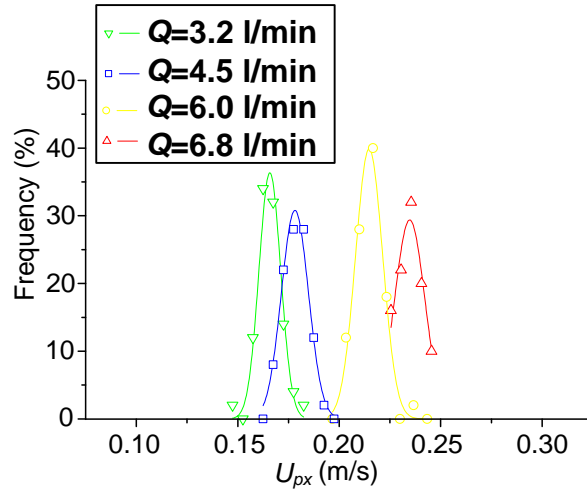


(a4) Channel slope $S_o=0.0105$, seepage outflow rate $Q_I=Q/10$ l/min

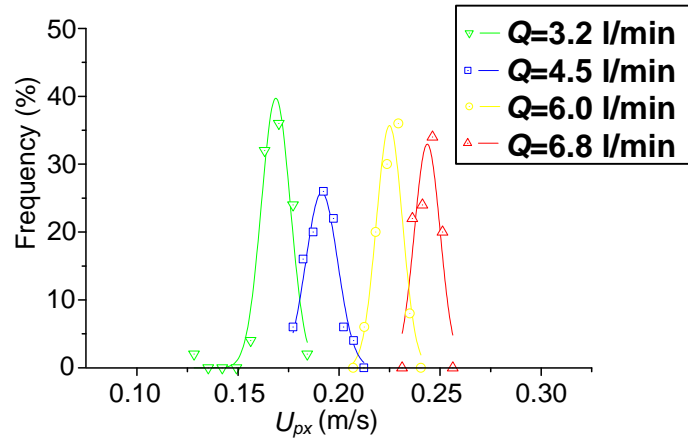


(b1) Channel slope $S_o=0.0105$, seepage outflow rate $Q_I=0$ l/min

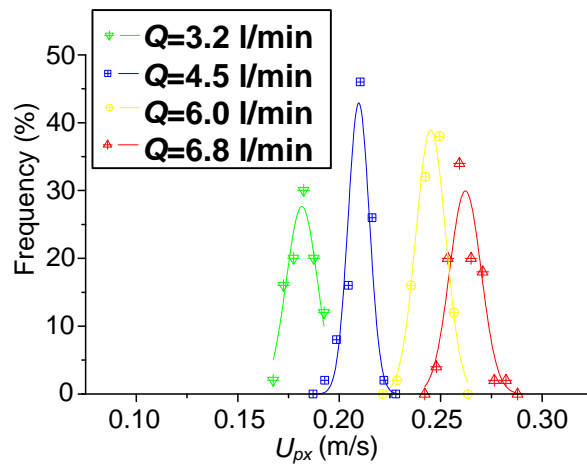
Appendix



(b2) Channel slope $S_o=0.0105$, seepage outflow rate $Q_I=Q/20$ l/min



(b3) Channel slope $S_o=0.0105$, seepage outflow rate $Q_I=Q/15$ l/min

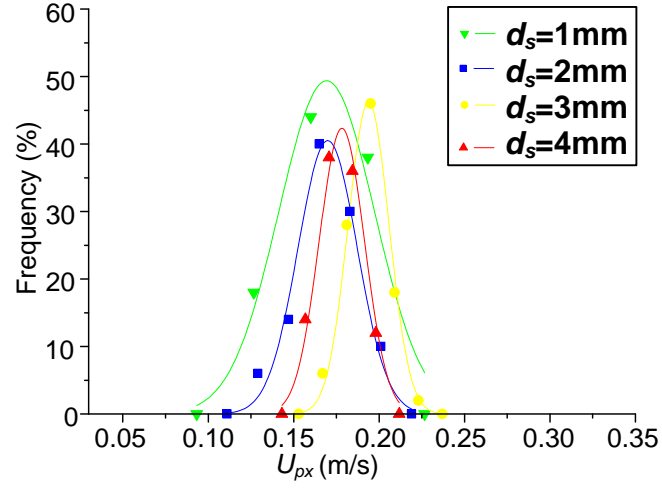


(b4) Channel slope $S_o=0.0105$, seepage outflow rate $Q_I=Q/10$ l/min

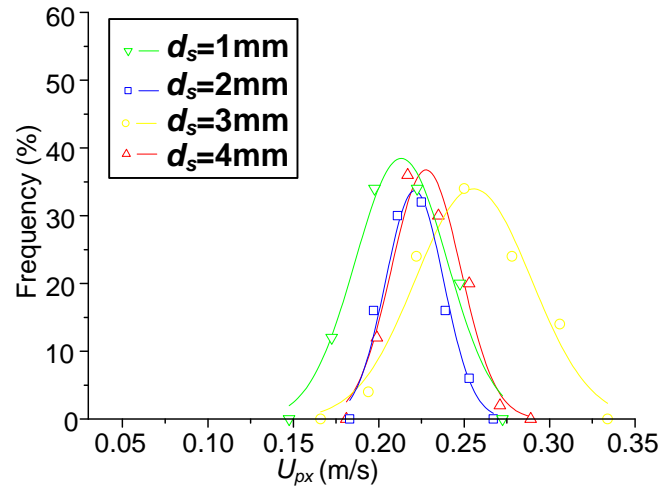
Appendix

Figure A-2. Distributions of average horizontal component of the particle velocity for different inflow rate, with different infiltration rates, lines correspond to Gaussian distribution.

(a), measured data; (b), simulated data

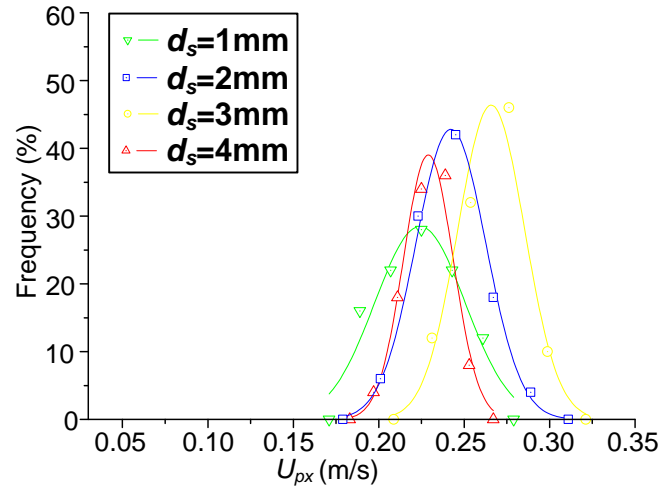


(a1) Inflow rate $Q=6$ l/min, seepage outflow rate $Q_I=0$ l/min, channel slope $S_o=0.0105$

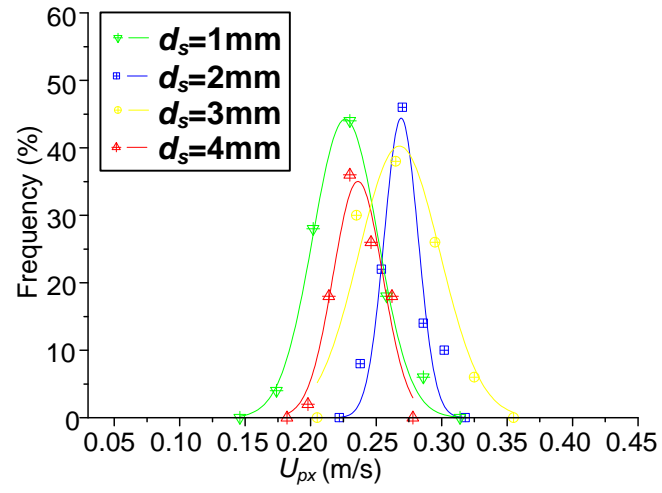


(a2) Inflow rate $Q=6$ l/min, seepage outflow rate $Q_I=0.3$ l/min, channel slope $S_o=0.0105$

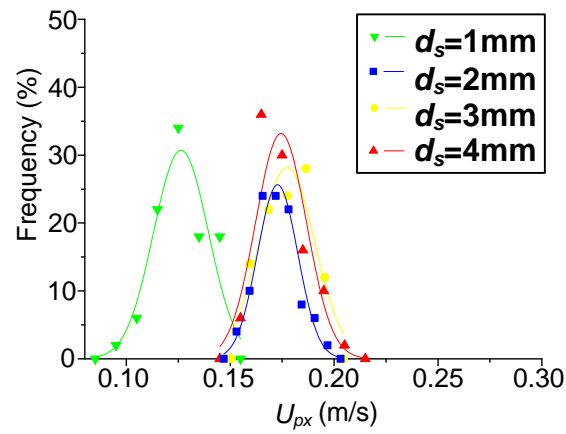
Appendix



(a3) Inflow rate $Q=6$ l/min, seepage outflow rate $Q_l=0.4$ l/min, channel slope $S_o=0.0105$

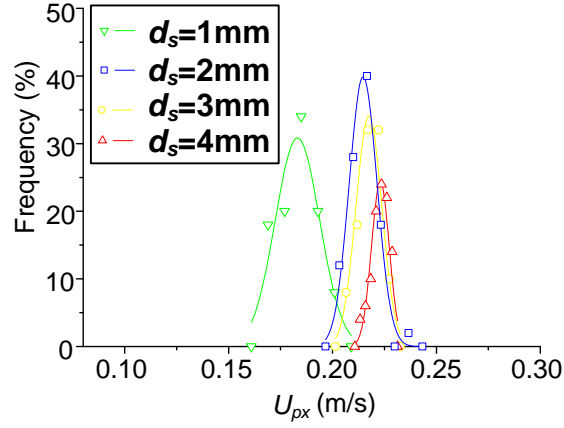


(a4) Inflow rate $Q=6$ l/min, seepage outflow rate $Q_l=0.6$ l/min, channel slope $S_o=0.0105$

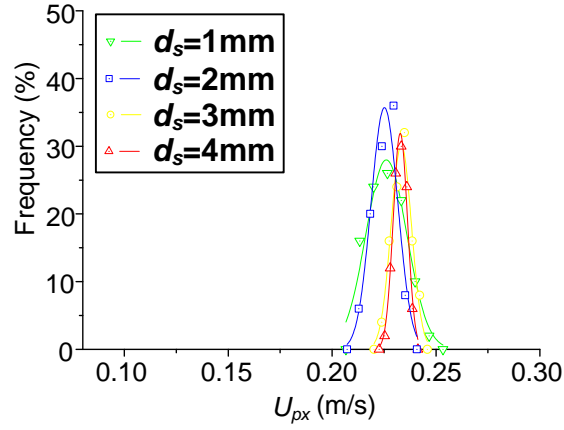


Appendix

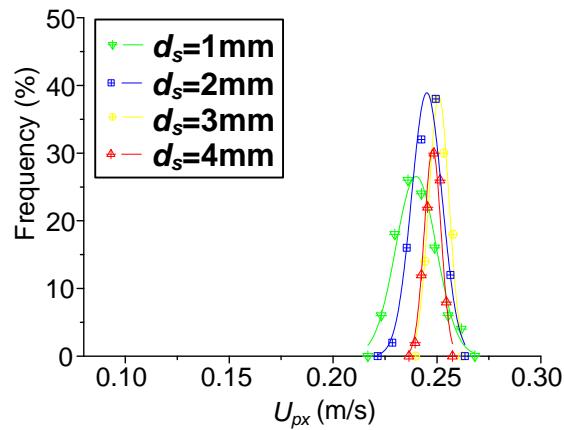
(b1) Inflow rate $Q=6$ l/min, seepage outflow rate $Q_I=0$ l/min, channel slope $S_o=0.0105$



(b2) Inflow rate $Q=6$ l/min, seepage outflow rate $Q_I=0.3$ l/min, channel slope $S_o=0.0105$



(b3) Inflow rate $Q=6$ l/min, seepage outflow rate $Q_I=0.4$ l/min, channel slope $S_o=0.0105$



(b4) Inflow rate $Q=6$ l/min, seepage outflow rate $Q_I=0.6$ l/min, channel slope $S_o=0.0105$

Appendix

Figure A-3. Distributions of average horizontal component of the particle velocity for different particle diameter, in different infiltration conditions, lines correspond to Gaussian distribution. (a), measured data; (b), simulated data

Appendix

Table A-1. Particle mean streamwise velocity and properties

Case	U_p (m/s)		Relative error of U_p	U_p/U_*		Re_p		w_0 (m/s)		Relative error of W_o	U_w-U_p (m/s)		ζ (= $(U_w-U_p)/w_0$)	
	simulation	experiment		simulation	experiment	simulation	experiment	simulation	experiment		simulation	experiment	simulation	experiment
1	0.1477	0.1404	0.0520	4.63	4.14	63.8	67.8	0.232	0.237	0.021	0.1562	0.1826	0.673	0.771
2	0.1779	0.1824	0.0247	5.28	4.77	67.3	76.4	0.232	0.237	0.021	0.1426	0.1758	0.614	0.742
3	0.1831	0.1953	0.0625	5.32	4.99	68.8	78.2	0.232	0.237	0.021	0.1456	0.1687	0.627	0.712
4	0.2078	0.2103	0.0119	5.81	5.23	71.6	80.4	0.232	0.237	0.021	0.1334	0.1626	0.575	0.686
5	0.1728	0.1699	0.0171	4.90	4.62	70.5	73.6	0.232	0.237	0.021	0.1607	0.1699	0.693	0.717
6	0.2147	0.2210	0.0285	5.64	5.83	76.1	75.8	0.232	0.237	0.021	0.1399	0.1339	0.603	0.565
7	0.2252	0.2422	0.0702	5.86	6.00	76.9	80.7	0.232	0.237	0.021	0.1383	0.1354	0.596	0.571
8	0.2451	0.2692	0.0895	6.23	6.55	78.7	82.2	0.232	0.237	0.021	0.1302	0.1146	0.561	0.484
9	0.2260	0.2152	0.0502	5.56	5.46	81.3	78.9	0.232	0.237	0.021	0.1489	0.1478	0.642	0.624
10	0.2600	0.2435	0.0678	6.28	5.90	82.8	82.6	0.232	0.237	0.021	0.1321	0.1477	0.570	0.623
11	0.2677	0.2667	0.0037	6.36	6.35	84.1	84.0	0.232	0.237	0.021	0.1316	0.1181	0.567	0.498
12	0.2786	0.2847	0.0214	6.42	6.53	86.8	87.2	0.232	0.237	0.021	0.1289	0.1227	0.556	0.518
13	0.2651	0.3110	0.1476	6.08	6.54	87.2	95.1	0.232	0.237	0.021	0.1435	0.1207	0.619	0.509
14	0.2907	0.3130	0.0712	6.40	6.49	90.9	96.4	0.232	0.237	0.021	0.1334	0.1268	0.575	0.535
15	0.2986	0.3219	0.0724	6.57	6.63	90.9	97.1	0.232	0.237	0.021	0.1255	0.1186	0.541	0.501
16	0.3112	0.3268	0.0477	6.62	6.64	94.1	98.4	0.232	0.237	0.021	0.1247	0.1124	0.538	0.474
17	0.1080	0.1132	0.0459	3.53	4.16	61.2	54.4	0.232	0.237	0.021	0.1491	0.1245	0.643	0.525
18	0.1658	0.1546	0.0724	5.05	5.27	65.7	58.6	0.232	0.237	0.021	0.1068	0.1094	0.461	0.461

Appendix

19	0.1690	0.1648	0.0255	5.04	5.50	67.0	59.9	0.232	0.237	0.021	0.1052	0.1070	0.453	0.452
20	0.1816	0.1936	0.0620	5.26	5.44	69.0	71.2	0.232	0.237	0.021	0.1023	0.1095	0.441	0.462
21	0.1444	0.1439	0.0035	4.28	4.67	67.5	61.6	0.232	0.237	0.021	0.1562	0.1375	0.673	0.580
22	0.1782	0.1838	0.0305	4.97	5.11	71.8	71.9	0.232	0.237	0.021	0.1364	0.1477	0.588	0.623
23	0.1917	0.2025	0.0533	5.22	5.35	73.5	75.7	0.232	0.237	0.021	0.1306	0.1384	0.563	0.584
24	0.2096	0.2254	0.0701	5.48	5.76	76.4	78.3	0.232	0.237	0.021	0.1225	0.1308	0.528	0.552
25	0.1885	0.1858	0.0145	5.20	4.92	72.4	75.4	0.232	0.237	0.021	0.1619	0.1771	0.698	0.747
26	0.2348	0.2213	0.0610	6.08	5.37	77.2	82.4	0.232	0.237	0.021	0.1403	0.1750	0.605	0.738
27	0.2439	0.2473	0.0137	6.22	6.16	78.4	80.2	0.232	0.237	0.021	0.1375	0.1474	0.593	0.622
28	0.2622	0.2741	0.0434	6.55	6.95	80.1	78.9	0.232	0.237	0.021	0.1329	0.1092	0.573	0.461
29	0.1265	0.1693	0.2528	3.58	4.61	35.3	36.8	0.134	0.139	0.036	0.2071	0.1705	1.545	1.227
30	0.1831	0.2132	0.1412	4.81	5.63	38.0	37.9	0.134	0.139	0.036	0.1715	0.1417	1.280	1.020
31	0.2261	0.2241	0.0089	5.88	5.55	38.5	40.4	0.134	0.139	0.036	0.1374	0.1534	1.025	1.104
32	0.2399	0.2265	0.0592	6.10	5.51	39.4	41.1	0.134	0.139	0.036	0.1354	0.1572	1.010	1.131
33	0.1774	0.1938	0.0846	5.03	5.27	105.8	110.3	0.308	0.301	0.023	0.1562	0.1460	0.507	0.485
34	0.2175	0.2554	0.1484	5.72	6.74	114.1	113.7	0.308	0.301	0.023	0.1372	0.0995	0.445	0.331
35	0.2333	0.2658	0.1223	6.07	6.59	115.4	121.1	0.308	0.301	0.023	0.1301	0.1117	0.423	0.371
36	0.2509	0.2678	0.0631	6.37	6.52	118.1	123.3	0.308	0.301	0.023	0.1244	0.1160	0.404	0.385
37	0.1745	0.1782	0.0208	4.95	4.85	141.1	147.1	0.371	0.379	0.021	0.1590	0.1616	0.429	0.427
38	0.2230	0.2277	0.0206	5.86	6.01	152.2	151.5	0.371	0.379	0.021	0.1316	0.1272	0.355	0.336
39	0.2328	0.2290	0.0166	6.05	5.68	153.8	161.4	0.371	0.379	0.021	0.1306	0.1485	0.352	0.392
40	0.2479	0.2361	0.0500	6.30	5.75	157.4	164.3	0.371	0.379	0.021	0.1274	0.1477	0.343	0.390

Appendix

where U_p is the particle mean streamwise velocity; Re_p is the particle Reynolds number, $Re_p = \frac{U_* d_s}{\nu}$; w_o is the particle settling velocity; relative error of the numerical result is calculated as: $\frac{|experimental\ result - simulation\ result|}{experimental\ result}$.

List of Symbols

$a_{\varphi j}$	linearize coefficient matrix
A	flow cross-sectional area (m^2), $A=dB$
A_s	particle cross-sectional area (m^2)
A_{φ}	a matrix of $N \times N$
b_{φ}	source term
B	channel width (m)
d	flow depth (m)
d_s	diameter of rolling particles (m)
c_{μ}	sliding friction coefficient
C	constant of logarithmic law
$C_{\text{Chézy}}$	Chézy coefficient ($\text{m}^{1/2}/\text{s}$)
C_d	drag coefficient
C_L	lift coefficient
$C_{\mu}, C_1, C_2, C_3, C_4, \sigma_k, \sigma_{\varepsilon}$	experimental constants in standard k - ε model (chapter 3)
σ_T	
D	diameter of the particle which made up the porous bed (m)
D_H	hydraulic diameter (m), or equivalent pipe diameter, $D_H = 4 \times \frac{\text{cross - sectional area}}{\text{wetted perimeter}} = \frac{4 \times A}{P_w}$
D_{φ}	a diagonal term of matrix A_{φ}
E	total energy per unit mass
f	Darcy friction factor
\vec{f}_b	volume force per unit volume
f_c	coefficient of restitution
F_b	buoyancy force
\vec{f}_{fluid}	total force applied by the fluid on the particle
F_i^c	the i th components of the contact force
F_i^n	normal contact force
ΔF_i^n	shear elastic force-increment
\vec{f}_{mech}	sum of additional forces acting on the particle
\vec{f}_0	force on a single particle
Fr	Froude number, $Fr = \frac{U_w}{\sqrt{gd}}$

List of Symbols

F_{\max}^S	maximum allowable shear contact force
g	gravity constant, $g = 9.80 \text{ m/s}^2$
\vec{g}	gravitational vector
g_i	the i th components of the gravity g
h_p	height of porous region
H	whole channel depth (Chapter 3)
ΔH	head loss due to friction (m)
I	moment of inertia
K	coefficient of permeability, (m/s)
K_{eff}	theoretical effective permeability of sand clogged or covered pervious concrete block systems, (m/s)
k	turbulent kinetic energy
k^+	normalized turbulent kinetic energy, $k^+ = k/U_*^2$
k^n	normal stiffness
k_p	intrinsic permeability of a soil (m^2)
k_s	equivalent sand roughness height (m)
k^s	shear stiffness at the contact
k^{rot}	rotational stiffnesses
k^{tran}	translational stiffnesses
L	length (m)
L_s	length of porous bed (m)
ΔL	small distance along the flow direction (m)
m	mass of the particle
\dot{m}_j	mass flux on the surface of the cell
m_s	sediment mass flow rate per unit width ($\text{kg s}^{-1} \text{ m}^{-1}$)
\vec{M}	moment acting on the particle
M_i^c	moment of the i th particle
\vec{n}	unit normal vector (outward pointing) of control volume face
n_f	number of surfaces comprising a cell
n_μ	bulk friction coefficient
$n_{Manning}$	Manning coefficient (units $\text{s/m}^{1/3}$)
N_c	number of contacts
p	fluid pressure
P_B	turbulent kinetic energy generated due to buoyancy
Pr	probability distribution
P_s	turbulent kinetic energy generated by shear

List of Symbols

q	flow rate per unit width
\vec{q}_h	a heat flux vector
q_s	sediment flow rate per unit width (m^2/s)
Q	inflow rate
Q_1	seepage outflow rate
Q_2	outflow rate
r	particle radius
Re	Reynolds number, $Re = \frac{U_w D_H}{\nu}$
Re_*	shear Reynolds number, $Re_* = \frac{U_* d_s}{\nu}$
Re_p	particle Reynolds number, $Re_p = \frac{U_* d_s}{\nu}$
R_H	hydraulic radius, $R_H = D_H/4$
s	relative density of sediment: $s = \rho_s/\rho$
s_h	heat source
S	area of a face of a control volume
S_f	flow slope
dS	surface element
S_o	channel slope
t	time
t_{crit}	critical time-step
δt_m	a time unit
Δt	time step
u, v	streamwise and vertical velocity components (m/s)
u^+	dimensionless streamwise velocity components $u^+ = u/U_*$
U_*	shear velocity (m/s), $U_* = \sqrt{\frac{\tau_0}{\rho}}$
U_c	critical velocity for a particle
U_i	instantaneous horizontal component of particle velocity within the sub-zone (m/s)
U_{int}	interfacial velocity
U^n	relative contact displacement in the normal direction
U_p	particle velocity
U_{pa}	mean horizontal component of particle velocity in ascent motion (m/s)
U_{pd}	mean horizontal component of particle velocity in descent motion (m/s)

List of Symbols

U_{px}	mean particle streamwise velocity (m/s)
U_s	mean flow velocity in porous medium (m/s)
ΔU_i^s	shear component of the contact displacement-increment
U_v	flow velocity in the pores (m/s)
U_w	mean flow velocity (m/s), $U_w = \frac{Q}{dB}$
v_j^*	velocity at the cell surface
\vec{V}	velocity vector
V_0	uniform equilibrium flow velocity (m/s)
V_i	instantaneous vertical component of particle velocity within the sub-zone (m/s)
V_p	mean vertical component of particle velocity (m/s)
V_{py}	mean vertical component of particle velocity (m/s)
V_s	mean vertical flow velocity in porous medium (m/s)
V_v	vertical flow velocity in the pores (m/s)
\vec{V}_s	vector of transfer velocity of the boundary
\vec{V}_p	particle velocity vector
w_o	particle settling velocity (m/s)
x, y	streamwise and vertical directions
x_i	position of the center of mass
\dot{x}_i	velocity of the center of mass
\ddot{x}_i	acceleration of the center of mass
y^+	dimensionless coordinates, $y^+ = yU_*/\nu$
β_φ	a relaxation coefficient, a value between 0 and 1 (chapter 3)
χ	empirical coefficient
Φ	porosity
Φ_{top}	average porosity of the top quarter of the pervious concrete block
Γ_φ	diffusion coefficient of φ on the cell surface
φ	conservative variables
φ_j^*	value of the flux of variable at the center of the surface comprising the cell
φ^{k-1}	a value before one step of the reiteration process
κ	von Karman constant (i.e. $\kappa=0.4$)
μ	dynamic viscosity (Pa s), at 20°C, the dynamic viscosity of water (at atmospheric pressure) $\mu=1.005\times 10^{-3}$ Pa s

List of Symbols

μ_c	friction coefficient
μ_t	eddy viscosity coefficient
ν	kinematic viscosity (m ² /s), $\nu=\mu/\rho$, water at atmospheric pressure and 20°C has a kinematic viscosity of 10 ⁻⁶ m ² /s
θ	angle of channel
ρ	fluid density (kg/m ³), At 20°C, the density of water (at atmospheric pressure) is: 998.2 kg/m ³
ρ_s	sediment density (kg/m ³)
ρ_j^*	density at the cell surface
τ_o	shear stress
τ_*	Shields parameter characterizing the onset of sediment motion
$\bar{\tau}$	Cauchy stress tensor
$\vec{\omega}$	angular velocity vector
ω_i	angular velocity of rotational motion
$\dot{\omega}_i$	angular acceleration of rotational motion
Ω_s	volume of the particle
Ω	control volume
ζ	a relative particle movement velocity, $\zeta = (U_w - U_p)/w_0$

List of Symbols

RESUME DE LA THESE

Investigations expérimentales et numériques de l'écoulement et du transport solide sur les surfaces urbaines

Contexte

Dans la société moderne, l'aménagement du territoire peut augmenter la quantité d'eaux de ruissellement et sa charge de polluants associée. Plusieurs auteurs ont étudié les eaux de ruissellement transportant la pollution dissoute, colloïdale et des composants solides de la ville.

Un milieu poreux, tel que le sol, les roches, etc , est un matériau contenant un grand nombre de vides (pores) de taille supérieure à l'échelle interatomique. Les phénomènes de transport à l'interface entre un écoulement fluide et un milieu poreux font l'objet de recherches importantes à la fois pour comprendre les phénomènes d'infiltration dans le milieu poreux et aussi en raison de leur large champ d'application, par exemple en hydrologie urbaine, la pollution et la dépollution des sols, le traitement de l'eau, etc.

Comme en hydrologie naturelle, l'hydrologie urbaine étudie l'érosion et les phénomènes de colmatage de la route qui causent beaucoup de pertes économiques et même menacent la vie des gens. Une meilleure compréhension des détails du flux de sédiments près de la surface de la route (milieu poreux) aiderait à améliorer leur conception et à fournir des solutions optimisées.

RESUME DE LA THESE

L'écoulement sur un milieu poreux combine une partie dessus et une partie à travers le milieu poreux. En raison de l'interaction entre l'écoulement de surface et l'écoulement d'infiltration à l'intérieur de la région poreuse, cette interaction affecte à la fois le flux liquide et le flux de sédiments.

L'effet de l'interaction entre le flux d'infiltration et l'écoulement de surface a été étudié par plusieurs précurseurs qui ont développé soit un modèle microscopique soit un modèle macroscopique permettant une simulation numérique de l'écoulement turbulent dans la région poreuse. La plupart des études sur les flux en milieu poreux utilise des modèles macroscopiques en une ou deux dimensions. Cependant en utilisant ces modèles il n'est pas possible d'avoir un aperçu détaillé de la structure de l'écoulement au voisinage de l'interface avec le milieu poreux.

Ces dernières années, en raison du développement de la capacité de calcul, des simulations de mécanique des fluides numérique (CFD) complexe peuvent être effectuées. De plus, la méthode des éléments discrets (DEM), développée par Cundall et Strack, a été largement utilisée pour étudier le comportement des solides granulaires soumis à une variété de conditions de chargement dans le but de comprendre et de prédire les résultats macroscopiques.

Dans cette thèse, les caractéristiques d'un écoulement à surface libre de faible profondeur, sur un lit poreux ainsi que le transport des sédiments induit sont étudiés tant numériquement qu'expérimentalement.

Méthode numérique

La méthode CFD-DEM a été utilisée pour la simulation de comportements complexes, y compris l'interaction entre les particules et le fluide, impliquant à la fois une région poreuse et une région de liquide clair. Cette méthodologie a une application plus large pour le transport de solides granulaires.

RESUME DE LA THESE

Le débit dans toute la région d'écoulement est résolu par un code CFD, il est calculé à partir des équations de continuité et de Navier-Stokes avec un terme de porosité et un terme de force de traînée pour tenir compte de la présence de particules dans le liquide.

Les particules rigides sphériques formant le milieu poreux et les grains transportés par le flux liquide sont décrits par un code DEM. Les équations du mouvement des particules sont résolus avec un terme aditionnel de traînée pour tenir compte de l'interaction avec le fluide.

L'ensemble de ces équations est résolu à l'aide du logiciel commercial CCFD et PFC3D 4.0. La vitesse du fluide et la pression du fluide dans chaque élément sont déterminées par le code CFD et renvoyées au code DEM à chaque boucle d'échange de données. Une comparaison avec les données expérimentales disponibles dans deux articles indépendants (Prinos *et al.*, 2003; Shimizu *et al.*, 1990) valide cet outil numérique.

Méthode expérimentale

Des expériences de laboratoire ont été effectuées en utilisant un canal rectiligne ouvert de longueur totale 2 mètres, de largeur 30 mm et de profondeur 8,5 mm (figure 1). Ce canal permet de créer des écoulements à surface libre de hauteur variable. Le canal est entièrement constitué de Plexiglas et permet ainsi une bonne vue des deux côtés. Ce canal est posé sur une surface de marbre lisse elle même posée sur une structure en acier réglable qui donne la possibilité de changer l'inclinaison. Le fluide écoulé dans le canal est récupéré dans un réservoir muni d'un filtre qui recueille donc les grains et l'eau claire pompée dans un réservoir à niveau constant situé en amont de l'installation. A l'entrée du canal, on a installé un dispositif permettant de réduire les turbulences, les bulles, etc ... avant la section d'étude.

RESUME DE LA THESE

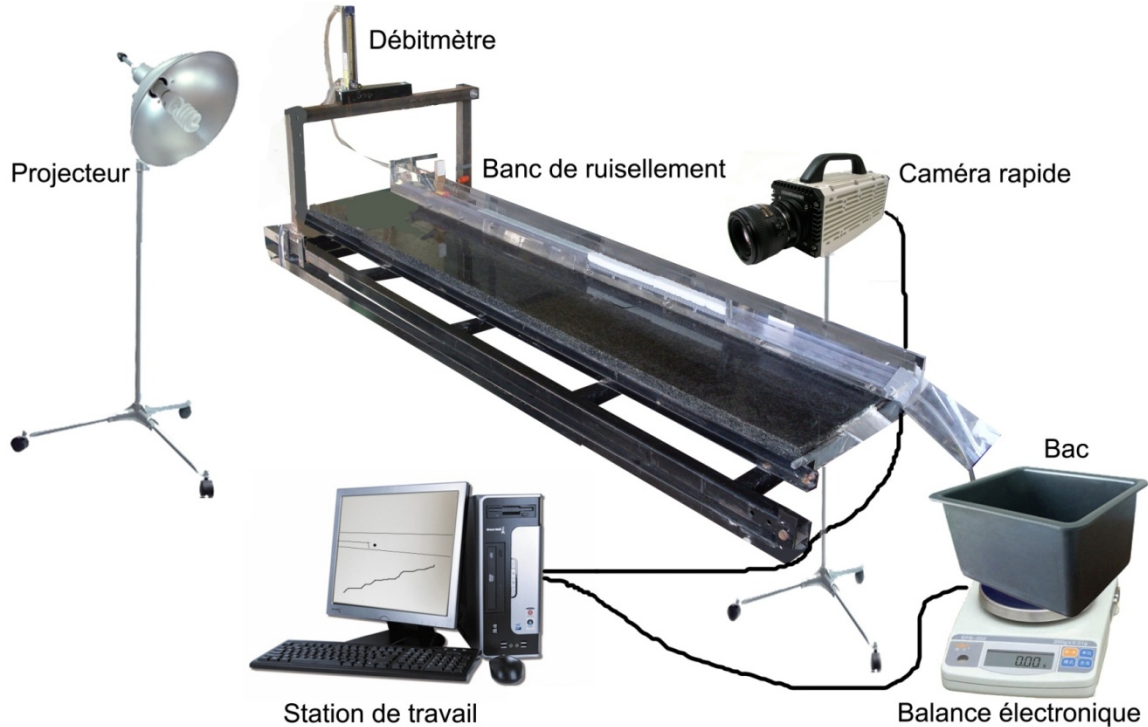


Figure 1. Schéma du montage expérimental

Le lit poreux est formé d'une couche de milieu poreux artificiel placée au fond du canal. Dans notre étude, le lit poreux de 201 mm x 30 mm x 9 mm est constitué d'un assemblage cubique de 2010 billes magnétiques de 3 mm de diamètre en acier inoxydable. Sous le lit poreux, un filtre tissé en fibres permet d'avoir une zone moins perméable que le lit poreux. La troisième couche est une plaque en plastique avec des trous, pour assurer le drainage dont on veut déterminer les effets sur le transport.

La technique de vélocimétrie par image de particules (PIV) a été utilisée pour mesurer le champ de vitesse fluide. Les particules utilisées sont des billes de nylon de 50 μm . Dans nos expériences, la résolution spatiale du système PIV est de 0,03 mm avec une acquisition qui correspond à une mesure toutes les 500 μs c'est-à-dire 1 double-frame images décalées de 1000 μs .

RESUME DE LA THESE

Le mouvement des particules millimétriques a été capté par une caméra très rapide (2000 images/s), avec une résolution de 1024×128 pixels et une cadence de 250 images par seconde.

La précision des mesures nous paraît satisfaisante pour notre recherche. Les résultats expérimentaux sont comparables aux résultats numériques.

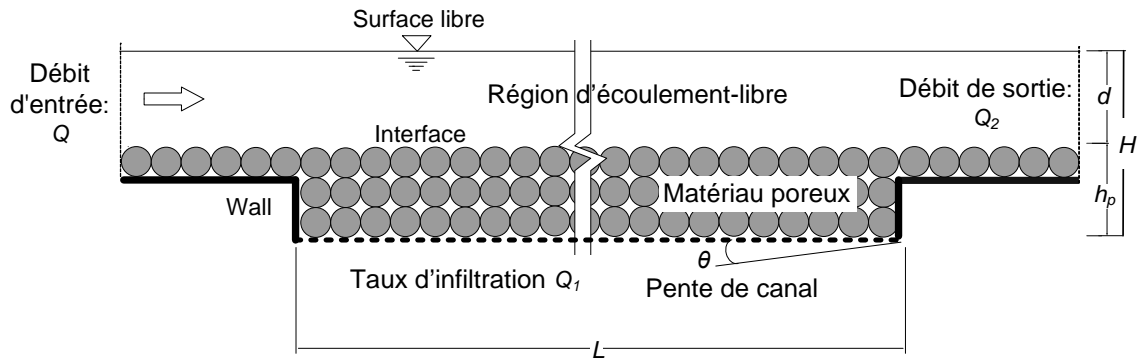


Figure 2. Schéma coupe transversale du domaine de calcul avec les conditions aux limites

Les méthodes numérique et expérimentale ont été utilisées pour étudier les caractéristiques de l'écoulement en canal ouvert sur un lit poreux, le transport des particules, le seuil de mise en mouvement des particules et le colmatage du milieu poreux.

La Figure 2 montre le domaine étudié ici. Le canal rectangulaire est partiellement rempli d'une couche de matériau poreux. Un écoulement à surface libre traverse longitudinalement de gauche à droite. Sous le lit poreux, le débit d'écoulement d'infiltration est contrôlé.

Écoulement à surface libre sur un lit poreux

Un écoulement turbulent 3D dans un canal ouvert sur un lit poreux a été étudié numériquement et expérimentalement avec une pente de canal S_o variant de 0,0035 à 0,0244; un débit d'entrée Q variant de 3,2 l / min à 6,8 l / min; et un débit d'infiltration Q_1 variant de 0 à 10% du débit d'entrée Q .

RESUME DE LA THESE

Les conclusions suivantes ont été obtenues:

La vitesse moyenne du fluide dans la région d'écoulement-libre augmente avec la pente du canal, avec le débit d'entrée, avec le débit d'infiltration; la hauteur d'eau augmente avec le débit d'entrée, mais diminue avec l'augmentation de la pente, et le débit d'infiltration.

La distribution de l'énergie cinétique turbulente normalisée k^+ dans l'écoulement-libre est plus uniforme que la relation empirique pour l'écoulement sur des lits imperméables développés par Nezu et Nakagawa (1993), $k^+ = 4.78 \exp(-2y/d)$. Il est à cause de une pénétration de la turbulence à des niveaux significatifs à la partie supérieure de la région poreuse. La relation empirique de l'énergie cinétique au-dessus de la région poreuse dans la limite de ces simulations est trouvée telle que:

$$k^+ = 2.97e^{(-2y/d)}$$

Le seuil de mise en mouvement des particules sur un lit poreux

Il est important de comprendre les conditions d'écoulement pour lesquelles le transport de sédiments commence à se produire lors des évènements pluvieux. Certains aspects du seuil de mise en mouvement des particules sur un lit poreux ont été étudiés à la fois expérimentalement et numériquement pour la pente du canal S_o variés de 0,0035 à 0,0244; le diamètre des particules d_s varie de 1 à 4 mm, avec ou sans débit d'écoulement d'infiltration Q_1 . Basé sur les valeurs du débit d'entrée et de la pente du canal, le nombre de Reynolds varie de 100 à 8900 pour chaque test et le seuil de mise en mouvement est étudié pour 100 particules de verre placées sur la surface du lit poreux. La probabilité de mise en mouvement des particules est déterminée en comptant le nombre de particules qui quittent leur position d'origine. Ce seuil de mise en mouvement des particules sur un lit poreux a été étudié numériquement en utilisant la

RESUME DE LA THESE

méthode de couplage CFD-DEM, et également expérimentalement avec une caméra rapide. Les principales conclusions sont les suivantes:

- les résultats numériques de simulation correspondent bien aux résultats expérimentaux dans la gamme du nombre de Reynolds testé. Un pourcentage important de mise en mouvement des particules peut être observé avec l'augmentation de la pente du canal .
- Ce pourcentage de mise en mouvement augmente également lorsque le diamètre des particules augmente de 1mm à 2mm, mais reste constant pour un diamètre de 2 à 4 mm .
- Le seuil de mise mouvement diminue avec le taux d'infiltration.

Transport de particules sur un lit poreux

Le transport induit par l'écoulement précédent a été étudié pour des particules millimétriques isolées. Ainsi, 50 particules sont ajoutées une par une à mi-distance du milieu du lit poreux. Les trajectoires des particules ont été simulées à l'aide d'une approche CFD-DEM d'une part et suivies expérimentalement avec une caméra rapide.

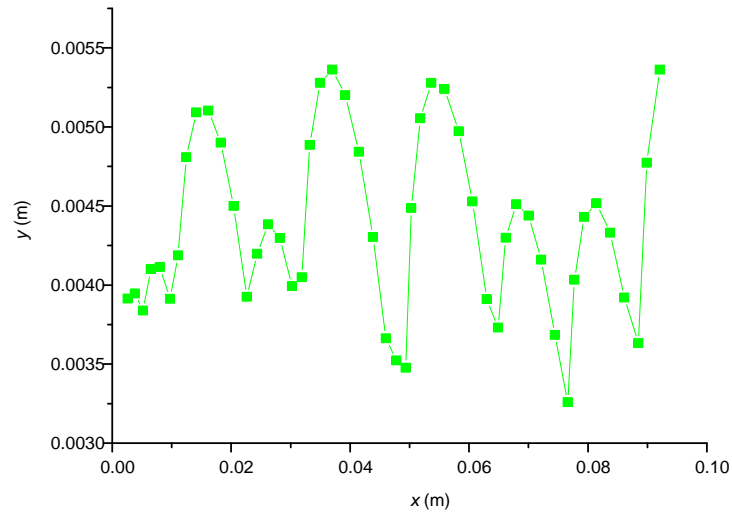
Les conclusions suivantes ont été obtenues:

Les résultats statistiques montrent que les distributions de vitesse des particules suivent des lois normales (Gaussienne) dans chaque cas. La vitesse moyenne des particules augmente avec la pente du canal, le débit d'entrée et le débit d'infiltration, mais il y n'a pas de corrélation positive entre la vitesse et la taille de particule.

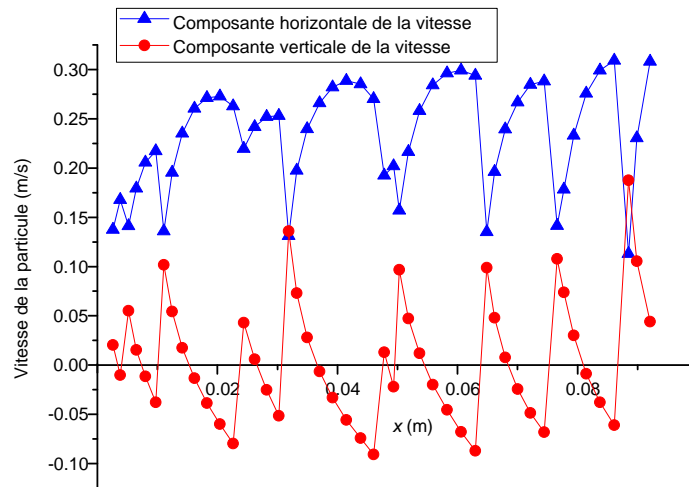
Le mouvement axial des particules est principalement contrôlé par le fluide. Pour une même profondeur d'eau, la composante horizontale de la vitesse des particules normalisée par la vitesse de frottement augmente encore légèrement avec le débit d'entrée, la pente du canal et avec la diminution du diamètre des particules. La vitesse des particules près de la surface du lit poreux est

RESUME DE LA THESE

généralement croissante avec le débit d'infiltration, cette tendance est compatible avec la variation de la vitesse d'écoulement.

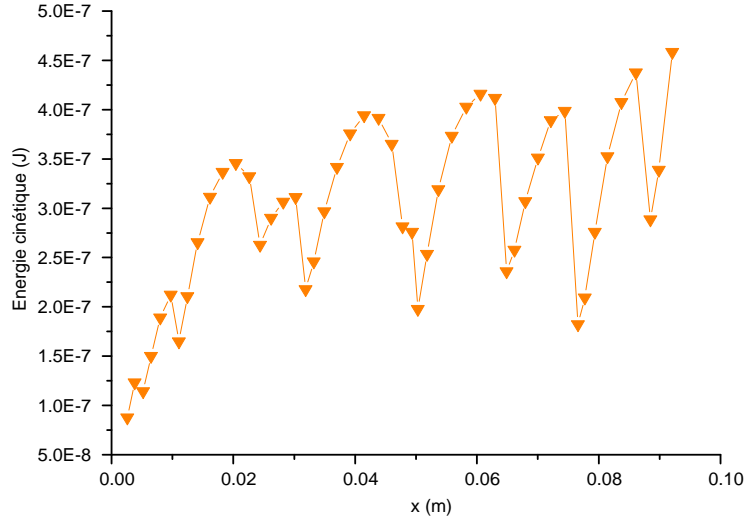


(a)



(b)

RESUME DE LA THESE



(c)

Figure 3. Comportement d'une particule le long du canal (débit d'entrée $Q=6.8$ l/min, débit d'infiltration $Q_1=0.34$ l/min, hauteur $d=9.75$ mm). (a), trajectoire; (b), variation de la vitesse, et (c), variation de l'énergie cinétique

La trajectoire des particules dans un plan vertical est composée d'une partie montante et d'une partie descendante (Figure 3). La composante horizontale de la vitesse moyenne des particules en mouvement de montée ou de descente augmente avec la hauteur des particules. La composante horizontale de la vitesse moyenne des particules en mouvement de montée est plus petite que celle en mouvement de descente. Ce résultat est en accord avec le mouvement de saltation pour lequel les particules accélérées par l'écoulement perdent leur énergie au rebond sur le fond. Les particules n'atteignent jamais leur vitesse terminale de chute lors de leur mouvement vers le bas dans la limite de notre expérience.

La vitesse de transport des particules sur un lit poreux peut être écrite avec une nouvelle formule du type:

$$U_p = U_w - w_0 \left(\frac{44}{Re_p} - \frac{Q_1}{Q} + 0.0734 \right)$$

RESUME DE LA THESE

Quand il n'y a pas de flux d'infiltration et pour $Re_p \approx 44$, cette relation correspond à une loi de Bagnold, par contre lorsque $Re_p > 44$, $\zeta (= (U_w - U_p)/w_0)$ est < 1 .

Le colmatage du lit poreux par des sédiments fins

Le transport et le colmatage par des sédiments fins ont été étudiées uniquement par les mesures expérimentales pour les mêmes valeurs de la pente, du débit et du taux d'infiltration et en utilisant deux types de billes de verre : un de diamètre compris entre 630 et 800 μm et l'autre de diamètre compris entre 1000 et 1250 μm . Une masse de 50 g de particules de verre est ajoutée en amont du lit poreux (201 mm de long) à un taux constant de 1 g/s. Les principales conclusions sont les suivantes:

- La masse de sédiments infiltrés et retenus dans le lit poreux diminue avec l'augmentation de la pente du canal, du débit d'entrée et du diamètre des sédiments.
- Le risque de colmatage augmente avec le débit d'infiltration.
- Le flux de sédiments transportés augmente avec la pente du canal, le débit d'entrée, le diamètre des sédiments et le débit de d'infiltration.

Nos résultats expérimentaux ont été comparés avec les lois classiques de Meyer-Peter-Muller et d'Einstein malgré des conditions d'expériences différentes. L'ensemble des mesures est en bon accord avec ces lois.

Perspectives

Cette thèse a présenté une étude détaillée sur le transport des particules dans un canal ouvert sur un lit poreux en utilisant deux méthodes : expérimentale et numérique. Plusieurs extensions sont envisageables:

- **Influence de la largeur du canal** : les ratios largeur / profondeur de l'écoulement utilisés dans notre expérience sont parfois inférieurs à 5.

RESUME DE LA THESE

L'influence de la largeur ne peut donc pas être ignorée et des expériences avec une largeur de canal variable seraient intéressantes.

- **Porosité du sol** : des études préliminaires avec un lit poreux de porosité moins grande que 0,476 devraient être envisagées pour déterminer l'influence sur le transport de sédiments.
- **Nature du sol** : de même des études avec d'autres types de matériaux poreux peuvent être développées, comme avec des matériaux de chaussée, des sols naturels et des fonds de rivières.
- **Nature du sédiment** : un sédiment plus fin pourrait être utilisé pour l'étude du colmatage.
- **Influence de la pluie** : l'influence de l'intensité de la pluie sur le transport de particules pourrait être considérée dans les recherches futures.
- **Simulation numérique** : le couplage de PFC-DEM a été validé dans de nombreuses situations par nos expériences. Ainsi il est envisageable de l'utiliser pour simuler les expériences susmentionnées. De cette façon, il offre la possibilité de faire varier les paramètres plus facilement. Le calcul parallèle pourrait être développé pour accélérer les capacités de simulation.

RESUME DE LA THESE